MCEER
EARTHQUAKE ENGINEERING TO EXTREME EVENTS

ISSN 1520-295X

A Study of the Coupled Horizontal-Vertical Behavior of Elastomeric and Lead-Rubber Seismic Isolation Bearings

by
Gordon P. Warn and Andrew S. Whittaker

Technical Report MCEER-06-0011

September 22, 2006

This research was conducted at the University at Buffalo, State University of New York and was supported by the Federal Highway Administration under contract number DTFH61-98-C-00094.

NOTICE

This report was prepared by the University at Buffalo, State University of New York as a result of research sponsored by MCEER through a contract from the Federal Highway Administration. Neither MCEER, associates of MCEER, its sponsors, the University at Buffalo, State University of New York, nor any person acting on their behalf:

a. makes any warranty, express or implied, with respect to the use of any information, apparatus, method, or process disclosed in this report or that such use may not infringe upon privately owned rights; or

b. assumes any liabilities of whatsoever kind with respect to the use of, or the damage resulting from the use of, any information, apparatus, method, or process disclosed in this report.

Any opinions, findings, and conclusions or recommendations expressed in this publication are those of the author(s) and do not necessarily reflect the views of MCEER or the Federal Highway Administration.

A Study of the Coupled Horizontal-Vertical Behavior of Elastomeric and Lead-Rubber Seismic Isolation Bearings

by

Gordon P. Warn[1] and Andrew S. Whittaker[2]

Publication Date: September 22, 2006
Submittal Date: August 1, 2006

Technical Report MCEER-06-0011

Task Number 094-D.1-5

FHWA Contract Number DTFH61-98-C-00094

1 Post Doctoral Research Associate, Department of Civil, Structural and Environmental Engineering, University at Buffalo, The State University of New York
2 Professor, Department of Civil, Structural and Environmental Engineering, University at Buffalo, The State University of New York

MCEER
University at Buffalo, The State University of New York
Red Jacket Quadrangle, Buffalo, NY 14261
Phone: (716) 645-3391; Fax (716) 645-3399
E-mail: *mceer@buffalo.edu*; WWW Site: *http://mceer.buffalo.edu*

Preface

The Multidisciplinary Center for Earthquake Engineering Research (MCEER) is a national center of excellence in advanced technology applications that is dedicated to the reduction of earthquake losses nationwide. Headquartered at the University at Buffalo, State University of New York, the Center was originally established by the National Science Foundation in 1986, as the National Center for Earthquake Engineering Research (NCEER).

Comprising a consortium of researchers from numerous disciplines and institutions throughout the United States, the Center's mission is to reduce earthquake losses through research and the application of advanced technologies that improve engineering, pre-earthquake planning and post-earthquake recovery strategies. Toward this end, the Center coordinates a nationwide program of multidisciplinary team research, education and outreach activities.

MCEER's research is conducted under the sponsorship of two major federal agencies, the National Science Foundation (NSF) and the Federal Highway Administration (FHWA), and the State of New York. Significant support is also derived from the Federal Emergency Management Agency (FEMA), other state governments, academic institutions, foreign governments and private industry.

The Center's Highway Project develops improved seismic design, evaluation, and retrofit methodologies and strategies for new and existing bridges and other highway structures, and for assessing the seismic performance of highway systems. The FHWA has sponsored three major contracts with MCEER under the Highway Project, two of which were initiated in 1992 and the third in 1998.

Of the two 1992 studies, one performed a series of tasks intended to improve seismic design practices for new highway bridges, tunnels, and retaining structures (MCEER Project 112). The other study focused on methodologies and approaches for assessing and improving the seismic performance of existing "typical" highway bridges and other highway system components including tunnels, retaining structures, slopes, culverts, and pavements (MCEER Project 106). These studies were conducted to:

- assess the seismic vulnerability of highway systems, structures, and components;
- develop concepts for retrofitting vulnerable highway structures and components;
- develop improved design and analysis methodologies for bridges, tunnels, and retaining structures, which include consideration of soil-structure interaction mechanisms and their influence on structural response; and
- develop, update, and recommend improved seismic design and performance criteria for new highway systems and structures.

The 1998 study, "Seismic Vulnerability of the Highway System" (FHWA Contract DTFH61-98-C-00094; known as MCEER Project 094), was initiated with the objective of performing studies to improve the seismic performance of bridge types not covered under Projects 106 or 112, and to provide extensions to system performance assessments for highway systems. Specific subjects covered under Project 094 include:

- development of formal loss estimation technologies and methodologies for highway systems;
- analysis, design, detailing, and retrofitting technologies for special bridges, including those with flexible superstructures (e.g., trusses), those supported by steel tower substructures, and cable-supported bridges (e.g., suspension and cable-stayed bridges);
- seismic response modification device technologies (e.g., hysteretic dampers, isolation bearings); and
- soil behavior, foundation behavior, and ground motion studies for large bridges.

In addition, Project 094 includes a series of special studies, addressing topics that range from non-destructive assessment of retrofitted bridge components to supporting studies intended to assist in educating the bridge engineering profession on the implementation of new seismic design and retrofitting strategies.

This report presents an analytical and experimental investigation of the coupled horizontal-vertical response of elastomeric and lead-rubber bearings focusing on the influence of lateral displacement on vertical stiffness. Component testing was performed with reduced scale low-damping rubber (LDR) and lead-rubber (LR) bearings to determine vertical stiffness at various lateral offsets. The numerical studies included finite element (FE) analysis of the reduced scale LDR bearing. The results of the experimental and FE investigations were used to evaluate three analytical formulations to predict vertical stiffness at a given lateral displacement. One of the three analytical formulations, based on the Koh-Kelly two-spring model, was shown to predict the measured reduction in vertical stiffness of the LDR and LR bearings at each lateral offset with reasonable accuracy. Earthquake simulation testing was performed to investigate the coupled horizontal-vertical response of a bridge model isolated with LDR or LR bearings. The results of simulations performed with three components of excitation were used to evaluate an equivalent linear static procedure to estimate vertical load due to vertical ground shaking. The procedure was shown to conservatively estimate measured maximum vertical loads due to the vertical component of excitation for most simulations.

ABSTRACT

Elastomeric and lead-rubber bearings are two types of seismic isolation hardware widely implemented in buildings, bridges and other infrastructure in the United States and around the world. These bearings consist of a number of elastomeric (rubber) layers bonded to intermediate steel (shim) plates. The total thickness of rubber controls the low horizontal stiffness and the close spacing of the intermediate shims provides a large vertical stiffness for a given bonded rubber area and elastomer shear modulus. Conceptually, a lead-rubber bearing differs from an elastomeric bearing only through the addition of a lead-core typically located in a central hole. During earthquake ground shaking, the low horizontal stiffness of elastomeric and lead-rubber bearings translates into large lateral displacements, typically on the order of $100-200\,\%$ rubber shear strain, that might lead to significant reductions in the axial load carrying capacity and vertical stiffness of the individual bearings.

This report presents an analytical and experimental investigation of the coupled horizontal-vertical response of elastomeric and lead-rubber bearings focusing on the influence of lateral displacement on the vertical stiffness. Component testing was performed with reduced scale low-damping rubber (LDR) and lead-rubber (LR) bearings to determine the vertical stiffness at various lateral offsets. The numerical studies included finite element (FE) analysis of the reduced scale LDR bearing. The results of the experimental and FE investigations were used to evaluate three analytical formulations to predict the vertical stiffness at a given lateral displacement. From component testing the vertical stiffness of the LDR and LR bearings was shown to decrease with increasing lateral displacement and at a lateral displacement equivalent to $150\,\%$ rubber shear strain a $40-50\,\%$ reduction in vertical stiffness was observed. One of the three analytical formulations, based on the Koh-Kelly two-spring model, was shown to predicted the measured reduction in vertical stiffness of the LDR and LR bearings at each lateral offset with reasonable accuracy. In addition, earthquake simulation testing was performed to investigate the coupled horizontal-vertical response of a bridge model isolated with either LDR or LR bearings. The results of simulations performed with three components of excitation were used to evaluate an equivalent linear static (ELS) procedure for the estimation of the vertical load due to the vertical ground shaking. The equivalent linear static procedure was shown to conservatively estimate measured maximum vertical loads due to the vertical component of excitation for most simulations.

ACKNOWLEDGEMENTS

The research presented in this report was supported by the Federal Highway Administration through Contract DTFH 61-98-C-0094 to the Multidisciplinary Center for Earthquake Engineering Research. However, the opinions expressed in this dissertation are those of the author and do not reflect the opinions of the Multidisciplinary Center for Earthquake Engineering Research or the Federal Highway Administration. No guarantee regarding the results, findings, and recommendations are offered by either the Multidisciplinary Center for Earthquake Engineering Research or the Federal Highway Administration.

The authors would like to thank Dr. Amarnath Kasalanati of Dynamic Isolation Systems, Inc. for generously donating the seismic isolation bearings that facilitated this study and Professor Gilberto Mosqueda for providing a filter routine used to analyze data from earthquake simulation testing. Also sincere thanks to the staff of the Structural Engineering and Earthquake Simulation Laboratory at the State University of New York at Buffalo for their assistance and expertise throughout the experimental portions of this study, including; Chris Budden, Jason Hanley, Goran Josipovic, Duane Kozlowski, Mark Pitman, Bob Staniszewski, Scot Weinreber and Chris Zwierlein. I would also like to thank Richard Vanderwedge of RJ Waston, Inc. for removing the rubber cover from one of the elastomeric bearings tested in this study.

TABLE OF CONTENTS

TABLE OF CONTENTS (CONT'D)

TABLE OF CONTENTS (CONT'D)

TABLE OF CONTENTS (CONT'D)

LIST OF FIGURES

LIST OF FIGURES (CONT'D)

LIST OF FIGURES (CONT'D)

LIST OF FIGURES (CONT'D)

LIST OF TABLES

LIST OF TABLES (CONT'D)

LIST OF NOTATIONS

SYMBOL	DESCRIPTION
a	Ratio of inner radius to outer radius for a hollow circular elastomeric pad
A_b	Bonded rubber area
A_e	Effective bonded rubber area
A_L	Cross-sectional area of lead-core
A_r	Overlapping area between top and bottom bearing end-plates
A_s	Cross-sectional area for equivalent beam-column
b	Radial bias exponent
C_{10}	Finite element material model parameter
D	Diameter of solid circular elastomeric pad
D_i	Inner diameter of hollow circular elastomeric pad
D_o	Outer diameter of hollow circular elastomeric pad
D_1	Finite element material model parameter
E	Young's modulus
E_c	Compression modulus of a single bonded elastomeric pad
Err	Error estimate
f	Frequency
f_n	Frequency of the *n*th mode
f_o	Resonant frequency
f_{st}	Strain amplification factor
f_v	Equivalent vertical frequency of the bridge-isolation system
f_{vo}	Equivalent vertical frequency of the bridge-isolation system considering the isolators with zero lateral displacement
f_1	Frequency ordinate
f_2	Frequency ordinate
F	Factor accounting for central hole in elastomeric pad and a function of the pad geometry
F_H	Lateral force
F_m	Generic force quantity of model
$F_{\max}$	Maximum shear force response of bearing from positive displacement excursion

SYMBOL	DESCRIPTION
$F_{\min}$	Maximum shear force response of bearing from negative displacement excursion
F_p	Generic force quantity of prototype
F_x	Shear force response in x – direction
F_y	Shear force response in y – direction
g	Gravitation acceleration constant
G	Shear modulus
G_{eff}	Effective shear modulus
h	Total height of multi-layer elastomeric bearing
H	Function of hollow elastomeric pad geometry
I	Moment of inertia based on bonded rubber diameter(s)
I_s	Moment of inertia for equivalent beam-column
$\bar{I}_1$	First strain invariant
J	Total volume ratio
K	Bulk modulus
K_b	Generalized stiffness of truss-bridge
K_{bh}	Generalized horizontal stiffness of truss-bridge
K_{bv}	Generalized vertical stiffness of truss-bridge
K_d	Second-slope stiffness of isolator
K_{eff}	Effective stiffness of isolator
K_{eff}^{12}	Effective stiffness of low-damping rubber bearing with 12mm of cover
K_{eff}^{3}	Effective stiffness of low-damping rubber bearing with 3mm of cover
$K_{eq,v}$	Equivalent vertical stiffness of bridge-isolation system
$K_{eq,vo}$	Equivalent vertical stiffness of bridge-isolation system considering the isolators with zero lateral displacement
K_H	Horizontal stiffness
K_i	Vertical stiffness of the *i*th rubber layer of a multi-layer elastomeric bearing
K_θ	Rotational stiffness
K_u	Elastic stiffness of isolator
K_v	Vertical stiffness of multi-layer elastomeric bearing at a given lateral offset

SYMBOL	DESCRIPTION
K_{vo}	Vertical stiffness of multi-layer elastomeric bearing under zero lateral displacement
K_{vo}^{e}	Experimentally determined vertical stiffness of elastomeric bearing with zero lateral displacement
K_{vo}^{t}	Theoretically calculated vertical stiffness of elastomeric bearing
l	Length between string potentiometer housing and point of attachment
l_m	Generic length quantity of model
l_p	Generic length quantity of prototype
m_m	Generic mass quantity of model
m_p	Generic mass quantity of prototype
M	Mass matrix
M^*	Generalized mass of bridge model
n	Number of rubber layers
N	Number of elements in radial direction of finite element models
p	Static pressure
P	Axial load
P_E	Euler buckling load
P_{EQ}	Maximum absolute value of the vertical load on the isolation system due to the vertical component of excitation
$P_{EQ,\max}$	Maximum vertical load on the isolation system due to the vertical component of excitation
$P_{EQ,\min}$	Minimum vertical load on the isolation system due to the vertical component of excitation
P_j	Axial load measured by jth load cell
$P_{\max}$	Maximum axial load
$P_{\min}$	Minimum axial load
P_o	Axial pre-load
P_v	Estimated vertical load on isolation system using equivalent static procedure
P_{vo}	Estimated vertical load on isolation system using equivalent static procedure considering zero lateral displacement across the isolators
Q_d	Zero-displacement force-intercept (Characteristic strength)
r	Polar coordinate axis

SYMBOL	DESCRIPTION
R	Radius of solid circular elastomeric pad
R_i	Inner radius of hollow circular elastomeric pad
R_m	Residual value
R_o	Outer radius of hollow circular elastomeric pad
s	Elongation of linear spring
S	Shape factor
S_a	Acceleration scale factor
$S_{a,v}$	Spectral acceleration from vertical component corresponding to T_v
$S_{a,vo}$	Spectral acceleration from vertical component corresponding to T_{vo}
S_F	Force scale factor
S_g	Gravitational scale factor
S_l	Length scale factor
S_m	Mass scale factor
S_t	Time scale factor
t	Time
t_m	Generic time quantity of model
t_p	Generic time quantity of prototype
t_r	Thickness of an individual rubber layer
t_s	Thickness of intermediate steel shim plate
T	Period of vibration
T_d	Second-slope period of isolator
T_{eff}	Effective period of isolator
T_{m}	Target model period of vibration
T_n	Period of vibration of the *n*th mode
T_{p}	Target prototype period of vibration
T_r	Total thickness of rubber in a multi-layer elastomeric bearing
T_v	Equivalent vertical period of bridge-isolation system
T_{vo}	Equivalent vertical period of bridge-isolation system considering zero lateral displacement across the isolators
$TR(f)$	Transfer function

SYMBOL	DESCRIPTION
$TR_{\max}$	Transfer function amplitude at resonant frequency
u	Displacement amplitude
$u_{\max}$	Maximum positive isolator displacement
$u_{\min}$	Maximum negative isolator displacement
u_o	Bulge amplitude
u_{STP1}	Absolute displacement recorded by string potentiometer number one
u_x	Maximum isolator displacement in the x – direction
u_y	Maximum isolator displacement in the y – direction
$\tilde{u}_y$	Displacement recorded by string potentiometer initially oriented in the y – direction
V	Volume
w	Radial width of individual element
W	Weight acting on an individual isolator
W_D	Energy dissipated per cycle by isolator
W_T	Total static weight of the bridge model
W^*	Effective weight of the bridge model
x	Cartesian coordinate axis
$x(t)$	Time varying input signal
$X(f)$	Frequency response function of time varying input signal
$X^*(f)$	Complex conjugate frequency response function of time varying input signal
y	Cartesian coordinate axis
$y(t)$	Time varying output signal
$Y(f)$	Frequency response function of time varying output signal
z	Cartesian coordinate axis
β_{eff}	Effective horizontal damping ratio of isolator
β_{v}	Effective vertical damping ratio of isolator
γ	Rubber shear strain
γ_{avg}	Average rubber shear strain due to compression
$\gamma_{\max}$	Maximum rubber shear strain due to compression
$\gamma_{t,\mathrm{avg}}$	Average total rubber shear strain

SYMBOL	DESCRIPTION
$\gamma_{t,\max}$	Maximum total rubber shear strain
δ	Vertical deformation of single bonded elastomeric pad
δ_v	Vertical displacement of multi-layer elastomeric bearing
δ_{vt}	Total vertical displacement of multi-layer elastomeric bearing
Δ	Lateral displacement or lateral offset of isolator
ΔR	Radial width of bearing
ΔV	Change in volume
ε_c	Compression strain
ε_i	Principle strain in the *i*th direction
ζ	Critical damping ratio
θ	Rotation
λ_i	Principle stretch ratio for the *i*th direction
$\bar{\lambda}_i$	Deviatoric stretch ratio for the *i*th direction
ν	Poisson's ratio
ρ	Target axial pressure
σ_L	Effective yield strength of lead-core
ϕ	Complementary angle for overlapping area
ϕ_n	Shape function for the *n*th mode

SECTION 1

INTRODUCTION

1.1 General

Seismic isolation is a method for reducing inertial forces that develop in a structure as a result of earthquake ground shaking by lengthening the period of vibration and through added damping. This is accomplished through the introduction of elements (isolators) with low horizontal and large vertical stiffness that decouple the superstructure from the supporting substructure. Elastomeric bearings are one type of isolator consisting of a number of elastomeric (rubber) layers bonded to intermediate steel (shim) plates. The horizontal flexibility (low shear stiffness) of an elastomeric bearing is dictated by the total thickness of rubber whereas the close spacing of the intermediate shim plates provides a large vertical (relative to the shear) stiffness for a given bonded rubber area and elastomer shear modulus.

Over the last two decades seismic isolation hardware has been implemented in numerous buildings, bridges and infrastructure around the world, indicating a growing acceptance amongst the structural engineering community that can be attributed to improved understanding of the behavior of existing seismic isolation hardware, development of new hardware, experimental validation, and the incorporation of design procedures into building and bridge design codes. Prior research has lead to a better understanding and ability to model elastomeric and lead-rubber bearings, including among others, the horizontal force-displacement response (Nagarajaiah et al., 1991) and the coupled horizontal response (Nagarajaiah et al., 1991; Huang, 2002). In addition, research was conducted to improve the understanding of the coupled horizontal-vertical response of elastomeric bearings (Koh and Kelly, 1987) focusing on the influence of axial load on the horizontal stiffness and damping properties. Expressions for the reduction in height and vertical stiffness of elastomeric bearing (Kelly, 1997), subjected to lateral displacement, were later derived from the Koh-Kelly two-spring model (1987).

1.2 Motivation and Objectives

The low horizontal (shear) stiffness required to lengthen a structure's period of vibration if isolated using elastomeric bearings is typically accompanied by large lateral displacements in the isolator (usually on the order of $100-200\%$ rubber shear strain) for design level earthquake ground shaking. These large lateral displacements might lead to substantial reductions in the load-carrying capacity and vertical stiffness of the elastomeric or lead-rubber bearing. The reduction in load-carrying capacity has been investigated (Kelly, 1997; Nararajaiah et al., 1999 and Buckle et al., 2002) and is currently considered for the design of seismic isolation systems composed of elastomeric and/or lead-rubber seismic isolation systems (Buckle and Liu, 1994; Naeim and Kelly, 1999). However, aside from the expression derived from the Koh-Kelly two-spring model (Kelly, 1997) there exists little information, in particularly experimental data, pertaining to the reduction in vertical stiffness. As a result, the state-of-the-art mathematical models implemented in response-history analysis software do not account for the reduction in vertical stiffness, but rather, represent the axial degree-of-freedom as a linear spring with constant stiffness. Furthermore, the impact of the reduction in vertical stiffness on the response of isolated structures subjected to earthquake ground shaking, if any, is largely unknown. However, there are several examples where this behavior might have a significant impact on the performance of the isolation system and surrounding components. For example, in a hybrid isolation system composed of flat sliding and elastomeric bearings. In such as system the elastomeric bearings will decrease in height under lateral deformation (translating into a reduction in vertical stiffness) whereas the flat sliders will remain at the same height (and thus vertical stiffness) likely resulting in axial load redistribution and additional moment in the diaphragm above the plane of isolation.

The objectives of this study are: (1) to investigate the influence of lateral displacement on the vertical stiffness of elastomeric and lead-rubber bearings and to evaluate three formulations for predicting the vertical stiffness at a given lateral displacement, and (2) to investigate the influence of the coupled horizontal-vertical response on the global response of the isolation system and structure. To accomplish these objectives, analytical and experimental studies were conducted to investigate the influence of lateral displacement on the vertical stiffness of low-damping rubber (LDR) and lead-rubber (LR). The results of the experimental and analytical investigation of the influence of lateral displacement on the vertical stiffness were used to evaluate three potential formulations for the design and analysis of seismic isolation systems consisting of elastomeric and lead-rubber bearings. The results of earthquake simulation testing of an isolated bridge model were used to evaluate an equivalent linear static procedure for the estimation of the effect of vertical shaking on axial loads in elastomeric bearings.

1.3 Scope of Work

The scope of work for this study is as follows:

1. Investigate existing and alternative formulations capable of describing the coupled vertical-horizontal response of elastomeric (and lead-rubber) seismic isolators, specifically focusing on the prediction of vertical stiffness at a given lateral offset (displacement).

2. Design model low-damping rubber (LDR) and lead-rubber (LR) bearings for component and earthquake simulation testing in accordance with similitude requirements for earthquake simulation testing using assumed prototype bearing properties.

3. Develop a testing program to characterize the LDR and LR bearings and to experimentally investigate the influence of lateral displacement on the vertical stiffness of these bearings.

4. Develop a program for earthquake simulation testing to investigate the effect of the coupled horizontal-vertical response of individual bearings on the global response of the isolation system and isolated structure.

5. Develop a three-dimensional (3D) finite element (FE) model of the LDR bearings to further investigate the influence of lateral displacement on the vertical stiffness of elastomeric bearings.

6. Evaluate the formulations for the reduction in vertical stiffness with lateral displacement using the experimental and analytical data.

7. Evaluate an equivalent linear static procedure for the estimation of the effect of vertical shaking on axial loads in elastomeric bearings.

1.4 Organization

This report contains ten sections, a list of references and four appendices, organized as follows. Section 2 presents the analysis of elastomeric bearings including a review of the analysis of a single bonded rubber layer in compression and three formulations to predict the vertical stiffness of elastomeric (and lead-rubber) bearings at a given lateral offset. Section 3 presents the design of the model low-damping rubber (LDR) and lead-rubber (LR) bearings that are used for the component and earthquake simulation testing. Section 4 presents the component testing program that consists of characterization testing to determine key mechanical and material properties of the model bearings and lateral offset testing to experimentally investigate the influence of lateral displacement on the vertical stiffness of these bearings. Section 5 presents summary results from characterization and lateral offset testing performed with two LDR and two LR bearings. Section 6 presents a brief discussion of the earthquake simulation testing facilities, the selected ground motion records, the isolated bridge model, instrumentation and the earthquake simulation testing program. Section 7 presents summary results from earthquake simulation testing performed with the LDR and LR bearings and white-noise testing of the bridge model in a fixed base configuration. Section 8 presents the results of a finite element (FE) study analyzing a 3D model of a LDR bearing with various loading conditions intended to replicate selected characterization and lateral offset tests. Section 9 provides a comparison of the results from experimental and analytical investigations of the influence of lateral displacement on the vertical stiffness of elastomeric bearings and an evaluation of an equivalent linear static procedure for the estimation of the effect of vertical earthquake shaking on the axial load in elastomeric bearings. Section 10 provides a summary of the work conducted and the key conclusions and recommendations of this study. Appendix A presents information and calibration data for the 5-channel reaction load cells utilized for component and earthquake simulation testing. Appendix B presents additional results from the characterization and lateral offset testing performed on the LDR and LR bearings. Appendix C presents information on the design of the steel truss-bridge including detailed drawings. Appendix D presents additional results from the earthquake simulation testing.

SECTION 2

ANALYSIS OF ELASTOMERIC SEISMIC ISOLATION BEARINGS

2.1 General

Elastomeric and lead-rubber seismic isolation bearings exhibit a reduction in height under conditions of combined compressive load and lateral displacement. This reduction in height translates into a reduction in the apparent vertical stiffness with lateral displacement. Three formulations to potentially predict the vertical stiffness at a given lateral offset are presented and discussed. The results of experimental and numerical investigations, presented in Section 5 and 8 respectively, are used to evaluate the validity of each of these formulations. The first of the formulations is presented in Kelly (1997) and based on a two-spring mechanical model introduced in Koh and Kelly (1987). The spring properties of the two-spring model are related to the shear and buckling properties of an elastomeric bearing to provide a simple physical understanding of the behavior of elastomeric bearing under conditions of combined loading. The second formulation is based on a widely accepted procedure for the estimation of the critical buckling load of an elastomeric bearing subjected to combined compression and lateral displacement (Naeim and Kelly, 1999). With this procedure, the critical buckling load of the bearings is reduced for lateral displacement using the ratio of the overlapping area between the top and bottom load plates to the bonded rubber area. The third formulation is a piecewise linear relationship empirically derived from the prediction of the two-spring model in conjunction with previous experimental evidence.

Section 2.3 presents the three formulation for the prediction of the vertical stiffness at a given lateral displacement. However, for the benefit of the subsequent sections, this discussion is preceded by a review of previous research related to the analysis of single bonded rubber layers in compression and then extended to multi-layer elastomeric bearings which is presented in Section 2.2. A section summary is presented in Section 2.4.

2.2 Analysis in Compression

2.2.1 General

Previous research by Chalhoub et al. (1990) and Constantinou et al. (1992) provided approximate expressions for the compression modulus of solid and hollow circular bonded elastomeric pads, respectively. The compression modulus is an important parameter for the design of elastomeric bearings and is related directly to the load carrying capacity (buckling load) and vertical stiffness. In addition, Constantinou et al. provided approximate expressions for the calculation of the maximum shear strain due to compressive loading, also an important design consideration. This section summarizes the results of Chalhoub et al. (1990) and Constantinou et al. (1992), focusing on the compression modulus of elastomeric pads, and extends these results to multi-layer elastomeric bearings.

2.2.2 Single Bonded Elastomeric Pad

Figure 2-1 presents illustrations of solid and hollow circular pads subjected to a compressive load, P. In this figure, each pad is shown in the un-deformed condition, with thickness t_r, and deformed condition (shown by dotted lines) with corresponding vertical deformation, δ, and bulge amplitude, u_o. The solid circular pad (figure 2-1a) has a radius, R, whereas the hollow circular pad has an outer radius, R_o, and inner radius, R_i. Also shown in figure 2-1 are the polar coordinate axes, z and r.

Chalhoub et al. derived and subsequently solved a differential equation for the hydrostatic pressure in a solid circular bonded elastomeric pad subjected to compressive loading. The derivation of the differential equation relies on the following assumptions: (1) the elastomer exhibits linear elastic behavior with infinitesimally small strains; (2) points lying on a vertical line parallel to the $z-$axis deform in a parabolic shape; (3) the material is assumed to be in a state of spherical (or tri-axial) state of stress at any point, except the free surface; and (4) the analysis may be treated as axisymmetric. The exact expression for the compression modulus derived by Chalhoub et al. is presented here:

$$E_c = 6GS^2\left(1-\frac{8GS^2}{K}\right)+O(\alpha^6) \tag{2-1}$$

where G is the elastomer shear modulus, K is the bulk modulus, S is the shape factor defined as the ratio of the loaded area to the area free to bulge, α is equal to $S\sqrt{48\,G/K}$, and $O\left(\alpha^6\right)$ is the error associated with neglecting the higher order terms.

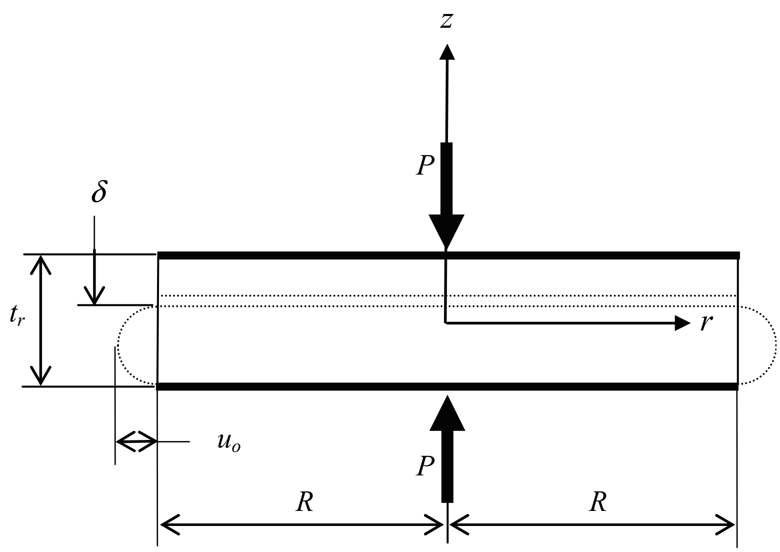

a. solid circular pad

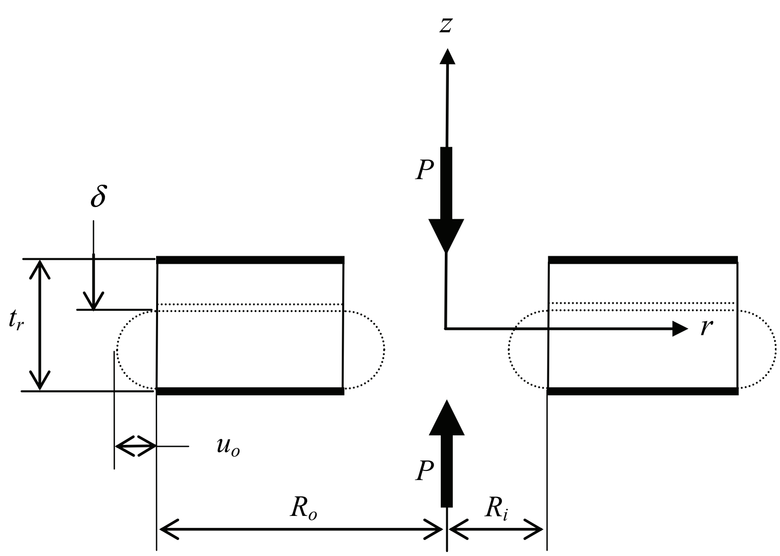

b. hollow circular pad

FIGURE 2-1 Illustration of a single bonded rubber layer subjected to compressive load

The shape factor (generally defined as the ratio of the loaded area to the area free to bulge) for a solid circular pad is:

$$S = \frac{D}{4t_r} \tag{2-2}$$

where D is the pad diameter equal to $2R$ and t_r is the pad thickness as defined previously. If the material is assumed to be incompressible, i.e., $K \to \infty$, then (2-1) reduces to (2-3).

$$E_c = 6GS^2 \tag{2-3}$$

In addition, Chalhoub et al. proposed an approximate expression for the compression modulus, for small values of $8GS^2/K$:

$$\frac{1}{E_c} \approx \frac{1}{6GS^2} + \frac{4}{3K} \tag{2-4}$$

and recommended its use for shape factors, S, ranging from 1 to 24. For seismic isolation bearings, the shape factor typically ranges from 10 to 15. Although shape factors outside this range are possible, bearings with shape factors less than 10 are prone to instability at large lateral displacements and the upper value of 15 intended to limit the maximum shear strain due to compressive loading (AASHTO, 1999). Additionally, Chalhoub et al. provided an equation to calculate the compression modulus for $S > 24$ but that equation is not presented here.

Often, multi-layer elastomeric bearings are constructed with a central hole serving the primary purpose of allowing heat to penetrate the center of the bearing during the curing process (Constantinou et al., 1992). Although the central hole is introduced for manufacturing purposes, it alters the pressure distribution and alters the shape factor, both of which reduce the compression modulus and consequentially the vertical stiffness. However, shape factor alone can not account for this effect, rather, the governing differential equation must be solved using the appropriate boundary conditions. The governing differential equation and general solution presented in Chalhoub et al. apply to hollow circular pads but the boundary conditions used to arrive at the particular solution do not. Constantinou et al. (1992) solved the governing equation using the appropriate boundary condition for a hollow circular pad arriving at the following expression for the compression modulus:

$$E_c = 6GS^2F\left[1 - \frac{8GS^2}{K}H\right] \tag{2-5}$$

where F is a function of the inner and outer pad diameter and H is a length function not presented here. Although not presented here, the ratio H/F was shown by Constantinou et al. to be approximately equal to 1.0 for D_o/D_i ranging from 1 to 100 a result utilized to simplify the expression for the compression modulus. Again, if the material is assumed to be incompressible, $K \to \infty$, (2-5) then reduces to:

$$E_c = 6GS^2F \tag{2-6}$$

and F is calculated according to:

$$F = \frac{\left(\frac{D_o}{D_i}\right)^2 + 1}{\left(\frac{D_o}{D_i} - 1\right)^2} + \frac{1 + \frac{D_o}{D_i}}{\left(1 - \frac{D_o}{D_i}\right)\ln\left(\frac{D_o}{D_i}\right)} \tag{2-7}$$

where D_o is the outer diameter of the pad equal to $2R_o$ and D_i is the outer diameter equal to $2R_i$, see figure 2-1b. Constantinou et al. showed that F approaches $2/3$ as D_o/D_i approaches 1 and F approaches 1 as D_o/D_i approaches ∞ (equivalent to a circular solid pad). The shape factor for a hollow circular pad is calculated according to (2-8).

$$S = \frac{D_o - D_i}{4t} \tag{2-8}$$

Constantinou et al. presented an approximate expression for the compression modulus, again for small values of $8GS^2H/K$, and is presented in (2-9).

$$\frac{1}{E_c} \approx \frac{1}{6GS^2F} + \frac{4}{3K}\left(\frac{H}{F}\right) \tag{2-9}$$

As previously stated, Constantinou et al. (1992) showed the ratio H/F to be approximately equal to 1.0 for D_o/D_i ranging from 1 to 100. Therefore, simplifying (2-9) accordingly yields (2-10).

$$\frac{1}{E_c} \approx \frac{1}{6GS^2F} + \frac{4}{3K} \tag{2-10}$$

The approximate expression presented in (2-10) was shown by Constantinou et al. to agree well with the exact solution and the results of finite element analyses for D_o / D_i equal to 5 and 10, which are typical values for hollow circular bearings.

2.2.3 Multi-layer Elastomeric Bearing

A multi-layer elastomeric bearing is composed of a number of elastomeric layers separated by intermediate steel (shim) plates. The total thickness of rubber dictates the shear stiffness whereas the close spacing of the intermediate shim plates results in a large (relative to the shear) vertical stiffness. The multi-layer elastomeric bearing is analogous to the series spring system illustrated in figure 2-2.

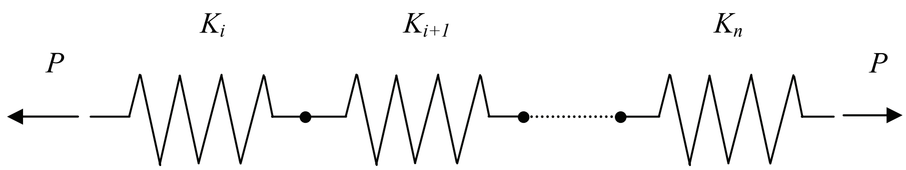

FIGURE 2-2 Illustration of a series spring system

In this figure, each individual spring represents a rubber layer and the entire system of springs a multi-layer elastomeric bearing with stiffness:

$$\frac{1}{K_{vo}} = \sum_{i=1}^{n} \frac{1}{K_i} \tag{2-11}$$

where K_i is the stiffness of the ith spring, K_{vo} is the stiffness of the spring system and n is the number of springs (rubber layers). The stiffness of an individual bonded rubber layer is calculated according to:

$$K_i = \frac{E_{c,i}\, A_{b,i}}{t_{r,i}} \tag{2-12}$$

where $E_{c,i}$ is the compression modulus of the ith bonded rubber layer as discussed in the previous section, $A_{b,i}$ is the bonded area of the ith layer and $t_{r,i}$ is the thickness of the ith rubber layer. Substituting (2-12) into (2-11) yields a general equation for the vertical stiffness of a multi-layer elastomeric bearing accommodating variations in the individual rubber layers.

$$\frac{1}{K_{vo}} = \sum_{i=1}^{n} \frac{t_{r,i}}{E_{c,i} A_{b,i}} \tag{2-13}$$

Typically the individual rubber layer are assumed to have equal thickness, bonded rubber area, and therefore compression modulus simplifying (2-13) to:

$$K_{vo} = \frac{E_c A_b}{T_r} \tag{2-14}$$

where T_r is the total thickness of rubber equal to $n t_r$. For the purpose of design, the individual rubber layers are assumed to be uniform and the vertical stiffness is calculated using (2-14).

2.3 Influence of Lateral Displacement on the Vertical Stiffness

2.3.1 Two-Spring

The two-spring mechanical model introduced by Koh and Kelly (1987) is presented here and used to illustrate the derivation of an expression for the reduction in height with lateral displacement and subsequently an expression for the vertical stiffness. An illustration of the two-spring model in the un-deformed and deformed configuration is presented in figure 2-3. This model consists of a linear spring with stiffness K_H, a rotational spring with stiffness K_θ, two frictionless rollers, and a rigid column all supported by a pin with applied axial load; P, and lateral force; F_H. Figure 2-3b shows the resulting lateral displacement at the top of the column; Δ, rotation about the pin; θ, reduction in height; δ_v, and deformation of the linear spring; s.

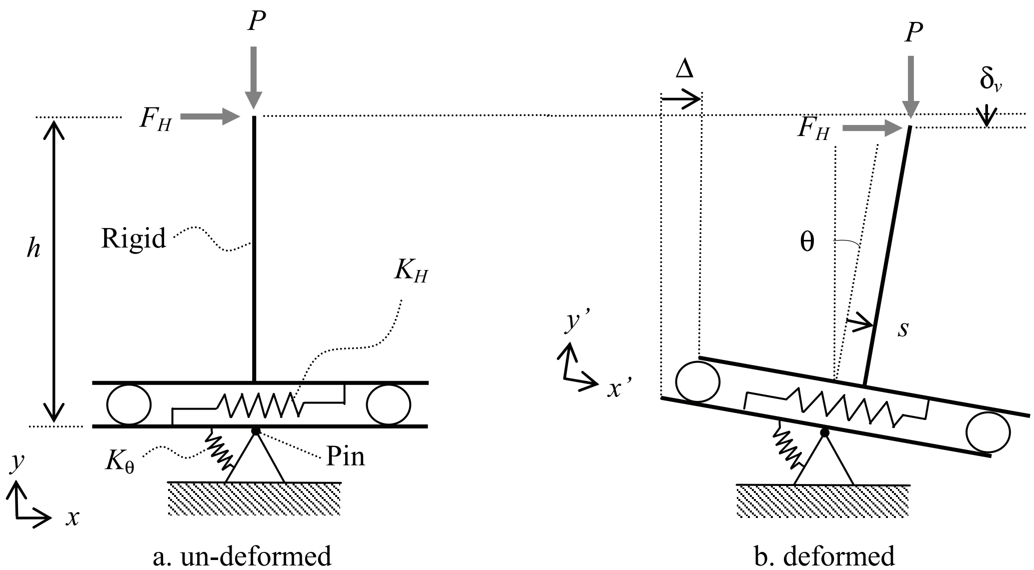

FIGURE 2-3 Illustration of the two-spring model in the un-deformed and deformed configurations

The derivation for the reduction in height, or vertical displacement, of the two-spring model due to F_H and P is obtained by first considering the deformed configuration; see figure 2-3b. The global deformation quantities Δ and δ_v can be related to the local deformation quantities s and θ through geometry according to (2-15) and (2-16).

$$\Delta = s\cos(\theta) + h\sin(\theta) \tag{2-15}$$

$$\delta_v = s\sin(\theta) + h[1-\cos(\theta)] \tag{2-16}$$

Two components contribute to the vertical displacement. The first, $s\sin(\theta)$, due to the component of deformation of the rotated linear spring and the second, $h[1-\cos(\theta)]$, due to the rotation of the column by an angle, θ. Equations (2-15) and (2-16) can be simplified by assuming small rotations and replacing $\sin(\theta)$ with θ and $\cos(\theta)$ with 1. However, approximating $\cos(\theta)$ with 1, the first term of the Taylor series expansion of $\cos(\theta)$, cancels the second term in (2-16). To retain this term, $\cos(\theta)$ is approximated with:

$$\cos(\theta) \approx 1 - \frac{\theta^2}{2} \tag{2-17}$$

representing the first two terms of the Taylor series expansion of $\cos(\theta)$. Substituting these approximation into (2-15) and (2-16) results in the following equations for the global deformation variables.

$$\Delta = s + h\theta \tag{2-18}$$

$$\delta_v = s\theta + \frac{h\theta^2}{2} \tag{2-19}$$

Considering equilibrium of the model in the deformed configuration and again assuming small rotations, the following equilibrium equations are obtained.

$$\Sigma F_{x'}: \quad -P\theta + K_H s = F_H \tag{2-20}$$

$$\Sigma M_{\text{pin}}: \quad (K_\theta - Ph)\theta - Ps = F_H h \tag{2-21}$$

To relate the spring properties of the two-spring model to the mechanical properties of an elastomeric bearing each degree-of-freedom is considered individually. Consider first the case of $K_\theta \to \infty$. For this case the deformation is solely a function of the linear spring and the spring stiffness can be related to the shear stiffness of an elastomeric bearing according to:

$$K_H = \frac{G A_b}{T_r} \tag{2-22}$$

Noting the equilibrium equations are in terms of h, the total height of the bearing. The shear stiffness is therefore re-expressed as:

$$K_H = \frac{G A_s}{h} \tag{2-23}$$

where $A_s = A_b h / T_r$. For the second case, consider $K_H \to \infty$ (i.e., no shear deformations) and $F_H = 0$, the buckling load of the model (i.e., a rigid column supported by a rotational spring and a pin) is given by (2-24).

$$P = \frac{K_\theta \theta}{h \sin(\theta)} = \frac{K_\theta}{h} \tag{2-24}$$

The buckling load of the model (K_θ / h) is equated to the Euler buckling load (P_E) of an elastomeric bearings to obtain an expression for the stiffness of the rotational spring and is shown in (2-25).

$$K_\theta = P_E h \tag{2-25}$$

Substituting the expressions for K_H [(2-23)] and K_θ [(2-25)] into the equilibrium equations yields:

$$-P\theta + G A_s \frac{s}{h} = F_H \tag{2-26}$$

$$(P_E - P)\theta - P\frac{s}{h} = F_H \tag{2-27}$$

that represent a system of equations with unknowns θ and s/h. The solution to the systems of equations, θ and s/h, are presented in (2-28) and (2-29).

$$\theta = F_H \frac{G A_s + P}{G A_s (P_E - P) - P^2} \tag{2-28}$$

$$\frac{s}{h} = F_H \frac{P_E}{G A_s (P_E - P) - P^2} \tag{2-29}$$

Substituting (2-28) and (2-29) into (2-18) and solving for F_H yields the following:

$$F_H = \frac{\left[GA_s (P_E - P) - P^2 \right]}{(GA_s + P + P_E)} \frac{\Delta}{h} \tag{2-30}$$

First, substituting (2-30) into (2-28) and (2-29) then substituting the resulting expressions into (2-18) provides the following expression for the reduction in height.

$$\delta_v = \frac{\Delta^2}{2h} \frac{(G A_s + P)(P + G A_s + 2P_E)}{(G A_s + P + P_E)^2} \tag{2-31}$$

However, for seismic isolation bearings it is reasonable to assume $G A_s << P_E$ and $P << P_E$. By neglecting the $G A_s$ and P terms where they are summed with P_E, (2-31) reduces to (2-32).

$$\delta_v = \frac{(G A_s + P)}{P_E} \frac{\Delta^2}{h} \tag{2-32}$$

Noting that the Euler buckling load of a column is $P_E = \pi^2 E I_s / h^2$. Assuming $E \approx E_c / 3$ (i.e., incompressible material) and substituting these expressions along with $I_s = Ih/T_r$ into (2-32) yields the vertical displacement of the two-spring model due to a compressive load P and a lateral displacement Δ.

$$\delta_v = \frac{3h(G A_b h + P T_r)\Delta^2}{\pi^2 T_r E_c I} \tag{2-33}$$

The total vertical displacement due to the applied compressive load plus the lateral displacement is presented in (2-34).

$$\delta_{vt} = \frac{P T_r}{E_c A_b} + \frac{3h(G A_b h + P T_r)\Delta^2}{\pi^2 T_r E_c I} \tag{2-34}$$

The expression for the total vertical displacement derived, in part, from the two-spring model is utilized to formulate an expression for the apparent vertical stiffness in the deformed configuration. Assuming at a particular lateral displacement the axial load versus vertical displacement response is linear the vertical stiffness can be expressed according to (2-35).

$$K_v = \frac{P}{\delta_{vt}} \tag{2-35}$$

Rearranging the terms in (2-34) and solving for P / δ_{vt} yields:

$$K_v = \frac{E_c A_b}{T_r} \frac{1}{\left[1 + \frac{3 G A_b^2 \Delta^2}{\pi^2 I P}\left(\frac{h}{T_r}\right) + \frac{3 A_b \Delta^2}{\pi^2 I}\right]} \tag{2-36}$$

noting, for the case $\Delta = 0$, the right hand side of (2-36) reduces to $E_c A_b / T_r$ and is equal to K_{vo}. Equation (2-36) represents the apparent vertical stiffness of an elastomeric bearing at a given lateral displacement. Normalizing (2-36) by K_{vo} and letting $A_b = A_s T_r / h$ gives (2-37).

$$\frac{K_v}{K_{vo}} = \frac{1}{\left[1 + \frac{3A_b\Delta^2}{\pi^2 I}\left(1 + \frac{GA_s}{P}\right)\right]} \tag{2-37}$$

Typically for seismic isolation bearings $GA_s < P$. For example, the "$500\,\text{kip}$" Lead-rubber bearing (HITEC, 1998a) with $G = 0.6\,\text{MPa}$, $A_b = 0.26\,\text{m}^2$ and a design load of $2224\,\text{kN}$ results in $GA_b / P = 0.06$. However, to investigate the sensitivity of (2-37) to the quantity GA_s / P, a solid circular cross-section is assumed for simplicity with $A_b = \pi R^2$ and $I = \pi R^4 / 4$. The cross sectional properties are substituted into (2-37) resulting in the following expression.

$$\frac{K_v}{K_{vo}} = \frac{1}{\left[1 + \frac{12}{\pi^2}\left(\frac{\Delta}{R}\right)^2\left(1 + \frac{GA_s}{P}\right)\right]} \tag{2-38}$$

Equation (2-38) is evaluated for several values of GA_s / P for Δ / R ranging from 0 to 2.2. The results of this evaluation are plotted in figure 2-4a. From the curves presented in figure 2-4a, K_v / K_{vo} is observed to increase as GA_s / P decreases for $\Delta / R > 0$. Based on the marginal impact of the GA_s / P term on the value of K_v / K_{vo} for the range of values considered, and the knowledge that elastomeric seismic isolation bearings are typically designed such that $GA_s < P$, it appears reasonable to simplify (2-38) by neglecting this term.

Therefore, neglecting the GA_b / P term in (2-37) results in (2-39).

$$\frac{K_v}{K_{vo}} = \frac{1}{\left[1 + \frac{3}{\pi^2}\left(\frac{A_b\Delta^2}{I}\right)\right]} \tag{2-39}$$

As stated previously elastomeric bearings are often constructed with a central hole. To gain an understanding of the influence of a central hole on the normalized vertical stiffness, a generic hollow circular cross-section with outer radius R_o and inner radius R_i is assumed. For simplicity let $R_i = a R_o$ where $0 \le a < 1$. Substituting $A_b = \pi\left(R_o^2 - R_i^2\right)$ and $I = \pi\left(R_o^4 - R_i^4\right)/4$ into (2-37) with $GA_s / P = 0$ results in (2-40).

$$\frac{K_v}{K_{vo}} = \frac{1}{\left[1+\frac{12}{\pi^2}\frac{\Delta^2}{\left(R_o^2+R_i^2\right)}\right]} \tag{2-40}$$

Further substituting $R_i = aR_o$ into (2-40) results in (2-41).

$$\frac{K_v}{K_{vo}} = \frac{1}{\left[1+\frac{12}{\pi^2}\left(\frac{1}{1+a^2}\right)\left(\frac{\Delta}{R_o}\right)^2\right]} \tag{2-41}$$

Consider, for example, $a = 1/10$ and $\Delta = 2R$; (2-41) gives $K_v / K_{vo} = 0.172$. In addition, for $a = 1/5$, (2-41) gives $K_v / K_{vo} = 0.176$. To further investigate the influence of the radius of the central hole, (2-41) is evaluated for several values of a (including $a = 0$ corresponding to a solid circular cross section) the results of which are plotted in figure 2-4b.

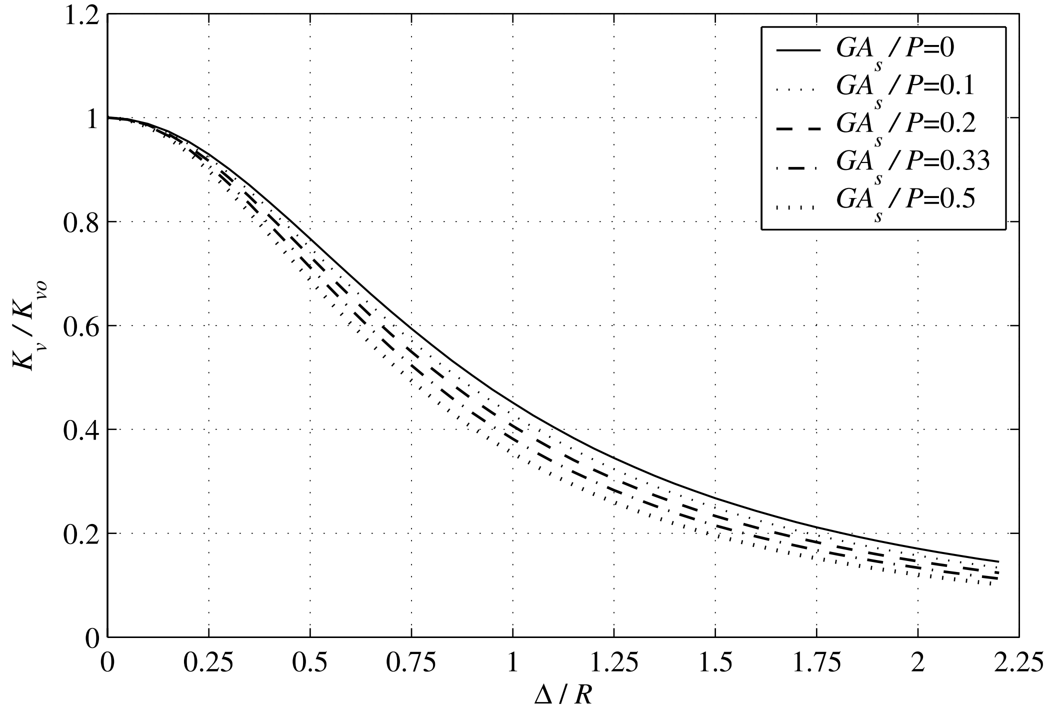

a. evaluation of (2-38)

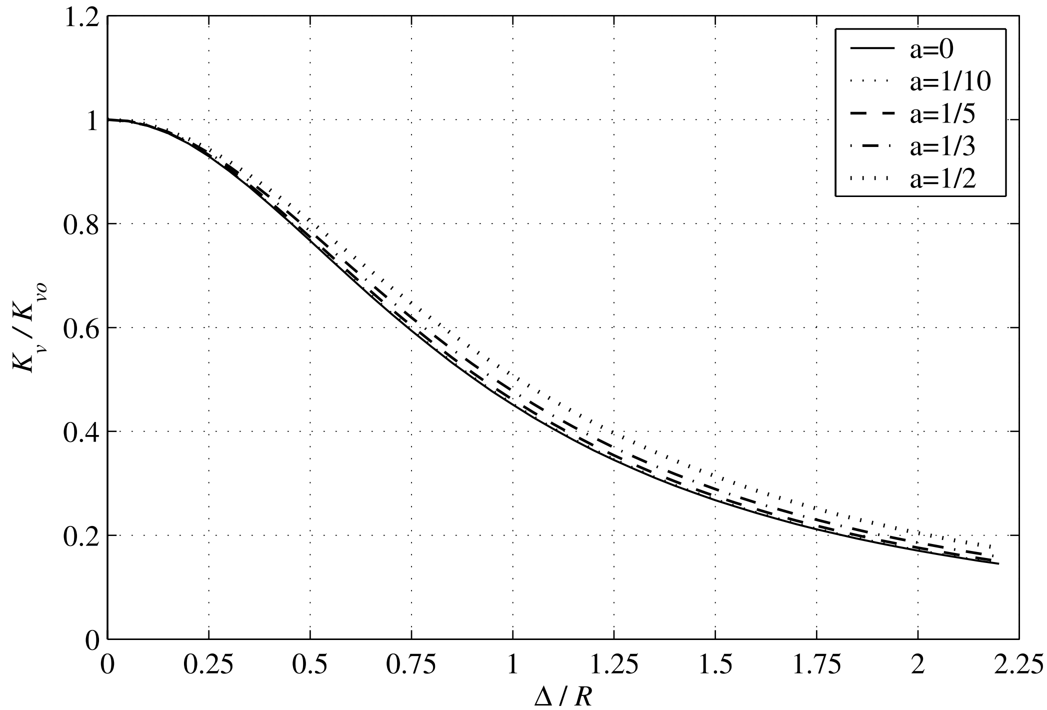

b. evaluation of (2-41)

FIGURE 2-4 Evaluation of the two-spring formulation

From the curves plotted in figure 2-4b and the sample calculations, the value of K_v / K_{vo} does not appear to be sensitive to the value of a even for $a = 1/2$, that is, a hollow circular bearing with an inner radius, R_i, equal to half the outer radius, R_o. Based on the results of this analysis it appears reasonable to neglect the GA_s / P term in (2-37) and to use the properties of a generic solid circular cross-section ($A_b = \pi R^2$ and $I = \pi R^4 / 4$), simplifying the normalized vertical stiffness expression to (2-42).

$$\frac{K_v}{K_{vo}} = \frac{1}{\left[1 + \frac{12}{\pi^2}\left(\frac{\Delta}{R}\right)^2\right]} \tag{2-42}$$

2.3.2 Overlapping Area

A concept widely accepted for the estimation of the critical buckling load of an elastomeric bearing subjected to combined compression and lateral displacement (Buckle and Liu, 1994; Naeim and Kelly, 1999) is adapted here for the estimation of the vertical stiffness at a given lateral displacement. This concept uses the ratio of the overlapping area between the top and bottom load plates to the bonded rubber area as a factor reducing the vertical stiffness for lateral displacements greater than zero and is illustrated in figure 2-5.

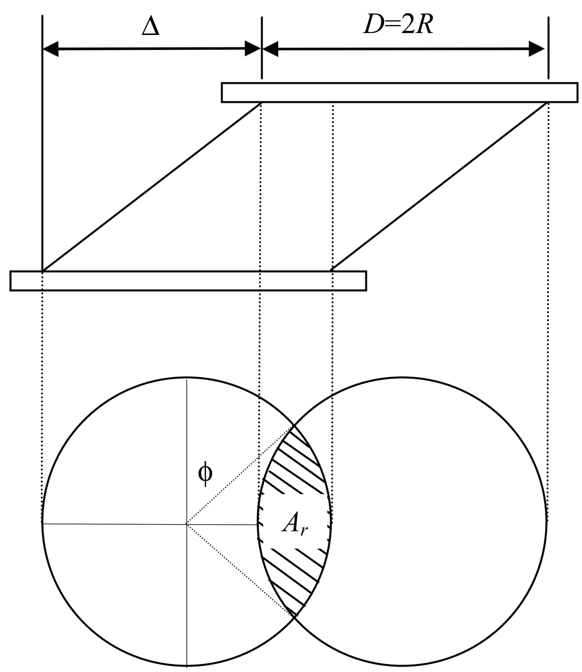

FIGURE 2-5 Illustration of the overlapping area for a solid circular bearing subjected to lateral displacement

The vertical stiffness, in normalized form, is then calculated according to:

$$\frac{K_v}{K_{vo}} = \left(\frac{A_r}{A_b}\right) \tag{2-43}$$

where A_r is the overlapping area for a solid circular bearing subjected to a lateral displacement, Δ, and A_b is again the bonded rubber area equal to πR^2 and K_{vo} is the initial vertical stiffness. The overlapping area is calculated according to:

$$A_r = \frac{D^2(\phi - \sin\phi)}{4} \tag{2-44}$$

where $D = 2R$ and ϕ calculated according to (2-45).

$$\phi = 2\arccos\left(\frac{\Delta}{D}\right) \tag{2-45}$$

From (2-45) for $\Delta = 2R$, $\phi = 0$ and A_r correctly equals 0. Also for $\Delta = 0$, (2-45) gives $\phi = \pi$. Substituting $\phi = \pi$ into (2-44) yields $A_r = \pi D^2/4$ which is equal to A_b for a solid circular cross section. Therefore the overlapping area correctly predicts $K_v / K_{vo} = 1$ at $\Delta = 0$ and predicts $K_v / K_{vo} = 0$ at $\Delta = 2R$. Equation (2-43) is plotted in figure 2-6 for Δ / R ranging from 0 to 2.25. Although the overlapping area concept is simple and could be easily implemented for the analysis of elastomeric isolation systems it is not based on any rigorous theory and does not fully capture the physical behavior of elastomeric bearings subjected to combined compressive and lateral loading.

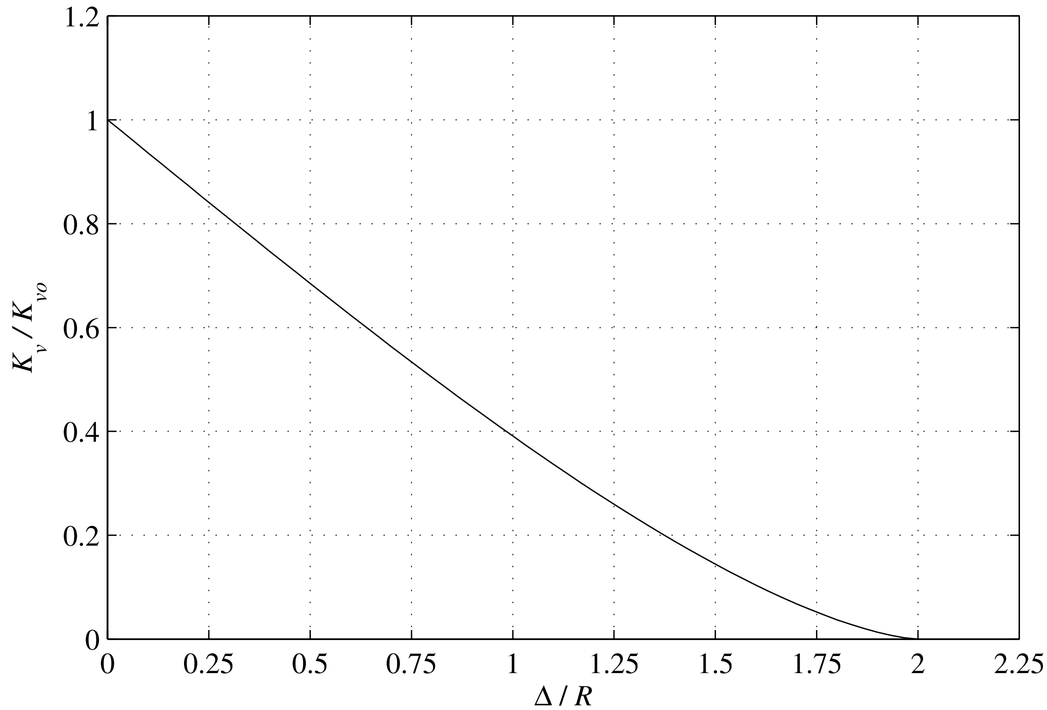

FIGURE 2-6 Evaluation of the overlapping area formulation

2.3.3 Piecewise Linear

A piecewise linear relationship for the vertical stiffness at a given lateral displacement is considered. This formulation is empirically derived based on two conditions: for $\Delta = 0$, K_v / K_{vo} must equal 1 and from the previous analysis of the two-spring model and previous experimental evidence, $K_v / K_{vo} \approx 0.2$ at $\Delta = 2R$. In addition, the vertical stiffness is assumed to decrease linearly with increasing lateral displacement up to $\Delta = 2R$ then remain constant that results in the piecewise linear expression presented in (2-46).

$$\begin{aligned} \frac{K_v}{K_{vo}} &= 1 - 0.4\left(\frac{\Delta}{R}\right) \quad \text{for} \quad \Delta/R \le 2 \\ \frac{K_v}{K_{vo}} &= 0.2 \qquad\qquad\quad \text{for} \quad \Delta/R > 2 \end{aligned} \tag{2-46}$$

Equation (2-46) is plotted in figure 2-7. Again, although not based on rigorous theory, (2-46) offers a simple relationship which according to empirical evidence predicts the vertical stiffness is greater than zero for $\Delta = 2R$.

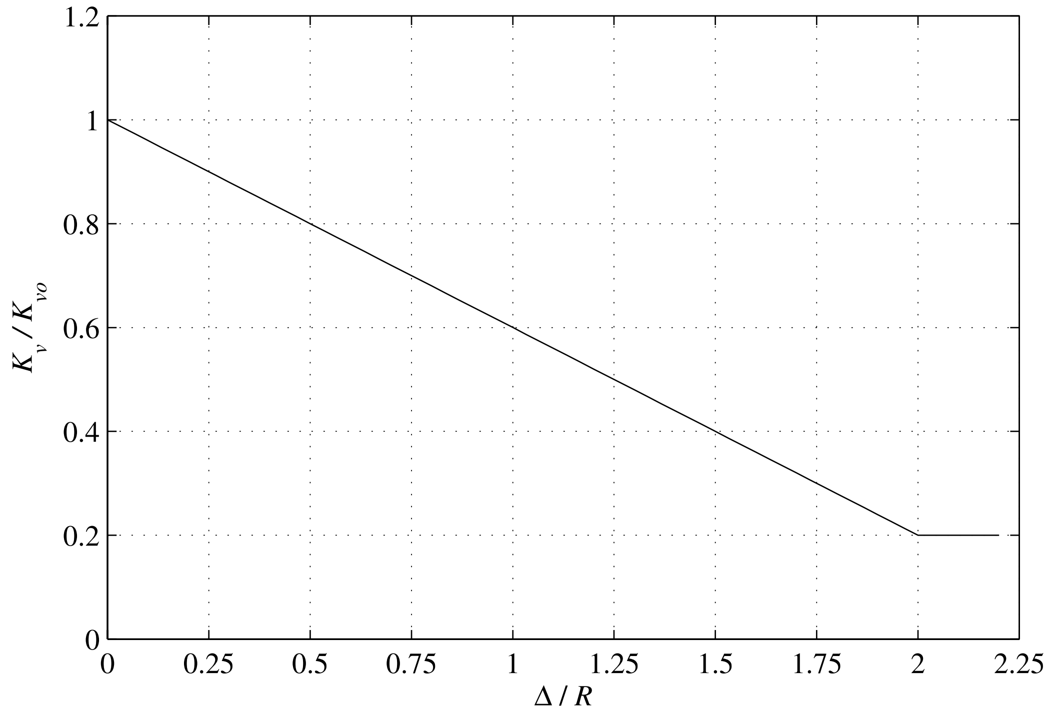

FIGURE 2-7 Evaluation of the piecewise linear formulation

2.4 Summary

This Section served to review previous research on the analysis of a single bonded rubber layer in compression focusing on the determination of the compression modulus for solid and hollow circular pads for compressible and incompressible material assumptions. In addition three formulation to account for the reduction in vertical stiffness with lateral displacement were presented and discussed.

General observation from the three formulations are as follows. The two-spring formulation is derived from a model capable of reproducing the behavior of elastomeric bearings subjected to combined loading and predicts $K_V > 0$ for $\Delta > 2R$ which agrees with experimental evidence. The overlapping area formulation although simple and based on an accepted procedure has no theoretical basis and predicts $K_V = 0$ for $\Delta = 2R$ which conflicts with experimental evidence. The piecewise linear is a simple expression however empirically derived from the evaluation of the two-spring model in conjunction with experimental evidence having no theoretical basis.

SECTION 3

SPECIMEN DESIGN

3.1 General

Model low-damping rubber (LDR) and lead-rubber (LR) seismic isolation bearings were designed and fabricated for the purpose of component and earthquake simulation testing. To facilitate the design of the model bearings, typical mechanical and material properties for elastomeric and lead-rubber seismic isolation bearings were selected for the prototype bearing. The model bearings were then proportioned according to the assumed prototype properties, similitude requirements, and manufacturing constraints, including among others, the maximum permissible outer diameter based on an existing mold (a cavity with specific diameter and depth used in the manufacturing process).

This section is organized into four sub-sections. Section 3.2 provides a discussion of the assumed prototype bearing properties. Section 3.3 presents the scaling procedure for dynamic similitude for earthquake simulation testing. The specified model bearing dimensions and properties, and the as-built bearing dimensions are presented in Section 3.4.

3.2 Prototype Bearing Properties

Typical values for the mechanical and material properties of elastomeric and lead-rubber seismic isolation bearings used in bridge (and building) construction were assumed for the prototype LR and LDR bearings (HITEC, 1998a and HITEC, 1998b). A list of key mechanical and material properties for the LR and LDR bearings along with assumed values is presented in table 3-1.

TABLE 3-1 Prototype bearing properties

Parameter			Bearing Type	
Description	Notation	Units	LDR	LR
Effective period	T_{eff}	s	2.5	TBD[1]
Second-slope period	T_d	s	NA[2]	2.5
Normalized characteristic strength	Q_d / W	-	NA	0.09
Static pressure	p	MPa	3.45	3.45
Effective yield strength of lead	σ_L	MPa	NA	10.3
Shear modulus	G	MPa	0.55	0.55
Effective damping	β_{eff}	%	≤ 5	20

Notes:
1. TBD indicates the value of the parameter will be determined in a subsequent section.
2. NA: indicates this parameter is not applicable to the particular type of bearing.

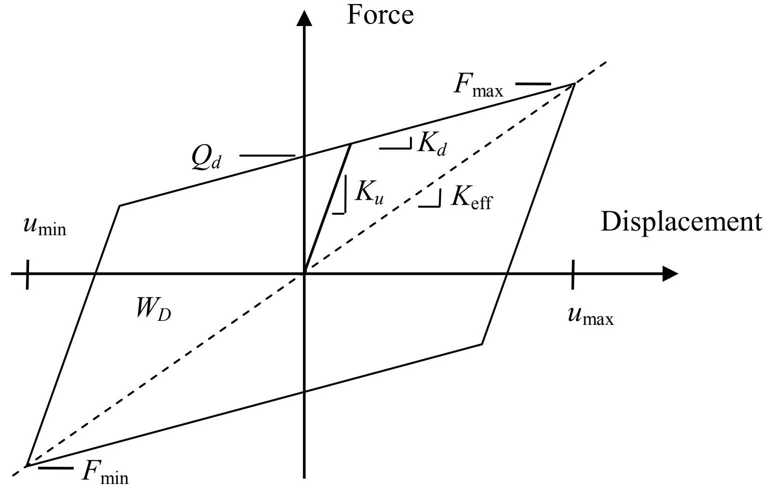

FIGURE 3-1 Idealized bilinear force-displacement relationship for a seismic isolation bearing

For illustrative purposes an idealized bilinear force-displacement relationship is presented in figure 3-1. This figure identifies key response quantities including: u_{max} the maximum isolator displacement in the positive direction; u_{min} the maximum isolator displacement in the negative direction; F_{max} the shear force corresponding to u_{max} and F_{min} the shear force corresponding to u_{min}. Also shown in figure 3-1 are important mechanical properties including: K_{eff} the effective stiffness; K_u the "elastic" stiffness; K_d the second-slope stiffness; Q_d the characteristic strength; and W_D the energy dissipated per cycle.

A primary design parameter of the prototype LDR and LR bearings is the period of vibration related to the shear stiffness of the rubber and the supported weight. For a LDR bearing this period is the effective period (T_{eff}) and is related to the effective stiffness (K_{eff}) while for the LR bearing it is the second-slope period (T_d) related to the second-slope stiffness (K_d), see figure 3-1. For the prototype LDR and LR bearings T_{eff} and T_d were assumed to be equal to $2.5\,\mathrm{s}$, respectively. In the subsequent section, this assumption along with the target model periods dictate the model scale. For lead-rubber bearings an additional mechanical property is required to define the force-displacement relationship, namely, the characteristic strength, presented here normalized by the weight acting on the isolator (denoted Q_d / W) and assumed to be equal to 0.09. In addition, both the LR and LDR prototype bearings are assumed to carry a design compressive load corresponding to a static pressure, p, equal to $3.45\,\mathrm{MPa}$. This assumption will form the basis for the added mass required for earthquake simulation testing.

The values assumed for the material properties of the prototype bearings are typical of those used in the construction of elastomeric and lead-rubber seismic isolation bearings in bridges. The effective yield strength, σ_L, of the lead-core in the LR bearings is assumed to be equal to $10.3\,\text{MPa}$ ($1500\,\text{psi}$) and is based on the average of the first three cycle from results presented in HITEC (1998a). The elastomeric material for both LR and LDR bearings is assumed to be low-damping, low-modulus natural rubber material with shear modulus, G, equal to $0.55\,\text{MPa}$ ($80\,\text{psi}$) at 100% rubber shear strain. Finally, the effective damping ratio, β_{eff}, is assumed to be 20% for the LR and 5% or less for the LDR bearings.

3.3 Similitude Requirements

The scaling procedure described in this section was used to design the seismic isolation system, proportion the individual seismic isolation bearings and to determine the required model weight. As the steel truss-bridge structure used for earthquake simulation testing was designed for general use in the Structural Engineering and Earthquake Simulation Laboratory (see Appendix C) the resulting isolated bridge model is not representative of a particular prototype structure and therefore does not represent a true model. However, the response of seismically isolated structures is primarily a function of the isolation system and not the super-structure therefore the isolated bridge model used in this study is considered adequate.

To facilitate the design of the bearing specimen, the model properties were related to the assumed prototype properties using the similitude requirements for dynamic loading (Harris and Sabnis, 1999). A brief outline of these requirements and resulting scale factors are presented here. For dynamic similitude a particular dimensionless ratio for the prototype and model must be equal as shown in (3-1):

$$\frac{F_m t_m^2}{m_m l_m} = \frac{F_p t_p^2}{m_p l_p} \tag{3-1}$$

where F is a generic force quantity, t is time, m is mass, and l is length whereas the subscripts m and p indicate model and prototype, respectively. The scale factors are defined as the ratio of the prototype quantity to the equivalent model quantity, as shown by:

$$S_l = \frac{l_p}{l_m} \tag{3-2}$$

where l_p is a particular length of the prototype and l_m is the corresponding length of the model. Defining the scale factors for the remaining dimensions and substituting into (3-1) yields (3-3), an expression relating scale factors.

$$S_F = \frac{S_l S_m}{S_t^2} \tag{3-3}$$

For traditional earthquake simulation testing (not performed in a centrifuge) the gravitational and acceleration scale factor are equal to 1 according to:

$$S_a = S_g = 1 \tag{3-4}$$

where S_a and S_g are the acceleration and gravitational acceleration scale factors, respectively. From equilibrium and with $S_a = 1$, the force scale factor is shown to equal the mass scale factor presented in (3-5).

$$S_F = S_m \tag{3-5}$$

Substituting this expression into (3-3) results in

$$S_t = \sqrt{S_l} \tag{3-6}$$

that is, the time scale factor is equal to the square root of the length factor. Other relevant quantities were related to the length scale factor in a similar manner and are presented in table 3-2. Also presented in this table are the target scale factor values based on:

$$S_T = S_t = \frac{T_p}{T_m} = \frac{2.5\text{s}}{1.25\text{s}} = 2 \tag{3-7}$$

where S_T is the period scale factor equal to the time scale factor and determined as the ratio of the assumed period of the prototype isolated structure to the target period of the model isolated structure resulting in a half scale model in the time dimension and a quarter scale model in the length dimension. Additional quantities of interest are presented in table 3-2. However, it is worth noting here that the pressure and acceleration scale factors are equal to 1 and that actual scale factors might deviate from the target scale factors due to differences in the specified and provided bearing properties.

TABLE 3-2 Similitude requirements

Quantity	Factor	Prototype / Model[1]
Time	$\sqrt{S_l}$	2
Length	S_l	4
Mass	S_l^2	16
Displacement	S_l	4
Velocity	$\sqrt{S_l}$	2
Acceleration	1	1
Stress	1	1
Strain	1	1
Force	S_l^2	16
Moment	S_l^3	64
Area	S_l^2	16
Shear modulus	1	1
Damping	1	1

Notes:
1. Values presented in this table represent target and not provided values.

3.4 Model Bearing Properties

The model bearings were proportioned using the assumed prototype properties and in accordance with the scale factors determined from the similitude requirements. This section provides an outline of the procedure used to proportion the model isolation bearings. It is noteworthy to mention the model bearings are hollow cylinders and that the difference between the LR and LDR bearings is the addition of a lead-core in the central hole.

The size, in terms of cross-sectional area, of the model bearings was constrained by the dimension of a manufacturers existing mold: a diameter of $178\,\text{mm}$ and a mandrel (central hole) diameter of $30\,\text{mm}$. Assuming $3\,\text{mm}$ of rubber cover, the maximum shim diameter and thus outer bonded rubber diameter is $172\,\text{mm}$ with an inner diameter of $30\,\text{mm}$ resulting in a bonded rubber area, A_b, equal to:

$$A_b = \frac{\pi}{4}\left[(172\,\text{mm})^2 - (30\,\text{mm})^2\right] = 22{,}528\,\text{mm}^2 \tag{3-8}$$

The weight acting on each isolators (four in total) was determined using the prototype static pressure, p, and considering the similitude requirements as:

$$W=\left(3.45\frac{\text{N}}{\text{mm}^2}\right)\left[\frac{\pi}{4}(172\,\text{mm})^2\right]\approx 80\,\text{kN} \tag{3-9}$$

where W is estimated neglecting the central hole. The required horizontal stiffness of the model was calculated using the target prototype period ($T_p = 1.25\,\text{s}$) and the calculated weight according to:

$$K_p=\left(\frac{2\pi}{T_p}\right)^2\left(\frac{W}{\text{g}}\right)=\left(\frac{2\pi}{1.25\,\text{s}}\right)^2\left(\frac{80\,\text{kN}}{9810\,\text{mm/s}^2}\right)=0.206\,\text{kN/mm} \tag{3-10}$$

The horizontal stiffness is related to the elastomer shear modulus, G, bonded rubber area, A_b, and total rubber thickness, T_r, as shown in (3-11).

$$K=\frac{GA_b}{T_r} \tag{3-11}$$

Since G is dictated by the prototype and similitude requirements and A_b is given by manufacturing constraints, the total thickness of rubber required to meet the target model period was determined according to:

$$T_r=\frac{GA_b}{K}=\frac{\left(0.55\,\text{N/mm}^2\right)\left(22{,}528\,\text{mm}^2\right)}{206\,\text{N/mm}}=60.1\,\text{mm} \tag{3-12}$$

and the required number of rubber layers using:

$$n=\frac{T_r}{t_r}=\frac{60.1\,\text{mm}}{3\,\text{mm}}=20 \tag{3-13}$$

where t_r is the individual rubber layer thickness equal to $3\,\text{mm}$, a manufacturers limit for minimum thickness. From the previously specified geometry and rubber layer thickness, the shape factors of the LDR and LR bearings are:

$$S=\frac{(D_o-D_i)}{4t_r}=\frac{(172\,\text{mm}-30\,\text{mm})}{4(3\,\text{mm})}=11.8$$

and

$$S = \frac{\left(D_o^2 - D_i^2\right)}{4\,D_o\,t_r} = \frac{\left[(172\,\text{mm})^2 - (30\,\text{mm})^2\right]}{4(172\,\text{mm})(3\,\text{mm})} = 13.9$$

respectively. These values are typical of seismic isolation bearings that range from 10 to 15. The shape factor for the LDR and LR differ in that the rubber in the central hole of the LR is not free to bulge (noting the definition for the shape factor of an elastomeric pad is the ratio of the loaded area to the area free to bulge).

A summary of the specified model bearing dimensions and material properties and comparison to the provided (or as-built) dimensions is presented in table 3-3. Note that the provided outer diameter, D_o, is equal to $152\,\text{mm}$. The reduction in bonded diameter results in shape factors for the LDR and LR bearings of 10.2 and 12.2, respectively. The material properties of the as-built model bearings such as: σ_L, G and β were determined from the results of characterization testing that is presented in Section 5. As-built LDR and LR bearing details are presented in figures 3-1 and 3-2, respectively. These figures show a half section plan view and a cross-section view of the model bearings. Note the provided cover thickness of $12\,\text{mm}$. Typically the contribution of the cover to the shear stiffness is negligible as the cover thickness is a small fraction of the bonded rubber diameter. However, for these bearings the cover thickness is approximately 10% of the bonded rubber diameter, therefore, the contribution of the cover is experimentally investigated and is discussed further in Section 5.

TABLE 3-3 Model bearing properties

Parameter			Bearing Type			
			Target		Provided	
Description	Notation	Unit	LDR	LR	LDR	LR
Outer diameter	D_o	mm	172	172	152	152
Inner diameter	D_i	mm	30	30	30	30
Individual rubber layer thickness	t_r	mm	3	3	3	3
Number of rubber layers	n	-	20	20	20	20
Shape factor	S	-	11.8	13.9	10.2	12.2
Static pressure	p	MPa	3.45	3.45	TBD[1]	TBD
Shear modulus	G	MPa	0.55	0.55	TBD	TBD
Effective yield strength of lead	σ_L	MPa	NA[2]	10.3	NA	TBD
Characteristic strength	Q_d	kN	NA	7.3	NA	TBD
Effective stiffness	K_{eff}	kN/mm	0.206	TBD	TBD	TBD
Second-slope stiffness	K_d	kN/mm	TBD	0.206	TBD	TBD
Normalized characteristic strength	Q_d / W	-	NA	0.091	TBD	TBD
Effective period	T_{eff}	s	1.25	NA	TBD	TBD
Second-slope period	T_d	s	NA	1.25	NA	TBD

Notes:
1. TBD indicates the value of the parameter will be determined in a subsequent Section.
2. NA: indicates this parameter is not applicable to the particular type of bearing.

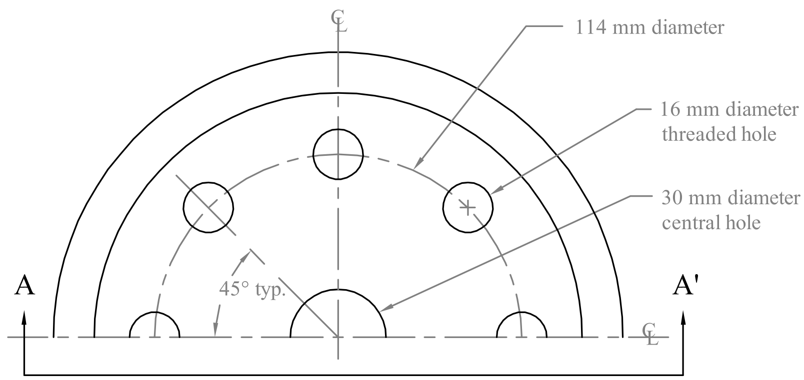

Plan View (Half-section)

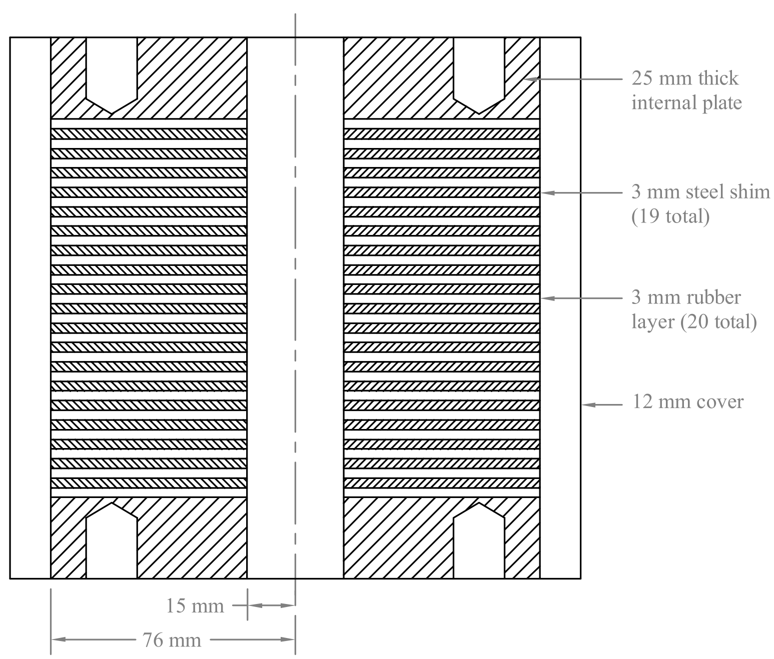

Section A-A'

FIGURE 3-2 As-built model LDR bearing details

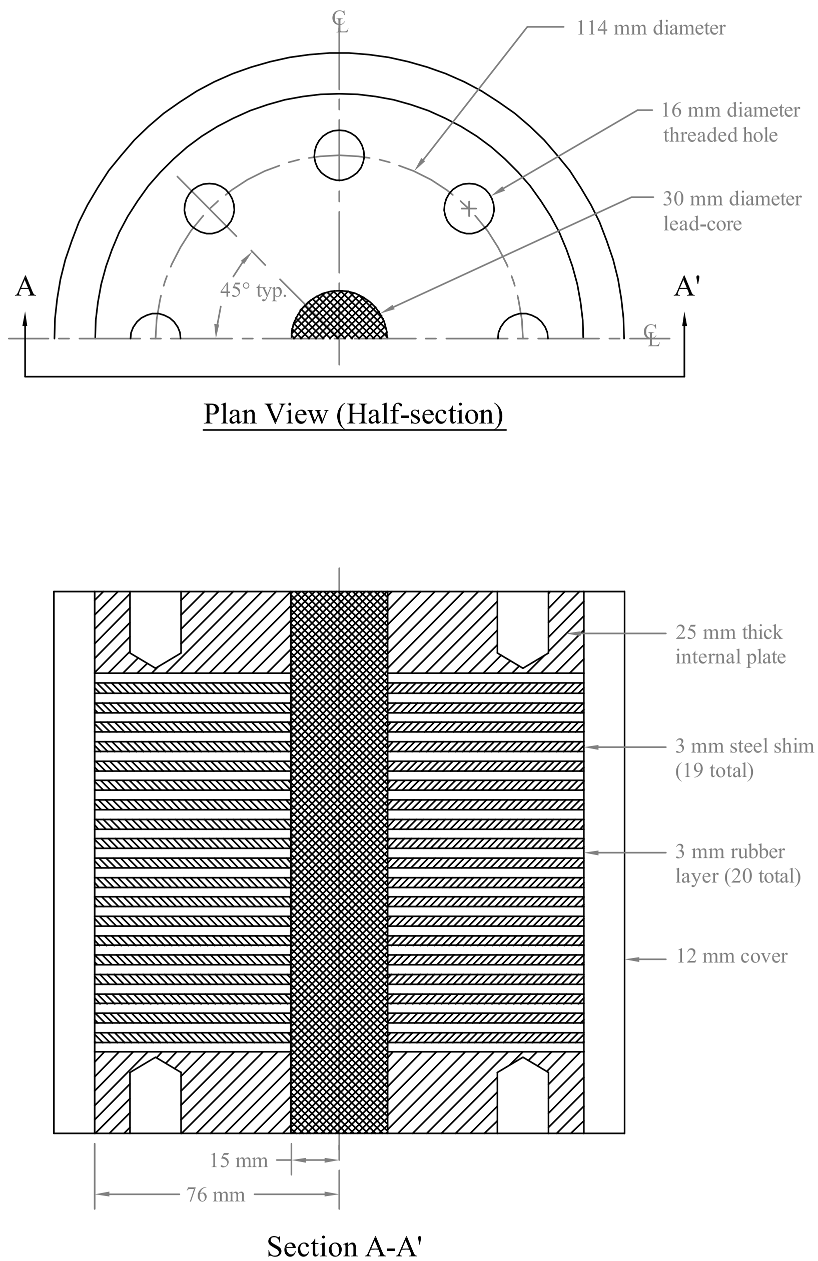

FIGURE 3-3 As-built model LR bearing details

SECTION 4

CHARACTERIZATION AND LATERAL OFFSET TESTING

4.1 General

Single bearing characterization testing was conducted to determine the mechanical properties of the model LR and LDR seismic isolation bearings and to investigate the influence of horizontal displacement on the vertical stiffness. Additionally, the results of characterization testing were utilized to validate a three-dimensional finite element model of the LDR bearing. The characterization testing program was carried out on the single bearing testing machine (SBTM) located in the Structural Engineering and Earthquake Simulation Laboratory (SEESL) at the University at Buffalo. This section presents a description of the single bearing testing machine, instrumentation, data acquisition and the test program.

4.2 Single Bearing Testing Machine

4.2.1 General

The single bearing testing machine (SBTM) was designed for the primary purpose of testing single seismic isolation bearing under conditions of unidirectional shear and combined axial load. The machine consists of a pedestal frame, a reaction frame, a loading beam, a horizontal (dynamic) MTS™ actuator, two vertical Parker actuators and a 5-channel reaction load cell. The 5-channel reaction load cell utilized for characterization testing is one of four identical load cells also used for the earthquake simulation testing program. A detailed description of the load cells is provided in Appendix A. A schematic of the SBTM, including approximate physical dimensions and standard U.S. sections sizes is shown in figure 4-1. Presented in figure 4-2 is a photograph of the SBTM taken during characterization testing.

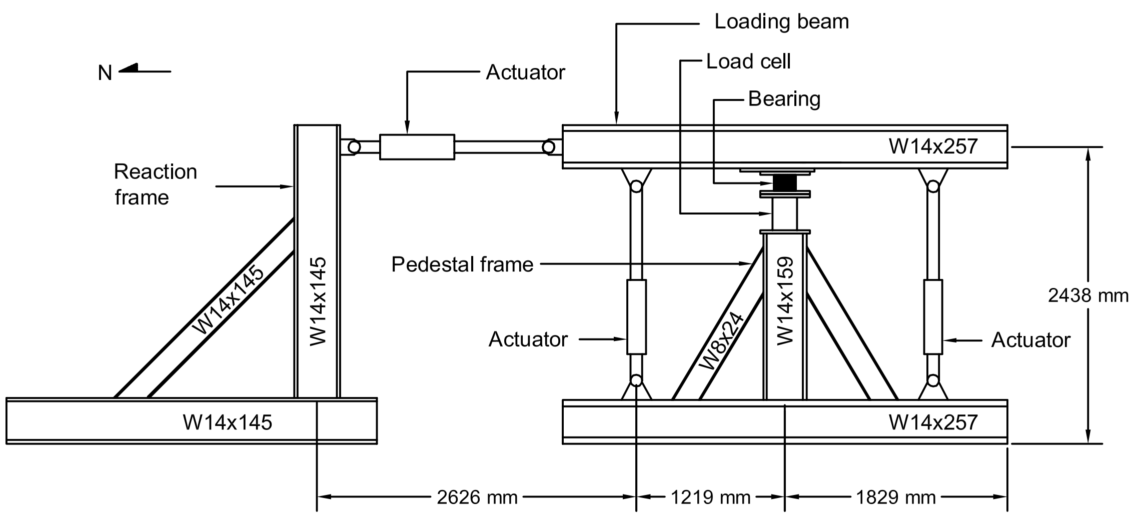

FIGURE 4-1 Schematic of single bearing testing machine

FIGURE 4-2 Photograph of single bearing testing machine

TABLE 4-1 Single bearing testing machine actuator capabilities

Actuator	Stroke (mm)	Velocity (mm/s)	Force (kN)
Horizontal (MTS)	±152	635	245
North Vertical (Parker)	±50	Not available	317 Compression 300 Tension
South Vertical (Parker)	±50	Not available	317 Compression 300 Tension

4.2.2 Capabilities

The SBTM is capable of imposing unidirectional shear and combined axial load or axial loading alone. The capabilities of the actuators of the SBTM, in terms of maximum force, stroke and velocity are presented in table 4-1. Noting, the maximum velocity of vertical actuators has not been determined and is therefore not included in table 4-1. Despite the force capabilities of the actuators presented in table 4-1, the capacity of the SBTM is typically limited by the elastic capacity of the reaction load cell. For this testing program, the elastic capacity of the 5-channel reaction load cell subjected to simultaneous actions, based on Von Mises yield criterion, was determined to be $89\,\text{kN}$ shear force, $22.5\,\text{kN-m}$ bending moment, and $222\,\text{kN}$ axial force (see Appendix A).

4.2.3 Instrumentation and Data Acquisition

A total of twelve data channel recorded the performance of the driving actuators and the response of the seismic isolation bearing during testing. Nine channels of data collected from stationary instruments and one data channel recording time is typically sufficient to operate the SBTM. However, for this testing program, two additional instruments and thus data channels were added to record relative vertical displacement across the bearing. Although data was collected from these instruments for each test, the instruments were only installed for tests involving variable axial loading.

The instruments are distributed throughout the SBTM as follows. The horizontal MTS™ actuator contains an inline uni-axial load cell (LC) and internal linear variable displacement transducer (LVDT) recording actuator axial load and relative displacement, respectively. The vertical Parker actuators each contain a inline uni-axial LC and externally attached MTS™ $\pm 50\,\text{mm}$ Temposonic displacement transducer recording axial load and relative displacement, respectively. A five-channel reaction LC fixed atop the pedestal frame records axial load (P), shear force

(F_x), and bending moment (M_x) at the base of the isolation bearing. Two types of instruments were used to measure relative vertical displacement across the bearing, specifically, two $\pm 6\,\mathrm{mm}$ liner potentiometers during force-controlled vertical loading and two MTS™ $\pm 50\,\mathrm{mm}$ Temposonic displacement transducers during displacement-controlled vertical loading.

A schematic diagram of the SBTM data acquisition system is presented in figure 4-3. This diagram depicts the individual components and connectivity of the SBTM data acquisition system including the two additional vertical displacement transducers. In this diagram, data flows from top down. Also, external power supply lines are dotted whereas data and data/power lines are solid. The MTS™ 408 Conditioner and 406 Controllers supply an excitation voltage to the corresponding instruments as illustrated in figure 4-3. An excitation voltage is supplied to the individual circuits of the 5-channel reaction load cell via three Measurements Group Instrument Division 2310 Analog Signal Conditioners. Individual external power supplies provided an excitation voltage to the external MTS™ $\pm 50\,\mathrm{mm}$ Temposonic displacement transducers and vertical displacement transducers. All signals are filtered at $10\,\mathrm{Hz}$ via a lowpass analog filter then digitized by a PCI DAS 6402 Analog-to-Digital (A-D) card installed in a Dell™ Dimension 8200 desktop PC.

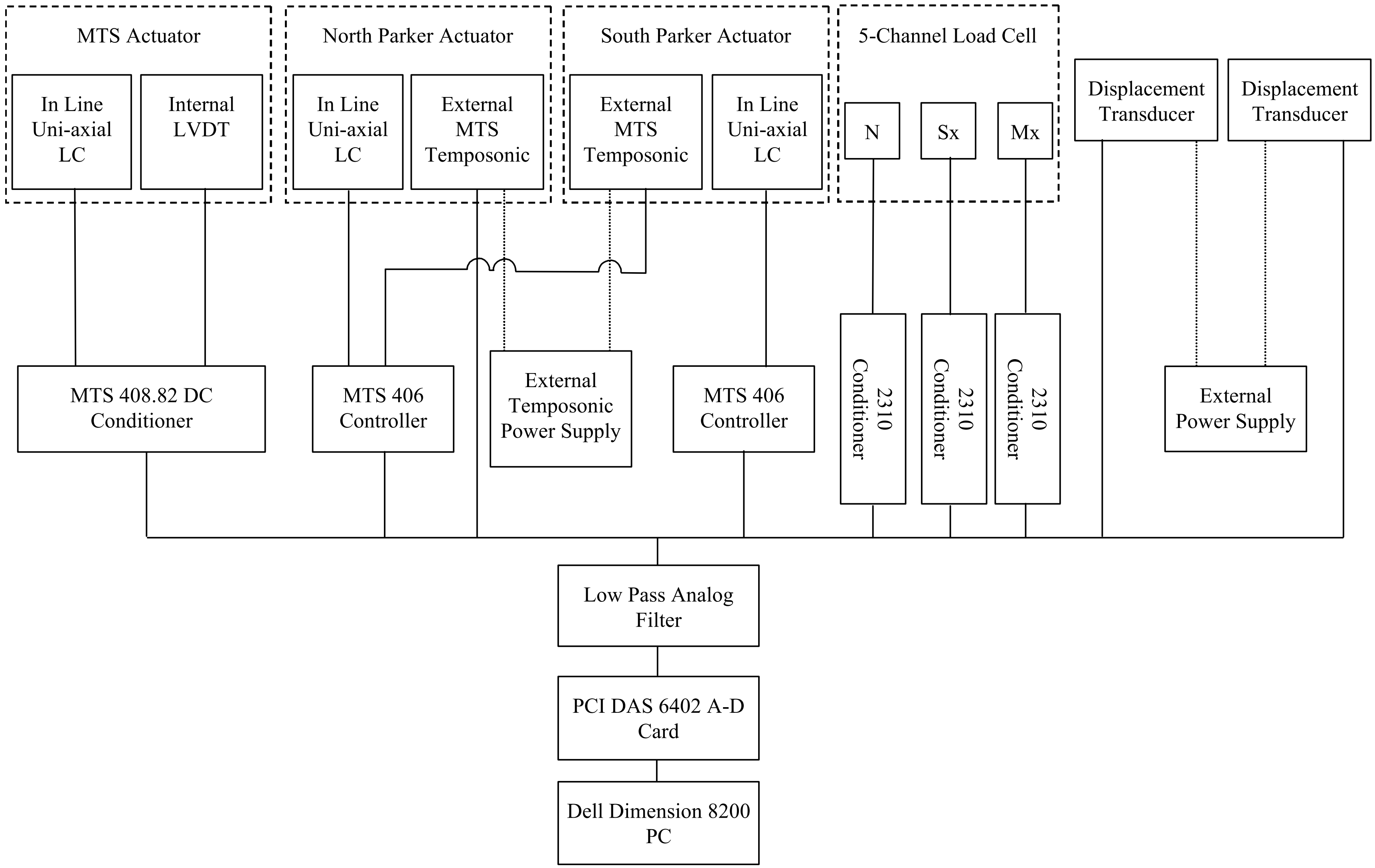

FIGURE 4-3 Single bearing test machine data acquisition diagram

4.3 Test Program

4.3.1 General

The single bearing characterization testing program was designed to: (1) determine the mechanical properties of the LR and LDR seismic isolation bearings; (2) investigate the influence of lateral displacement on vertical stiffness; (3) investigate the influence of lateral displacement on the axial-force response under large tensile deformations; and (4) monitor the mechanical properties of the bearing throughout the testing program.

4.3.2 Description

Four model seismic isolation bearings, two LR and two LDR, were dedicated to single bearing characterization testing. Two bearings of each type were arbitrarily assigned numbers 5 and 6, i.e., LR 5, LDR 6, etc. Bearings assigned numbers 1 through 4 were utilized for earthquake simulation testing.

The model bearings were tested according to the program presented in table 4-2. This program consisted of a series of lateral, vertical, and combined loading tests organized such that demand on the bearing specimen increases through the program. Benchmark unidirectional shear ($100\,\%$ shear strain) with a constant axial load tests were repeated throughout the program to monitor the mechanical properties. Table 4-2 presents the following information for each test: number, type, input signal, preload P_o, amplitude of the axial load signal P, lateral offset Δ, displacement amplitude u, frequency f and number of cycles.

A brief description of each type of test is provided below and identified in the footnote of table 4-2. Illustrations of the displacement and force input signals are presented in figures 4-4 and 4-5, respectively. In each of these figures, the basic wave form is presented along with relevant annotations, including, signal amplitudes and periods, which are listed for each test in table 4-2. Both displacement and force-control were utilized throughout the program. In general, shear tests were conducted using displacement control whereas vertical tests were conducted using force-control for reasons of control device sensitivity and safety.

A brief description of each type of test follows:

A. ***Shear***: Unidirectional shear and constant axial load tests conducted to measure the shear force response of the model LR and LDR bearings. Shear tests were conducted at varying strain amplitudes and frequencies to estimate bearing mechanical properties including: shear modulus, effective damping ratio, and effective lead yield strength (LR only). Additionally a *benchmark* shear test (to a displacement corresponding to 100% shear strain) was repeated throughout the program to monitor possible degradation of bearing mechanical properties.

B. ***Axial***: Axial load tests conducted to measure the vertical displacement of the model LR and LDR bearings and to estimate the vertical stiffness and compression moduli. Axial load tests were repeated for varying load amplitudes and frequencies and conducted under conditions of zero lateral offset.

C. ***Cyclic***: Cyclic axial load tests were conducted to measure the vertical displacement response. Cyclic axial load tests were conducted under conditions of zero lateral offset.

D. ***Combine Shear and Axial***: Combined shear and axial load tests were conducted to simulate rocking motion and to determine the influence of variable axial load on the shear force response. Combined shear and axial load test utilized a sinusoidal (S) displacement signal in the lateral direction and a ramp axial load signal passing through zero (RTZ) in the vertical direction.

E. ***Axial with Lateral Offset***: Axial load tests were conducted at various lateral offsets to investigate the influence of lateral displacement on the vertical stiffness of the model LR and LDR bearings. Tests were conducted at varying load amplitudes and lateral offsets.

F. ***Large deformation tensile***: Large deformation tensile load tests were conducted to measure the axial force response of the model LR and LDR bearings when subjected to large tensile deformations. This test was conducted under conditions of zero lateral offset and a lateral offset corresponding to 150% shear strain to investigate the influence of lateral deformation on tensile failure.

For the *axial with lateral offset* tests, an interface plate, connecting the bearing top end-plate to the loading beam, was required to allow the vertical actuators to remain plumb while simultaneously shearing the bearing specimen. To allow the vertical actuators to remain plumb and allow the loading beam to translate vertically an interface plate was designed and fabricated to accommodate lateral offsets of: 0, 30, 60, 90, 120 and $152\,\text{mm}$. A schematic of the SBTM and isolation bearing for the *axial with lateral offset* testing is shown in figure 4-6. In this figure the model isolation bearing is shaded and shown in each configuration for lateral offset testing.

TABLE 4-2 Single bearing characterization testing program

Test	Type[1]	Signal[2]	Preload P_o (kN)	Axial Load Amplitude[3] P (kN)	Lateral Offset Δ (mm)	Displ. Amplitude[3] $u,\ \delta$ (mm)	Freq.[4] f (Hz)	No. of Cycles
1	A	S	60	n.a.	n.a.	±15	0.01	4
2	A	S	60	n.a.	n.a.	±15	1	4
3	A	S	60	n.a.	n.a.	±30	0.01	4
4	A	S	60	na.	n.a.	±30	1	4
5	A	S	60	n.a.	n.a.	±60	0.01	4
6	A	S	60	na.	n.a.	±60	1	4
7	B	R	24	36	0	n.a.	0.01	3
8	B	R	24	97	0	n.a.	0.01	3
9	B	R	24	97	0	n.a.	0.1	3
10	B	R	24	97	0	n.a.	0.333	3
11	B	R	24	157	0	n.a.	0.01	3
12	B	R	0	-13	0	n.a.	0.01	3
13	C	R	60	-74	0	n.a.	0.01	3
14	D	S,RTZ	60	74	n.a.	±60	0.01, 0.01	3
15	A	S	60	na.	n.a.	±60	0.01	4
16	E	R	24	36	30	n.a.	0.01	3
17	E	R	24	97	30	n.a.	0.01	3
18	E	R	24	157	30	n.a.	0.01	3
19	E	R	0	-13	30	n.a.	0.01	3
20	A	S	60	na.	n.a.	±60	0.01	4
21	E	R	24	36	60	n.a.	0.01	3
22	E	R	24	97	60	n.a.	0.01	3
23	E	R	24	157	60	n.a.	0.01	3
24	E	R	0	-13	60	n.a.	0.01	3
25	A	S	60	na.	n.a.	±60	0.01	4
26	A	S	60	na.	n.a.	±90	0.01	4
27	E	R	24	36	90	n.a.	0.01	3
28	E	R	24	97	90	n.a.	0.01	3
29	E	R	0	-13	90	n.a.	0.01	3
30	A	S	60	na.	n.a.	±60	0.01	4
31	A	S	60	na.	n.a.	±120	0.01	4
32	E	R	24	na.	121	n.a.	0.01	3
33	E	R	24	97	121	n.a.	0.01	3
34	E	R	0	-13	121	n.a.	0.01	3
35	A	S	60	na.	n.a.	±60	0.01	4
36	E	R	24	36	152	n.a.	0.01	3
37	E	R	0	-13	152	n.a.	0.01	3
38	F	SR	0	na.	0	-6, -30, -89	0.01	3
39	F	SR	0	na.	90	-6, -30, -89	0.01	3
40	A	S	60	na.	n.a.	±60	0.01	4

Notes:
1. A=shear; B=axial; C=cyclic; D=combine shear and axial; E=axial with lateral offset; F=tensile large deformation tensile
2. S=sinusoidal, R=ramp, RTZ=ramp through zero, SR=stepped ramp
3. Negative value indicates loading in the direction of applied tension
4. First and second value correspond to horizontal and vertical signal, respectively
5. Test 33 to be performed on Lead-rubber (LR) bearings only
6. Test 38 performed on bearings LR 5 and LDR 5
7. Test 39 performed on bearings LR 6 and LDR 6

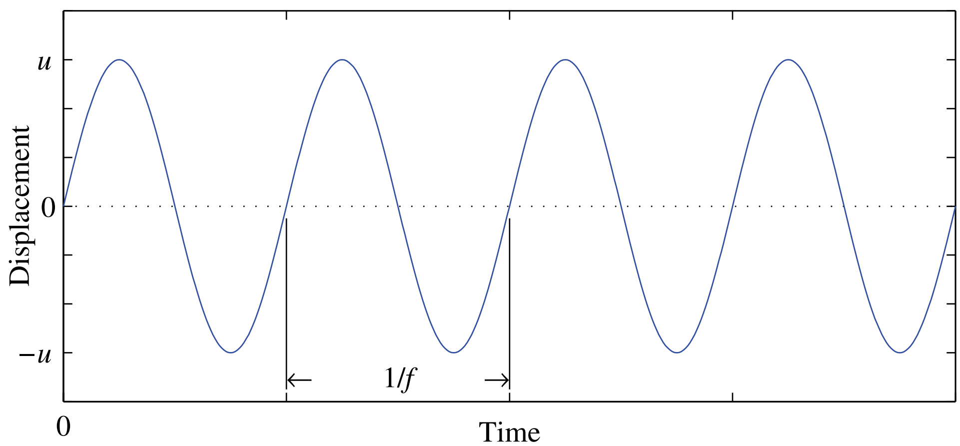

a. sinusoidal (S)

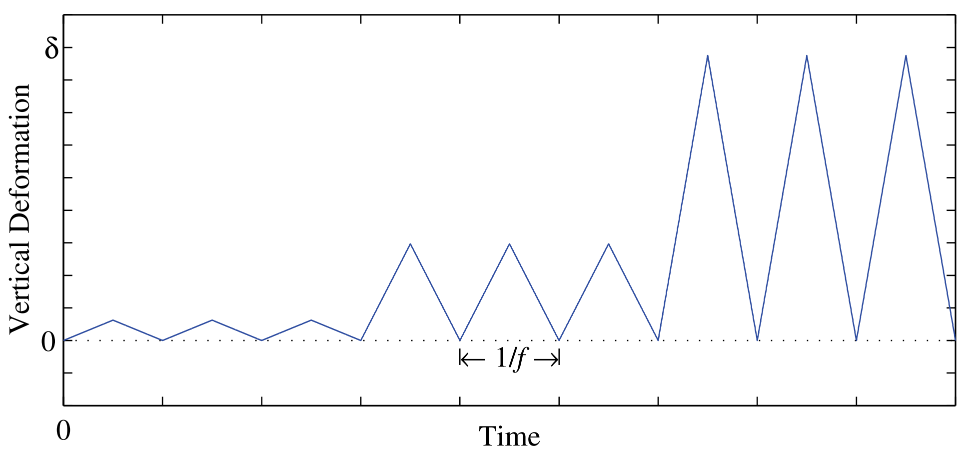

b. stepped ramp (SR)

FIGURE 4-4 Imposed displacement signals

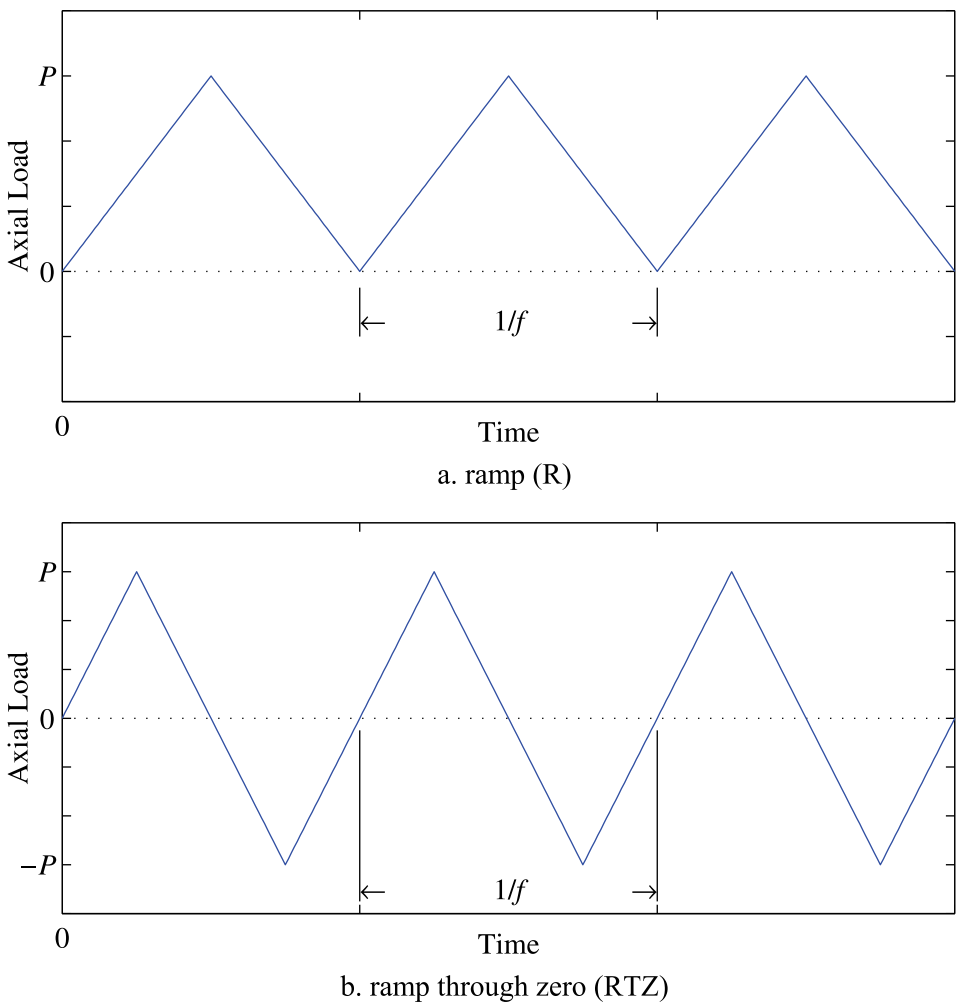

FIGURE 4-5 Imposed force signals

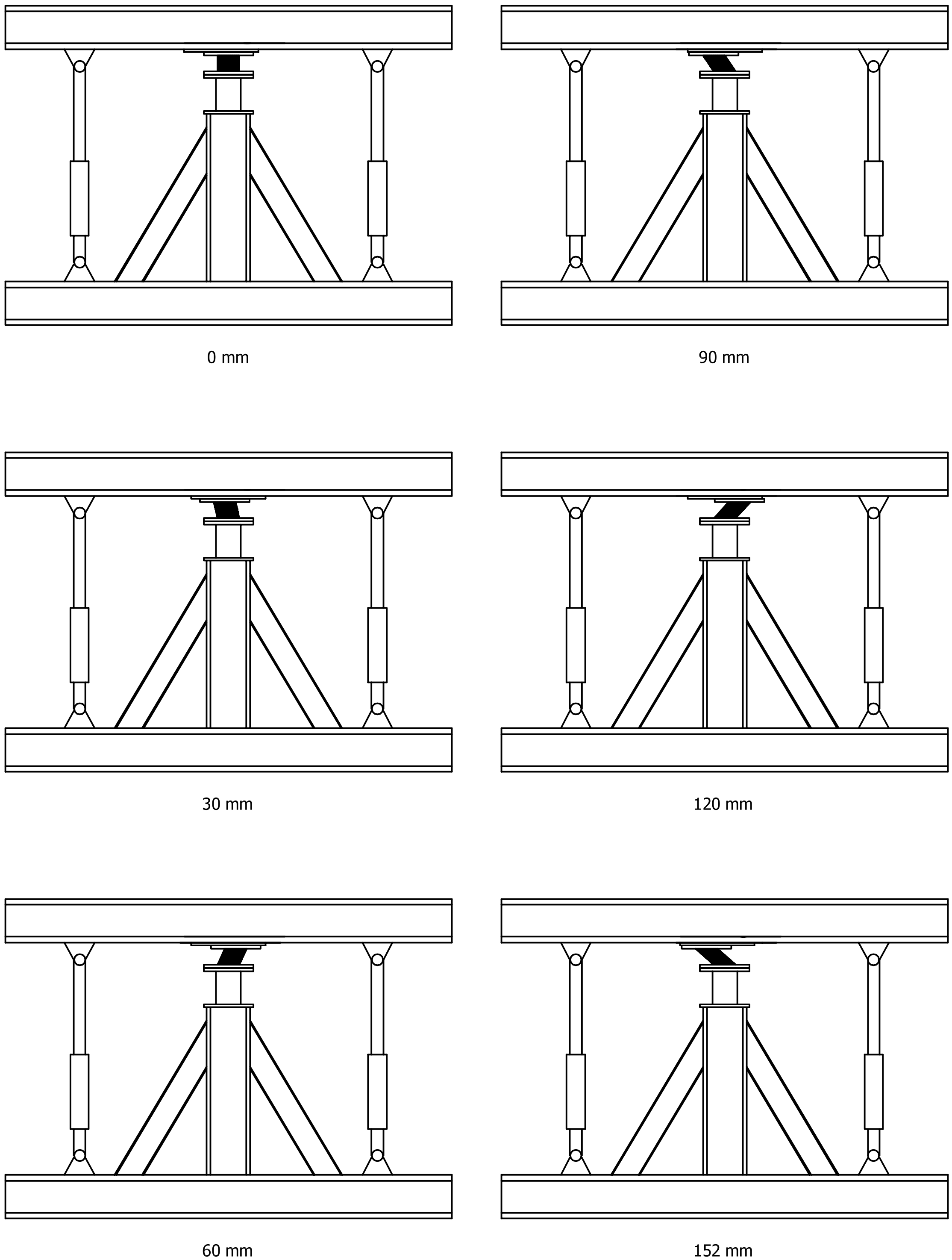

FIGURE 4-6 Illustrations of bearing and testing machine configurations for lateral offset testing

SECTION 5

RESULTS OF CHARACTERIZATION AND LATERAL OFFSET TESTING

5.1 General

Four model bearings, two low-damping rubber (LDR) and two lead-rubber (LR), were dedicated to characterization and lateral offset testing following the program presented in table 4-2. The primary objectives of this testing program were to determine the mechanical properties of the LDR and LR seismic isolation bearings and to experimentally investigate the influence of lateral displacement on the vertical stiffness of elastomeric and lead-rubber seismic isolation bearings. Additionally, the results of intermittent "benchmark" *Shear* tests were used to monitor the mechanical and material properties of the LDR and LR bearings throughout the testing program.

This section is organized into four sub-sections as follows. Section 5.2 describes the analysis of data obtained from tests performed on the LDR and LR bearings. Section 5.3 presents sample results from characterization testing performed on the LDR and LR bearings including mechanical and material properties. Section 5.4 presents results from lateral offset testing and a comparison with a simplified formulation derived from the two-spring model described in Section 2. A summary is presented in Section 5.5. Additional results of characterization and lateral offset testing are presented in Appendix B.

5.2 Data Analysis

5.2.1 General

The mechanical properties of the LDR and LR seismic isolation bearings were determined from the recorded shear force and vertical displacement responses during *Shear* (Type A, see table 4-2) and *Axial* (Type B) tests, respectively. Resulting mechanical properties were used with physical properties (e.g., bonded rubber diameter, total rubber thickness) to estimate key material properties, including, the effective shear modulus of the rubber and the effective yield strength of the lead core.

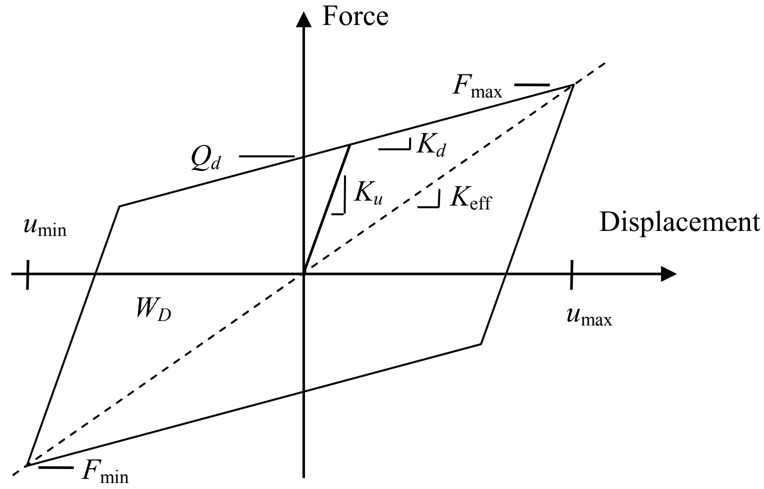

FIGURE 5-1 Idealized bilinear force-displacement schematic for seismic isolation bearing

5.2.2 Mechanical Properties

The illustration of the idealized bilinear shear force versus lateral displacement response of a seismic isolation bearing presented in Section 2 is presented here, again, in figure 5-1 for convenience.

The mechanical properties of the seismic isolation bearings were calculated from the recorded response data as follows. The effective stiffness was calculated according to:

$$K_{eff} = \frac{|F_{max}| + |F_{min}|}{|u_{max}| + |u_{min}|} \tag{5-1}$$

where u_{min}, u_{max}, F_{max} and F_{min} were defined previously. The characteristic strength, Q_d, was estimated according to:

$$Q_d = \frac{\left|F^{+}(u=0)\right| + \left|F^{-}(u=0)\right|}{2} \tag{5-2}$$

where $F^{+}(u=0)$ and $F^{-}(u=0)$ are the positive and negative zero-displacement force-intercepts, respectively. The zero-displacement intercepts, $F^{+}(u=0)$ and $F^{-}(u=0)$, were determined by linearly interpolating adjacent data points with opposite signs of displacement. The energy dissipated per cycle, W_D, was determined by numerically integrating the shear force versus lateral displacement response using a cumulative trapezoidal algorithm.

The vertical stiffness, K_{vo}, was calculated as:

$$K_{vo} = \frac{P^+ - P^-}{\delta^+ - \delta^-} \tag{5-3}$$

where P^+ is an axial load corresponding to a pressure equal to the target pressure (ρ) plus $0.35\ \text{MPa}$; P^- is an axial load corresponding to a pressure equal to $\rho - 0.35\ \text{MPa}$; δ^+ is the average relative vertical displacement coincidental with P^+ from the ascending branch of the loading curve and δ^- is the average relative vertical displacement coincidental with P^-. The vertical stiffness calculated in this fashion represents a secant stiffness calculated for target pressures of $2.75\ \text{MPa}$, $5.2\ \text{MPa}$ and $9\ \text{MPa}$.

Other researchers (Kasalanati et al., 1999) have documented rotation of the loading beam of the single bearing test machine about its $x-$axis (North axis, see figure 5-2) during axial load testing. As it is not possible to measure relative vertical displacement at the center of the bearing and in anticipation of rotation of the loading beam about its $x-$axis, two displacement transducers were used to measure vertical relative displacement on each side of the bearing. These transducers were placed on the east and west sides of the bearing and equidistant from the center. Figure 5-2 presents a photograph of bearing LDR 6 taken during test number 28 and shows the west transducer, in this case, a linear potentiometer.

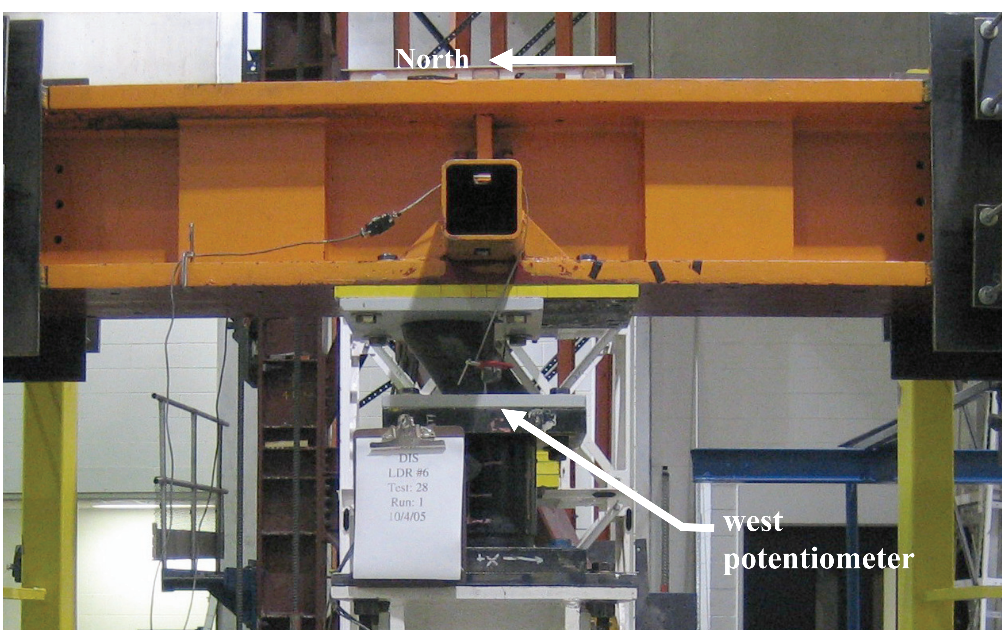

FIGURE 5-2 Photograph of LDR 6 and potentiometer placement during Test 28

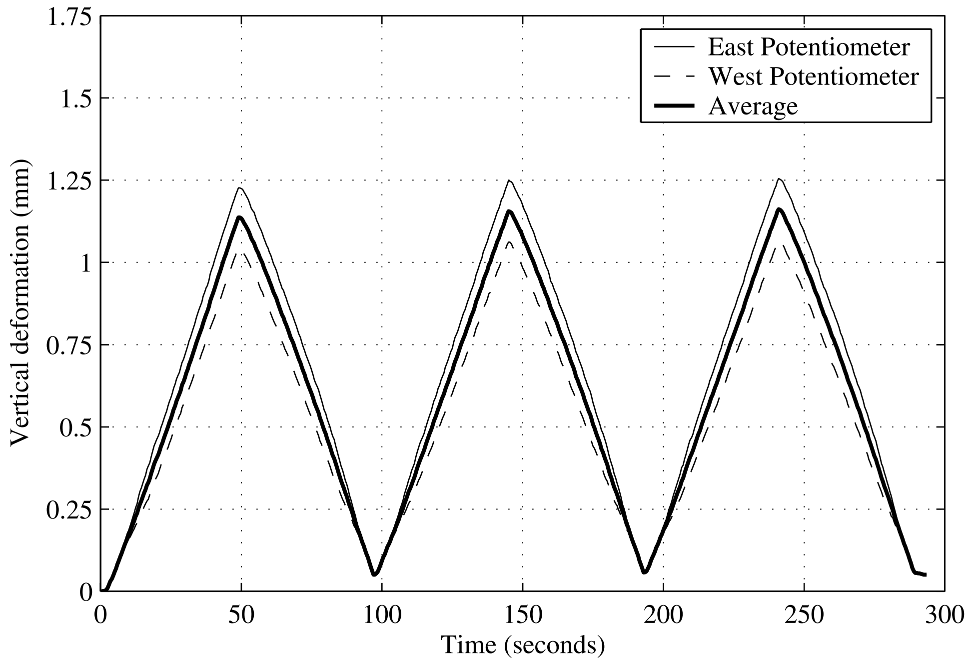

FIGURE 5-3 Relative vertical displacement signals from LDR 5 for Test 8

Figure 5-3 presents a plot of the relative vertical displacement signals from the east (solid) and west (dashed) potentiometers from test number 8 for LDR 5. Also plotted in this figure is the calculated average of the east and west signals shown by a thick solid line. This figure illustrates the difference in potentiometer signals, approximately $17\,\%$ relative to the west potentiometer, which corresponds to a beam rotation of approximately $0.045\,\text{deg}$. Although this rotation is small, the difference in potentiometer signals is increased by the outboard positioning and is significant in terms of the amplitude of the relative vertical displacement signals. Therefore the average of the two potentiometer signals was used for graphical presentation and calculation of the vertical stiffness.

5.2.3 Material Properties

Material properties of the LDR and LR seismic isolation bearing were estimated using mechanical properties determined from characterization testing, physical properties of the seismic isolation bearings and established relationships. These material properties include: G_{eff}, the effective shear modulus; β_{eff}, the effective damping ratio; and σ_L, the effective yield strength of the lead-core (LR only). A brief description of the relationships used to estimate the material properties for the LDR and LR bearings is presented in the following section.

Typically the effective shear modulus for elastomeric bearings, in this case the LDR, is related to the effective stiffness according to:

$$K_{\text{eff}} = \frac{G_{\text{eff}} A_b}{T_r} \tag{5-4}$$

where A_b is the bonded rubber diameter equal to $17,535\ \text{mm}^2$ and T_r is the total rubber thickness equal to $60\ \text{mm}$.

An additional, nominal, thickness of rubber is provided around the circumference and over the full height of elastomeric and lead-rubber bearings. This additional rubber is referred to as the "cover" and serves to protect the bearing internal components from corrosion and accelerated aging. Typically, the cover thickness is on the order of the individual rubber layer thickness and assumed to provide negligible stiffness to the bearing. For example, the $500\ \text{kip}$ prototype LR bearing described in CERF report (HITEC, 1998a) is proportioned with a bonded rubber diameter of $594\ \text{mm}$, an individual rubber layer thickness of $8\ \text{mm}$ and a cover thickness of $12\ \text{mm}$ resulting in a cover thickness to bonded rubber diameter ratio of $1/50$. However, the model LDR and LR bearings used in this study were manufactured with a cover layer of approximately $12\ \text{mm}$ in thickness or four times the individual rubber layer thickness for a cover thickness to bonded rubber diameter ratio of $1/12$. To determine the contribution of the cover to the bearing stiffness and to more accurately estimate the shear modulus of the elastomer, the $12\ \text{mm}$ cover of LDR 5 was lathed down to approximately $3\ \text{mm}$, denoted LDR 5M herein, and re-tested. The results of tests performed on LDR 5 with $12\ \text{mm}$ and $3\ \text{mm}$ cover thicknesses were used to determine an effective area for the estimation of the shear modulus for bearings tested with the full ($12\ \text{mm}$) cover and calculated using:

$$K_{\text{eff}} = \frac{G_{\text{eff}} A_e}{T_r} \tag{5-5}$$

where A_e is an effective area derived in the subsequent experimental results section. For lead-rubber bearings, the effective shear modulus is related to the second-slope stiffness, K_d, and estimated according to (5-6), see figure 5-1.

$$K_d = \frac{G_{\text{eff}} A_e}{T_r} \tag{5-6}$$

The effective damping ratio, β_{eff}, was calculated for both the LDR and LR bearings according to:

$$\beta_{\text{eff}} = \frac{2}{\pi}\left[\frac{W_D}{K_{\text{eff}}\,(|u_{\max}|+|u_{\min}|)^2}\right] \tag{5-7}$$

where W_D, K_{eff}, $u_{\max}$ and $u_{\min}$ were defined previously. For the calculation of β_{eff}, the average of $|u_{\max}|$ and $|u_{\min}|$ was used to account for slight differences in these values. For lead-rubber bearings, the effective lead yield strength, σ_L, is assumed to be related to the characteristic strength according to:

$$Q_d = \sigma_L A_L \tag{5-8}$$

where Q_d is the characteristic strength (see figure 5-1) and A_L is the cross-sectional area of the lead-core equal to $706\ \text{mm}^2$ and calculated using the nominal inner diameter, D_i. The total rubber shear strain was calculated for each test according to:

$$\gamma = \frac{(|u_{\max}|+|u_{\min}|)}{2T_r} \tag{5-9}$$

where $u_{\max}$, $u_{\min}$ and T_r were defined previously. Similar to the β_{eff} calculation, an average value of the maximum positive and negative displacements was used for the shear strain calculation. If these displacements were equal the expression would reduce to the more traditional expression shown by (5-10).

$$\gamma = \frac{u_{\max}}{T_r} \tag{5-10}$$

Theoretical predictions of the vertical stiffness were calculated and compared to experimental values to determine the validity of two assumptions, namely, material compressibility and uniform rubber layer thickness. Theoretical predictions were calculated for the following cases: uniform rubber layer thickness with incompressible material; uniform rubber layer thickness with compressible material; measured rubber layer thickness with incompressible material and measured rubber layer thickness with compressible material. The vertical stiffness of a multilayered laminated rubber bearing, for the general case of non-uniform rubber layer thickness, is calculated according to:

$$K_{vo} = \frac{1}{\sum_{i=1}^{n} \frac{t_{r,i}}{E_{c,i}\, A_{b,i}}} \tag{5-11}$$

where $E_{c,i}$ is the compression modulus of the ith rubber layer; $A_{b,i}$ is the bonded area of the ith rubber layer; $t_{r,i}$ is the thickness of the ith rubber layer and n is the number of layers. If the individual rubber layers are assumed to have identical thickness and diameter, (5-11) simplifies to:

$$K_{vo} = \frac{E_c\, A_b}{T_r} \tag{5-12}$$

where E_c is the compression modulus calculated for a typical rubber layer; A_b is the bonded area and T_r the total rubber thickness, in this case, equal to $n\,t_r$ where n is the number of rubber layers. The effective damping in the vertical direction, β_v, was estimated using:

$$\beta_v = \frac{Area\ of\ loop}{2\pi(|P_{\max} - P_{\min}|)(|\delta_{\max} - \delta_{\min}|)} \tag{5-13}$$

where $P_{\max}$ is the maximum axial load; $P_{\min}$ is the minimum axial load; $\delta_{\max}$ is the maximum relative vertical displacement corresponding to $P_{\max}$ and $\delta_{\min}$ is the minimum relative vertical displacement corresponding to $P_{\min}$. The *Area of loop* was determined using a cumulative trapezoidal integration algorithm.

The analysis of a single bonded rubber layer in compression was discussed in Section 2. However, for convenience, portions of this presentation are repeated here. The compression modulus, E_c, for a nearly incompressible material is calculated according to (5-14) per Constantinou et al. (1992):

$$\frac{1}{E_c} = \frac{1}{6GS^2F} + \frac{4}{3\mathrm{K}} \tag{5-14}$$

where G is the shear modulus; S is the shape factor defined as the ratio of the loaded area to the area free to bulge and F is a geometric factor accounting for the central hole in the bearing [see (2-7)]. For the theoretical calculations a standard value of $2000\ \mathrm{MPa}$ was assumed for the bulk modulus, K. Assuming the rubber material is incompressible, that is K approaches infinity, then (5-14) reduces to (5-15).

$$E_c = 6GS^2 F \tag{5-15}$$

For both the LR and LDR bearings, the compression modulus was calculated using the effective shear modulus (G_{eff}) at a shear strain corresponding to the estimated average shear strain due to the applied compressive load. In addition, for both bearings F equal to 0.694.

5.3 Characterization Testing

5.3.1 General

This section presents the results of characterization tests performed on the LDR and LR bearings. Following completion of testing performed on LDR 5, the $12\,\text{mm}$ rubber cover was lathed to an approximate thickness of $3\,\text{mm}$ and re-tested to evaluate the influence of the rubber cover thickness. The results of re-testing LDR 5 (LDR 5M) with $3\,\text{mm}$ of cover are discussed in Section 5.3.2.1. Table 5-1 presents a summary of tests performed on each bearing.

TABLE 5-1 Summary of tests performed on LDR and LR bearings

Test	Type	Description	LDR No.	LR No.
1	A	Shear	5, 5M, 6	5, 6
2	A	Shear	5, 5M,6	5, 6
3	A	Shear	5, 5M,6	5, 6
4	A	Shear	5, 5M,6	5, 6
5	A	Shear	5, 5M,6	5, 6
6	A	Shear	5, 5M,6	5, 6
7	B	Axial	5, 5M,6	5, 6
8	B	Axial	5, 5M,6	5, 6
9	B	Axial	5, 6	5, 6
10	B	Axial	5, 6	5, 6
11	B	Axial	5, 5M,6	5, 6
12	B	Axial	5, 6	5, 6
13	C	Cyclic	5, 6	5, 6
14	D	Combine shear and axial	5, 6	5, 6
15	A	Shear	5, 5M,6	5, 6
16	E	Axial with lateral offset	5, 5M,6	5, 6
17	E	Axial with lateral offset	5, 5M,6	5, 6
18	E	Axial with lateral offset	5, 5M,6	5, 6
19	E	Axial with lateral offset	5, 6	5, 6
20	A	Shear	5, 5M,6	5, 6
21	E	Axial with lateral offset	5, 5M,6	5, 6
22	E	Axial with lateral offset	5, 5M,6	5, 6
23	E	Axial with lateral offset	5, 5M,6	5, 6
24	E	Axial with lateral offset	5, 6	5, 6
25	A	Shear	5, 5M,6	5, 6
26	A	Shear	5, 5M,6	5, 6
27	E	Axial with lateral offset	5, 5M,6	5, 6
28	E	Axial with lateral offset	5, 5M,6	5, 6
29	E	Axial with lateral offset	5, 6	5, 6
30	A	Shear	5, 5M,6	5, 6
31	A	Shear	5, 5M,6	5, 6
32	E	Axial with lateral offset	5, 5M,6	5, 6
33	E	Axial with lateral offset	None	5, 6
34	E	Axial with lateral offset	5, 6	5, 6
35	A	Shear	5, 5M,6	5, 6
36	E	Axial with lateral offset	5	5
37	E	Axial with lateral offset	5	5
38	F	Large deformation tensile	5	5
39	F	Large deformation tensile	6	6
40	A	Shear	5	5

5.3.2 Low-Damping Rubber

5.3.2.1 Influence of Rubber Cover Thickness

The result of characterization tests performed on the LDR 5M were used to more accurately estimate the material properties of the natural rubber compound and to evaluate the contribution of the 12 mm cover to the horizontal stiffness.

Material properties of LDR 5M, including G_{eff} and β_{eff}, were estimated from the results numerous *Shear* tests conducted to various maximum shear strain amplitudes and at two frequencies. Material properties estimated from third cycle results are plotted in figure 5-4 as a function of the maximum shear strain amplitude, γ. Values of G_{eff} and β_{eff} were determined to be $0.82\,\mathrm{MPa}$ and $2.7\,\%$, respectively, for $\gamma = 104\,\%$ at $f = 0.01\,\mathrm{Hz}$. Results from tests conducted on LDR 5 with 12 mm and 3 mm of cover were compared to quantify the contribution of the cover and to determine an "effective" area (A_e) for the estimation of the shear modulus for bearings tested with the full 12 mm cover. In addition, the results of axial load tests conducted on LDR 5 with 12 mm and 3 mm cover were compared to determine the contribution of the cover to the vertical stiffness. Although the influence of the cover on the vertical stiffness was expected to be small the comparison was conducted for completeness.

Effective stiffness results from *Shear* tests conducted to various maximum shear strain amplitudes with $f = 0.01\,\mathrm{Hz}$ performed on LDR 5 with 12 mm and 3 mm of cover were compared to quantify the contribution of the cover thickness to the horizontal stiffness. Figure 5-5a presents a plot of effective stiffness, K_{eff}, versus shear strain amplitude, γ, for LDR 5 with 12 mm and 3 mm of cover. The results presented in this figure demonstrate the significant contribution of the 12 mm cover to the effective shear stiffness. From figure 5-5b, the ratio (or difference) ranges from 1.2 at $52\,\%$ shear strain to 1.3 at $207\,\%$ shear strain. Based on the significant contribution of the cover and consistency of this contribution over the range of maximum shear strain an effective area for estimating the effective shear modulus for bearings tested with the full, 12 mm, cover thickness is proposed. The effective area was determined using the ratio of effective stiffness and bonded rubber area according to:

$$A_e = \left(\frac{K_{\mathrm{eff}}^{12}}{K_{\mathrm{eff}}^{3}} \right) A_b \tag{5-16}$$

where A_b is the bonded rubber area, $K_{\text{eff}}^{12} / K_{eff}^{3}$ equal to 1.2 and A_e is the effective area equal to $21{,}043\ \text{mm}^2$.

Although the $12\ \text{mm}$ cover thickness was not expected to substantially influence the vertical stiffness of the LDR, bearings which is governed by the shape factor of the individual rubber layers, for completeness, a series of axial load tests were repeated on LDR 5 with the $3\ \text{mm}$ cover and compared to test results with $12\ \text{mm}$ cover, specifically Tests 8, 9 and 11 (see table-5-1). Presented in figure 5-6 is a plot of experimentally determined values of the vertical stiffness for LDR 5 with $12\ \text{mm}$ and $3\ \text{mm}$ of cover as a function of the target pressure, ρ. The results presented in this figure show the cover thickness had marginal influence on the vertical stiffness with differences of $12\ \%$, $6\ \%$ and $2\ \%$ for target pressures of $2.75\ \text{MPa}$, $5.2\ \text{MPa}$ and $9\ \text{MPa}$, respectively. Based on these results, the bonded rubber diameter, A_b, will be used in the traditional fashion for the calculation of the compression modulus and vertical stiffness.

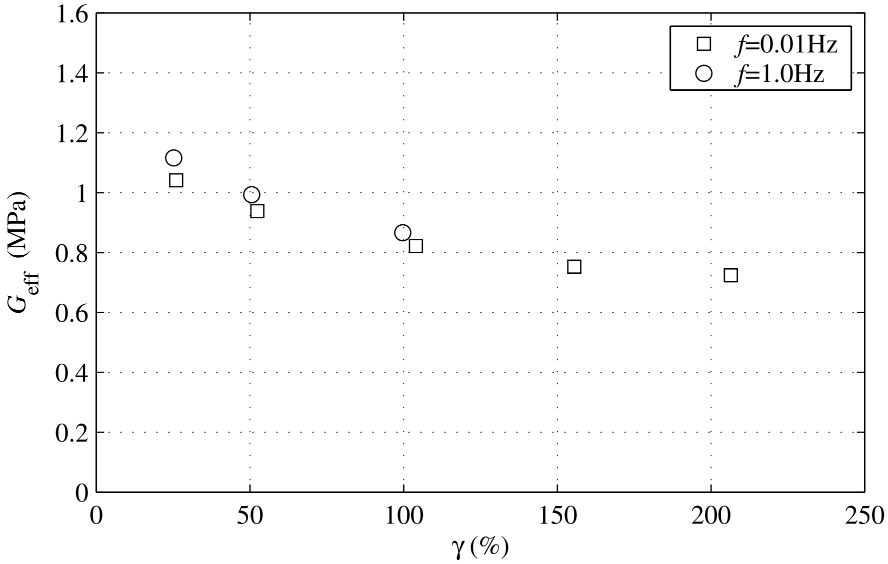

a. effective shear modulus

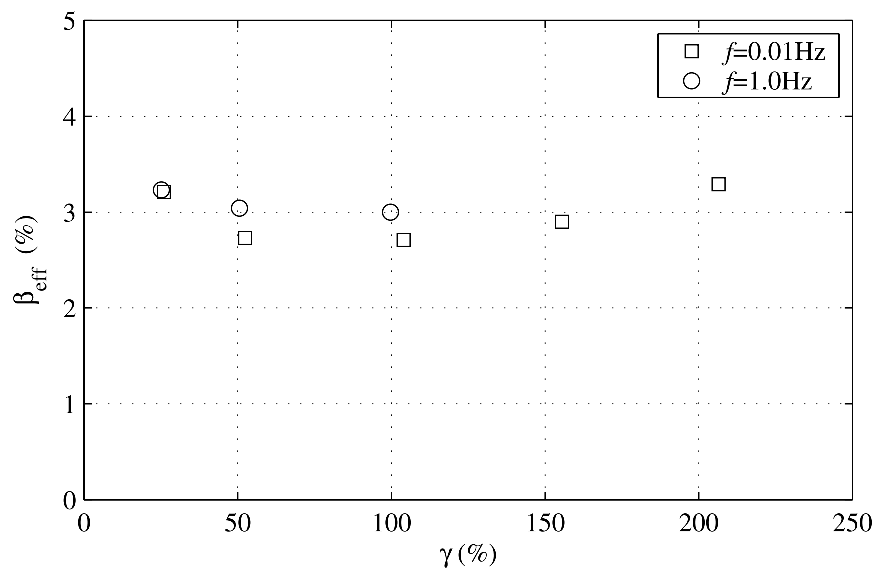

b. effective damping

FIGURE 5-4 Material properties of LDR 5M

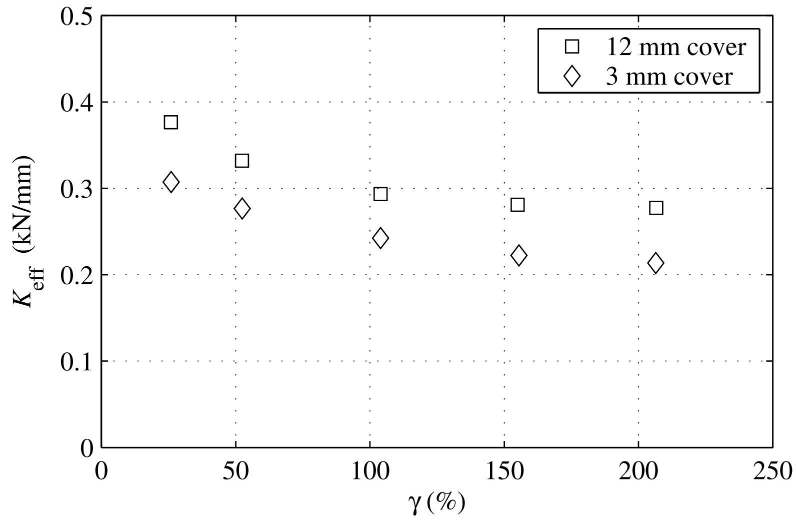

a. effective horizontal stiffness

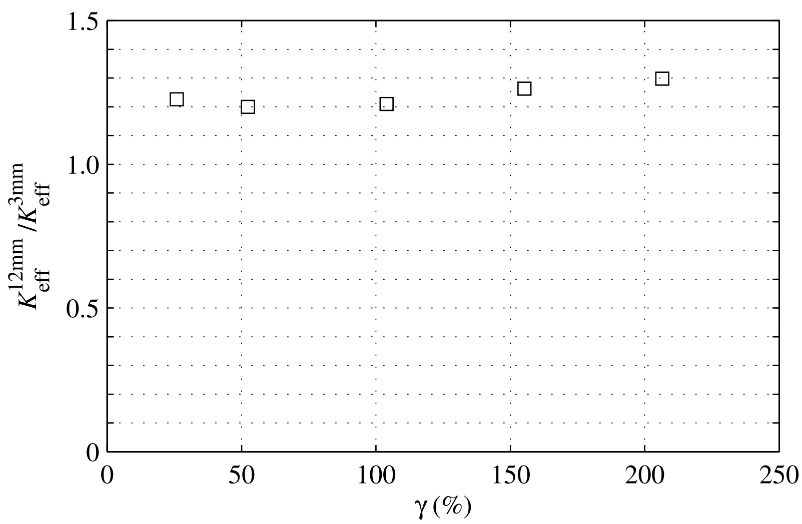

b. ratio of effective horizontal stiffness

FIGURE 5-5 Influence of cover thickness on the horizontal response of LDR 5

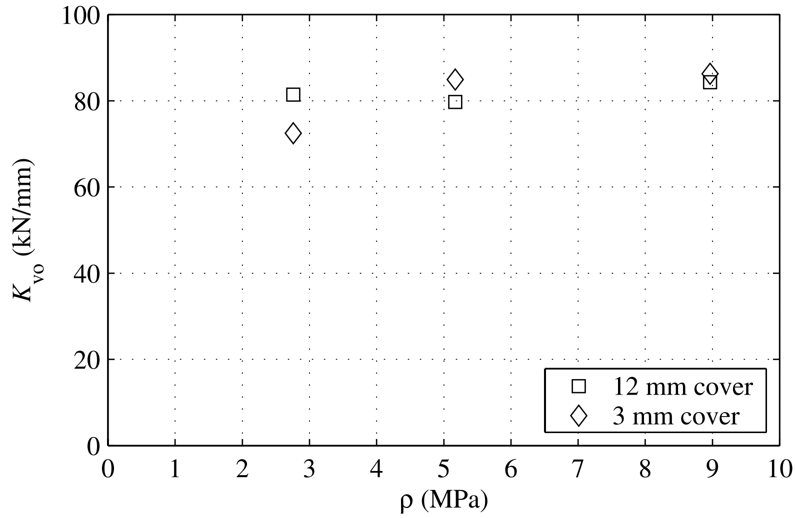

FIGURE 5-6 Influence of cover thickness on the vertical stiffness of LDR 5

5.3.2.2 Lateral Response

A series of *Shear* tests were conducted on the LDR bearings to increasing displacement amplitudes and at two frequencies to determine the variation of mechanical and material properties with strain amplitude and strain rate, identified by the frequency of the input signal. Sample shear force versus lateral displacement results (loops) from Tests 1 through 6 (see table 5-1) performed on LDR 5 are presented in figure 5-7. Loops are presented for shear strain amplitudes of $25\,\%$ (figure 5-7a and 5-7d), 50% (figure 5-7b and 5-7e) and $100\,\%$ (figure 5-7c and 5-7f) and frequencies of $0.01\,\mathrm{Hz}$ (figure 5-7a, 5-7b, and 5-7c) and $1.0\,\mathrm{Hz}$ (figure 5-7d, 5-7e, and 5-7f).

The relatively rate-independent response of the LDR bearings is demonstrated by comparing the loops from tests conducted at $0.01\,\mathrm{Hz}$ (figure 5-7a, 5-7b, and 5-7c) and $1.0\,\mathrm{Hz}$ (figure 5-7d, 5-7e, and 5-7f). Loops from tests conducted at $1.0\,\mathrm{Hz}$ show a marginal increase in K_{eff}, approximately $6-8\,\%$, and W_D, approximately $0-6\,\%$, compared to those conducted at $0.01\,\mathrm{Hz}$. These results suggest the mechanical properties, i.e., effective stiffness and energy dissipation, are relatively rate-independent as an increase in frequency by a factor of 100 resulted in a less than $10\,\%$ increase in the mechanical properties. The effect of strain amplitude is illustrated through a comparison of loops from tests conducted to displacements corresponding to shear strain amplitudes of $25\,\%$, $50\,\%$ and $100\,\%$. For both frequencies, an appreciable reduction in K_{eff}, approximately $24\,\%$, is observed between tests conducted to shear strain amplitudes of 25% and 100%. The effective stiffness, K_{eff}, and effective damping ratio, β_{eff}, from Test 5 performed on LDR 5 were determined to be $0.29\ \mathrm{kN/mm}$ and 2.7%, respectively.

Additional *Shear* tests were conducted to shear strain amplitudes of 150% (Test 26) and 200% (Test 31) at a frequency of $0.01\ \mathrm{Hz}$. Shear force versus lateral displacement loops for these tests performed on LDR 5 are presented in figure 5-8. The loops presented in this figure show a higher degree of nonlinearity and some evidence of scragging, the difference between first and third cycle shear force response. The ratio of first cycle shear force response to third cycle shear force response at 150% and 200% shear strain is approximately 1.05 and 1.09, respectively.

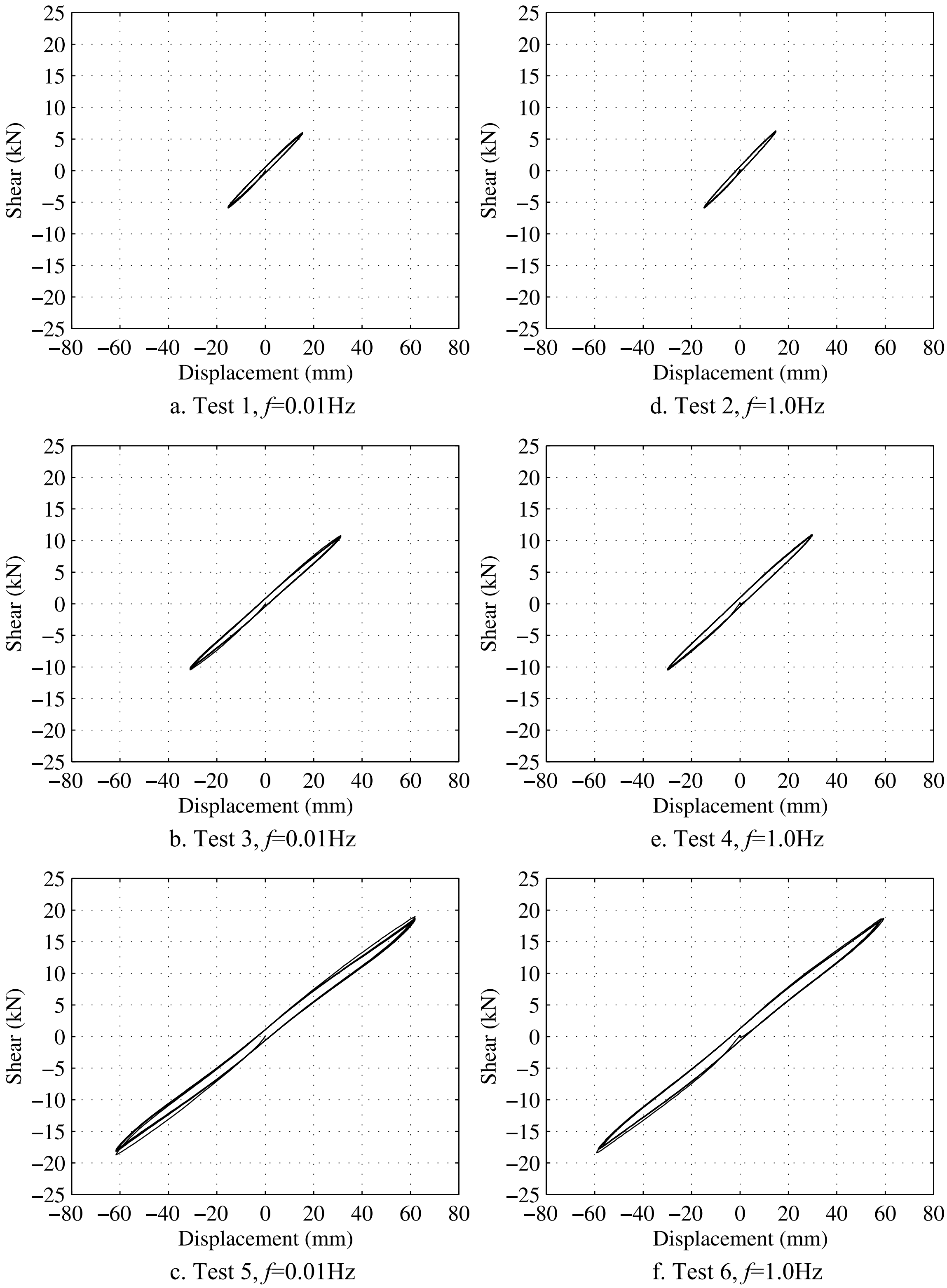

a. Test 1, f=0.01Hz

d. Test 2, f=1.0Hz

b. Test 3, f=0.01Hz

e. Test 4, f=1.0Hz

c. Test 5, f=0.01Hz

f. Test 6, f=1.0Hz

FIGURE 5-7 Shear force versus lateral displacement loops from LDR 5 for Tests 1 through 6

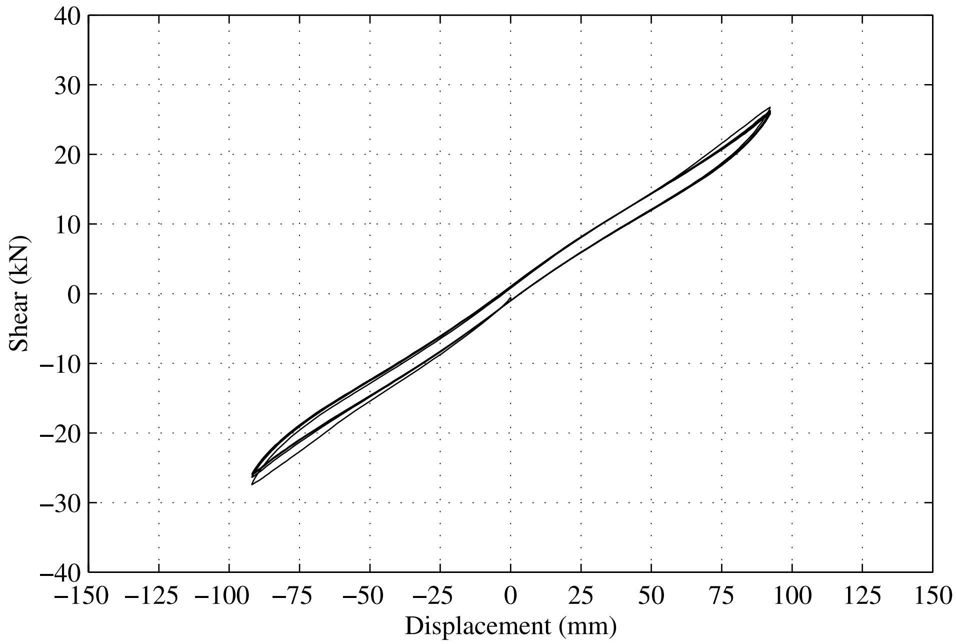

a. Test 26, γ=150 %

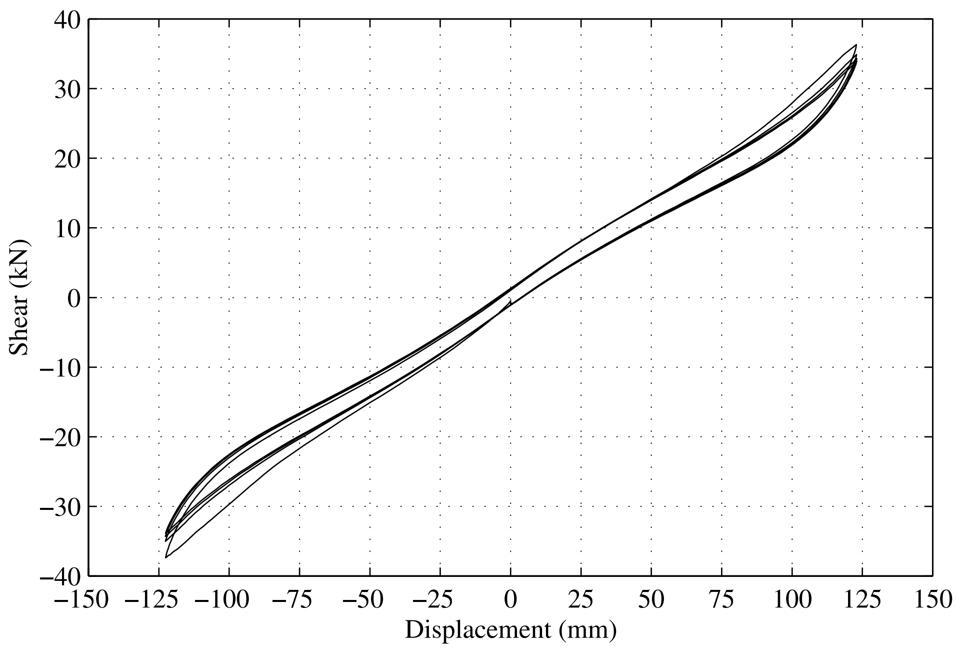

b. Test 31, γ=200 %

FIGURE 5-8 Shear force versus lateral displacement loops from LDR 5 for Tests 26 and 31

Material properties for the LDR bearings, estimated from the results of characterization testing, are plotted in figure 5-9. In this figure, G_{eff} (figure 5-9a) and β_{eff} (figure 5-9b) are plotted as a function of γ for tests performed on LDR 5 and 6 at frequencies of $0.01\,\mathrm{Hz}$ and $1.0\,\mathrm{Hz}$ with an axial pressure of $3.45\,\mathrm{MPa}$. From the results presented in figure 5-9a, G_{eff}, decreases with increasing γ up to approximately $120\,\%$ shear strain and then remains relatively constant up to the maximum shear strain of $207\,\%$ for both bearings. As expected from the resulting mechanical properties, values of G_{eff} and β_{eff} for both bearings appear to be relatively rate-independent. In addition values of G_{eff} and β_{eff} for LDR 5 and 6 agree well for all tests. More specifically, the effective shear modulus and damping ratio from Test 5 ($\gamma = 100\,\%$ and $f = 0.01\,\mathrm{Hz}$) were determined to be $0.99\,\mathrm{MPa}$ and $2.7\,\%$ for LDR 5, and $0.98\,\mathrm{MPa}$ and $2.8\,\%$ for LDR 6, respectively.

A summary of mechanical and material properties from LDR 5 and 6 for Tests 1 through 6, 26 and 31 are presented in table 5-2. In this table, mechanical and material properties are presented for each cycle. Also included is relevant test information such as signal frequency and compressive pressure, p.

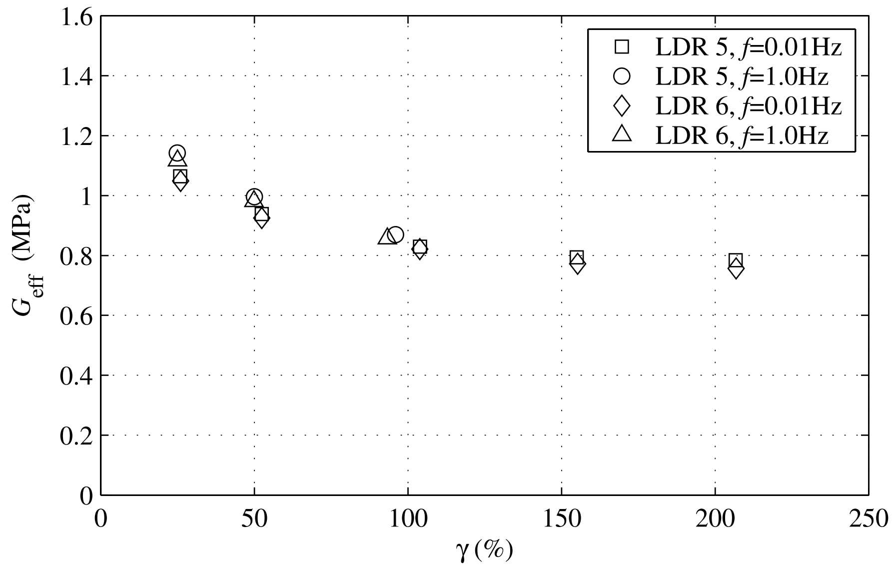

a. effective shear modulus

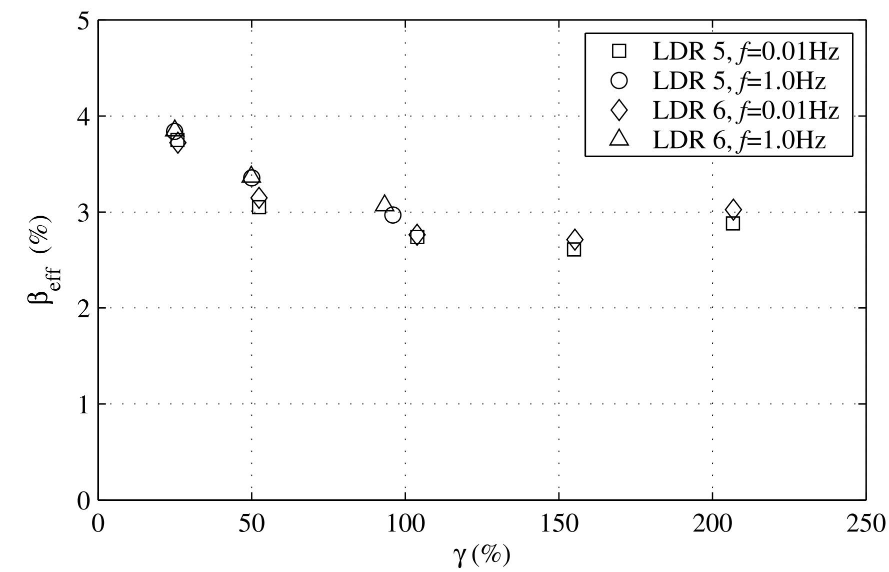

b. effective damping

FIGURE 5-9 Variation of LDR properties with shear strain amplitude and rate

TABLE 5-2 Summary of LDR bearing properties from *Shear* tests

Test	Cycle	f (Hz)	p (MPa)	LDR 5 γ (%)	LDR 5 K_{eff} $\left(\frac{kN}{mm}\right)$	LDR 5 W_D (J)	LDR 5 G_{eff} (MPa)	LDR 5 β_{eff} (%)	LDR 6 γ (%)	LDR 6 K_{eff} $\left(\frac{kN}{mm}\right)$	LDR 6 W_D (J)	LDR 6 G_{eff} (MPa)	LDR 6 β_{eff} (%)
1	1	0.01	3.4	26	0.39	23	1.09	4.0	26	0.38	24	1.08	4.1
	2	0.01	3.4	26	0.38	21	1.07	3.7	26	0.37	21	1.06	3.7
	3	0.01	3.4	26	0.38	21	1.06	3.8	26	0.37	20	1.05	3.7
	4	0.01	3.4	26	0.38	21	1.06	3.7	26	0.37	20	1.05	3.6
2	1	1.00	3.4	25	0.41	23	1.16	4.0	25	0.40	23	1.13	4.0
	2	1.00	3.4	25	0.41	21	1.15	3.8	25	0.40	21	1.12	3.9
	3	1.00	3.4	25	0.40	21	1.14	3.8	25	0.40	21	1.12	3.8
	4	1.00	3.4	25	0.40	21	1.14	3.8	25	0.39	21	1.12	3.8
3	1	0.01	3.4	52	0.34	68	0.96	3.3	52	0.33	68	0.94	3.4
	2	0.01	3.4	52	0.33	63	0.95	3.1	52	0.33	63	0.93	3.2
	3	0.01	3.4	52	0.33	62	0.94	3.0	52	0.33	62	0.93	3.1
	4	0.01	3.4	52	0.33	62	0.94	3.1	52	0.33	60	0.92	3.0
4	1	1.00	3.4	50	0.36	69	1.01	3.5	50	0.35	69	0.99	3.5
	2	1.00	3.4	50	0.35	66	1.00	3.4	50	0.35	65	0.98	3.4
	3	1.00	3.4	50	0.35	66	1.00	3.4	50	0.35	64	0.98	3.4
	4	1.00	3.4	50	0.35	64	0.99	3.3	50	0.35	63	0.98	3.3
5	1	0.01	3.4	104	0.30	218	0.86	3.0	104	0.30	221	0.84	3.1
	2	0.01	3.4	104	0.30	192	0.84	2.7	104	0.29	197	0.83	2.8
	3	0.01	3.4	104	0.29	190	0.83	2.7	104	0.29	193	0.82	2.8
	4	0.01	3.4	104	0.29	188	0.83	2.7	104	0.29	191	0.82	2.7
6	1	1.00	3.4	99	0.31	214	0.88	3.1	99	0.31	212	0.87	3.1
	2	1.00	3.4	96	0.31	189	0.87	3.0	96	0.30	191	0.86	3.0
	3	1.00	3.4	96	0.31	188	0.87	3.0	93	0.30	180	0.86	3.1
	4	1.00	3.4	99	0.31	197	0.87	2.9	96	0.30	187	0.86	2.9
26	1	0.01	3.4	155	0.29	421	0.83	2.7	155	0.28	438	0.80	2.9
	2	0.01	3.4	155	0.28	386	0.80	2.6	155	0.28	402	0.78	2.7
	3	0.01	3.4	155	0.28	387	0.79	2.6	155	0.27	397	0.77	2.7
	4	0.01	3.4	155	0.28	385	0.79	2.6	155	0.27	397	0.77	2.7
31	1	0.01	3.4	207	0.30	866	0.84	3.1	207	0.29	901	0.81	3.3
	2	0.01	3.4	207	0.28	751	0.80	2.9	207	0.27	789	0.77	3.0
	3	0.01	3.4	207	0.28	740	0.78	2.9	207	0.27	771	0.76	3.0
	4	0.01	3.4	207	0.27	728	0.77	2.8	207	0.26	761	0.75	3.0

5.3.2.3 Vertical Response

A series of *Axial* load tests were conducted to determine the vertical stiffness of the LDR bearings for varying levels of applied load and rate-of-load application. Tests 7, 8 and 11 were conducted to maximum axial loads of $60\,\text{kN}$, $120\,\text{kN}$ and $180\,\text{kN}$, respectively, each with a rate of application equal to $0.01\,\text{Hz}$, from zero to the maximum load and back to zero. Tests 8, 9 and 10 were each conducted to $120\,\text{kN}$ with load application rates of $0.01\,\text{Hz}$, $0.1\,\text{Hz}$ and $0.33\,\text{Hz}$, respectively. For this testing program, the maximum load application rate under force control was limited to $0.33\,\text{Hz}$. Higher loading rates resulted in significant inertial forces developing due to the acceleration of the loading beam, which adversely affected the control of the system.

Experimentally determined values of K_{vo} and β_v from Tests 7 through 11 performed on LDR 5 and 6 are presented in table 5-3. The vertical stiffness of LDR 5 and 6 were determined to be $84.3\,\text{kN/mm}$ and $90.4\,\text{kN/mm}$, respectively, from the results of Test 11, $P_{\max} = 180\,\text{kN}$ and $f = 0.01\,\text{Hz}$. Additionally, the vertical effective damping ratio, β_v, for LDR 5 and 6 were determined to be $1.2\,\%$ and $1.0\,\%$, respectively. A marginal increase in K_{vo} was observed comparing the results of Tests 10 ($0.33\,\text{Hz}$) to Test 8 ($0.01\,\text{Hz}$) for LDR 5 and 6 ($7\,\%$ and $5\,\%$, respectively), see table 5-3. Sample axial load versus vertical displacement loops for LDR 5 from Tests 8, 9 and 10 are presented in figure 5-10. The results plotted in this figure show a slight reduction in maximum displacement (value indicated in each plot) and thus increase in vertical stiffness with increasing frequency.

TABLE 5-3 Vertical stiffness results from *Axial* load tests performed on LDR bearings

Test	$P_{\max}$ (kN)	f (Hz)	LDR 5		LDR 6	
			K_{vo} (kN/mm)	β_v (%)	K_{vo} (kN/mm)	β_v (%)
7	60	0.01	81.4	3.4	93.8	2.7
8	120	0.01	79.7	1.5	86.8	1.4
9	120	0.1	83.8	1.2	90.0	1.2
10	120	0.33	85.4	1.1	91.5	1.1
11	180	0.01	84.3	1.2	90.4	1.0

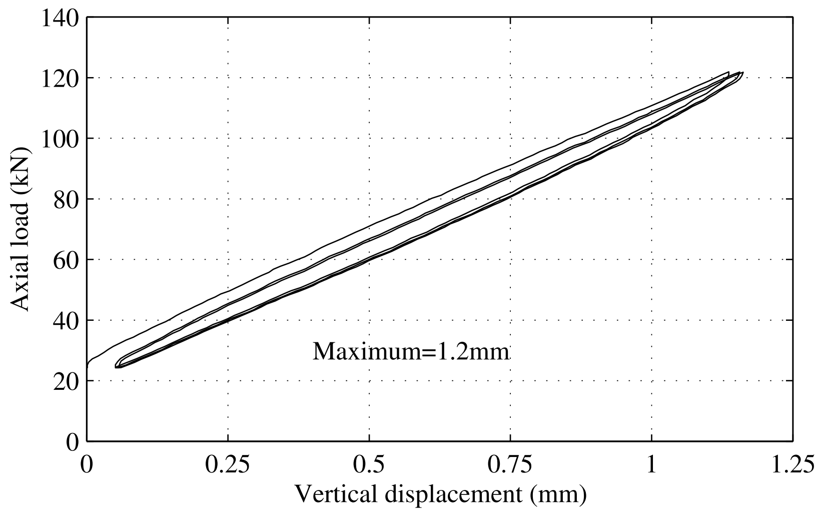

a. Test 8, f=0.01 Hz

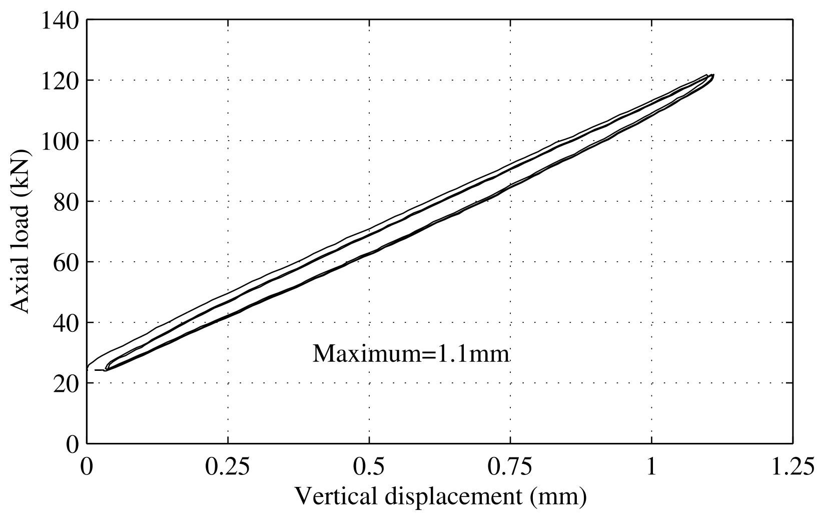

b. Test 9, f=0.1 Hz

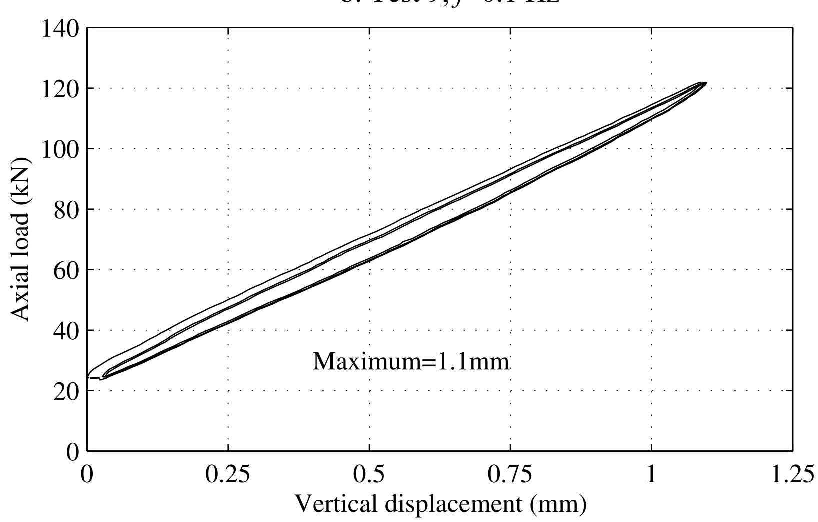

c. Test10, f=0.33 Hz

FIGURE 5-10 Axial load versus vertical displacement loops from tests performed on LDR 5 with various rates of load application

TABLE 5-4 Comparison of vertical stiffness for LDR bearings

No.	Experimental	Theoretical							
		Uniform t_r				Measured t_r			
	K_{vo}^{e}	Incompressible		Compressible		Incompressible		Compressible	
		K_{vo}^{t}	Err	K_{vo}^{t}	Err	K_{vo}^{t}	Err	K_{vo}^{t}	Err
	(kN/mm)	(kN/mm)	(%)	(kN/mm)	(%)	(kN/mm)	(%)	(kN/mm)	(%)
5	84.3	103.9	23	84.0	0.2	NA	-	NA	-
6	90.4	103.9	15	84.0	7	111.4	23	89.3	1

Experimentally determined values of the vertical stiffness were compared to theoretical predictions to verify the compressibility and uniform rubber layer thickness assumptions. Theoretical values were calculated for the following cases: (1) uniform rubber layer thickness and incompressible material; (2) uniform rubber layer thickness and compressible material; (3) measured rubber layer thickness and incompressible material (LDR 6 only); and (4) measured rubber layer thickness and compressible material (LDR 6 only). The resulting theoretical predictions are presented in table 5-4 including an error estimate, denoted Err, between the theoretical and experimental values and calculated according to:

$$Err = \frac{\left|K_{vo}^{t} - K_{vo}^{e}\right|}{K_{vo}^{e}} \cdot 100\% \tag{5-17}$$

where K_{vo}^{t} is the theoretical prediction for a specific case and K_{vo}^{e} is the experimentally determined value. Experimental values of the vertical stiffness presented in table 5-4 were determined from the results of Test 11 ($P_{\max} = 180\,\text{kN}$) using (5-3). Considering the case of uniform t_r (with total rubber thickness equal to $60\,\text{mm}$), the incompressible material assumption results in theoretical predictions of $104\,\text{kN/mm}$ for both bearings over predicting the experimental results with errors of 24% and 15% for LDR 5 and 6, respectively. Assuming the material to be compressible with $K = 2000\,\text{MPa}$, the theoretical predictions estimate the experimentally determined value very well with errors of less than 1% for LDR 5 and 7%, for 6. After testing was completed, LDR 6 (and LR 6 as discussed later in this section) was cut in half using a band saw for inspection and to facilitate measurement of the thickness of the individual rubber layers. The thickness of each rubber layer was measured at the inner and outer edge of one side of the bearing using a digital caliper. Based on the measured individual rubber layer thickness of LDR 6 and assuming incompressible material the theoretical prediction overestimates the experimentally determined value with an error of 23%. Assuming material compressibility, $K = 2000\,\mathrm{MPa}$, the theoretical prediction agrees well with experimentally determined value with an error of 1%. The results presented in table 5-4 suggest the incompressible material assumption tends to overestimate the experimentally determined vertical stiffness for both bearings and that an assumed value of $2000\,\mathrm{MPa}$ for the bulk modulus appears to be reasonable although experimental determination of this parameter would be preferred. Second, calculating the vertical stiffness using the measured individual rubber layer thicknesses results in very good agreement with the experimentally determined value, for this case.

Table 5-5 presents a tabular calculation of the vertical stiffness for LDR 6 based on the measured thickness of the individual rubber layers. Three significant figures are presented for the calculation of $E_{c,i}$ to facilitate tracking of results. The average thickness of an individual rubber layer was used to calculate the shape factor, compression modulus and vertical stiffness of the individual rubber layers. Note that the variation in rubber layer thicknesses and levelness resulting in a range of shape factors from 9.5 to 15.9.

TABLE 5-5 Sample calculation of vertical stiffness for LDR 6 based on the measured individual rubber layer thickness

Rubber Layer	Layer Thickness t_r			Shape Factor S_i	Shear Modulus G	Compression Modulus $E_{c,i}$	Vertical Stiffness $K_{vo,i}$
	Left edge (mm)	Right edge (mm)	Average (mm)		(MPa)	(MPa)	(kN/mm)
1	2.0	1.9	1.9	15.9	0.82	546	195.2
2	2.2	3.2	2.7	11.3		336	85.3
3	3.5	2.2	2.8	10.9		318	78.1
4	2.3	3.7	3.0	10.1		281	63.8
5	3.2	2.6	2.9	10.6		304	72.5
6	3.4	2.9	3.2	9.7		264	57.5
7	3.2	3.1	3.2	9.6		260	56.3
8	2.9	3.2	3.1	10.0		279	63.1
9	2.9	3.4	3.1	9.8		269	59.4
10	3.1	3.3	3.2	9.5		258	55.5
11	3.3	3.0	3.1	9.7		266	58.5
12	2.8	3.0	2.9	10.4		297	69.7
13	3.5	2.8	3.2	9.6		262	56.9
14	2.3	4.0	3.2	9.6		261	56.6
15	3.2	2.3	2.8	11.1		329	82.4
16	3.1	2.8	2.9	10.4		298	70.1
17	3.0	2.8	2.9	10.5		299	70.5
18	2.7	2.6	2.6	11.8		359	95.2
19	2.3	2.6	2.5	12.4		387	107.9
20	2.9	2.7	2.8	11.1		329	82.4
Total			58.0				89.4

5.3.3 Lead-Rubber

5.3.3.1 Lateral Response

As with the LDR bearings, a series of *Shear* tests were performed on the LR bearings to determine the shear force response under conditions of varying displacement amplitude and frequency, see table 4-2. Results from these tests were used to determine nominal mechanical properties and to estimate bearing material properties, specifically, the effective yield strength of the lead-core. In addition results from these tests were used to determine the dependency of the estimated material properties on strain amplitude, γ, and strain rate defined by the signal frequency, f.

Sample shear force versus lateral displacement loops from Tests 1 through 6 performed on LR 5 are presented in figure 5-11 to illustrate the influence of strain amplitude and rate on the response of the LR bearings. Loops presented in this figure are for shear strain amplitudes of approximately $25\,\%$, $50\,\%$ and $100\,\%$ conducted at frequencies of $0.01\,\mathrm{Hz}$ and $1.0\,\mathrm{Hz}$. Three observations are provided based on the loops presented in figure 5-11. First, for both frequencies, an increase in characteristic strength, Q_d, is observed with increasing maximum displacement (shear strain amplitude) suggesting the lead exhibits some level of isotropic hardening. Second, for each displacement amplitude, the LR bearing exhibits an increase in Q_d, K_d and W_D, energy dissipated per cycle, for tests conducted at $1.0\,\mathrm{Hz}$ (figures 5-11d, 5-11e and 5-11f) compared to those at $0.01\,\mathrm{Hz}$ (figures 5-11a, 5-11b and 5-11c) suggesting the effective yield strength of the lead-core shows some rate-dependency. Third, tests conducted to displacement amplitudes corresponding to $\gamma = 100\,\%$, figures 5-11c and 5-11f, exhibited an unusual "bow-tie" shaped loop. Although the cause for this bow-tie shape is not explored in great detail a plausible explanation is provided. The bow-tie shape appears to be the result of an expanding yield surface, Q_d, between shear strain amplitudes of $25\,\%$ and $100\,\%$, referred to in this section as intermediate shear strain.

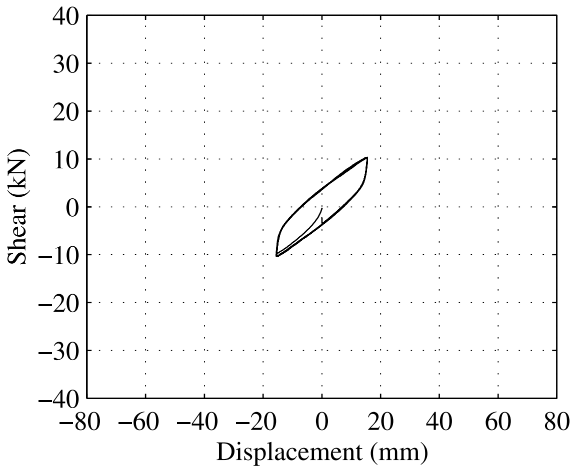

a. Test 1, *f*=0.01Hz

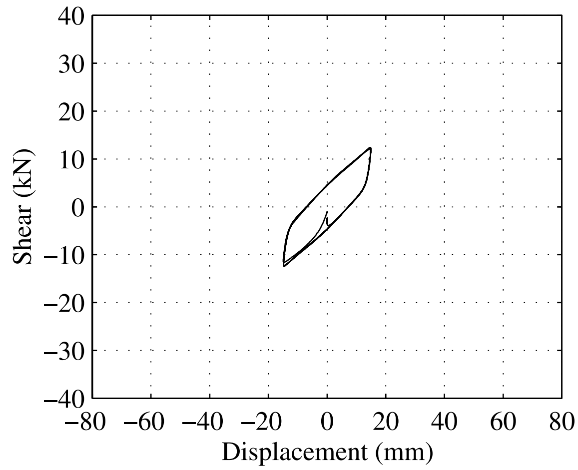

d. Test 2, *f*=1.0Hz

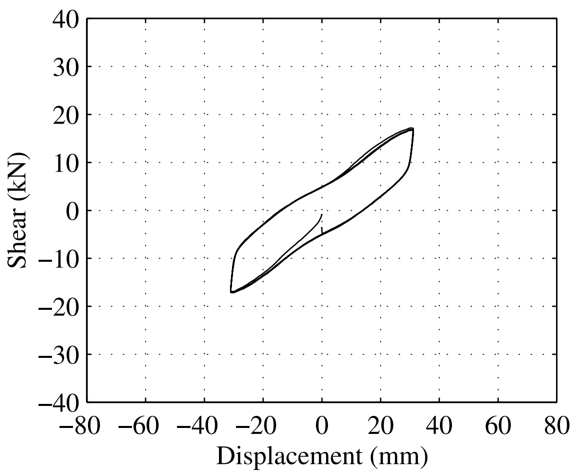

b. Test 3, *f*=0.01Hz

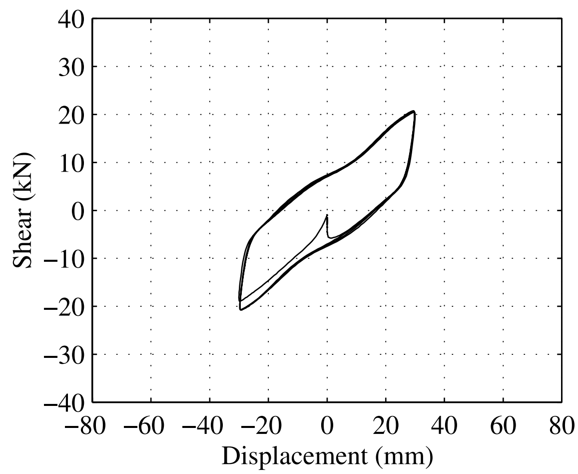

e. Test 5, *f*=1.0Hz

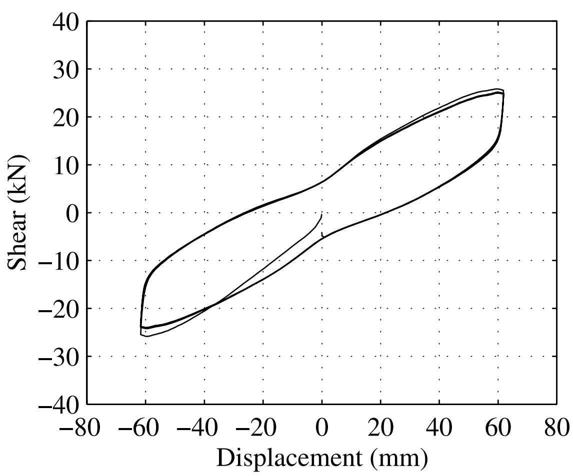

c. Test 4, *f*=0.01Hz

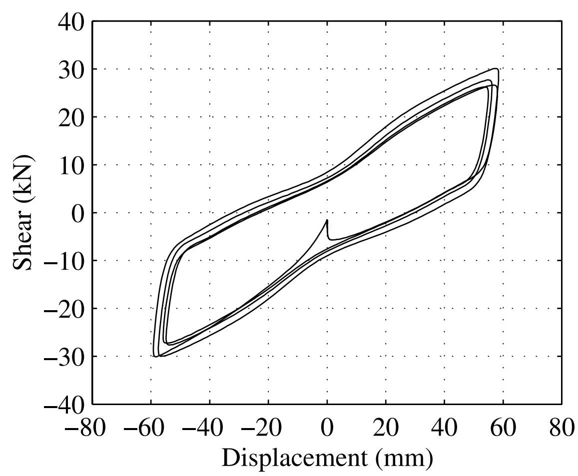

f. Test 6, *f*=1.0Hz

FIGURE 5-11 Shear force versus lateral displacement loops from LR 5 for Tests 1 through 6

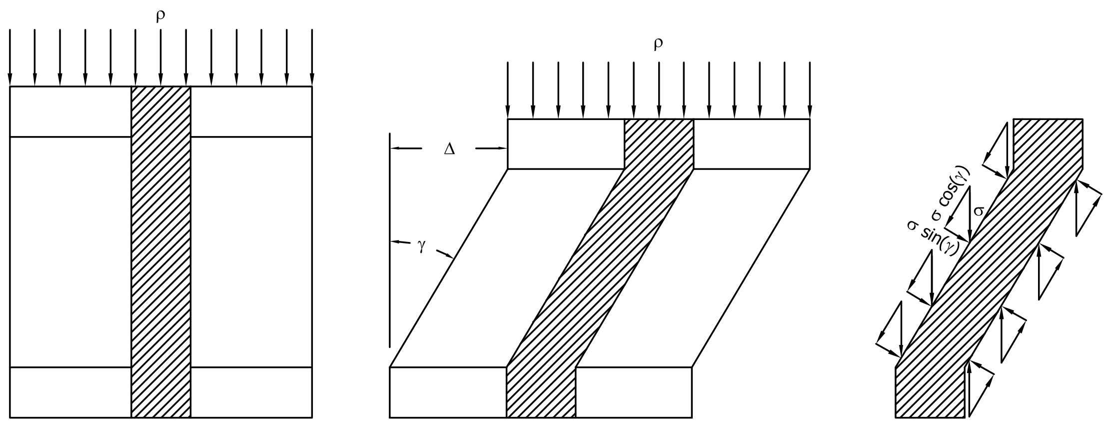

FIGURE 5-12 Illustration of LR bearing and core subjected to combined lateral displacement and compressive pressure

The bow-tie shape might be attributed to confining stress applied to the core in the deformed configuration due to the applied compressive load. This concept is illustrated in figure 5-12 which presents an illustration of a LR bearing with an applied compressive pressure, p, in both the un-deformed and sheared configuration. Also shown, is the resulting pressure on the core, σ, due to the applied compressive pressure and its components, $\sigma\cos(\gamma)$ and $\sigma\sin(\gamma)$ a function of the shear strain, γ, corresponding to a lateral displacement, Δ. In the intermediate shear strain range, the $\sigma\sin(\gamma)$ component acts as a confining pressure on the lead core thus increasing Q_d. This behavior is believed to be apparent in these LR bearings due to the lack of initial confinement of the lead-core.

The LR bearings were subjected to large lateral displacements during Tests 26 and 31, corresponding to $\gamma = 150\ \%$ and $\gamma = 200\ \%$, respectively. Shear force versus lateral displacement loops from these test performed on LR 5 are presented in figure 5-13. Both tests were conducted at $0.01\ \mathrm{Hz}$. The loops presented in figure 5-13 show an increase in the thickness of the loops in the intermediate strain range consistent with the previous results. This increase in thickness is not apparent for strains greater than $150\ \%$ which may be due to the small overlapping area of the top and bottom end plates at this level of lateral displacement.

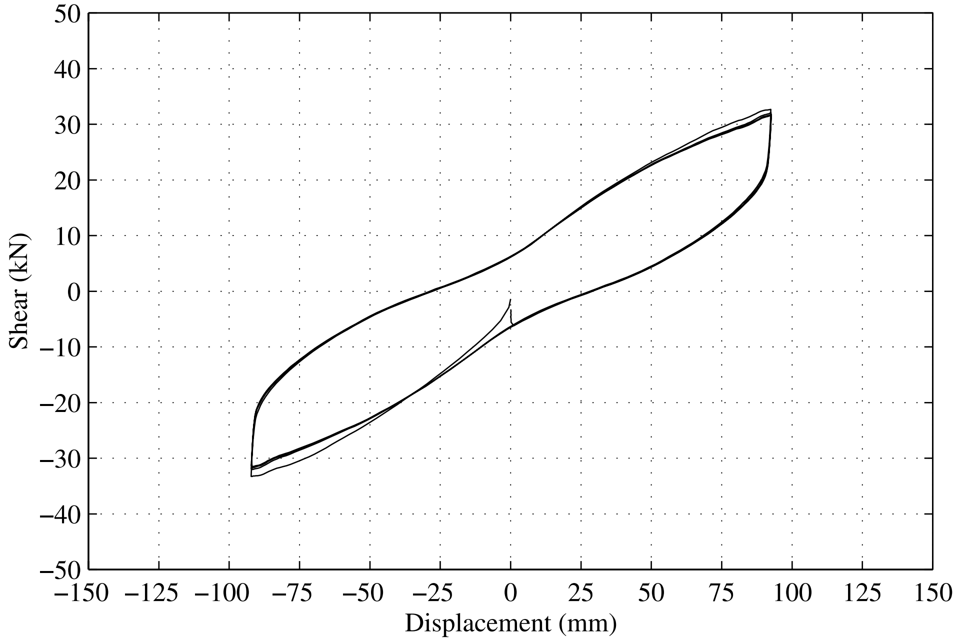

a. Test 26, γ=150 %

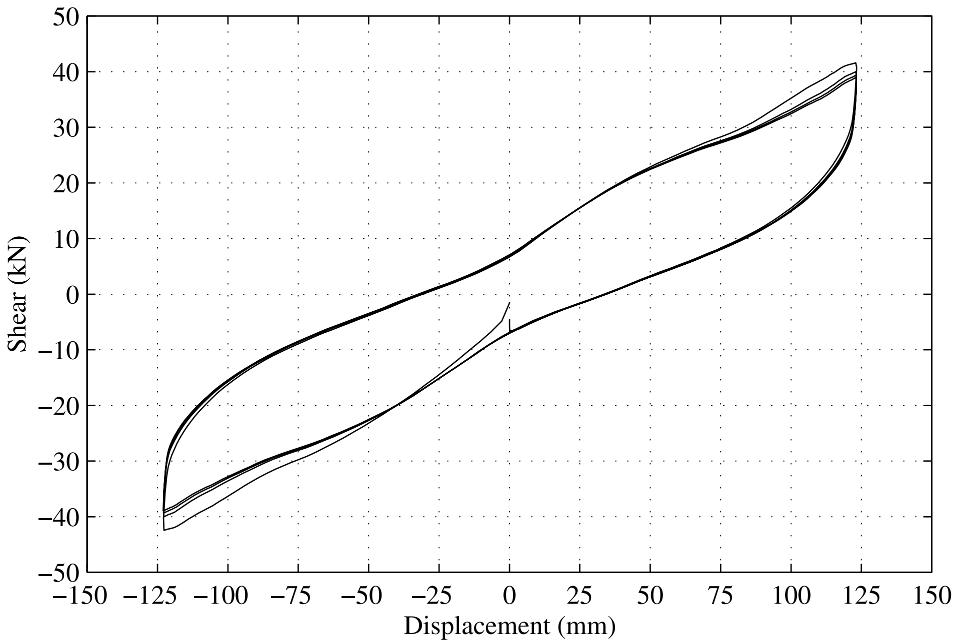

b. Test 31, γ=200 %

Figure 5.13 Shear force versus lateral displacement loops from LR 5 for Tests 26 and 31.

Material properties of the LR bearings, namely, the effective lead-core yield strength, σ_L, and effective damping ratio, β_{eff}, were calculated from the results of the *Shear* tests. Figure 5-14 presents plots of σ_L and β_{eff} as a function of γ from tests performed on LR 5 and 6. Values of σ_L and β_{eff} presented in this figure were calculated from the third cycle response. From figure 5-14a, σ_L (and analogously Q_d) is observed to increase with increasing maximum shear strain amplitude. For example, σ_L for LR 5 and $0.01\,\text{Hz}$, increases from $5.3\,\text{MPa}$ at $\gamma \approx 25\,\%$ to $9.8\,\text{MPa}$ at $\gamma \approx 200\%$. The lead yield strength of LR 6 exhibited similar results. Additionally, figure 5-14a illustrates the influence of frequency (or strain-rate) on the yield strength of the lead-core. For example, σ_L for LR 6 increases from $7.3\,\text{MPa}$ for $0.01\,\text{Hz}$ to $10.7\,\text{MPa}$ for $1.0\,\text{Hz}$ at a maximum shear strain amplitude of approximately $50\,\%$. Plotted in figure 5-14b is β_{eff} versus γ for LR 5 and 6. The β_{eff} results presented in figure 5-14b show no appreciable dependency on f and decrease with increasing maximum shear strain amplitude as expected. The lead yield strength and effective damping ratio for LR 5 and 6 from the third cycle of Test 5, $\gamma = 100\,\%$ and $0.01\,\text{Hz}$, were determined to be approximately $8.3\,\text{MPa}$ and $19\,\%$, respectively. A summary of the mechanical and material properties for the LR bearings determined from Tests 1 through 6, 26 and 31 are presented in table 5-6. Values of the mechanical and material properties are presented for each cycle.

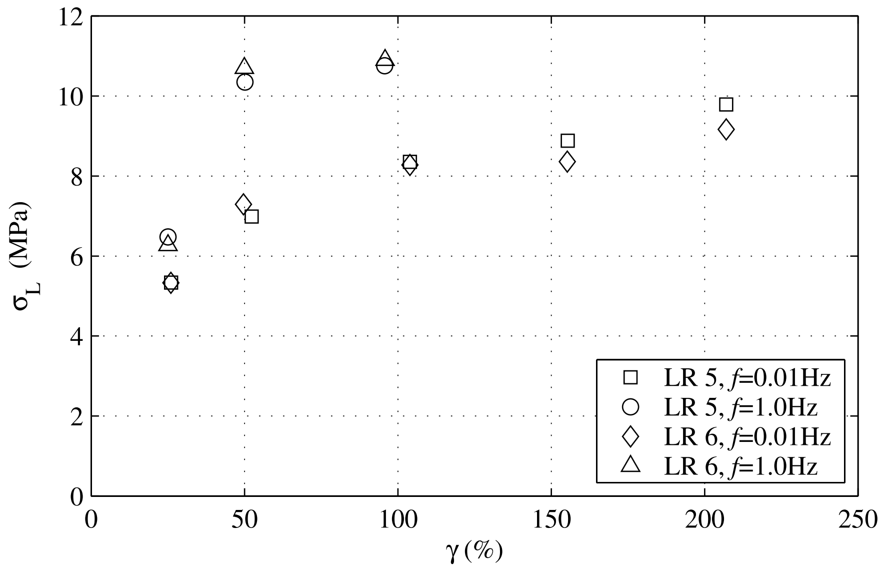

a. effective lead yield strength

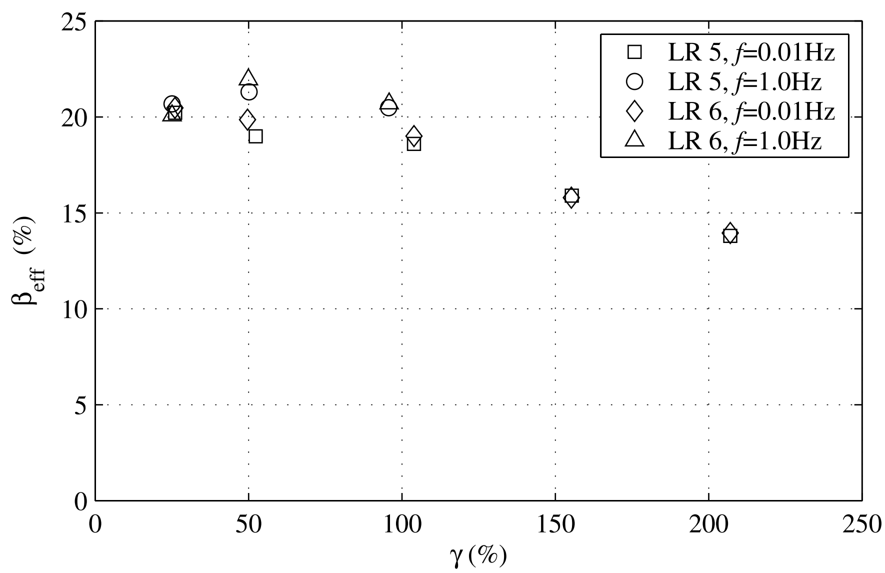

b. effective damping

FIGURE 5-14 Variation of LR properties with shear strain amplitude and rate

TABLE 5-6 Summary of LR bearing properties from *Shear* tests

Test	Cycle	f (Hz)	p (MPa)	LR 5 γ (%)	LR 5 Q_d (kN)	LR 5 K_{eff} $\left(\frac{\text{kN}}{\text{mm}}\right)$	LR 5 W_D (J)	LR 5 σ_L (MPa)	LR 5 β_{eff} (%)	LR 6 γ (%)	LR 6 Q_d (kN)	LR 6 K_{eff} $\left(\frac{\text{kN}}{\text{mm}}\right)$	LR 6 W_D (J)	LR 6 σ_L (MPa)	LR 6 β_{eff} (%)
1	1	0.01	3.4	26	3.6	0.64	184	5.0	19.0	26	3.7	0.63	177	5.4	18.9
	2	0.01	3.4	26	3.8	0.66	205	5.4	20.6	26	3.8	0.65	201	5.4	20.9
	3	0.01	3.4	26	3.8	0.66	202	5.3	20.2	26	3.7	0.65	197	5.3	20.5
	4	0.01	3.4	26	3.7	0.66	200	5.3	20.0	26	3.7	0.65	196	5.3	20.4
2	1	1.00	3.4	25	4.7	0.79	224	6.7	20.2	25	3.9	0.74	189	5.6	18.4
	2	1.00	3.4	25	4.6	0.81	239	6.5	21.1	25	4.3	0.77	212	6.2	19.9
	3	1.00	3.4	25	4.6	0.82	236	6.5	20.7	25	4.4	0.77	215	6.3	20.1
	4	1.00	3.4	25	4.5	0.82	235	6.4	20.5	25	4.4	0.78	218	6.3	20.2
3	1	0.01	3.4	52	4.8	0.55	595	6.9	17.9	50	5.2	0.55	560	7.3	18.7
	2	0.01	3.4	52	5.0	0.55	629	7.0	19.3	50	5.3	0.56	603	7.5	20.1
	3	0.01	3.4	52	4.9	0.54	614	7.0	19.0	50	5.1	0.55	589	7.3	19.9
	4	0.01	3.4	52	4.9	0.54	605	6.9	18.9	50	5.1	0.55	583	7.2	19.8
4	1	1.00	3.4	51	7.1	0.65	762	10.0	20.6	50	7.0	0.63	738	9.9	20.9
	2	1.00	3.4	50	7.4	0.68	821	10.4	21.6	50	7.5	0.67	814	10.7	22.2
	3	1.00	3.4	50	7.3	0.69	811	10.3	21.3	50	7.6	0.68	819	10.7	21.9
	4	1.00	3.4	50	7.2	0.69	802	10.2	21.0	50	7.6	0.68	810	10.7	21.6
5	1	0.01	3.4	104	5.8	0.42	1723	8.2	17.3	104	6.2	0.41	1741	8.8	17.7
	2	0.01	3.4	104	5.9	0.40	1770	8.3	18.6	104	5.9	0.39	1781	8.3	19.1
	3	0.01	3.4	104	5.9	0.40	1744	8.4	18.6	104	5.8	0.39	1745	8.3	19.0
	4	0.01	3.4	104	5.9	0.40	1729	8.3	18.6	104	5.9	0.39	1740	8.3	19.0
6	1	1.00	3.4	99	9.2	0.51	2298	13.0	20.6	99	9.5	0.51	2323	13.5	20.8
	2	1.00	3.4	98	8.0	0.51	2330	11.4	21.2	98	8.2	0.52	2381	11.6	21.4
	3	1.00	3.4	96	7.6	0.50	2131	10.8	20.5	96	7.7	0.51	2178	10.9	20.7
	4	1.00	3.4	93	7.3	0.49	1952	10.3	20.0	94	7.4	0.50	2011	10.4	20.5
26	1	0.01	3.4	155	6.1	0.35	2929	8.6	15.4	155	6.0	0.35	2873	8.6	15.5
	2	0.01	3.4	155	6.2	0.35	2906	8.8	15.9	155	5.9	0.34	2864	8.3	15.9
	3	0.01	3.4	155	6.3	0.34	2882	8.9	15.9	155	5.9	0.34	2820	8.4	15.8
	4	0.01	3.4	155	6.3	0.34	2862	8.9	15.8	155	5.9	0.33	2817	8.4	15.8
31	1	0.01	3.4	207	6.5	0.34	4354	9.3	13.4	207	6.8	0.33	4285	9.6	13.6
	2	0.01	3.4	207	6.8	0.33	4311	9.7	13.7	207	6.4	0.32	4238	9.1	14.0
	3	0.01	3.4	207	6.9	0.32	4253	9.8	13.8	207	6.5	0.31	4144	9.2	14.0
	4	0.01	3.4	207	7.0	0.32	4242	9.9	13.9	207	6.5	0.31	4132	9.2	14.0

TABLE 5-7 Vertical stiffness results from *Axial* load tests performed on LR bearings

Test	P_{max} (kN)	f (Hz)	LR 5		LR 6	
			K_{vo} (kN/mm)	β_v (%)	K_{vo} (kN/mm)	β_v (%)
7	60	0.01	138.7	5.4	116.0	6.3
8	120	0.01	154.1	2.6	131.8	2.7
9	120	0.1	164.1	2.4	140.4	2.2
10	120	0.33	167.2	2.3	144.4	2.2
11	180	0.01	163.3	1.9	145.1	2.0

5.3.3.2 Vertical Response

The LR bearings were subjected to a series of *Axial* load tests to various maximum compressive and tensile loads. This section presents results from compressive *Axial* load tests and the subsequently determined values of the vertical stiffness and vertical effective damping ratio. Experimentally determined values of the vertical stiffness and effective damping for LR 5 and 6 are presented in table 5-7. Also presented in this table is relevant test information such as approximate maximum axial load, P_{max}, and rate of load application, denoted f, for each test. From Test 11 ($P_{max} = 180\text{ kN}$ and $f = 0.01\text{ Hz}$), the vertical stiffness of LR 5 and 6 were determined to be 163 kN/mm and 145 kN/mm, respectively. Additionally, the vertical effective damping was estimated to be approximately $2\,\%$ for both bearings.

Tests 8, 9 and 10 were conducted to an axial load amplitude of 120 kN with load application rates of 0.01 Hz, 0.1 Hz and 0.33 Hz, respectively. A comparison of K_{vo} from Test 8 (0.01 Hz) and Test 10 (0.33 Hz) indicates an $9\,\%$ and $10\,\%$ increase in vertical stiffness for LR 5 and 6, respectively. For the same tests, the vertical effective damping decreased from $2.6\,\%$ to $2.3\,\%$ for LR 5 and from $2.7\,\%$ to $2.2\,\%$ for LR 6. Sample axial load versus vertical displacement loops for LR 5 from Tests 8, 9 and 10 are presented in figure 5-15. These plots include the maximum displacement value and illustrate the slight increase in stiffness with increased rate of load application. Two observations are made from the results of Test 8, 9 and 10. First, the rate of load application resulted in a marginal increase in vertical stiffness and therefore reduction in vertical effective damping for the range of load application rates consider here. Second, the vertical effective damping for the LR and the LDR bearings were determined to be, approximately, $2\,\%$ and $1\,\%$, respectively, suggesting the lead-core did not participate in the vertical direction.

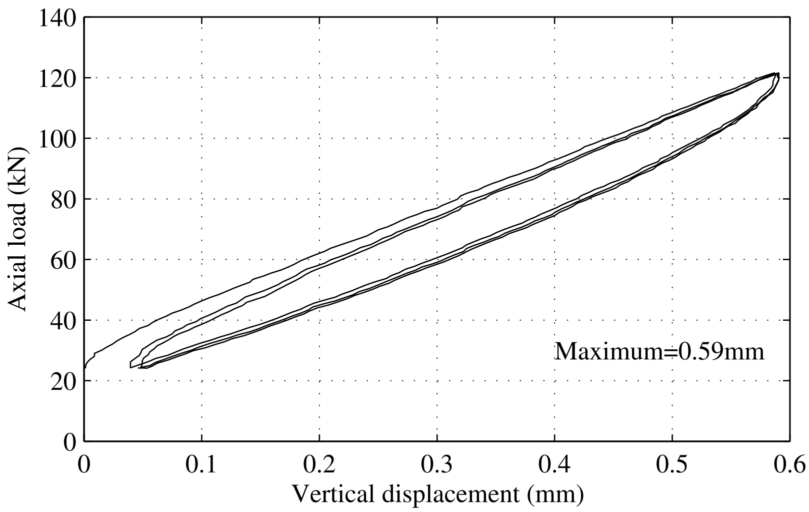

a. Test 8, f=0.01 Hz

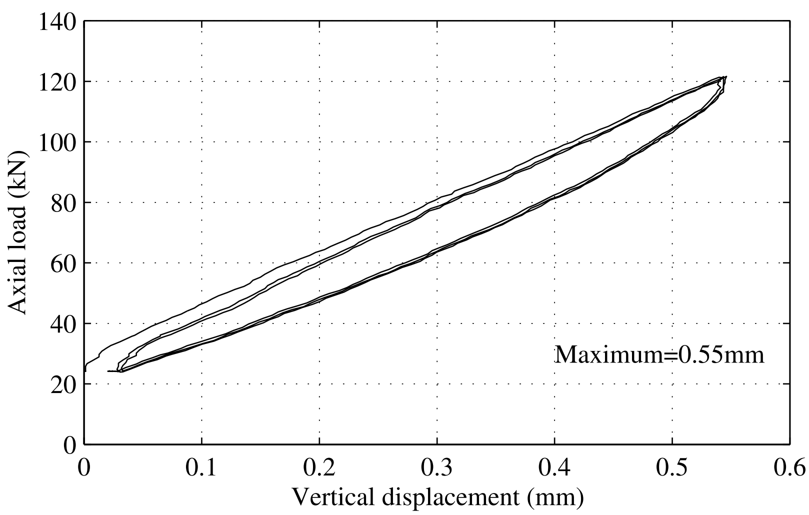

b. Test 9, f=0.1 Hz

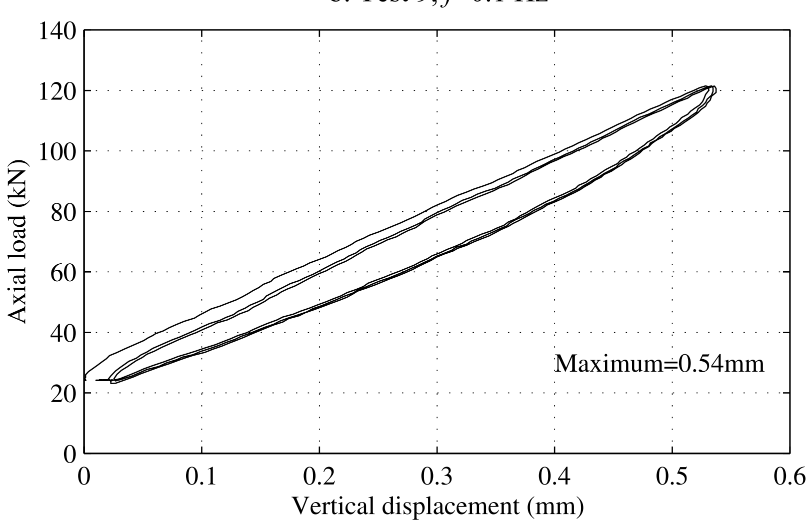

c. Test10, f=0.33 Hz

FIGURE 5-15 Axial load versus vertical displacement loops from LR 5 for various rates of load application

Experimentally determined values of the vertical stiffness were compared to theoretical values, calculated for the considerations described in Section 5.3.2.3, to validate the compressibility and uniform thickness assumption. Table 5-8 presents experimentally determined and theoretically calculated values of the vertical effective stiffness, denoted K_{vo}^{e} and K_{vo}^{t}, respectively. As stated previously, the vertical stiffness was calculated using the effective shear modulus (G_{eff}) estimated at a maximum shear strain corresponding to the estimated average shear strain due to compressive loading as determined from Test 11 with $P_{\max} = 180\,\text{kN}$ and $f = 0.01\,\text{Hz}$. An estimate of the error between the calculated values and the experimentally determined value is included in table 5-8. The error estimates are denoted, Err, and calculated according to (5-17). Based on the results presented in table 5-8 the following comments are provided. First, for uniform individual rubber layer thickness, the incompressible assumption substantially overestimates the experimentally determined values for LR 5 and 6 by $72\,\%$ and $97\,\%$ error, respectively. If the rubber is assumed to be compressible, with $K = 2000\,\text{MPa}$, the calculated values show better agreement with K_{vo}^{e} for both bearings, with errors of $5\,\%$ and $19\,\%$ for LR 5 and 6, respectively. Similar to the LDR 6 bearings, the LR 6 was cut in half following completion of the testing program to inspect and measure individual rubber layer thicknesses. Using the measured rubber layer thicknesses the incompressible assumption again results in a vertical stiffness which overestimates the K_{vo}^{e} with an error of $96\,\%$. Assuming the rubber is compressible and using the measured individual rubber layer thicknesses, the calculated value results in $173\,\text{kN/mm}$ and an approximate error of $20\,\%$ when compared to the experimental value. For the LR bearings, the incompressible assumption resulted in a substantial overestimation of the vertical stiffness. Assuming the material to be compressible resulted in vertical stiffness predictions that agreed reasonably well with the experimental values. In addition, unlike LDR 6, accounting for variations in the individual rubber layer thicknesses did result in an improved prediction.

TABLE 5-8 Comparison of vertical stiffness for LR bearings

No.	Experimental	Theoretical							
		Uniform t_r				Measured t_r			
		Incompressible		Compressible		Incompressible		Compressible	
	K_{vo}^{e}	K_{vo}^{t}	Err	K_{vo}^{t}	Err	K_{vo}^{t}	Err	K_{vo}^{t}	Err
	(kN/mm)	(kN/mm)	(%)	(kN/mm)	(%)	(kN/mm)	(%)	(kN/mm)	(%)
5	163.3	280.0	71.4	170.8	4.6	NA	-	NA	-
6	145.1	285.0	96.5	172.7	19.0	283.8	95.6	173.2	19.4

5.3.4 Monitoring

A benchmark *Shear* test was repeated intermittently throughout the testing program for the purpose of monitor changes in the mechanical properties. The benchmark test subjected the bearing to four fully reversed cycles to a lateral displacement equal to approximately $60\,\text{mm}$ ($\gamma = 100\,\%$) at a frequency of $0.01\,\text{Hz}$ with a compressive load of $60\,\text{kN}$ ($3.5\,\text{MPa}$), see table 4-2.

Figure 5-16 presents plots of the effective shear modulus, G_{eff}, effective damping, β_{eff}, and energy dissipated per cycle, W_D, from third cycle results of the benchmark test performed on LDR 5 and 6 as a function of the test number. From figure 5-16a, the effective shear modulus appears relatively constant for Test 5 through Test 25 then decreases with Tests 30, 35, and 40. The effective shear modulus for LDR 5 from Tests 5 and 40 are $0.83\,\text{MPa}$ and $0.74\,\text{MPa}$, respectively, corresponding to a $10\,\%$ change through the program. Similarly, β_{eff}, (figure 5-16b) is relatively constant for Tests 5 through Test 25 then increases for Tests 30, 35 and 40. This is likely due to a combination of the reduction in effective stiffness (as observed from the effective shear modulus) and a slight increase in W_D (figure 5-16c) for Tests 30, 35 and 40. The bearing LDR 6 was significantly damaged during Test 39 and was not subjected to Test 40.

Figure 5-17 presents the third cycle results from benchmark tests performed on LR 5 and 6. These results include: σ_L the lead yield strength; β_{eff} the effective damping ratio and W_D, the energy dissipated per cycle. As noted previously, benchmark Test 40 was not performed on LR 6 due to significant damage that occurred during Test 39. From figure 5-17a, σ_L for LR 5 is observed to increase from $8.4\,\text{MPa}$ to $9.4\,\text{MPa}$ from Test 5 to Test 40, respectively. The σ_L for LR 6 from the benchmark tests showed similar trends to LR 5. The effective damping ratio for both bearings, shown in figure 5-17b, remained relatively constant up to Test 25, then increased for Tests 30, 35 and 40. Figure 5-17c shows the energy dissipated per cycle for LR 5 and 6 which remains relatively constant throughout the testing program. Based on the results presented in figure 5-17, the mechanical and material properties of the LR bearings remained fairly constant throughout the testing program with the exception of the lead yield strength, which appeared to increase perhaps due to repeated cycling.

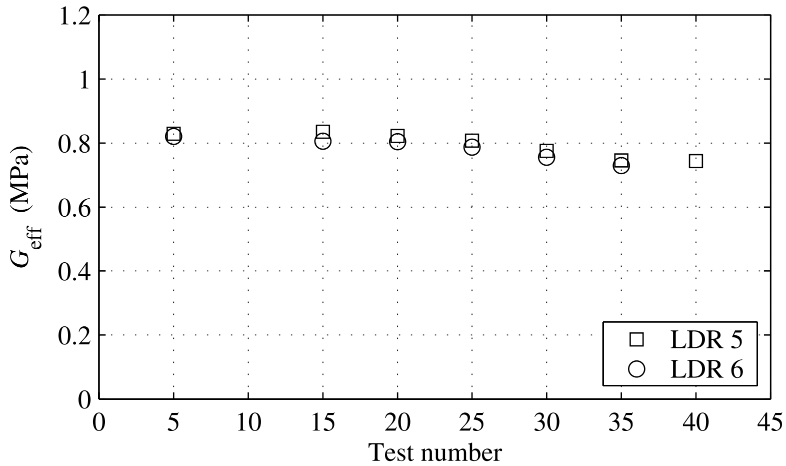

a. effective shear modulus

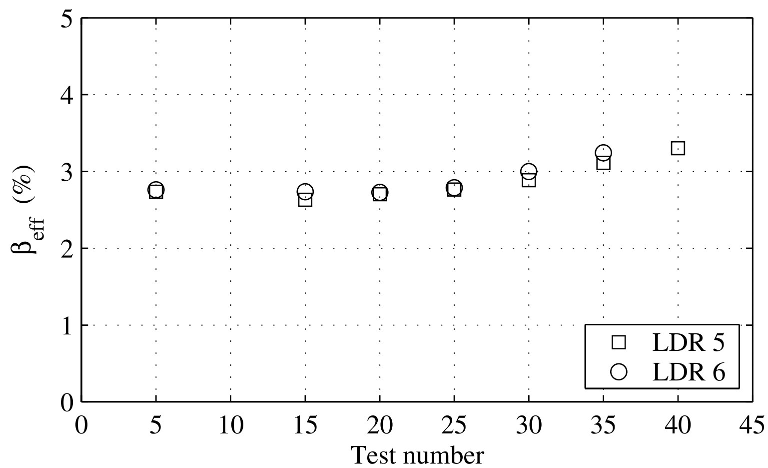

b. effective damping

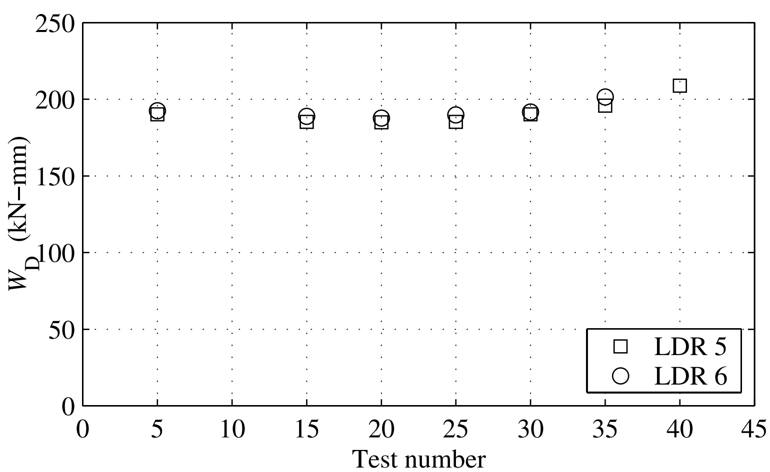

c. energy dissipated

FIGURE 5-16 Third cycle properties of the LDR bearings from benchmark *Shear* tests

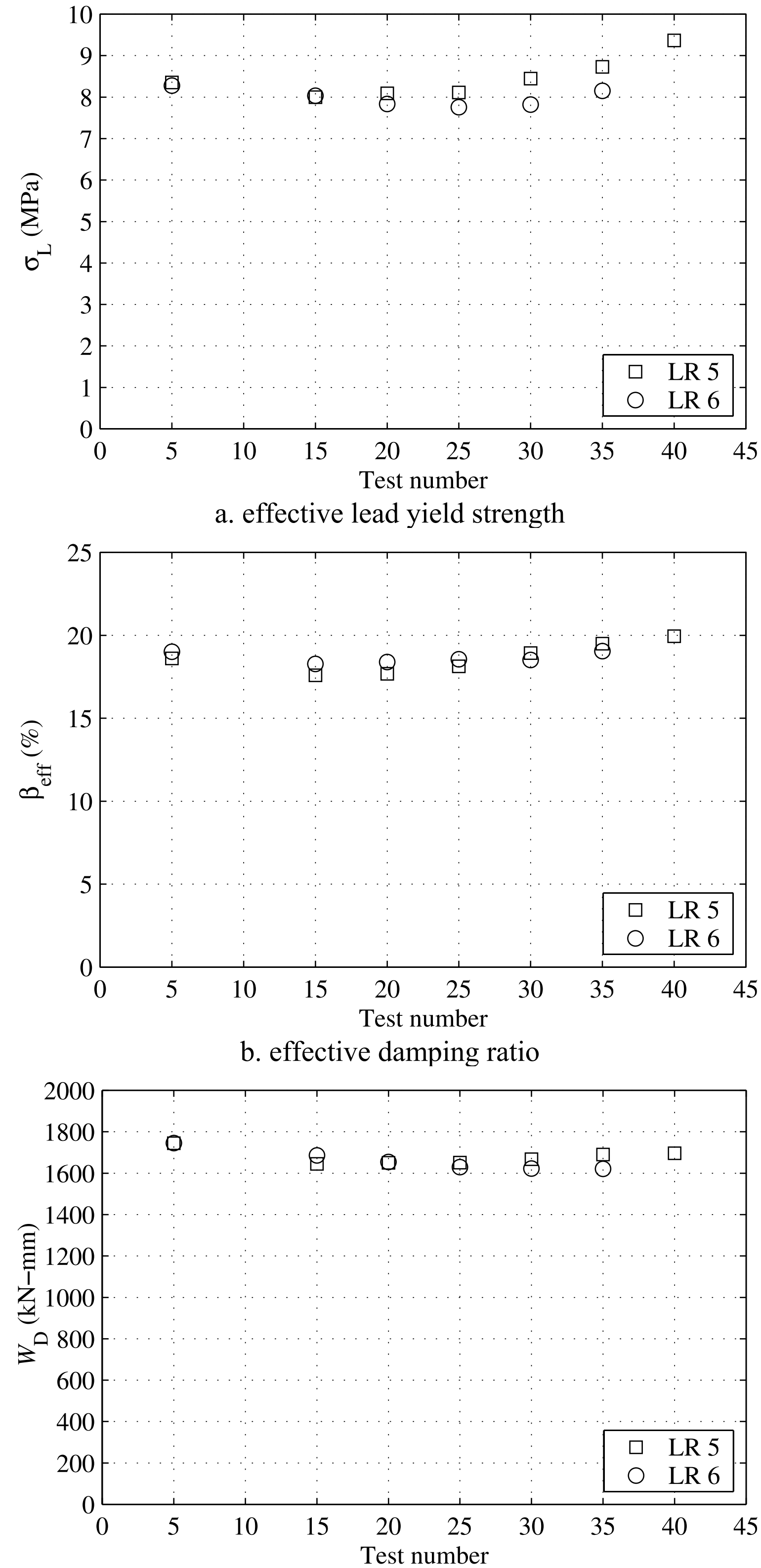

a. effective lead yield strength

b. effective damping ratio

c. energy dissipated per cycle

FIGURE 5-17 Third cycle properties of the LR bearings from benchmark *Shear* tests

5.4 Lateral Offset Testing

5.4.1 General

This section presents the results of an experimental investigation of the influence of lateral displacement on the vertical stiffness of elastomeric and lead-rubber seismic isolation bearings. Normalized results from this investigation are compared to the simplified expression derived from the two-spring model presented in Section 2 of this report.

5.4.2 Experimental Observations

The LDR and LR bearings were subjected to axial loading under condition of varying lateral offset, termed herein as *lateral offset* testing. Photographs of the LR bearings taken for each offset, including the *Axial* load test with zero lateral offset, are presented in figure 5-18. This figure illustrates the condition of the bearings during lateral offset testing as well as placement of the displacement transducers (two linear potentiometers) mounted magnetically to the loading beam and attached to the middle of the bottom bearing end plate, equidistant from the center of the bearing, for each offset. The potentiometers were placed in this fashion in an attempt to minimize possible errors in the relative vertical displacement measurement due to rotation of the load cell about the $y-\text{axis}$ (into page), due to the eccentrically applied axial loading.

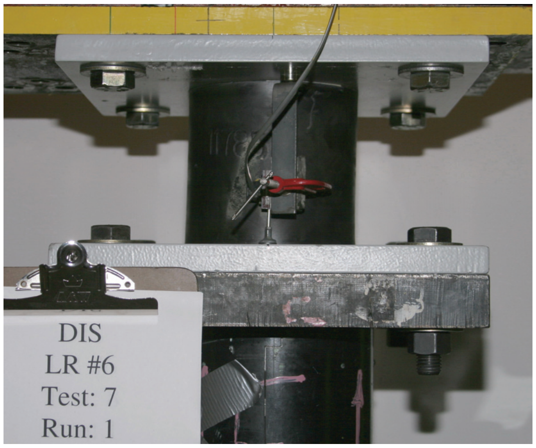

a. LR 6, Test 7, Δ=0 mm

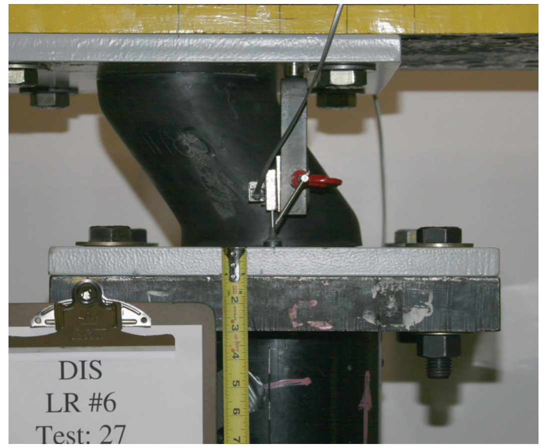

d. LR 6, Test 27, Δ=90 mm

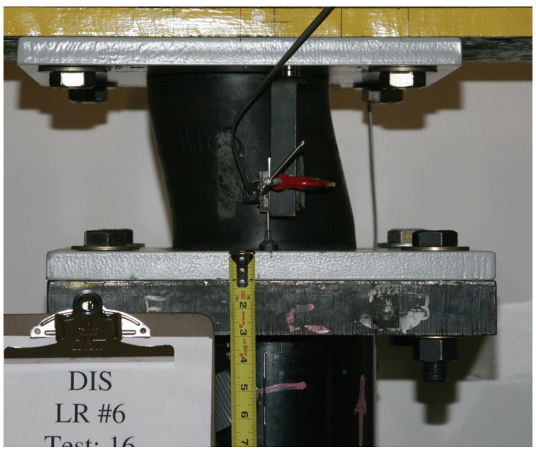

b. LR 6, Test 16, Δ=30 mm

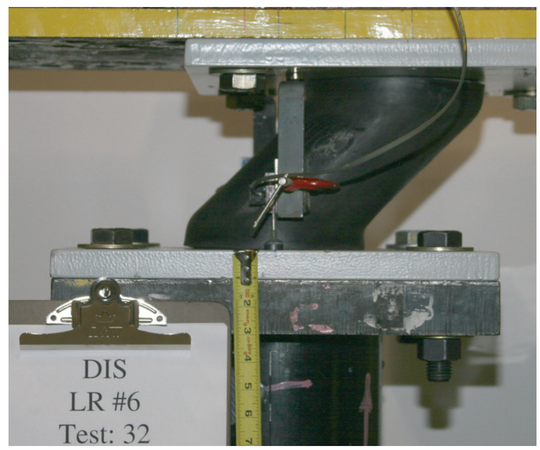

e. LR 6, Test 32, Δ=120 mm

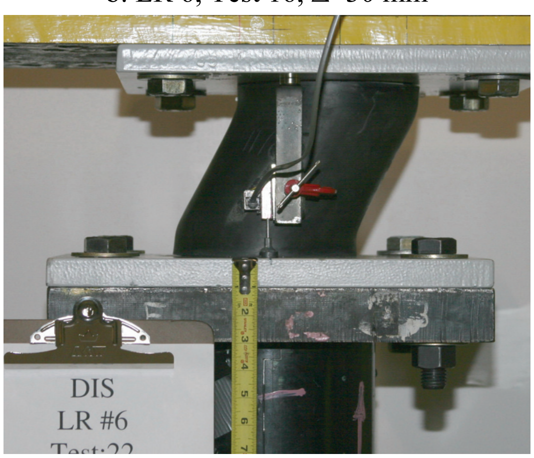

c. LR 6, Test 22, Δ=60 mm

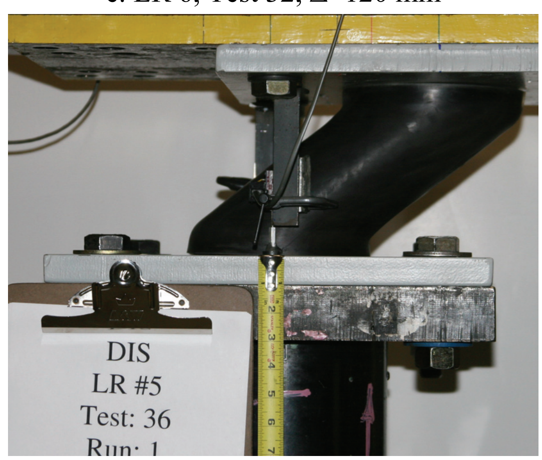

f. LR 5, Test 36, Δ=152 mm

FIGURE 5-18 Photographs of LR 5 and 6 taken during lateral offset testing

5.4.3 Experimental Results

Tests were conducted for lateral offsets, Δ, of approximately 30, 60, 90, 120 and $152\,\text{mm}$. Actual offset displacements were recorded prior to testing from the LVDT (linear variable displacement transducer) housed in the horizontal actuator, which is part of the single bearing testing machine.

Figure 5-19 presents axial load versus vertical displacement loops from *Axial* (figure 5-19a) and *lateral offset* (figure 5-19b through 5-19f) tests performed on LDR 5 and conducted to a maximum axial load of approximately $60\,\text{kN}$ corresponding to a maximum pressure of $3.45\,\text{MPa}$ and a target pressure of $2.75\,\text{MPa}$. The loops presented in this figure illustrate the increase in relative vertical displacement with increasing lateral offset as indicated by the rotation of the loops. The loops presented in figures 5-19e and 5-19f, corresponding to offsets of $120\,\text{mm}$ and $152\,\text{mm}$, respectively, exhibit some residual displacement (distance from zero force intercepts between consecutive cycles). The residual displacements are more pronounced at larger lateral offsets due to the increased contribution of the shear deformation to the total vertical displacement as the intermediate rubber layers rotate. *Lateral offset* tests were conducted to larger maximum axial loads, specifically, $120\,\text{kN}$ and $180\,\text{kN}$, for a subset of lateral offsets: limited by the anticipated reduced load carrying capacity of the bearing (buckling load). The $120\,\text{kN}$ maximum axial load test was performed for lateral offsets of 30, 60 and $90\,\text{mm}$ whereas the $180\,\text{kN}$ tests were performed for lateral offsets of 30 and $60\,\text{mm}$. Vertical stiffness results from *Axial* and *lateral offset* tests performed on LDR 5 and 6 are presented for each cycle in table 5-9. Table 5-9 also includes measured lateral offsets, Δ, recorded maximum axial loads, $P_{\max}$, and calculated vertical effective damping ratios, β_v.

Figure 5-20 presents sample axial load versus lateral displacement loops from *Axial* (figure 5-20a) and *lateral offset* (figure 5-20b through 5-20f) tests performed on LR 5 for a maximum axial load of approximately $60\,\text{kN}$. Again, the loops presented in this figure show an increase in the maximum relative vertical displacement with increasing lateral offset. Also, the residual displacement appears to increase with increasing lateral offset, with the exception of $\Delta = 120\,\text{mm}$ (figure 5-20e) that shows less residual displacement than the preceding offset of $90\,\text{mm}$. Similar to the LDR bearings, *lateral offset* tests were performed to larger maximum axial loads for a subset of lateral offsets, again limited according to the estimated buckling load (at the specified lateral displacement). *Lateral offset* tests with a maximum axial load of $120\,\text{kN}$ were conducted for offsets of 30, 60, 90 and $120\,\text{mm}$ whereas $180\,\text{kN}$ tests were performed for offsets of 30, 60 and $90\,\text{mm}$. Vertical stiffness results from *Axial* and *Lateral offset* tests performed on LR 5 and 6 are presented by cycle in table 5-10. Table 5-10 also lists the recorded Δ and $P_{\max}$ and the calculated β_v values.

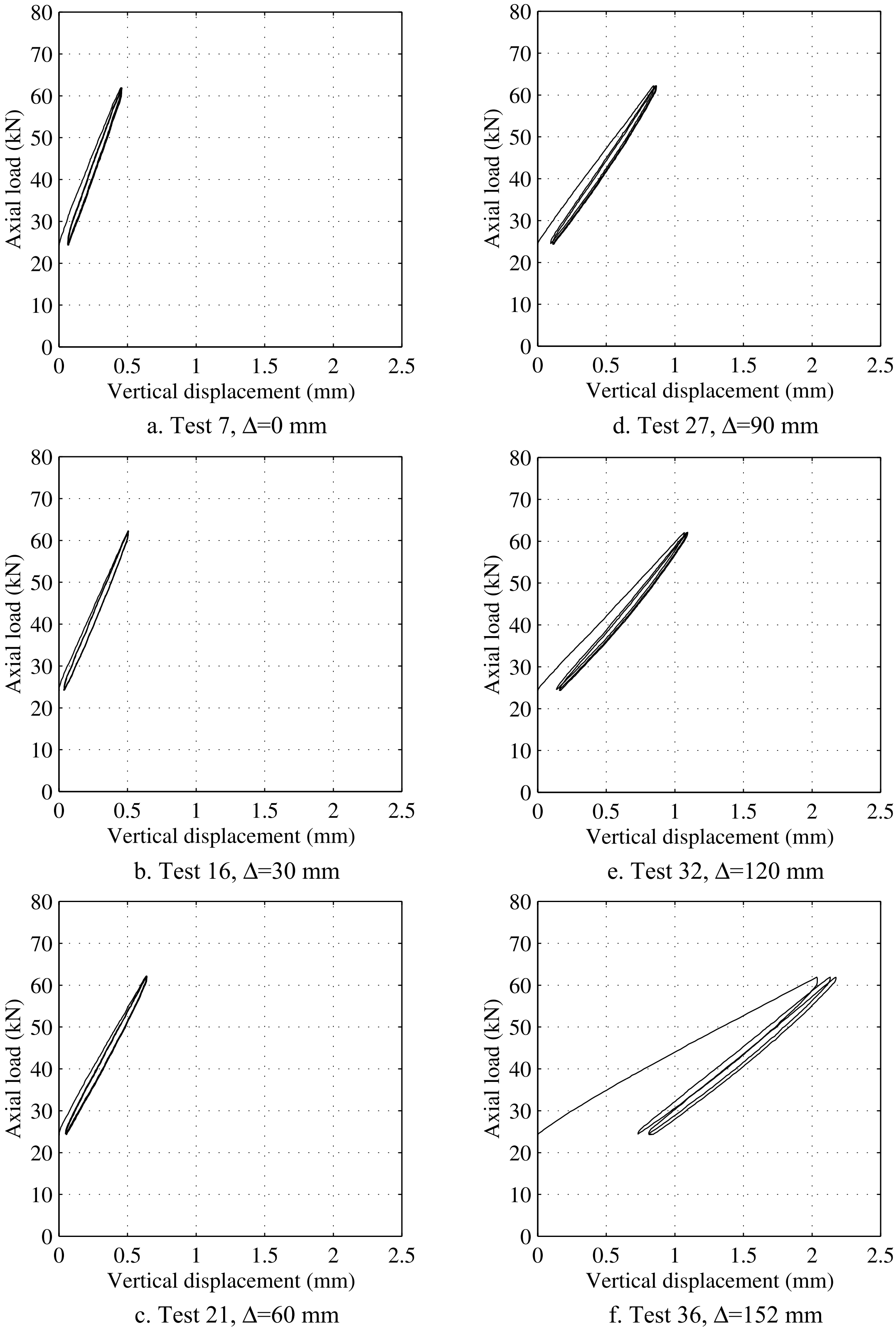

FIGURE 5-19 Axial load versus vertical displacement loops from LDR 5 at each lateral offset

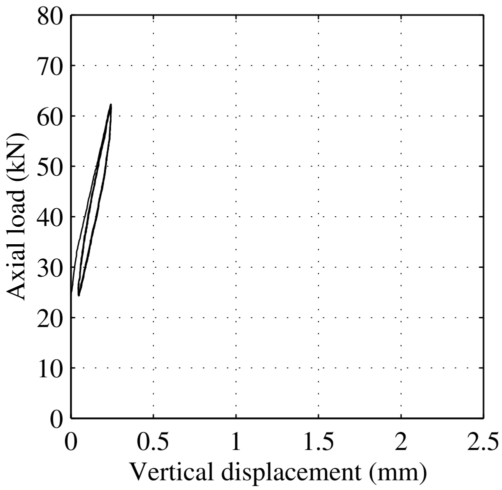

a. Test 7, Δ=0 mm

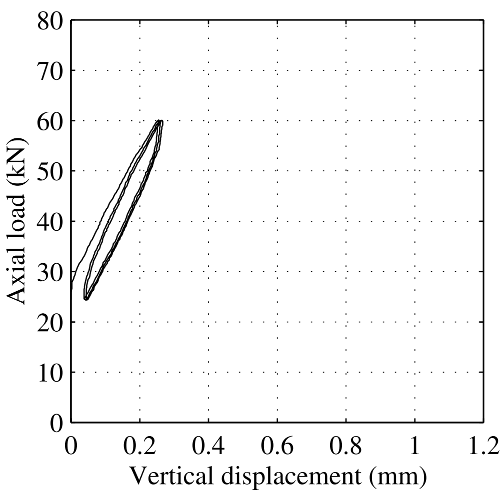

b. Test 16, Δ=30 mm

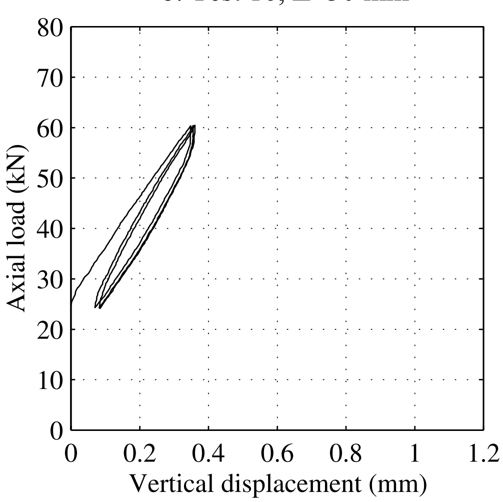

c. Test 21, Δ=60 mm

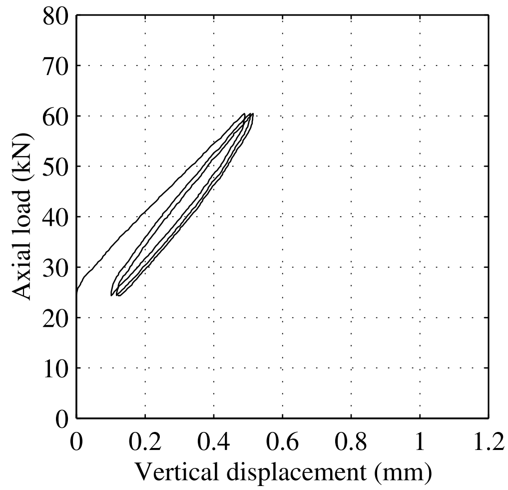

d. Test 27, Δ=90 mm

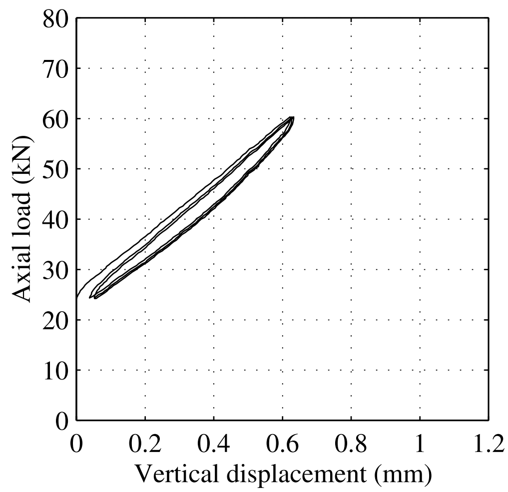

e. Test 32, Δ=120 mm

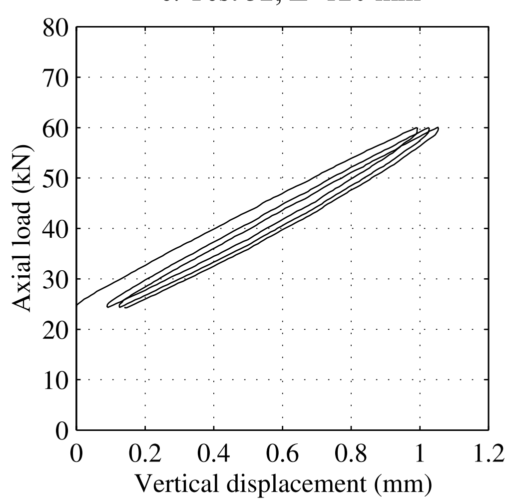

f. Test 36, Δ=152 mm

FIGURE 5-20 Axial load versus vertical displacement loops from LR 5 at each lateral offset

TABLE 5-9 Summary of results from *Axial* and *Axial with lateral offset* testing performed on LDR bearings

Test	Cycle	LDR 5 Δ (mm)	LDR 5 P_{max} (kN)	LDR 5 K_v $\left(\frac{kN}{mm}\right)$	LDR 5 β_v (%)	LDR 6 Δ (mm)	LDR 6 P_{max} (kN)	LDR 6 K_v $\left(\frac{kN}{mm}\right)$	LDR 6 β_v (%)
7	1	0	61.5	81.4	3.4	0	58.8	93.8	2.7
	2	0	61.5	86.5	1.4	0	58.7	99.8	1.3
	3	0	61.4	88.3	1.2	0	58.7	99.2	1.4
8	1	0	121.0	79.7	1.5	0	118.3	86.8	1.4
	2	0	121.0	85.4	0.9	0	118.0	88.4	0.9
	3	0	120.9	85.9	0.9	0	118.0	90.1	0.9
11	1	0	180.5	84.3	1.2	0	177.6	90.4	1.0
	2	0	180.5	92.1	0.8	0	177.8	89.3	0.8
	3	0	180.3	90.1	0.8	0	177.3	90.6	0.8
16	1	29	61.8	72.9	2.3	30	62.0	74.9	2.4
	2	29	61.8	77.2	1.2	30	62.0	80.2	1.3
	3	29	61.8	77.0	0.9	30	62.1	81.7	1.1
17	1	29	121.2	74.4	1.2	30	121.4	74.4	1.4
	2	29	121.3	74.9	0.8	30	121.4	80.9	0.9
	3	29	121.3	76.4	0.8	30	121.2	81.0	0.9
18	1	29	180.9	85.9	1.0	30	181.1	83.6	1.1
	2	29	181.1	85.8	0.8	30	180.7	86.1	0.8
	3	29	181.3	87.8	0.7	30	180.4	86.8	0.8
21	1	61	61.7	57.1	2.2	61	61.9	57.0	2.8
	2	61	61.7	61.1	1.2	61	61.8	61.4	1.5
	3	61	61.7	61.2	0.9	61	61.8	62.6	1.3
22	1	61	121.1	63.3	1.5	61	121.1	61.9	1.4
	2	61	121.0	66.2	1.0	61	121.2	66.2	1.1
	3	61	121.1	67.0	0.9	61	121.0	67.7	1.0
23	1	61	180.0	73.7	1.4	61	180.3	76.3	1.3
	2	61	179.9	81.3	1.0	61	180.2	82.3	1.0
	3	61	180.1	81.5	0.9	61	180.6	80.5	0.9
27	1	96	61.7	42.9	2.9	89	61.7	43.8	2.9
	2	96	61.7	47.8	1.3	89	61.6	48.6	1.5
	3	96	61.8	48.4	1.0	89	61.6	49.9	1.2
28	1	96	120.9	47.4	2.2	89	120.7	52.2	1.8
	2	96	120.9	55.4	1.1	89	120.6	60.0	1.1
	3	96	120.8	55.7	0.9	89	120.6	60.1	0.9
32	1	117	61.6	34.7	3.1	122	61.6	33.9	3.7
	2	117	61.6	40.1	1.2	122	61.8	39.4	1.4
	3	117	61.7	40.1	0.9	122	61.7	40.3	1.1
36	1	152	61.5	17.3	7.5	-	-	-	-
	2	152	61.5	26.3	1.9	-	-	-	-
	3	152	61.4	27.2	1.3	-	-	-	-

TABLE 5-10 Summary of results from *Axial* and *Axial with lateral offset* testing performed on LR bearings

Test	Cycle	LR 5				LR 6			
		Δ (mm)	P_{max} (kN)	K_v $\left(\frac{kN}{mm}\right)$	β_v (%)	Δ (mm)	P_{max} (kN)	K_v $\left(\frac{kN}{mm}\right)$	β_v (%)
7	1	0	61.8	138.7	5.4	0	61.8	116.0	6.3
	2	0	61.9	160.9	3.1	0	61.8	142.9	3.0
	3	0	61.9	158.0	2.8	0	61.7	140.8	2.6
8	1	0	120.7	154.1	2.6	0	121.3	131.8	2.7
	2	0	120.7	161.2	2.1	0	121.2	138.5	2.0
	3	0	120.5	164.7	2.1	0	120.9	140.6	1.9
11	1	0	180.9	163.3	1.9	0	180.9	145.1	2.0
	2	0	180.9	173.0	1.7	0	180.4	155.5	1.7
	3	0	180.7	171.3	1.6	0	180.3	151.4	1.6
16	1	34	59.7	121.2	5.1	27	61.5	114.0	5.8
	2	34	59.6	137.0	3.3	27	61.6	130.8	2.8
	3	34	59.6	139.1	2.9	27	61.7	134.9	2.6
17	1	34	119.6	112.3	2.9	27	121.0	124.4	2.4
	2	34	119.8	124.3	2.2	27	120.8	133.5	1.8
	3	34	119.7	126.0	2.1	27	121.1	135.0	1.6
18	1	34	178.6	132.1	2.1	27	180.1	133.6	1.8
	2	34	178.6	135.1	1.8	27	180.5	142.2	1.4
	3	34	178.3	140.5	1.7	27	180.8	145.5	1.3
21	1	57	59.9	94.9	5.5	64	61.6	78.7	5.0
	2	57	60.0	111.5	3.1	64	61.7	96.3	2.5
	3	57	60.0	116.3	2.4	64	61.6	103.8	2.2
22	1	57	121.1	97.7	2.7	64	121.1	89.8	2.7
	2	57	121.0	114.0	1.9	64	121.3	94.6	1.9
	3	57	120.8	110.4	1.8	64	121.0	101.0	1.7
23	1	57	179.9	118.7	2.0	64	180.2	106.9	2.1
	2	57	180.2	128.5	1.6	64	180.3	119.8	1.6
	3	57	180.4	129.5	1.5	64	180.7	115.9	1.5
27	1	92	60.0	67.5	5.4	88	61.6	62.3	5.0
	2	92	60.0	78.7	2.6	88	61.6	77.4	2.3
	3	92	60.0	81.4	2.2	88	61.6	79.2	1.9
28	1	92	119.7	72.3	3.2	88	121.2	72.7	2.7
	2	92	119.6	88.4	1.9	88	120.9	82.9	1.6
	3	92	119.6	90.2	1.6	88	120.9	85.6	1.4
32	1	115	59.9	55.4	2.4	124	61.6	44.2	5.0
	2	115	59.9	58.8	1.7	124	61.6	53.2	2.3
	3	115	59.9	60.2	1.5	124	61.6	54.9	1.7
36	1	115	59.5	34.5	3.0	124	120.9	50.5	3.1
	2	115	59.5	36.4	1.9	124	121.2	60.1	1.6
	3	115	59.6	36.2	1.6	124	121.2	61.7	1.4

The vertical stiffness determined at each lateral offset test was normalized by the vertical stiffness determined from *Axial* tests ($\Delta = 0$ mm) for corresponding maximum axial loads. Normalizing the vertical stiffness in this fashion facilitates comparison between the results of an experimental investigation and a simplified expression derived from the two-spring model presented in Section 2 [see (2-42)]. In addition, the measured lateral offsets were normalized by the outer radius of the bonded rubber area, denoted Δ / R, to facilitate a direct comparison. Figures 5-21 and 5-22 present normalized K_v data for the LDR and LR bearings, respectively. Also plotted in these figures is the curve (solid line) generated using the two-spring formulation presented in Section 2 [see (2-42)] and a horizontal (dashed) reference line at 1.0. For both the LDR and LR bearings normalized K_v values are presented for tests with maximum axial loads of approximately 60 kN, 120 kN and 180 kN corresponding to target pressures of 2.75 MPa, 5.2 MPa and 9 MPa, respectively. The experimental data presented in figures 5-21 illustrates the significant reduction in K_v exhibited by the LDR bearings over the range of Δ considered with the exception of LDR 5 for $\Delta / R \approx 0.39$ and $\rho = 9$ MPa. For a given normalized lateral offset, Δ / R, K_v / K_{vo} is observed to increase with increasing axial load or target pressure: ρ. The vertical stiffness at a given lateral offset predicted by the two-spring formulation compares well with experimental data for tests with ρ equal to 2.75 MPa and over predicts the reduction in vertical stiffness for larger target pressures.

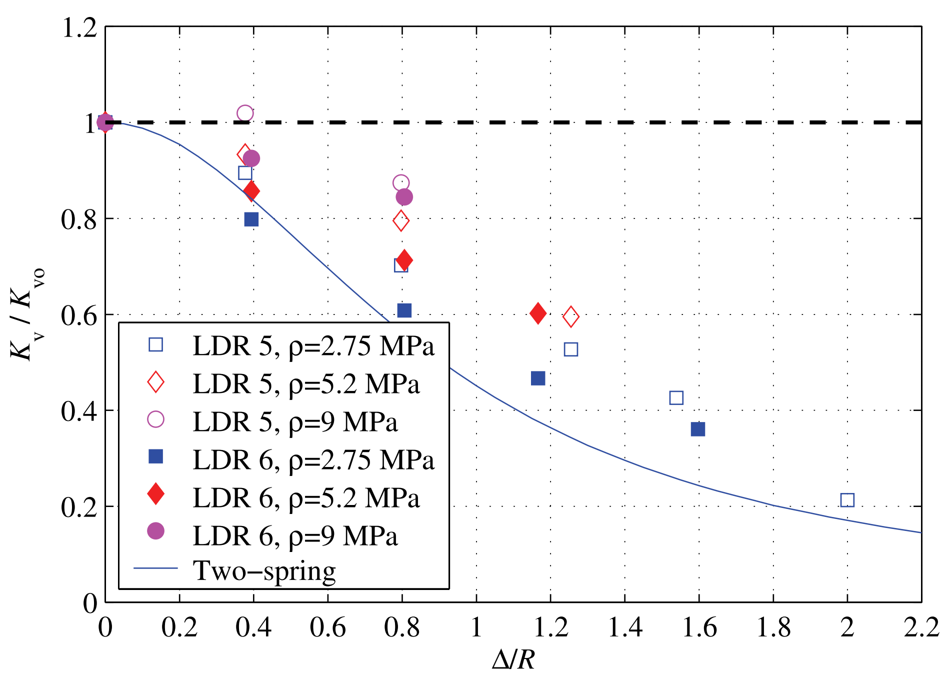

FIGURE 5-21 Normalized vertical stiffness results from the LDR bearings

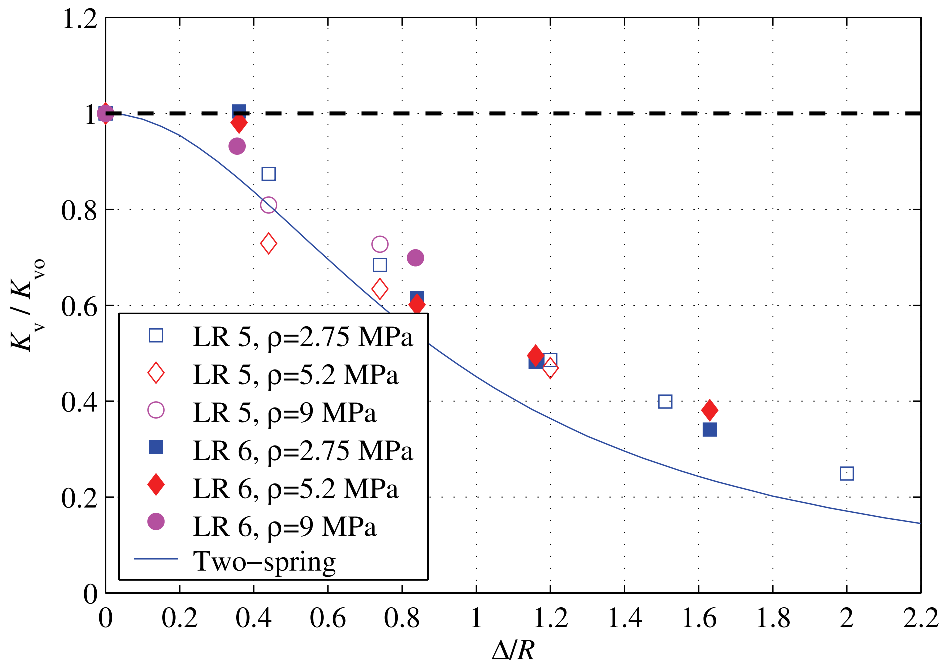

FIGURE 5-22 Normalized vertical stiffness results from the LR bearings

Figure 5-22 presents normalized vertical stiffness data from testing performed on the LR bearings. From this plot the normalized vertical stiffness for both LR bearings reduces with increasing normalized lateral displacement, Δ / R. Dissimilar to the LDR bearings, the maximum axial load, and thus target pressure, does not appear to systematically effect the normalized vertical stiffness. In addition, the experimental data agrees well with the two-spring formulation for each level of axial load. However, as stated previously a more detailed comparison of the experimental results and various formulations is discussed in Section 9.

5.5 Summary

In this section, sample results from characterization and lateral offset testing performed on two LDR and two LR seismic isolation bearings were presented. Results of the characterization tests were used to determine the nominal mechanical properties and to estimate material properties. A series of lateral offset tests were performed on the LDR and LR bearings to experimentally investigate the influence of lateral displacement on the vertical stiffness. The results of this investigation were normalized by the vertical stiffness (K_{vo}) determined during characterization testing (*Axial*) for purpose of comparison.

The results of characterization testing are summarized as follows. The disproportionately thick cover was shown to contribute significantly to the horizontal stiffness from the results of test performed on LDR 5 with 12 mm and then 3 mm of cover thickness and used to determine an effective area for the calculation of the shear modulus for bearings tested with the full 12 mm cover. Results from tests performed on LDR 5 with 3 mm of cover (LDR 5M) resulted in an effective shear modulus and damping ratio of 0.82 MPa and 2.7 %, respectively, at a shear strain amplitude of 104 % and frequency of 0.01 Hz. Results from *Axial* load tests were used to determine the vertical stiffness of the LDR and LR bearings. Experimentally determined values were compared to theoretical predictions to evaluate various assumptions. This comparison indicated the elastomer behaves as a nearly compressible material. In addition, the assumed value of the bulk modulus, 2000 MPa, resulted in predicted values that were shown to agree well with experimentally determined values. Additionally, variations in the individual rubber layer thickness were shown to have an impact on the resulting vertical stiffness as indicated by the deviation in experimentally determined value of K_{vo} from the LDR 5 and 6. However this deviation in rubber layer thickness can not be deduced without destroying the bearings, therefore, the individual rubber layer thickness must be assumed uniform for practical purposes. Experimental results from the lateral offset testing showed the LDR and LR bearings exhibited a significant reduction in vertical stiffness over the range of lateral offsets considered.

SECTION 6

EARTHQUAKE SIMULATION TESTING

6.1 General

Earthquake simulation testing was performed on a quarter-scale isolated bridge model utilizing the two six degree-of-freedom (DOF) earthquake simulators housed in the Structural Engineering and Earthquake Simulation Laboratory (SEESL), serving the George E. Brown Jr. Network for Earthquake Engineering Simulation (NEES) Equipment site, at the University at Buffalo. A brief description of the testing facility and earthquake simulator capabilities is provided in Section 6.2. The isolated bridge structure was tested in a total of four configurations using two types of isolation bearings. Four low-damping rubber (LDR) and four lead-rubber (LR) bearing were dedicated to this testing program and are identical to those tested according to the program presented in Section 4. Two transverse support widths were considered: $1.8\,\text{m}$ and $1.2\,\text{m}$. The results of the earthquake simulation testing program are used to: (1) investigate the influence of multiple components of excitation on the response of isolation system and individual bearings focusing on the vertical component of excitation and (2) investigate the influence lateral displacement on the vertical response of the isolation system for tests conducted with the vertical component of excitation.

The remaining portion of this section is organized as follows. Section 6.3 presents a description of the isolated truss-bridge and the instrumentation layout. Section 6.4 provides a brief discussion of the selected earthquake simulator input motions. Section 6.5 presents the earthquake simulation testing program and Section 6.6 presents a brief discussion of the data acquisition.

6.2 Earthquake Simulation Testing Facility

The SEES laboratory at the University at Buffalo is a $900\,\text{m}^2$ facility with two relocatable six DOF earthquake simulators, $114\,\text{m}^2$ of strong wall ($9\,\text{m}$ in height), and $340\,\text{m}^2$ of strong floor. The remainder of this section is devoted to the capabilities of the two earthquake simulators. Each earthquake simulator is $3.6\,\text{m}$ by $3.6\,\text{m}$ in plan and can be located adjacent to each other or up to $30.5\,\text{m}$ apart, center-to-center. The payload capacity of each simulator is $500\,\text{kN}$ ($1000\,\text{kN}$ in total) with an overturning moment capacity of $450\,\text{kN-m}$. Each simulator is capable of moving $\pm 150\,\text{mm}$ in the $x-$, $y-$ and $z-$directions with maximum velocities of $1250\,\text{mm/s}$ in the (horizontal) $x-$ and $y-$directions and $500\,\text{mm/s}$ in the (vertical) $z-$direction. Each simulator is capable of producing maximum accelerations of $\pm 1.15\,\text{g}$ in all three directions with a payload of $196\,\text{kN}$.

Two earthquake simulator extension platforms with plan dimension of $7\,\text{m}$ by $7\,\text{m}$ were installed prior to the testing program described herein. Noting, the weight of the extension platforms (approximately $87\,\text{kN}$ each) reduces the maximum payload, but not the dynamic characteristics and the performance of the earthquake simulators.

6.3 Isolated Bridge Model

6.3.1 General

An illustration of the isolated truss-bridge is shown in figure 6-1. This figure contains three views of the truss-bridge, specifically, one elevation and two side views. The truss-bridge, steel plates (added mass), earthquake simulator extension platforms and seismic isolation bearings are identified in the elevation view. The side views illustrate the transverse bearing spacing in the $1.2\,\text{m}$ and $1.8\,\text{m}$ configurations. Also shown in each view are the coordinate axes of the earthquake simulators, referred to later with respect to the directions of excitation, as well as the direction with respect to magnetic north.

The truss is a steel structure with a single span length of approximately $10.7\,\text{m}$ supported at each end by two seismic isolation bearings each connected to a load cell (see Appendix A) themselves connected to the extension platforms through steel interface plates. A detailed description of the truss-bridge is presented in Appendix C. The height of the isolated bridge model, from the center of the isolation system to the center of the added mass, is approximately $2.3\,\text{m}$. The truss-bridge itself weighs approximately $89\,\text{kN}$. To reach the target static pressure on the individual bearings of ($3.45\,\text{MPa}$) per the similitude requirements discussed in Section 3, three mass packages were designed and added to the model. Each mass package consists of 2 steel plates ($2992 \times 2004 \times 89\,\text{mm}$), 120 lead bricks and some ancillary steel section together weighing, approximately, $89\,\text{kN}$ and resulting in an approximate total model weight of $356\,\text{kN}$. The actual model weight, determined from the sum of the initial load cell readings, is reported in Section 7.

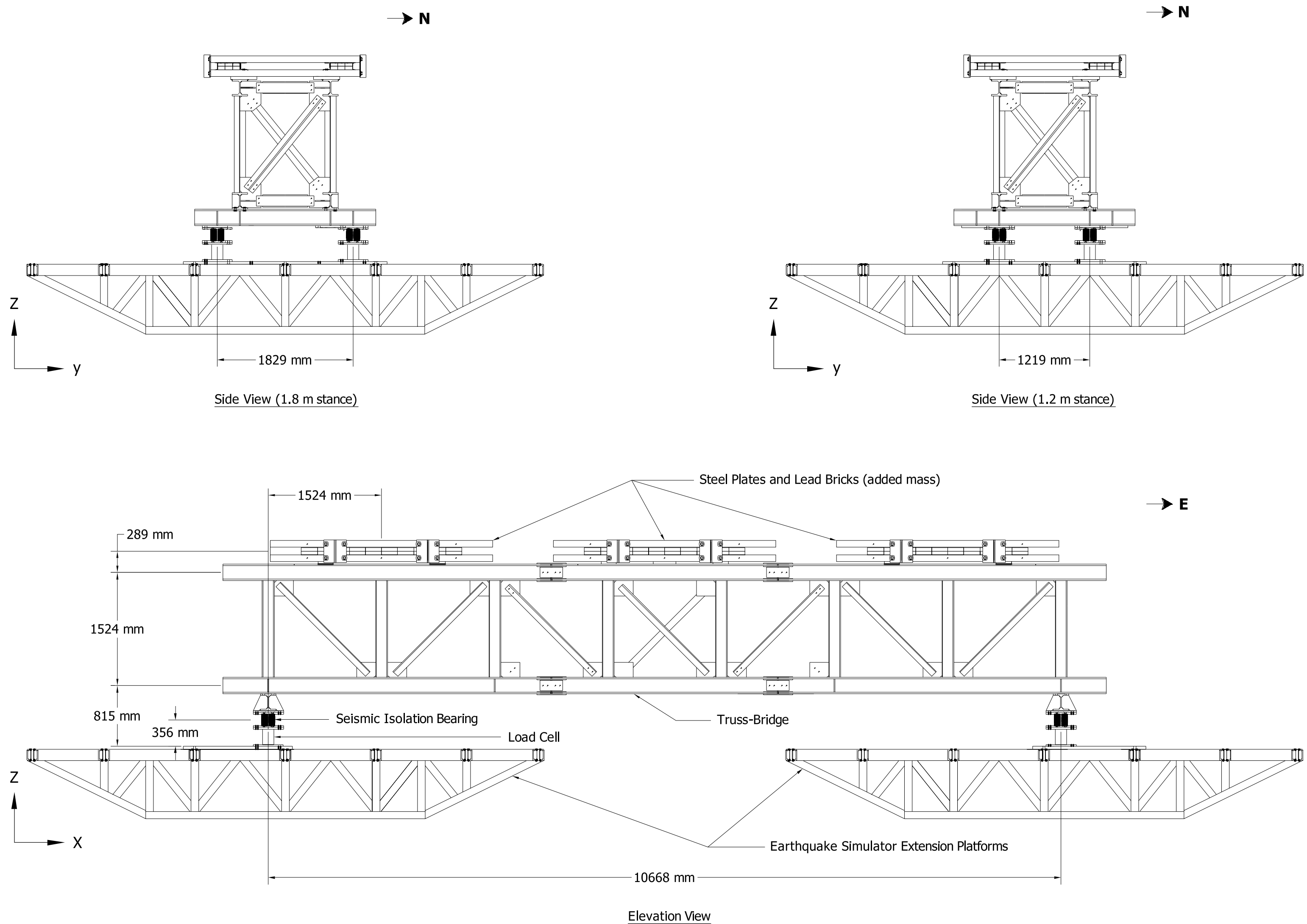

FIGURE 6-1 Illustration of the isolated truss-bridge model

6.3.2 Instrumentation

6.3.2.1 General

The instrumentation layout was designed to measure the global response of the isolated truss-bridge and the local response of the individual seismic isolation bearings during earthquake simulation testing. In addition, numerous instruments were placed on each simulator extension platform to record the input motion. In total, one hundred and twenty four channels of data were collected for each test from a variety of instruments including; accelerometers, clock, portable coordinate measurement machine (Krypton), load cells, and string potentiometers. A brief description of each type of instrument and it's capabilities, as specified by the manufacture, follows:

1. Accelerometer (ACC): Model JTF manufactured by Honeywell Sensotec of Columbus Ohio with a peak acceleration range of $\pm 10\,\text{g}$ and a frequency range of $0-400\,\text{Hz}$.

2. Clock: part of the Pacific Instruments 6000 Series Acquisition and Control System.

3. Krypton (KRY): K600 Portable Coordinate Tracking and Measurement System manufactured by Krypton Industrial Metrology capable of measuring 6 degrees-of-freedom using a minimum of 3 light emitting diodes (LED) on a rigid body or 3 degrees-of-freedom for a single LED at a maximum sample rate equal to 3000 divided the number of LEDs.

4. Load Cells (LC): five-channel load cells designed and fabricated by faculty of the Structural Engineering and Earthquake Simulation Laboratory at the University of Buffalo. A detailed description including calibration procedures is presented in Appendix A.

5. String Potentiometers (STP): Series 162 Analog-Output Miniature Position Transducers manufactured by SpaceAge Control, Inc. of Palmdale, California with $1080\,\text{mm}$ of maximum travel ($\pm 540\,\text{mm}$) and an infinite signal resolution.

The instrumentation layout used for this testing program is presented in figures 6-2 and 6-3. In each of these figures an instrument legend is provided along with the coordinate axes associated with each view. Each instrument is shown by a unique symbol and identified with a three letter abbreviation followed by the instrument number, channel number in parenthesis, and for string potentiometers the approximate distance between the potentiometer housing and point of attachment in millimeters. Figure 6-2 shows an elevation and plan view of the isolated bridge model and the location of the various instruments. Also shown in this figure are the earthquake simulator extension platforms, the approximate location and field of view of the Krypton camera and the location of each isolation bearing. Each string potentiometer housing was located on reference framing (not shown in these figures) on the north, east, and west sides of the bridge model, and connected to the model using magnets resulting in an absolute displacement measurement. The Krypton camera was located on the west reference frame and positioned such that Bearings 1 and 2 were located within the field of view with enough room for movement during earthquake simulation testing. Figure 6-3 shows a side view of the west end of the model instrumented with the Krypton LEDs. Again this figure shows the bridge model, the west earthquake simulator extension platform, various instruments and the coordinate axes. Also included in figure 6-3 is the instrument legend and a detailed view of Bearing 1 showing the approximate location of the Krypton LEDs, noting, that each LED provided three channels of data, specifically, absolute displacements in the $x-$, $y-$ and $z-$directions. A list of data channels including the associated instrument type, notation, measured quantity, unit of measurement, brief description of the location, and axis in which the quantity is being measured is presented in table 6-1.

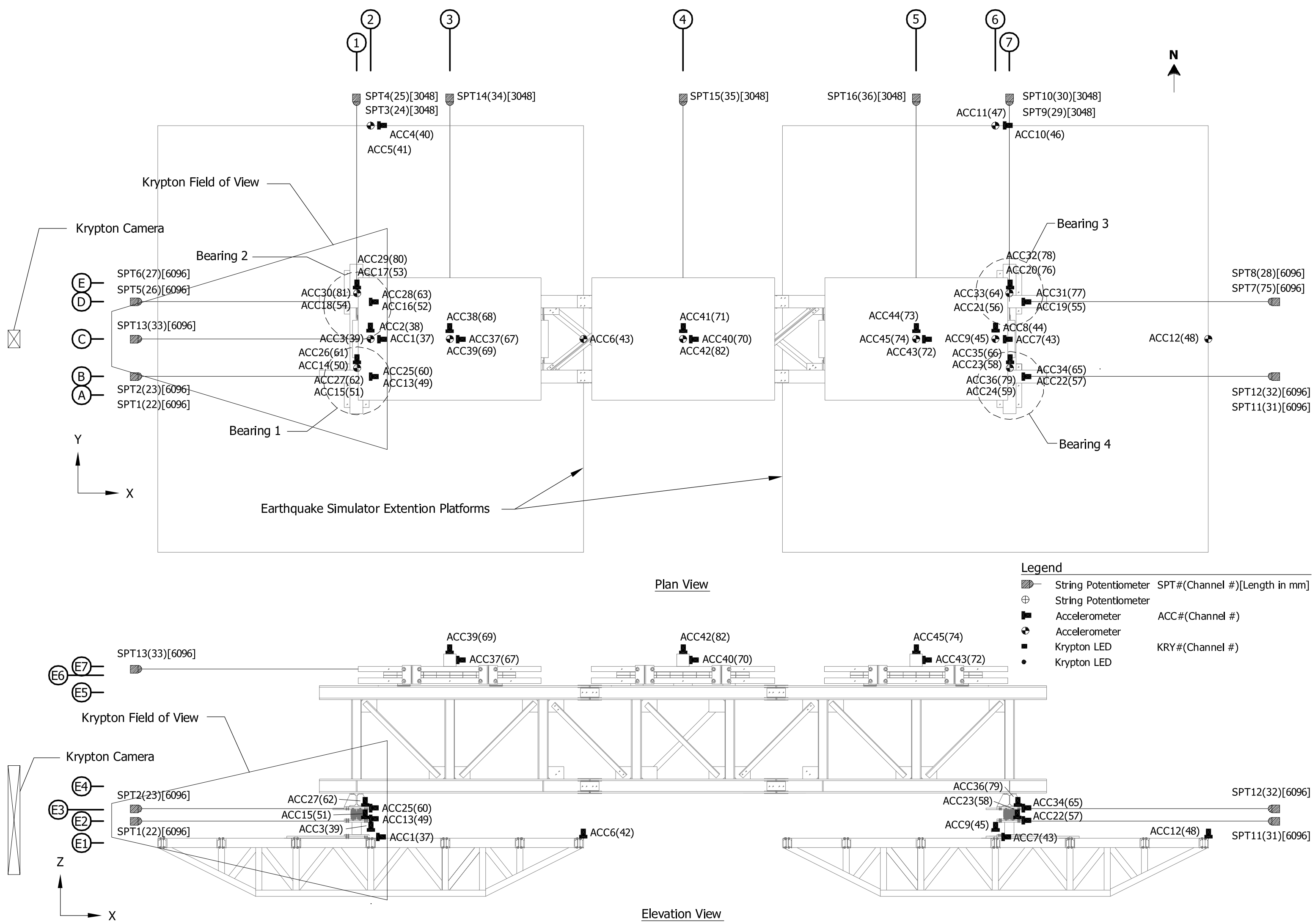

FIGURE 6-2 Instrumentation layout shown on elevation and plan views

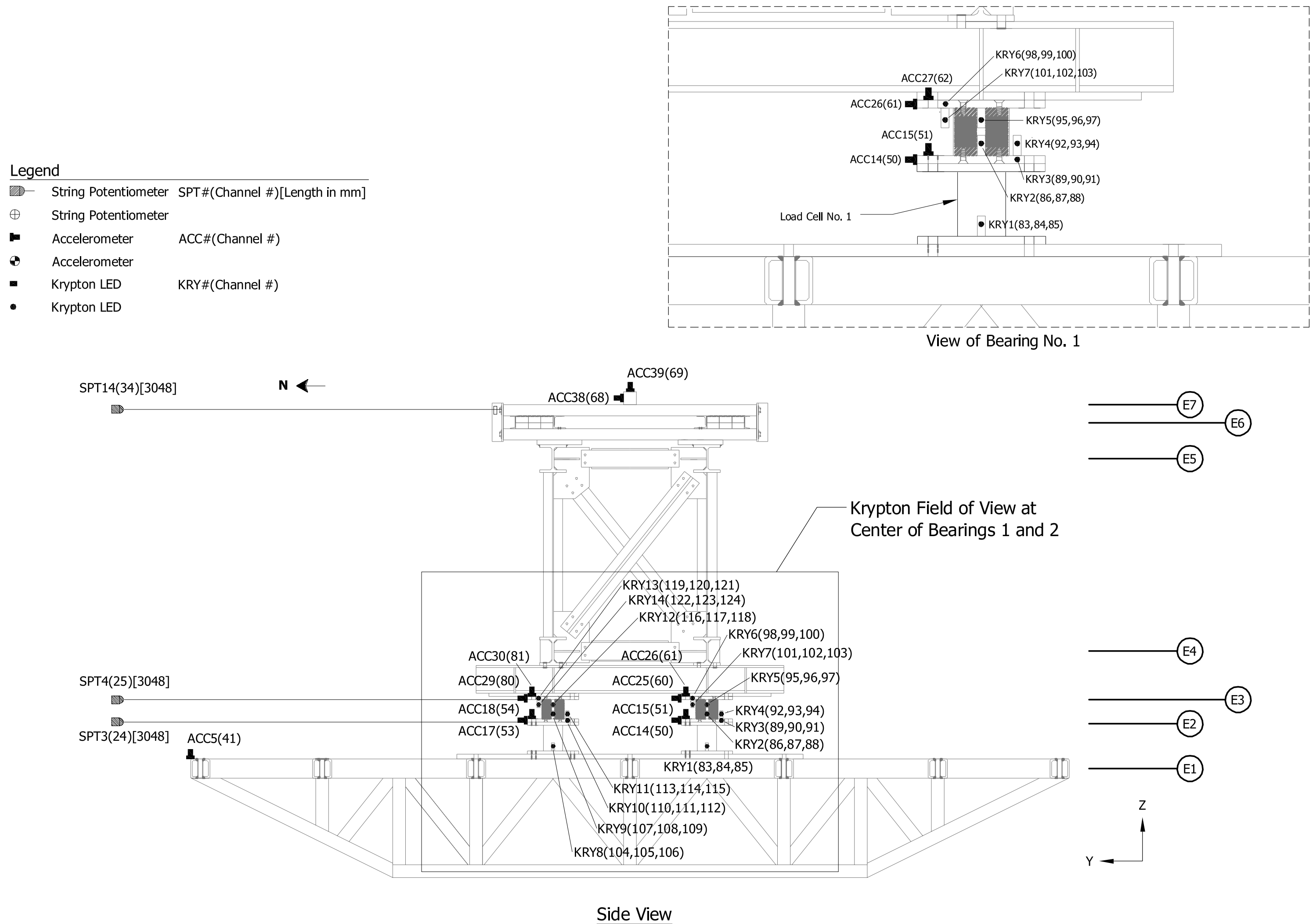

FIGURE 6-3 Instrumentation layout shown on side view

6.3.2.2 Earthquake Simulator Motion

Eighteen channels of data recorded the motion of the earthquake simulator extension platforms and thus the base motion for the isolated truss-bridge. The motion was captured through a combination of instruments including: 12 accelerometers, 6 string potentiometers, and 2 Krypton LEDs (located only on the west platform).

The instruments were located on the earthquake simulator extension platforms as follows. Three accelerometers were located at the centers of the east (Channels 43 – 45; ACC 7 – 9) and west (Channels 37 – 39; ACC 1 – 3) earthquake simulator platforms recording absolute acceleration in the $x-$, $y-$ and $z-$directions. Additionally, three accelerometers were located around the perimeter of the east (Channels 46 – 48; ACC 10 – 12) and west (Channels 40 – 42; ACC 4 – 6) extension platforms recording absolute accelerations in the $x-$ and $z-$directions eccentric to the center of the platform. The placement of the accelerometers was selected to determine the acceleration at the center of the platform and the perimeter to detect any rocking (angular acceleration) during testing. Three string potentiometers were attached to the bearing bottom end-plates on the east (Channels 75, 29 and 31; STP 7, 9 and 11) and west (Channels 22, 24 and 26; STP 1, 3 and 5) platforms each recording absolute displacement. Two of these string potentiometers were oriented in the $x-$direction and one in the $y-$direction, see figure 6-2. Two Krypton LEDs (Channels 83 – 85 and 104 – 106; KRY 1 and 8) were located at the base of LC 1 and LC 2 (beneath Bearing numbers 1 and 2, respectively) on the west extension platform recording absolute displacements in the $x-$, $y-$ and $z-$directions.

6.3.2.3 Local Response

Eighty-six channels of data recorded the response of the isolation system and individual seismic isolation bearings during each test. Four load cells (Channels 2 – 21; LC 1 – 4) located under each bearing of corresponding number recorded axial load, shear force (in the $x-$and $y-$directions) and moment (about the $x-$ and $y-$axes). Three accelerometers were located on each bearing end-plate (Channels 49 – 66 and 76 – 81; ACC 13 – 36) recording absolute accelerations in the $x-$, $y-$ and $z-$directions. Three string potentiometers (Channels 23, 25 and 27; STP 2, 4 and 6) were attached to the top end-plates of Bearings 1 and 2 recording absolute displacement in the horizontal $x-$ and $y-$directions. Similarly, three string potentiometers (Channels 28, 30 and 32; STP 8, 10 and 12) were attached to the top end-plates of Bearings 3 and 4, again, recording absolute displacement in the horizontal $x-$and $y-$directions.

The relative displacement across each isolation bearing was determined by subtracting recorded data from the appropriate string potentiometers. For example the relative displacement across Bearing 1 (B1) in the $x-$direction was obtained by subtracting the absolute displacement data of STP 1 from STP 2, see figure 6-3. In addition six Krypton LEDs were located on Bearings 1 (Channels 86 – 103; KRY 2 – 7) and 2 (Channels 107 – 124; KRY 9 – 14), three on the top-plate and three on the bottom end-plate recording absolute displacements. Again, relative displacements across each of these bearings in the $x-$, $y-$ and $z-$directions were determined by subtracting data from the appropriate LED signals (the Krypton LEDs provided the only vertical displacement signals across the isolation bearings, typically, a difficult response quantity to measure given the magnitude of the measured quantity and the capabilities of traditional measurement devices).

6.3.2.4 Global Response

Thirteen channels of data recorded the global response of the isolated truss-bridge during each test. Three accelerometers were placed at the approximate center of each of the top steel (mass) plates (Channels 67 – 74; ACC 37 – 45) recording absolute accelerations in the global $x-$, $y-$ and $z-$directions. One string potentiometer (Channel 33; STP 13) was attached to the middle of the west edge of the top steel (mass) plate recording absolute displacement in the $x-$direction. Three string potentiometers (Channels 33 – 35; STP 14 – 16) were attached to the middle of the north edge of the three top steel (mass) plates recording absolute displacements in the $y-$direction.

6.4 Earthquake Simulator Input Motions

Four sets of earthquake ground motion records were selected from the following earthquake events: March 25th, 1992 Cape Mendocino; January 17th, 1994 Northridge; January 16th, 1995 Hyogo-Ken Nanbu (Kobe); and November 12th, 1999 Duzce. Each set consists of three components (two horizontal and one vertical) and were obtained from the Pacific Earthquake Engineering Research strong motion database (http://peer.berkeley.edu/smcat/). Relevant information for each earthquake ground motion record is summarized in table 6-2, including, country of origin, fault mechanism, event magnitude, station name, distance-to-fault, site information, component identification, component peak ground acceleration (PGA) in units of g, peak ground velocity (PGV) in units of cm/s, and peak ground displacement (PGD) in units of cm. Note, the PGA, PGV and PGD values presented in table 6-2 correspond to the original records and do not represent peak values for the input motions that were time scaled (compressed by a factor of 2) according to the similitude requirements presented in Section 3.

6.5 Test Program

A number of variables were incorporated into the earthquake simulation test program, including two types of bearings (LDR and LR), two transverse support configurations ($1.8\,\mathrm{m}$ and $1.2\,\mathrm{m}$), three ground motion records for each type of isolation system (two records common to both) and two intensity levels for each record. The primary purpose of the testing program was to subject the bridge model to a sequence of three simulations. For each set of ground motions the sequence of simulations was performed as follows. The first simulation in the sequence subjected the model to a single component of excitation in the $y-$direction (transverse). The second simulation subjected the model to two components of excitation simultaneously applied in the $x-$ and $y-$directions (transverse plus longitudinal). The third simulation subjected the model to three components of excitation simultaneously applied in the $x-$, $y-$ and $z-$directions (transverse plus longitudinal plus vertical).

Table 6-3 lists the earthquake simulation test schedule, noting, that a low amplitude white-noise test was performed preceding each earthquake simulation test. The initial white-noise tests served to identify the dynamic characteristic of the isolated structure and the subsequent white-noise tests to re-center the bridge model following each earthquake simulation test. For each test listed in table 6-3, the bearing type, transverse support configuration, record, direction of excitation, and intensity are identified. Simulations were performed at two intensity levels for each record: (1) either 25% or 50% to verify the performance of the earthquake simulators, the instrumentation and to compare measured bearing properties to those used for analytical predictions, and (2) 100%, as representative earthquake ground motion shaking. However, due to safety consideration, there were instances when the second level was conducted at an intensity less than 100%. In these instances the second intensity level was chosen erring on the side of caution as the goal of the test program was not to push the system to failure. After earthquake simulation testing of the isolated bridge model was completed, the seismic isolation bearings were removed and the bridge was subjected to two white-noise tests in the fixed base configuration, see table 6-3: Tests 149 and 150. These tests were conducted to identify the dynamic characteristic of the fixed base model.

6.6 Data Acquisition

A Pacific Instruments™ 6000 series acquisition and control system managed and recorded transducer signals during earthquake simulation testing, with the exception of the Krypton camera and associated LEDs. The Pacific system served as the power source, signal conditioner, low-pass filter, multiplexer, and analog-to-digital (A-D) converter and functioned as follows. The Pacific supplied an excitation voltage to the various transducers (Load Cells, String Potentiometers and Accelerometers), amplified the transducer output signal, low-pass filtered the amplified signals at a cut-off frequency of $50\,\mathrm{Hz}$. The channels were scanned by the multiplexer at a rate of $2.5\,\mathrm{MHz}$ then digitized by the A-D converter at a sample rate of $256\,\mathrm{Hz}$. The digitized data was then saved to a PC hard disk in ASCII format.The Krypton camera system functioned autonomously with a built-in proprietary data acquisition system. Details of the Krypton data acquisition system are not presented here, however, due to the number of LEDs (14 in total) the sample rate (maximum possible of $214\,\mathrm{Hz}$) was chosen to be $128\,\mathrm{Hz}$, or one half that of the Pacific system. The Krypton data was then saved to a PC hard disk in ASCII format. For data analysis the Krypton data was linearly interpolated at a rate of $256\,\mathrm{Hz}$ to facilitate a direct comparison with data obtained from transducers handled through the Pacific system. Importantly, the Pacific and Krypton data acquisition systems were simultaneously triggered using a common low voltage signal at the onset of each test.

TABLE 6-1 List of instrumentation for earthquake simulation testing

Channel	Instrument	Notation	Measured Quantity	Unit	Location	Axis
1		Clock	time	s		
2	LC1N	Load Cell	force	kip	B1	Z
3	LCISx	Load Cell	force	kip	B1	Y
4	LC1Sy	Load Cell	force	kip	B1	Y
5	LC1Mx	Load Cell	moment	kip-in	B1	X
6	LC1My	Load Cell	moment	kip-in	B1	Y
7	LC2N	Load Cell	force	kip	B2	Z
8	LC2Sx	Load Cell	force	kip	B2	X
9	LC2Sy	Load Cell	force	kip	B2	Y
10	LC2Mx	Load Cell	moment	kip-in	B2	X
11	LC2My	Load Cell	moment	kip-in	B2	Y
12	LC3N	Load Cell	force	kip	B3	Z
13	LC3Sx	Load Cell	force	kip	B3	X
14	LC3Sy	Load Cell	force	kip	B3	Y
15	LC3Mx	Load Cell	moment	kip-in	B3	X
16	LC3My	Load Cell	moment	kip-in	B3	Y
17	LC4N	Load Cell	force	kip	B4	Z
18	LC4Sx	Load Cell	force	kip	B4	X
19	LC4Sy	Load Cell	force	kip	B4	Y
20	LC4Mx	Load Cell	moment	kip-in	B4	X
21	LC4My	Load Cell	moment	kip-in	B4	Y
22	STP1	String Pot.	displacement	inch	B1 bottom end-plate	X
23	STP2	String Pot.	displacement	inch	B1 top end-plate	X
24	STP3	String Pot.	displacement	inch	B2 bottom end-plate	Y
25	STP4	String Pot.	displacement	inch	B2 top end-plate	Y
26	STP5	String Pot.	displacement	inch	B2 bottom end-plate	X
27	STP6	String Pot.	displacement	inch	B2 top end-plate	X
28	STP8	String Pot.	displacement	inch	B3 top end-plate	X
29	STP9	String Pot.	displacement	inch	B3 bottom end-plate	Y
30	STP10	String Pot.	displacement	inch	B3 top end-plate	Y
31	STP11	String Pot.	displacement	inch	B4 bottom end-plate	X
32	STP12	String Pot.	displacement	inch	B4 top end-plate	X
33	STP13	String Pot.	displacement	inch	mass plate 4	X
34	STP14	String Pot.	displacement	inch	mass plate 4	Y
35	STP15	String Pot.	displacement	inch	mass plate 5	Y
36	STP16	String Pot.	displacement	inch	mass plate 6	Y
37	ACC1	Accelerometer	acceleration	g	center of W. platform	X
38	ACC2	Accelerometer	acceleration	g	center of W. platform	Y
39	ACC3	Accelerometer	acceleration	g	center of W. platform	Z
40	ACC4	Accelerometer	acceleration	g	N. edge of W. platform	X
41	ACC5	Accelerometer	acceleration	g	N. edge of W. platform	Z

TABLE 6-1 List of instrumentation for earthquake simulation testing (continued)

Channel	Instrument	Notation	Measured Quantity	Unit	Location	Axis
42	ACC6	Accelerometer	acceleration	g	E. edge of W. platform	Z
43	ACC7	Accelerometer	acceleration	g	center of E. platform	X
44	ACC8	Accelerometer	acceleration	g	center of E. platform	Y
45	ACC9	Accelerometer	acceleration	g	center of E. platform	Z
46	ACC10	Accelerometer	acceleration	g	N. edge of E. platform	X
47	ACC11	Accelerometer	acceleration	g	N. edge of E. platform	Z
48	ACC12	Accelerometer	acceleration	g	E. edge of E. platform	Z
49	ACC13	Accelerometer	acceleration	g	B1 bottom end-plate	X
50	ACC14	Accelerometer	acceleration	g	B1 bottom end-plate	Y
51	ACC15	Accelerometer	acceleration	g	B1 bottom end-plate	Z
52	ACC16	Accelerometer	acceleration	g	B2 bottom end-plate	X
53	ACC17	Accelerometer	acceleration	g	B2 bottom end-plate	Y
54	ACC18	Accelerometer	acceleration	g	B2 bottom end-plate	Z
55	ACC19	Accelerometer	acceleration	g	B3 bottom end-plate	X
56	ACC21	Accelerometer	acceleration	g	B3 bottom end-plate	Z
57	ACC22	Accelerometer	acceleration	g	B4 bottom end-plate	X
58	ACC23	Accelerometer	acceleration	g	B4 bottom end-plate	Y
59	ACC24	Accelerometer	acceleration	g	B4 bottom end-plate	Z
60	ACC25	Accelerometer	acceleration	g	B1 top end-plate	X
61	ACC26	Accelerometer	acceleration	g	B1 top end-plate	Y
62	ACC27	Accelerometer	acceleration	g	B1 top end-plate	Z
63	ACC28	Accelerometer	acceleration	g	B2 top end-plate	X
64	ACC33	Accelerometer	acceleration	g	B3 top end-plate	Z
65	ACC34	Accelerometer	acceleration	g	B4 top end-plate	X
66	ACC35	Accelerometer	acceleration	g	B4 top end-plate	Y
67	ACC37	Accelerometer	acceleration	g	center of mass plate 4	X
68	ACC38	Accelerometer	acceleration	g	center of mass plate 4	Y
69	ACC39	Accelerometer	acceleration	g	center of mass plate 4	Z
70	ACC40	Accelerometer	acceleration	g	center of mass plate 5	X
71	ACC41	Accelerometer	acceleration	g	center of mass plate 5	Y
72	ACC43	Accelerometer	acceleration	g	center of mass plate 6	X
73	ACC44	Accelerometer	acceleration	g	center of mass plate 6	Y
74	ACC45	Accelerometer	acceleration	g	center of mass plate 6	Z
75	STP7	String Pot.	displacement	inch	B3 bottom end-plate	X
76	ACC20	Accelerometer	acceleration	g	B3 bottom end-plate	Y
77	ACC31	Accelerometer	acceleration	g	B3 top end-plate	X
78	ACC32	Accelerometer	acceleration	g	B3 top end-plate	Y
79	ACC36	Accelerometer	acceleration	g	B4 top end-plate	Z
80	ACC29	Accelerometer	acceleration	g	B2 top end-plate	Y
81	ACC30	Accelerometer	acceleration	g	B2 top end-plate	Z
82	ACC42	Accelerometer	acceleration	g	center of mass plate 5	Z

TABLE 6-1 List of instrumentation for earthquake simulation testing (continued)

Channel	Instrument	Notation	Measured Quantity	Unit	Location	Axis
83	KRY1	Krypton LED	displacement	mm	LC1 bottom end-plate	X
84	KRY1	Krypton LED	displacement	mm	LC1 bottom end-plate	Y
85	KRY1	Krypton LED	displacement	mm	LC1 bottom end-plate	Z
86	KRY2	Krypton LED	displacement	mm	B1 bottom end-plate	X
87	KRY2	Krypton LED	displacement	mm	B1 bottom end-plate	Y
88	KRY2	Krypton LED	displacement	mm	B1 bottom end-plate	Z
89	KRY3	Krypton LED	displacement	mm	B1 bottom end-plate	X
90	KRY3	Krypton LED	displacement	mm	B1 bottom end-plate	Y
91	KRY3	Krypton LED	displacement	mm	B1 bottom end-plate	Z
92	KRY4	Krypton LED	displacement	mm	B1 bottom end-plate S.	X
93	KRY4	Krypton LED	displacement	mm	B1 bottom end-plate S.	Y
94	KRY4	Krypton LED	displacement	mm	B bottom end-plate S.	Z
95	KRY5	Krypton LED	displacement	mm	B1 top end-plate	X
96	KRY5	Krypton LED	displacement	mm	B1 top end-plate	Y
97	KRY5	Krypton LED	displacement	mm	B1 top end-plate	Z
98	KRY6	Krypton LED	displacement	mm	B1 top end-plate	X
99	KRY6	Krypton LED	displacement	mm	B1 top end-plate	Y
100	KRY6	Krypton LED	displacement	mm	B1 top end-plate	Z
101	KRY7	Krypton LED	displacement	mm	B1 top end-plate N.	X
102	KRY7	Krypton LED	displacement	mm	B1 top end-plate N.	Y
103	KRY7	Krypton LED	displacement	mm	B1 top end-plate N.	Z
104	KRY8	Krypton LED	displacement	mm	LC2 bottom end-plate	X
105	KRY8	Krypton LED	displacement	mm	LC2 bottom end-plate	Y
106	KRY8	Krypton LED	displacement	mm	LC2 bottom end-plate	Z
107	KRY9	Krypton LED	displacement	mm	B2 bottom end-plate	X
108	KRY9	Krypton LED	displacement	mm	B2 bottom end-plate	Y
109	KRY9	Krypton LED	displacement	mm	B2 bottom end-plate	Z
110	KRY10	Krypton LED	displacement	mm	B2 bottom end-plate	X
111	KRY10	Krypton LED	displacement	mm	B2 bottom end-plate	Y
112	KRY10	Krypton LED	displacement	mm	B2 bottom end-plate	Z
113	KRY11	Krypton LED	displacement	mm	B2 bottom end-plate S.	X
114	KRY11	Krypton LED	displacement	mm	B2 bottom end-plate S.	Y
115	KRY11	Krypton LED	displacement	mm	B2 bottom end-plate S.	Z
116	KRY12	Krypton LED	displacement	mm	B2 top end-plate center	X
117	KRY12	Krypton LED	displacement	mm	B2 top end-plate center	Y
118	KRY12	Krypton LED	displacement	mm	B2 top end-plate center	Z
119	KRY13	Krypton LED	displacement	mm	B2 top end-plate	X
120	KRY13	Krypton LED	displacement	mm	B2 top end-plate	Y
121	KRY13	Krypton LED	displacement	mm	B2 top end-plate	Z
122	KRY14	Krypton LED	displacement	mm	B2 top end-plate N.	X
123	KRY14	Krypton LED	displacement	mm	B2 top end-plate N.	Y
124	KRY14	Krypton LED	displacement	mm	B2 top end-plate N.	Z

TABLE 6-2 Summary information for the earthquake ground motion records

Year	Country	Event	Mechanism	Moment Magnitude	Station Name	Distance[1] (km)	Site Class / Classification	Component ID	PGA[2] (g)	PGV[2] (cm/s)	PGD[2] (cm)
1992	USA	Cape Mendocino	Reverse Normal	7.1	Rio Dell Overpass	18.5	B / USGS	270	0.39	43.9	22.0
								360	0.55	42.1	18.6
								Up	0.2	10.6	7.1
1994	USA	Northridge	Reverse Normal	6.7	Sylmar - Olive View	6.4	C / USGS	90	0.6	78.2	16.1
								360	0.84	129.6	32.7
								Up	0.54	19.1	8.5
1995	Japan	Kobe	Strike Slip	6.9	JMA	0.6	B / USGS	0	0.82	81.3	17.7
								90	0.6	74.3	19.9
								Up	0.34	38.3	10.3
1999	Turkey	Duzce	Strike Slip	7.1	Bolu	17.6	C / USGS	0	0.73	56.4	23.1
								90	0.82	62.1	13.6
								Up	0.2	17.3	14.3

Notes:
1. Distance value represents closest distance to fault rupture
2. Peak ground acceleration (PGA), velocity (PGV) and displacement (PGD) for original record

TABLE 6-3 Earthquake simulation testing schedule

Test	Bearing Type[1]	Width[2] (m)	Record[3]	Direction x	Direction y	Direction z	Intensity[4] (%)
1	LDR	1.8	white-noise				
2	LDR	1.8	RIO	-	270	-	25
3	LDR	1.8	white-noise				
4	LDR	1.8	RIO	360	270	-	25
5	LDR	1.8	white-noise				
6	LDR	1.8	RIO	360	270	UP	25
7	LDR	1.8	white-noise				
8	LDR	1.8	BOL	-	0	-	25
9	LDR	1.8	white-noise				
10	LDR	1.8	BOL	90	0	-	25
11	LDR	1.8	white-noise				
12	LDR	1.8	BOL	90	0	UP	25
13	LDR	1.8	white-noise				
14	LDR	1.8	KJM	-	0	-	25
15	LDR	1.8	white-noise				
16	LDR	1.8	KJM	90	0	-	25
17	LDR	1.8	white-noise				
18	LDR	1.8	KJM	90	0	UP	25
19	LDR	1.8	white-noise				
20	LDR	1.8	RIO	-	270	-	100
21	LDR	1.8	white-noise				
22	LDR	1.8	RIO	360	270	-	100
23	LDR	1.8	white-noise				
24	LDR	1.8	RIO	360	270	UP	100
25	LDR	1.8	white-noise				
26	LDR	1.8	BOL	-	0	-	50
27	LDR	1.8	white-noise				
28	LDR	1.8	BOL	90	0	-	50
29	LDR	1.8	white-noise				
30	LDR	1.8	BOL	90	0	UP	50
31	LDR	1.8	white-noise				
32	LDR	1.8	KJM	-	0	-	50
33	LDR	1.8	white-noise				
34	LDR	1.8	KJM	90	0	-	50
35	LDR	1.8	white-noise				
36	LDR	1.8	KJM	90	0	UP	50
37	LDR	1.8	white-noise				

Notes:
1. LDR=Low-damping rubber; LR=lead-rubber; Fixed=fixed base
2. Transverse support width, see figure 6-1
3. RIO=Rio Dell; BOL=Bolu; KJM=JMA; SYL=Sylmar, see table 6-2
4. Intensity is in percent of peak ground acceleration (PGA), see table 6-2 for value of PGA

TABLE 6-3 Earthquake simulation testing schedule (continued)

Test	Bearing Type[1]	Width[2] (m)	Record [3]	Direction			Intensity [4] (%)
				x	y	z	
38	LR	1.8	white-noise				
39	LR	1.8	BOL	-	0	-	50
40	LR	1.8	white-noise				
41	LR	1.8	BOL	90	0	-	50
42	LR	1.8	white-noise				
43	LR	1.8	BOL	90	0	UP	50
44	LR	1.8	white-noise				
45	LR	1.8	KJM	-	0	-	50
46	LR	1.8	white-noise				
47	LR	1.8	KJM	90	0	-	50
48	LR	1.8	white-noise				
49	LR	1.8	KJM	90	0	UP	50
50	LR	1.8	white-noise				
51	LR	1.8	SYL	-	360	-	50
52	LR	1.8	white-noise				
53	LR	1.8	SYL	90	360	-	50
54	LR	1.8	white-noise				
55	LR	1.8	SYL	90	360	UP	50
56	LR	1.8	white-noise				
57	LR	1.8	BOL	-	0	-	100
58	LR	1.8	white-noise				
59	LR	1.8	BOL	90	0	-	100
60	LR	1.8	white-noise				
61	LR	1.8	BOL	90	0	UP	100
62	LR	1.8	white-noise				
63	LR	1.8	KJM	-	0	-	100
64	LR	1.8	white-noise				
65	LR	1.8	KJM	90	0	-	100
66	LR	1.8	white-noise				
67	LR	1.8	KJM	90	0	UP	100
68	LR	1.8	white-noise				
69	LR	1.8	SYL	-	360	-	75
70	LR	1.8	white-noise				
71	LR	1.8	SYL	90	360	-	75
72	LR	1.8	white-noise				
73	LR	1.8	SYL	90	360	UP	75
74	LR	1.8	white-noise				

Notes:
1. LDR=Low-damping rubber; LR=lead-rubber; Fixed=fixed base
2. Transverse support width, see figure 6-1
3. RIO=Rio Dell; BOL=Bolu; KJM=JMA; SYL=Sylmar, see table 6-2
4. Intensity is in percent of peak ground acceleration (PGA), see table 6-2 for value of PGA

TABLE 6-3 Earthquake simulation testing schedule (continued)

Test	Bearing Type[1]	Width[2] (m)	Record [3]	Direction x	Direction y	Direction z	Intensity[4] (%)
75	LR	1.2	white-noise				
76	LR	1.2	BOL	-	0	-	50
77	LR	1.2	white-noise				
78	LR	1.2	BOL	90	0	-	50
79	LR	1.2	white-noise				
80	LR	1.2	BOL	90	0	UP	50
81	LR	1.2	white-noise				
82	LR	1.2	KJM	-	0	-	50
83	LR	1.2	white-noise				
84	LR	1.2	KJM	90	0	-	50
85	LR	1.2	white-noise				
86	LR	1.2	KJM	90	0	UP	50
87	LR	1.2	white-noise				
88	LR	1.2	SYL	-	360	-	50
89	LR	1.2	white-noise				
90	LR	1.2	SYL	90	360	-	50
91	LR	1.2	white-noise				
92	LR	1.2	SYL	90	360	UP	50
93	LR	1.2	white-noise				
94	LR	1.2	BOL	-	0	-	100
95	LR	1.2	white-noise				
96	LR	1.2	BOL	90	0	-	100
97	LR	1.2	white-noise				
98	LR	1.2	BOL	90	0	UP	100
99	LR	1.2	white-noise				
100	LR	1.2	KJM	-	0	-	100
101	LR	1.2	white-noise				
102	LR	1.2	KJM	90	0	-	100
103	LR	1.2	white-noise				
104	LR	1.2	KJM	90	0	UP	100
105	LR	1.2	white-noise				
106	LR	1.2	SYL	-	360	-	75
107	LR	1.2	white-noise				
108	LR	1.2	SYL	90	360	-	75
109	LR	1.2	white-noise				
110	LR	1.2	SYL	90	360	UP	75
111	LR	1.2	white-noise				

Notes:
1. LDR=Low-damping rubber; LR=lead-rubber; Fixed=fixed base
2. Transverse support width, see figure 6-1
3. RIO=Rio Dell; BOL=Bolu; KJM=JMA; SYL=Sylmar, see table 6-2
4. Intensity is in percent of peak ground acceleration (PGA), see table 6-2 for value of PGA

TABLE 6-3 Earthquake simulation testing schedule (continued)

Test	Bearing Type[1]	Width[2] (m)	Record[3]	Direction			Intensity[4] (%)
				x	y	z	
112	LDR	1.2	white-noise				
113	LDR	1.2	RIO	-	270	-	25
114	LDR	1.2	white-noise				
115	LDR	1.2	RIO	360	270	-	25
116	LDR	1.2	white-noise				
117	LDR	1.2	RIO	360	270	UP	25
118	LDR	1.2	white-noise				
119	LDR	1.2	BOL	-	0	-	25
120	LDR	1.2	white-noise				
121	LDR	1.2	BOL	90	0	-	25
122	LDR	1.2	white-noise				
123	LDR	1.2	BOL	90	0	UP	25
124	LDR	1.2	white-noise				
125	LDR	1.2	KJM	-	0	-	25
126	LDR	1.2	white-noise				
127	LDR	1.2	KJM	90	0	-	25
128	LDR	1.2	white-noise				
129	LDR	1.2	KJM	90	0	UP	25
130	LDR	1.2	white-noise				
131	LDR	1.2	RIO	-	270	-	100
132	LDR	1.2	white-noise				
133	LDR	1.2	RIO	360	270	-	100
134	LDR	1.2	white-noise				
135	LDR	1.2	RIO	360	270	UP	100
136	LDR	1.2	white-noise				
137	LDR	1.2	BOL	-	0	-	50
138	LDR	1.2	white-noise				
139	LDR	1.2	BOL	90	0	-	50
140	LDR	1.2	white-noise				
141	LDR	1.2	BOL	90	0	UP	50
142	LDR	1.2	white-noise				
143	LDR	1.2	KJM	-	0	-	50
144	LDR	1.2	white-noise				
145	LDR	1.2	KJM	90	0	-	50
146	LDR	1.2	white-noise				
147	LDR	1.2	KJM	90	0	-	50
148	LDR	1.2	white-noise				
149	Fixed	1.2	white-noise				
150	Fixed	1.2	white-noise				

Notes:
1. LDR=Low-damping rubber; LR=lead-rubber; Fixed=fixed base
2. Transverse support width, see figure 6-1
3. RIO=Rio Dell; BOL=Bolu; KJM=JMA; SYL=Sylmar, see table 6-2
4. Intensity is in percent of peak ground acceleration (PGA), see table 6-2 for value of PGA

SECTION 7

RESULTS OF EARTHQUAKE SIMULATION TESTING

7.1 General

This section presents sample results from testing performed on the quarter-scale bridge model in both the isolated and fixed base configurations as described in Section 6. Results from white-noise testing performed in the fixed base configuration (Test 150, see table 6-3) are used to identify the dynamic properties of the truss-bridge (with added mass) and to estimate the generalized dynamic properties. Results from the numerous earthquake simulations performed on the isolated bridge are used to: (1) investigate the influence of multiple components of excitation on the response of the isolation system and the individual bearings focusing on the vertical component of excitation, and (2) investigate the influence of lateral displacement on the vertical response of the isolation system and to identify the contribution of vertical load on the isolation system due to the vertical component of excitation. Additional results, not presented in this section, are located in Appendix D. However, the results presented in this section and Appendix D are from earthquake simulations conducted only at the largest of the two intensity levels, see table 6-3.

The remaining portions of this section are organized as follows. Section 7.2 describes the procedures used for data analysis. Section 7.3 provides general comments and observations from the testing program. Section 7.4 presents the results of white-noise testing performed in the fixed base configuration and Section 7.5 presents the results of earthquake simulation testing performed in the isolated configuration including earthquake simulator input motion, global structural response and local response of the isolation system and individual isolation bearings. A summary is provided in Section 7.6.

7.2 Data Analysis

7.2.1 General

The various procedures used to process and analyze the data acquired during earthquake simulation and white-noise testing performed on the bridge model in both the isolated and fixed base configurations is described in this section. Throughout this section reference is made to both the global coordinate system (x , y and z) and the direction with respect to truss-bridge, namely, transverse (T), longitudinal (L), and vertical (V). As a point of clarification, the longitudinal (L) axis of the bridge coincides with the global $x-$direction. Additionally, the transverse axis (L) coincides with the $y-$direction and the vertical (V) with the $z-$direction; see figures 6-1 and 6-2. In general the global coordinate system is used to described a particular response quantity (i.e., maximum displacement) whereas orientation with respect to the bridge (T, L and V) are used to describe the direction(s) of excitation.

7.2.2 Relative Displacement

Several string potentiometers (SPT) and Krypton LEDs (KRY) were used to measure and record the absolute displacement response of particular points either on the bridge or the earthquake simulator extension platforms during testing. Each string potentiometer housing was fixed to a reference frame and attached to the particular point of interest using a magnet. The Krypton camera was located on the west reference frame and the individual LEDs attached to various points on the bearings and load cells on the west simulator extension platform (see figure 6-2). The relative displacement response between any two points of interests, for example the top and bottom of a seismic isolation bearing, was calculated by subtracting the recorded absolute displacement responses obtained from the appropriate instruments. For example, the relative displacement of bearing 1 in the $x-$direction was calculated according to:

$$u_x(t_i) = u_{STP2}(t_i) - u_{STP1}(t_i) \tag{7-1}$$

where $u_{STP2}(t_i)$ is the recorded absolute displacement from STP2 at time t_i and $u_{STP1}(t_i)$ is the recorded absolute displacement from STP1 at time t_i. The relative displacement between two Krypton LEDs was calculated in a similar manner.

Unlike the Krypton camera system, error is introduced in the string potentiometer measurement if the point of interest travels in a plane (or three dimensional space) rather than along a single axis. One method of minimizing this error, and utilized here, is to maximize (within reason) the distance between the instrument (string potentiometer housing) and the point of attachment. For this setup, the reference frames on the east and west sides of the bridge model were positioned so that the distance between the string potentiometer housing and the point of attachment were 6096 mm, a distance resulting in negligible error from the anticipated transverse motion. However, due to the proximity of the North wall, to the bridge model the distance between the string potentiometer housing and the point of attachment in the north-south direction (see figures

6-2 and 7-1) was limited to $3048\,\text{mm}$. To illustrate the error introduced from horizontal motion, take for example STP3 (see figure 6-2). Assuming the point of attachment (in this case the top end-plate of bearing 2) displaces $120\,\text{mm}$ (200% rubber shear strain) in both the $x-$ and $y-$direction (u_x and u_y). The displacement recorded by STP3 is:

$$\tilde{u}_y = \sqrt{\left(l + u_y\right)^2 + u_x^2} - l = 122.3\,\text{mm} \tag{7-2}$$

corresponding to an error of:

$$Err = 100 \cdot \left| \frac{\tilde{u}_y - u_y}{u_y} \right| \approx 2\% \tag{7-3}$$

For the north-south potentiometers, the error at the measured maximum displacement in the $y-$direction is approximately 2%. However, if the displacement in the $y-$direction is small, for example, $2\,\text{mm}$ then $\tilde{u}_y = 4.36\,\text{mm}$ and the error is 118%.

The maximum horizontal displacement was determined from the square-root-sum-of-squares (SRSS) response calculated with the relative displacements u_x and u_y according to:

$$u_{\max} = \max\left(\sqrt{u_x(t_i)^2 + u_y(t_i)^2}\right) \tag{7-4}$$

where $u_x(t_i)$ is the relative displacement in the $x-$direction at time t_i and $u_y(t_i)$ is the relative displacement in the $y-$direction at time t_i.

7.2.3 Forces and Moments

The response of the individual bearings, in terms of axial load, shear force, and bending moment, was measured using the four 5-channel reaction load cells (see Appendix A) located beneath the individual bearings. The axial load response (P) and shear force response in the $x-$ and $y-$directions (F_x and F_y, respectively) are of primary importance to this study and although moments were recorded, the data was not processed and therefore is not presented here. For each bearing, the maximum horizontal shear force ($F_{\max}$) was calculated from the shear force responses F_x and F_y in a similar manner to the maximum horizontal displacement calculated according to (7-4).

Another important quantity for this study is the contribution of the vertical load on the isolation system (P_{EQ}) due to vertical ground shaking. For simulations performed with three components of excitation (T+L+V), the vertical load response, P_{EQ}, was calculated from equilibrium of the bridge in the vertical $z-$direction using the recorded data from the normal channels of each load cell. From equilibrium in the $z-$direction:

$$\Sigma F_z = 0 \quad P_{EQ}(t_i) = \sum_{j=1}^{4} P_j(t_i) - W_T \tag{7-5}$$

where $P_j(t_i)$ is the axial load from the jth load cell at time t_i and W_T is the total static weight of the bridge model calculated as the sum of the initial readings from each of the load cells.

7.2.4 Absolute Accelerations

The absolute acceleration response was recorded during earthquake simulation and white-noise testing using accelerometers (45 in total) distributed across the bridge model and the earthquake simulator extension platforms (see, figure 6-2). For the purpose of data analysis, all acceleration records were low-pass filtered at $30\,\text{Hz}$ to eliminate noise and local high frequency spikes. The cutoff frequency of $30\,\text{Hz}$ was chosen to be larger than the highest mode of interest ($22\,\text{Hz}$) determined from the results of white-noise testing (presented in Section 7.4). The records were digitally filtered in the frequency domain using Matlab (Math Works, 1999) and its built-in discrete Fast Fourier Transform (FFT) and Inverse Fast Fourier Transform (IFFT) algorithms.

The motion of the earthquake simulator extension platforms, in terms of absolute (input) velocity and displacement, were determined from the recorded acceleration records using a combination of the digital filtering, numerical integration and linear correction procedures outlined below. The digital filter uses a trapezoidal window with corners chosen at $1/5\,\text{Hz}$, $1/4\,\text{Hz}$, $30\,\text{Hz}$ and $31\,\text{Hz}$. The lower cutoff frequency of $1/5\,\text{Hz}$ and the transition frequency of $1/4\,\text{Hz}$ were chosen based on the low spectral acceleration response for periods greater than $3\,\text{seconds}$ from elastic response spectra generated from the recorded input acceleration. The upper transition frequency of $30\,\text{Hz}$ and cutoff frequency of $31\,\text{Hz}$ were chosen to be consistent with the low-pass filtering. The procedure used to obtain the velocity and displacement records is outlined below:

1. Zero correct the acceleration records to remove any initial offset and multiply by value of g, the gravitational acceleration constant, in units of interest

2. Calculate frequency response using Fast Fourier Transform (FFT) algorithm

3. Modulate the frequency response using the trapezoidal window function with corner frequencies at $1/5\,\text{Hz}$, $1/4\,\text{Hz}$, $30\,\text{Hz}$ and $31\,\text{Hz}$

4. Calculate time response from the filtered frequency response data using the Inverse Fast Fourier Transform (IFFT) algorithm

5. Numerically integrate the filtered acceleration record using a cumulative trapezoidal algorithm to obtain velocity record

6. Fit a first order polynomial to velocity data to obtain slope and y-intercept

7. Linearly correct velocity data with slope and y-intercept obtained in Step 6

8. If desired, repeat Steps 5 through 7 using the velocity record to obtain a displacement response

7.2.5 Frequency Response Analysis

Frequency response analysis was utilized to identify the modal frequencies of the truss-bridge and corresponding critical damping ratios. The modal frequencies were identified from plotted transfer function amplitudes calculated using frequency response functions of various input and output signals and calculated according to:

$$TR(f) = \frac{Y(f) \cdot X^*(f)}{X(f) \cdot X^*(f)} \tag{7-6}$$

where $X(f)$ is the frequency response function of the input signal $x(t)$ determined using the FFT algorithm in Matlab (Math Works, 1999), $X^*(f)$ is the complex conjugate of the frequency response function $X(f)$ and $Y(f)$ is the frequency response function of the output signal $y(t)$.

The transfer function generated using (7-6) assumed no input noise and uncorrelated output noise (Reinhorn, 2005).

The critical damping ratio (ζ) for each mode was estimated from the plotted transfer function amplitudes using the Half-Power method (Clough and Penzien, 1975). The method relies on identification of the resonant amplitude ($TR_{\max}$) and frequencies (denoted, f_1 and f_2) corresponding to $TR_{\max}$ divided by $\sqrt{2}$. Then the critical damping ratio is estimated according to:

$$\zeta = \frac{f_2 - f_1}{f_2 + f_1} \tag{7-7}$$

where f_1 and f_2 are frequencies on each side of the resonant frequency, f_o , coincidental with $TR_{\max} / \sqrt{2}$.

Additionally, frequency response analysis was used to identify the frequency content of the vertical load response due to the vertical component of excitation during earthquake simulation testing. For this analysis, transfer function amplitudes were calculated using the recorded vertical ground acceleration (input) and calculated vertical load response (output).

7.3 Experimental Observations

This section provides general comments and observation from the earthquake simulation testing program. Photographs of the bridge model in the isolated configuration taken prior to testing are presented in figure 7-1. The photograph presented in figure 7-1a shows a view of the bridge model and the two earthquake simulator extension platforms and has been annotated with an arrow illustrating the direction of East. Figure 7-1b contains a photograph showing a view of bearing 1, the Krypton camera, and the west reference frame all identified by arrows and text.

a. view of bridge model

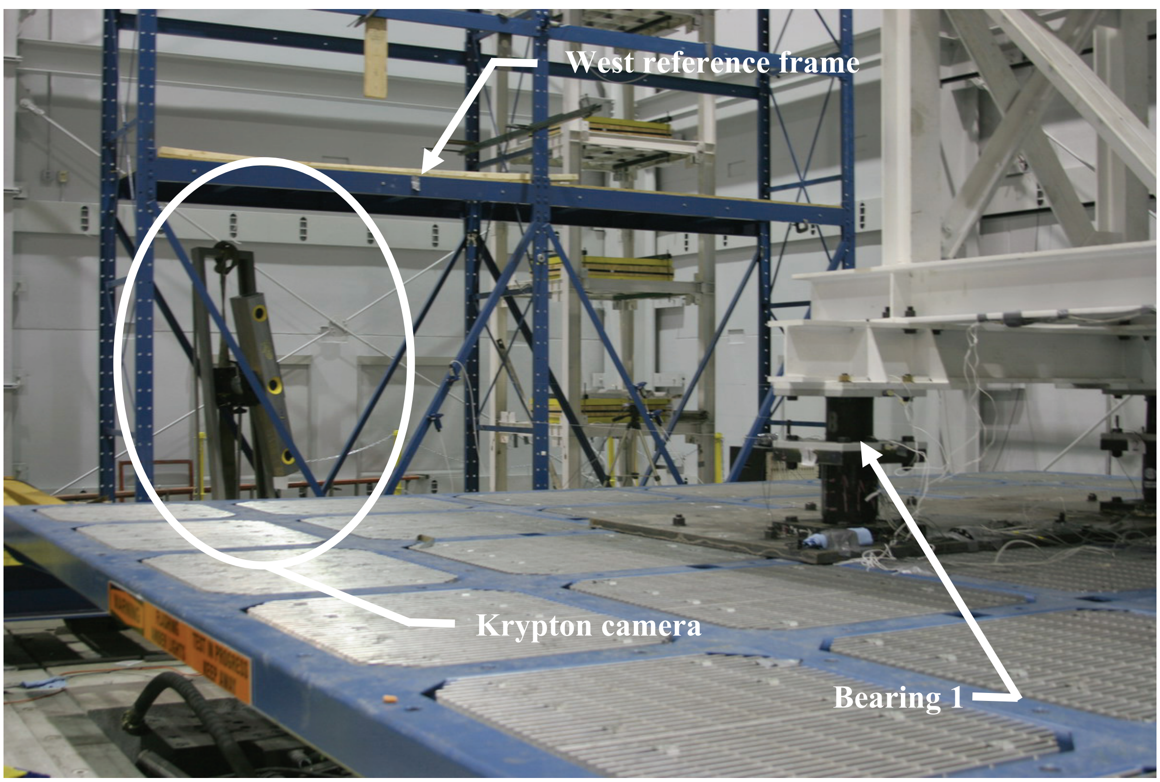

b. view of bearing 1 and Krypton camera

FIGURE 7-1 Photographs of isolated bridge model

To ensure equal distribution of load to each of the four supports, the 5-channel reaction load cells were installed on the steel interface plates attached to the simulator extension platforms and connected to the data acquisition system prior to the installation of the isolation bearings and the truss-bridge. Once connected to the data acquisition system, all signal offsets were removed (zeroed) enabling the weight of the truss-bridge and supplemental lead to be measured. The low-damping rubber (LDR) bearings were then installed atop the load cells followed by the truss-bridge and the added mass plates and supplemental lead. At this time the earthquake simulators were lifted from their respective parking frames and leveled to ensure accurate initial readings that indicated an unequal distribution of load amongst the four load cells. The earthquake simulators were returned to their respective parking frames and previously fabricated light gauge steel shims were installed between the bottom end-plate of bearings 1 and 3 and their supporting load cells. Shim plates were added until the load was, within reason, evenly distributed to each support. Table 7-1 presents initial (normal channel) load cell readings from the first test following each re-configuration. From Test 1, the load cell readings presented in table 7-1 vary from $91.1\,\mathrm{kN}$ to $102.6\,\mathrm{kN}$, a deviation of approximately $10\,\%$. The total model weight was determined from the sum of the initial load cell readings which ranged from $381.9\,\mathrm{kN}$ (Test 112) to $388.2\,\mathrm{kN}$ (Test 38), a 1.6% deviation.

The total model weight of, approximately, $382\,\mathrm{kN}$ exceeded the target weight of $320\,\mathrm{kN}$ as required from the similitude requirements for a target static pressure of $3.45\,\mathrm{MPa}$ and outer bearing diameter of $172\,\mathrm{mm}$ (see Section 3). The additional weight can be attributed to the combined weight of fasteners, gusset plates, and stiffener plates used in the fabrication of the truss-bridge and ancillary steel plates and angle sections used to connect the mass plates to the truss-bridge. In addition, the added weight in combination with the reduced outer diameter of the LDR and lead rubber (LR) bearings ($152\,\mathrm{mm}$) resulted in a static pressure of approximately $5.2\,\mathrm{MPa}$.

TABLE 7-1 Initial load cell readings and total static weight of model

Test	LC 1N (kN)	LC 2N (kN)	LC 3N (kN)	LC 4N (kN)	W_T (kN)
1	94.5	102.6	91.1	96.3	384.5
38	97.0	101.9	92.7	96.6	388.2
75	103.0	92.7	98.1	88.1	381.9
112	99.7	95.3	95.1	91.7	381.8

A thermocouple was used to measure the temperature of the lead-core of bearing 4 between each earthquake simulation for testing performed with the LR bearings (Test 38 through 111). The core temperature was monitored so that testing could be paused to prevent the core from reaching a temperature that might result in strength degradation. Prior to the initial test and following each earthquake simulation the thermocouple was inserted into a groove in the top end-plate of bearing 4 terminating at the lead-core. The thermocouple was held in place until the temperature reading stabilized then was recorded by hand. Over the period of time (approximately eight hours) between Test 38 and 74 the initial core temperature increased from $20^\circ\mathrm{C}$ (the ambient temperature of the laboratory) to $22^\circ\mathrm{C}$. This is not to say the core temperature did not exceed $22^\circ\mathrm{C}$ during earthquake simulation testing but rather the residual temperature at the end of the lead-core at the onset of each earthquake simulation was no more than $22^\circ\mathrm{C}$. This process was repeated for Tests 75 through 111 resulting in a similar range of temperatures.

7.4 White-Noise Testing

7.4.1 General

Upon completion of earthquake simulation testing performed on the isolated bridge model, the bearings (at this time LDR) were removed and the bridge was connected directly to the four load cells providing a fixed base condition. Two white-noise tests, numbers 149 and 150 (see table 6-3), were conducted in this configuration to determine the dynamic characteristics of the loaded truss-bridge, namely, the modal frequencies and critical damping ratios. The resulting modal frequencies were then used to estimate the vertical and lateral stiffness of the truss-bridge.

Each white-noise test consisted of a low amplitude, broad-band, excitation applied simultaneously in the $x-$, $y-$ and $z-$directions for a duration of approximately 80 seconds. For brevity, only the results from Test 150 are presented. The input excitation during white-noise testing (and earthquake simulation testing) was recorded by three accelerometers located at the center of each earthquake simulator extension platform (ACC1 through 3 on the west platform and ACC7 through 9 on the east, see figure 6-2). The peak ground (base) acceleration (PGA) determined from the recorded acceleration histories was approximately $0.25\mathrm{g}$ in the $x-$and $y-$direction and $0.35\mathrm{g}$ in the $z-$direction.

7.4.2 Frequency Response Analysis

Transfer functions were generated using (7-6) and various combinations of input and output signals recorded during white-noise testing. Slight discrepancies were observed between the input from the east and west earthquake simulators, therefore, two transfer functions were generated for each output signal. Input acceleration histories were obtained from accelerometers located at the center of each earthquake simulator extension platform in the $y-$direction (ACC2 and ACC8) and $z-$direction (ACC3 and ACC9); see figure 6-3. The output acceleration histories were obtained from accelerometers located at the approximate center of each of the top mass plates oriented in the $y-$direction (ACC38, ACC41 and ACC44) and $z-$direction (ACC39, ACC42 and ACC45); see figures 6-3 and 7-1.

Figure 7-2 presents the transfer function amplitudes generated from the recorded response on the east (ACC44), center (ACC41) and west (ACC38) mass plates (see figure 7-1). Again, two transfer functions are plotted for each output signal, one from the input signal recorded on the east platform (ACC8) and one from the input signal recorded on the west platform (ACC2). From the curves presented in figure 7-2b, peaks are observed at approximately $4.5\,\text{Hz}$ and $22\,\text{Hz}$. Figures 7-2a and 7-2c show spikes at $4.5\,\text{Hz}$ with similar amplitudes and spikes at $22\,\text{Hz}$ with smaller amplitudes than shown in figure 7-2b. The amplitudes of the $22\,\text{Hz}$ spike at the three locations suggest a lateral sway mode and is consistent with the results of modal analysis performed with a commercially available software package SAP2000 (CSI, 2002). The approximately equal amplitude of the $4.5\,\text{Hz}$ peak at each location suggests the response might be attributed to a local mode from the mass plate assembly and/or connection to the truss-bridge.

Figure 7-3 presents transfer functions generated from recorded acceleration responses in the $z-$direction. The curves plotted in figure 7-3 correspond to output signals from accelerometers located on the west (ACC39), center (ACC42) and east (ACC45) mass plates. From figure 7-3b (center), two peaks are observed, one at $12\,\text{Hz}$ with an amplitude of approximately 30 (ACC42/ACC9) and the other at $28\,\text{Hz}$ with an amplitude of approximately 20 (ACC42/ACC9). The transfer function amplitudes plotted in figures 7-3a and 7-3c also show frequency peaks at $12\,\text{Hz}$ and $28\,\text{Hz}$. The amplitude of the $12\,\text{Hz}$ peaks in figures 7-3a and 7-3c is, approximately 20 or $2/3$ the amplitude of the $12\,\text{Hz}$ peak in figure 7-3b, suggesting a vertical mode with peak deformation at the center of the bridge. Again, this result is consistent with the results of modal analysis performed with SAP2000. The amplitudes of the $28\,\text{Hz}$ peak in figures 7-3a and 7-3b is

20 (ACC9) and 50 in figure 7-3c which is inconsistent with those expected from a higher frequency vertical mode. Therefore, the amplification at this frequency is believed to be due to a local mode from the mass plate assembly and/or connection to the truss-bridge.

Based on the results presented in figures 7-2 and 7-3, the first and second modes of the truss-bridge were identified as a vertical mode at, approximately, $12\,\text{Hz}$ and a lateral sway mode at, approximately, $22\,\text{Hz}$. The critical damping ratio, ζ, for each mode was estimated from the transfer function amplitudes plotted in figures 7-2b and 7-3b using the Half-Power method (Clough and Penzien, 1975) and (7-7). Table 7-2 presents the calculated damping ratio, ζ, the resonant frequency, f_o, the response amplitude $TR_{\max}$, $TR_{\max}/\sqrt{2}$ and the corresponding frequencies f_1 and f_2 for each mode and input instrument. The critical damping ratios for the first mode of $12\,\text{Hz}$ are 1.8% and 1.5% based on ACC3 and ACC9, respectively. The critical damping ratio for the second mode at $22\,\text{Hz}$ was estimated to be 0.6% and 1.1% based on ACC3 and ACC9, respectively.

TABLE 7-2 Dynamic properties of fixed base truss-bridge from the results of white-noise testing (Test 150)

Mode	Instrument Combination	f_n (Hz)	$TR_{\max}$	$\frac{TR_{\max}}{\sqrt{2}}$	f_1 (Hz)	f_2 (Hz)	ζ (%)
1	ACC42/ACC3	12.25	22.7	16.0	12.0	12.4	1.8
	ACC42/ACC9	12.00	35.8	25.3	11.9	12.2	1.5
2	ACC41/ACC2	21.88	9.6	6.8	21.6	22.1	1.1
	ACC41/ACC8	21.75	14.9	10.6	21.6	21.9	0.6

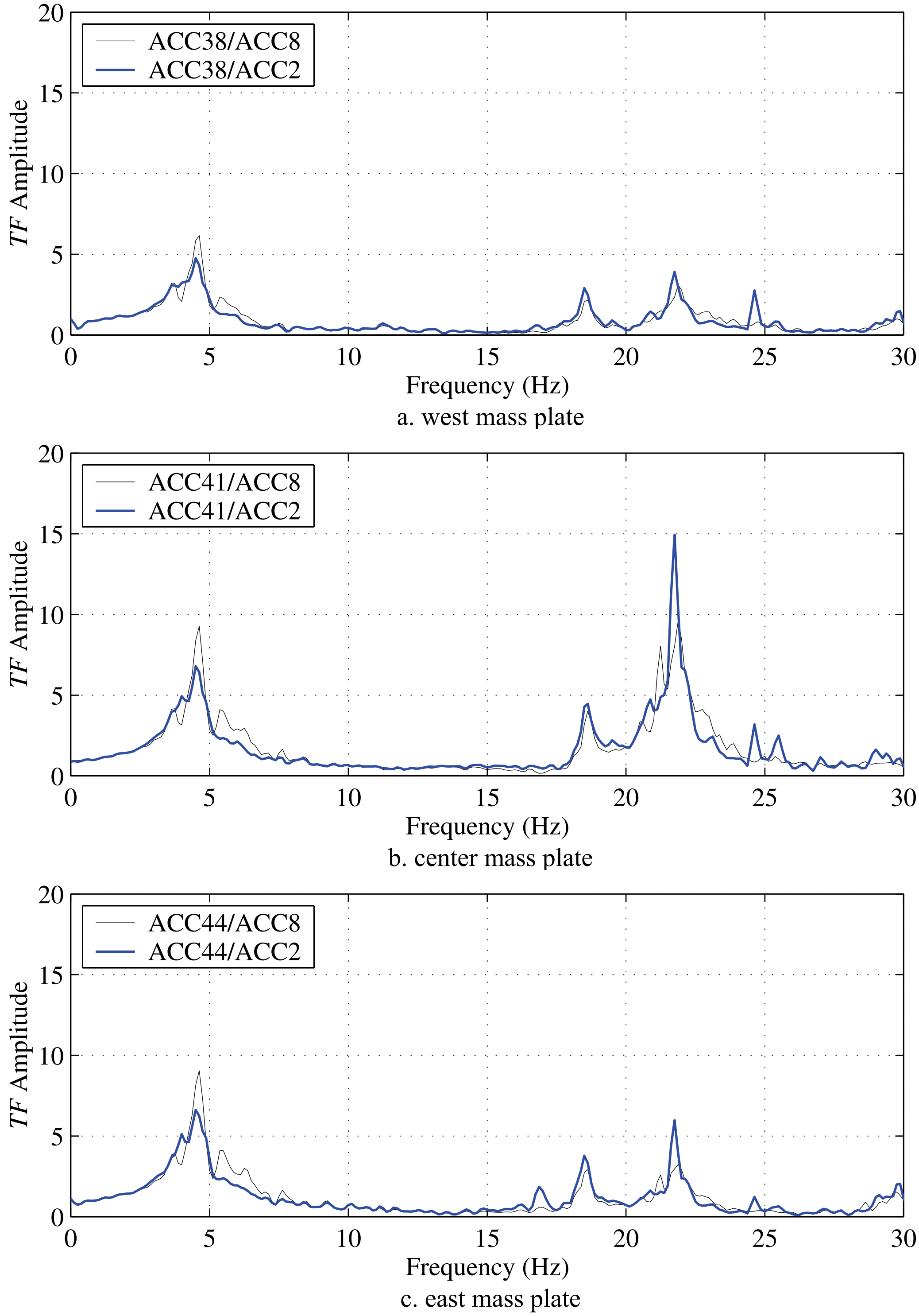

FIGURE 7-2 Transfer function amplitudes from recorded motion in the $y-$direction during white-noise testing (Test 150)

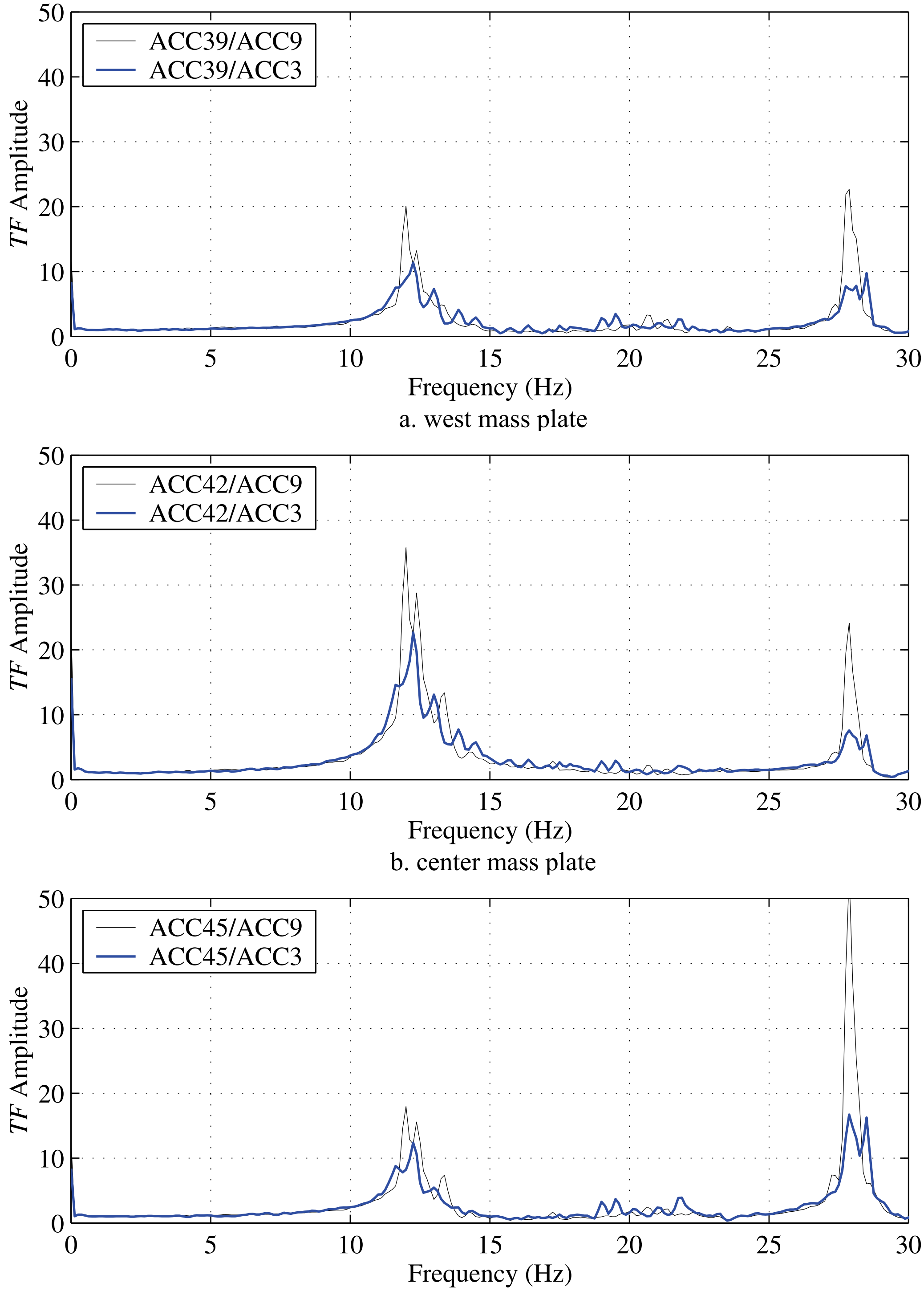

c. east mass plate

FIGURE 7-3 Transfer function amplitudes from recorded motion in the $z-$direction during white-noise testing (Test 150)

7.4.3 Generalized Properties of the Truss-Bridge

The generalized stiffness of the truss-bridge was back calculated using the resonant frequencies identified from the frequency response analysis with:

$$K_b = \left(\frac{2\pi}{T_n}\right)^2 \frac{W^*}{g} \tag{7-8}$$

where T_n is the period of the nth mode and equal to $1/f_n$; g is the gravitational acceleration constant equal to $9810\,\text{mm/s}^2$; and W^* is the effective weight equal to $204\,\text{kN}$. The effective weight was calculated as M^*g where M^* is the generalized mass:

$$M^* = \phi_n^T M \phi_n \tag{7-9}$$

calculated with the 3x3 lumped mass matrix, M, and a shape function, ϕ_n, determined assuming a parabolic deformed shape for both the horizontal and vertical directions and equal to $\{0.48, 1.0, 0.48\}$. The shape function was calculated assuming maximum deflection at the center of the bridge and lumped masses of: $11,723\,\text{kg}$, $14,964\,\text{kg}$ and $11,723\,\text{kg}$ at $1524\,\text{mm}$, $5,334\,\text{mm}$ and $9,144\,\text{mm}$ along the length of the truss-bridge, respectively (see figure 6-1). Based on this procedure, the generalized stiffness of the truss-bridge in the horizontal (K_{bh}) and vertical (K_{bv}) directions were estimated to be approximately $400\,\text{kN/mm}$ and $118\,\text{kN/mm}$, respectively.

In the isolated configuration the isolation system and truss-bridge can be approximated as series spring systems in both the transverse and vertical directions. In the transverse direction, the bridge structure is essentially "rigid" relative to the horizontal stiffness of the isolators. For example, the effective stiffness (K_{eff}) of a LR bearing is approximately $0.4\,\text{kN/mm}$ at 100% rubber shear strain (see Section 5, table 5-6). The ratio of the estimated bridge stiffness to the stiffness of the isolation system $K_{bh}/4K_{\text{eff}}$ is equal to 250 and the equivalent horizontal stiffness calculated using:

$$\frac{1}{K_{eq,h}} = \frac{1}{K_{bh}} + \frac{1}{4 \cdot K_{\text{eff}}} \tag{7-10}$$

and equal to $1.593\,\text{kN/mm}$ or approximately $4K_{\text{eff}}$. However, in the vertical direction, the stiffness of each LDR bearing under zero lateral displacement (K_{vo}) is approximately equal to $80\,\text{kN/mm}$ (see Section 5, table 5-3). The ratio of the vertical stiffness of the truss-bridge ($118\,\text{kN/mm}$) to the vertical stiffness of the isolation system composed of LDR bearings ($320\,\text{kN/mm}$) is equal to 0.37 and an equivalent vertical stiffness ($K_{eq,vo}$) of approximately $86\,\text{kN/mm}$. Based on the results of the previous calculations, it is reasonable to assume in the isolated configuration that the truss-bridge behaves rigidly in the horizontal direction. However in the vertical direction, the stiffness of the truss-bridge is approximately $1/3$ the stiffness of the isolation system composed of LDR bearings and should be considered. Table 7-3 presents the equivalent vertical stiffness of the bridge-isolation system considering the vertical stiffness of the isolators under zero lateral displacement (K_{vo}) and with a vertical stiffness at a lateral displacement corresponding to the maximum horizontal displacement (K_v) calculated using the two-spring formulation [(2-42)], denoted $K_{eq,vo}$ and $K_{eq,v}$, respectively. Also presented in this table are the corresponding equivalent vertical frequencies, f_{vo} and f_v calculated using the effective weight W^*. The equivalent vertical frequencies for the LDR and LR isolation system, assuming zero lateral displacement in the isolation system are $10.2\,\text{Hz}$ and $10.8\,\text{Hz}$, respectively. Using the estimated reduced vertical stiffness (corresponding to the maximum displacement) the equivalent vertical frequencies for the LDR and LR isolation system are $9.7\,\text{Hz}$ and $10.3\,\text{Hz}$, respectively.

TABLE 7-3 Equivalent vertical frequencies in the isolated configuration

Bearing Type	K_{vo} $\left(\frac{\text{kN}}{\text{mm}}\right)$	K_v^1 $\left(\frac{\text{kN}}{\text{mm}}\right)$	$4 \cdot K_{vo}$ $\left(\frac{\text{kN}}{\text{mm}}\right)$	$4 \cdot K_v$ $\left(\frac{\text{kN}}{\text{mm}}\right)$	K_{bv} $\left(\frac{\text{kN}}{\text{mm}}\right)$	$K_{eq,vo}$ $\left(\frac{\text{kN}}{\text{mm}}\right)$	$K_{eq,v}$ $\left(\frac{\text{kN}}{\text{mm}}\right)$	W^{*2} (kN)	f_{vo} (Hz)	f_v (Hz)
LDR	80	55	320	218	118.8	87	77	204	10.2	9.7
LR	130	82	520	327		97	87		10.8	10.3

Notes:

1. $K_v = K_{vo} / \left[1 + 12/\pi^2 (\Delta / R)^2\right]$; LDR: $\Delta = u_{\max} = 47$ mm and LR: $\Delta = u_{\max} = 53$ mm

2. $W^* = M^* g$; $M^* = \phi_n^T M \phi_n$

7.5 Earthquake Simulation Testing

7.5.1 Input Motion

Four simulations were chosen to illustrate the performance of the earthquake simulators. Here performance is being measured in terms of synchronization of the two simulators and whether the motion reproduced by the simulators matched the target motion. In addition, displacement histories, determined from the recorded acceleration histories, for one of these simulations are used to investigate the presence of torsion and/or rocking. The synchronization of the two simulators is assessed through a graphical comparison of recorded (and numerically obtained) motion from instruments located on each simulator. Target matching is assessed through a comparison of elastic response spectra generated from both the target and recorded motions assuming 5% critical damping. For brevity, only the recorded motion from two of these simulations is presented in this section, specifically, Test 110 (SYL 75%) and Test 135 (RIO 100%). The recorded earthquake simulator motion from Tests 98 (BOL 100%) and 104 (KJM 100%) are presented in Appendix D. These tests represent the most adverse condition for the earthquake simulator with the largest intensity and overturning demand due to the $1.2\ \text{m}$ support width configuration of the isolated bridge.

Figures 7-4, 7-5 and 7-6 present recorded earthquake simulator motion in the $x-$, $y-$ and $z-$direction, respectively, from Test 110 (SYL 75%). Figure 7-4 presents acceleration, velocity, and displacement histories for the west (ACC1 and STP1) and east (ACC7 and STP11) earthquake simulator extension platforms in the $x-$direction. In figure 7-4a the acceleration histories from ACC1 (center of west platform) and ACC7 (center of east platform) agree well with peak ground accelerations (PGA) of $0.57\ \text{g}$ and $0.62\ \text{g}$, respectively. Figure 7-4b presents velocity histories determined using the procedure described in Section 7.2 and acceleration histories from ACC1 and ACC7. The velocity histories of each simulator agree well with peaks (PGV) of $326\ \text{mm/s}$ and $315\ \text{mm/s}$ for the west and east platforms, respectively. Figure 7-4c presents displacement histories for the west (STP1) and east (SPT11) simulator platforms. Again, the simulator platforms histories agree well with peak ground displacements (PGD) of $31\ \text{mm}$ and $32\ \text{mm}$. Figure 7-4d presents elastic acceleration response spectra generated with 5% critical damping using the target motion (and the recorded acceleration from ACC1 and ACC7. The spectra presented in this figures show the response from the recorded motion matches the target response well for periods greater than $T > 0.5\ \text{s}$ and exceeds the target for $T < 0.5\ \text{s}$, where T is the period of vibration. From the results plotted in figure 7-5, the recorded acceleration, and displacement histories show the motion of the west and east tables again agree reasonably well, however, the elastic response spectra presented in figure 7-4d show the response from the recorded input exceeds the target, again, for $T < 0.5\,\mathrm{s}$. Figure 7-6 presents the recorded motion of the earthquakes simulators in the $z-$direction (SYL-UP). From figure 7-6a, the PGA of the west platform ($0.69\,\mathrm{g}$) is substantially larger than the east platform ($0.39\,\mathrm{g}$). The elastic response spectra presented in figure 7-6d illustrate the difference between the east and west platforms, both of which, exceeded the target for periods less than approximately $0.1\,\mathrm{s}$. A difference in vertical input from the west (usually higher) and east simulators was observed on several occasions generally occurring on large intensity motions such as SYL 75% and BOL 100%.

Figures 7-7, 7-8 and 7-9 present the earthquake simulator motion and elastic response spectra for the $x-$, $y-$ and $z-$direction, respectively, from Test 135 (RIO 100%). The recorded motion from Test 135 (RIO 100%) showed closer agreement with the target than was observed from Test 110 (SYL 75%), which can be attributed to the difference in demand associated with reproducing the motion of these two events. For example, the PGV from SYL 75% is $503\,\mathrm{mm/s}$ whereas the PGV from RIO 100% is $289\,\mathrm{mm/s}$, or approximately half.

To identify torsion or rocking during earthquake simulation testing, accelerometers were placed around the perimeter (and at the center) of each earthquake simulator extension platform, see the instrument layout in figure 6-2. The presence of torsion or rocking can be identified by comparing the displacement histories determined from recorded accelerations at the edge and center of the platforms. The difference, if any, was then used to estimate the amount of rotation about each axis. Figure 7-10 presents displacement histories numerically obtained from the recorded acceleration histories from Test 110 (SYL 75%). Plotted in figure 7-10a are the displacement histories obtained from ACC7 (center of east platform) and ACC10 (center of the North edge of east platform) each oriented in the $x-$direction and, approximately, $3350\,\mathrm{mm}$ apart. The maximum displacements differ by $18\,\mathrm{mm}$ corresponding to an angle of rotation about the $z-$axis of, approximately, 0.3 degrees. Figure 7-10b presents displacement histories obtained from accelerations recorded with ACC9 (center of the east platform), ACC11 (center of the North edge of the east platform), and ACC12 (center of the east edge of the east platform). A $2\,\mathrm{mm}$ difference is observed comparing the displacement histories obtained from ACC9 and ACC11 which translates into a negligibly small rotation about the $x-$axis. Comparing the displacement histories obtained from ACC12 and ACC9 almost no difference in maximum value is observed and therefore no rotation about the $y-$axis. This result could be expected since the bridge support is approximately $230\,\text{mm}$ eccentric to the center of the simulator, or 3.4% of the width of the earthquake simulator extension platforms ($6706\,\text{mm}$). Figures 7-10c and 7-10d present displacement histories obtained from accelerometers located on the west platform. The displacement histories shown in these figures agree well suggesting again negligible rocking and torsion during this simulation.

7.5.2 Global Response

For this testing program, global response refers to the truss-bridge and added mass plate assemblies focusing on the relative displacement response and acceleration response at various points along the length of the bridge and up the height. Sample global response results from Test 110 (SYL 75% with LR bearings) and Test 135 (RIO 100% with LDR bearings) are presented to illustrate the concentration of relative displacement response across the plane of isolation and the absence of torsion in the horizontal displacement response for both types of isolation systems. In addition, acceleration response results from these tests are presented to illustrate the effectiveness of each isolation system in reducing acceleration demands above the plane of isolation.

Plotted in figure 7-11 are acceleration histories recorded with instruments oriented in the $y-$(Transverse) direction at three different elevations from Test 110 (SYL 75%). Figure 7-11a presents acceleration recorded at the approximate centers of the top mass plate. Figure 7-11b presents acceleration recorded directly above the plane of isolation atop bearings 2 and 3 and figure 7-11c presents acceleration recorded at the center of each earthquake simulator extension platform. From the results presented in these figures, an approximately 50% reduction in peak acceleration is observed between the base (ACC2 and ACC8) and the center mass plate (ACC41). Figure 7-12 presents relative displacement responses from Test 110. Figure 7-12a presents the displacement response of the three mass plate assemblies relative to extension platforms. The relative displacement responses plotted in figures 7-12a agree well with a difference in maximum relative displacement of only a few millimeters indicating the horizontal motion is translation without torsion. Figures 7-12b and 7-12c present the relative displacement response at two elevations, bearing 2 and the west mass plate, in the $y-$ (Transverse) and $x-$ (Longitudinal) directions, respectively. The results plotted in figure 7-12b, show maximum relative displacements above bearing 2 and at the west mass plate of $70\,\text{mm}$ and $77\,\text{mm}$, respectively, illustrating the displacement response is concentrated across the isolation system (as expected).

The results plotted in figure 7-12c also show the displacement response to be concentrated across the isolation system.

Figures 7-13 and 7-14 present acceleration and relative displacement responses from Test 135 (RIO 100%) with the LDR bearings and a $1.2\,\mathrm{m}$ support width. The effectiveness of the LDR isolation system in reducing acceleration demands is evident by the 60% reduction in peak acceleration between the center mass plate (ACC41) and the east extension platform (ACC8) shown in figure 7-13. Figure 7-14a presents plotted relative displacement responses at the west, center and east mass plates in the $y-$direction that again differ by a few millimeters, illustrating that the displacement response with the LDR bearings is translation without the presence of torsion. Figures 7-14b and 7-14c present plots of the relative displacement response above bearing 2 and at the west mass-plate assembly in the $y-$ and $x-$directions, respectively. Again, it is clear the deformation is concentrated across the isolation system

7.5.3 Local Response

7.5.3.1 General

This section presents sample results of the response of the isolation system and individual bearings from earthquake simulation testing conducted with the LR and LDR bearings in both the $1.8\,\mathrm{m}$ and $1.2\,\mathrm{m}$ support width configurations. In Section 7.5.3.2, maximum response quantities including: horizontal displacement; horizontal shear force; maximum axial load; and minimum axial load values obtained from simulation performed with: transverse (T); transverse plus longitudinal (T+L); and transverse plus longitudinal plus vertical (T+L+V) components of excitation. The results of these simulations are compared to investigate the influence of multiple components of excitation and the coupled horizontal-vertical response exhibited by elastomeric and lead-rubber seismic isolation bearings. In Section 7.5.3.3, the results obtained from simulations performed with three components of excitation (T+L+V) are used to quantify the contribution of vertical load carried by the isolation system and individual bearings due to the vertical component of excitation.

7.5.3.2 The Influence of Multiple Components of Excitation

Figure 7-15 presents plots of the $x-$ and $y-$direction force displacement response of LR 1 from Tests 106 (T), 108 (T+L) and 110 (T+L+V), corresponding to SYL 75%. Figure 7-15d illustrates the unidirectional force displacement response of the LR bearing whereas Figure 7-15a shows the absence of response in the $x-$direction (L) during Test 106. From the force-displacement response presented in 7-15d, the maximum displacement and shear force are observed to be $62\ \mathrm{mm}$ ($103\,\%$ rubber shear strain) and $19.7\ \mathrm{kN}$, respectively. Figures 7-15b and 7-15e present the force-displacement response in the $x-$ and $y-$directions from Test 108, respectively. The maximum displacement and shear force in the $y-$direction are $68\ \mathrm{mm}$ (a $10\,\%$ increase from Test 106) and $19.3\ \mathrm{kN}$, respectively. The increase in maximum $y-$direction displacement is a result of the second (L) component of excitation and the coupled horizontal response (circular yield surface) exhibited by LR bearings, among others (Mokha et al., 1993; Huang, 2002; Mosqueda et al., 2003). Comparing the $y-$direction force displacement responses presented in figures 7-15d and 7-15e illustrates the effect of the second component of excitation on the unidirectional response that in this case resulted in a $10\,\%$ increase in maximum $y-$direction displacement. Figures 7-15c and 7-15f present the $x-$ and $y-$direction force displacement response, respectively, for LR 1 from Test 110 (T+L+V). The maximum $y-$direction displacement and shear force presented in figure 7-15f are $70\ \mathrm{mm}$ and $19.7\ \mathrm{kN}$, respectively. Comparing the results plotted in figure 7-15f (T+L+V) to those plotted in figure 7-15e (T+L), there is some additional fluctuation in the force-displacement response due to the vertical component and a slight increase in the maximum $y-$direction displacement and shear force of $3\,\%$ and $2\,\%$, respectively.

To illustrate the influence of the vertical component of excitation on the axial load of LR 1, axial load responses from Tests 108 (T+L) and 110 (T+L+V) are presented in figure 7-16. A maximum compressive force of $197\,\mathrm{kN}$ and minimum (compressive in this case) force of $14\ \mathrm{kN}$ are observed from the axial load response plotted in figure 7-16a. The substantial fluctuation in axial load observed from the results plotted in figure 7-16a are due the $1.2\ \mathrm{m}$ support width and the overturning moment generated by inertial forces in the $y-$directions during earthquake excitation. From the axial load response plotted in figure 7-16b, the influence of the vertical component is clear and is a high (relative to the overturning) frequency response. The maximum (compressive) load of $243\,\mathrm{kN}$ corresponds to an, approximately, $24\,\%$ increase in axial load due to the vertical component of excitation.

Figure 7-17 presents the force displacement response of LDR 1 in the $x-$ and $y-$direction from Tests 131 (T), 133 (T+L) and 135 (T+L+V) with RIO 100%. The force-displacement response of

LDR 1 under conditions of unidirectional (T) excitation is plotted in figure 7-17d. The force-displacement plot presented in this figure clearly shows a difference in effective stiffness for the positive and negative displacement excursions with maximum displacements of $38\,\text{mm}$ and $-46\,\text{mm}$, respectively. A lower effective stiffness is observed for the negative displacement excursions due to the increased compressive load as a result of the overturning moment. The influence of axial load on the horizontal stiffness of elastomeric bearings is well documented (Koh and Kelly, 1987; Kelly, 1997) and can be predicted with reasonable accuracy using the two-spring model presented in Section 2 as part of the investigate the influence of lateral displacement on the vertical stiffness of elastomeric bearings. Similar results are observed from the $y-$direction force displacement response of LDR 1 presented in figures 7-17e (T+L) and 7-17f (T+L+V).

Figures 7-18 through 7-21 present maximum and minimum response data for bearings 1 and 2 for the largest intensity simulations (see table 6-3) performed with the LR bearings configured in both the $1.8\,\text{m}$ and $1.2\,\text{m}$ support widths. Maximum horizontal displacement ($u_{\max}$) data, calculated according to (7-4), from the various simulations performed with the LR bearings is presented in figure 7-18. Comparing the $u_{\max}$ data in figure 7-18a ($1.8\,\text{m}$) for simulations with T and T+L components of excitation illustrates the increase in maximum horizontal displacement due to bidirectional excitation. Again the increase is due to the second component of excitation and the coupled response exhibited by LR bearings. For SYL the increase in displacement is less substantial than was observed with BOL and KJM. This is due to the near-fault characteristics of the SYL motion, where the response is dominated by one component (SYL 360) and can be seen from the elastic response spectra; see figures 7-4d and 7-5d. Comparing $u_{\max}$ results from T+L and T+L+V components of excitation shows the addition of the vertical component has a marginal effect on the maximum horizontal displacement, with the exception of KJM where the addition of the vertical component resulted in a $25\,\%$ reduction in maximum horizontal displacement. The maximum horizontal displacement data plotted in figure 7-18b ($1.2\,\text{m}$) shows similar results.

Figure 7-19 presents maximum horizontal shear force ($F_{\max}$) data for simulations performed with the LR bearings. From figure 7-19a ($1.8\,\text{m}$), an increase in $F_{\max}$ is observed for the T+L simulations when compared to the unidirectional excitation (L) and is a result of the increase in displacement illustrated in figure 7-18a. A small decrease in $F_{\max}$ is observed comparing the results of simulations with T+L and T+L+V components of excitation with the exception of KJM which exhibited a substantial reduction in maximum horizontal shear force (a results of the reduction in horizontal displacement previously shown in figure 7-18a). The difference in $F_{\max}$ of bearing 1 and bearing 2 for BOL 100%, KJM 100% and SYL 75% (T only) illustrates the influence of the axial load fluctuation (from the overturning moment) on the shear force response. The impact of the axial load fluctuation on the maximum shear force response is further illustrated by comparing the results presented in figure 7-19a (1.8 m) with those in figure 7-19b (1.2 m). The maximum shear force data presented in figure 7-19b (1.2 m) is consistently lower than $F_{\max}$ presented in figure 7-19a (1.8 m) for each simulation. The results presented in figure 7-19 suggest that for this system the vertical component of excitation has minimum impact on the shear force response.

Figure 7-20 presents maximum axial load data ($P_{\max}$) for bearings 1 and 2 from each simulation. From the BOL 100% and KJM 100% results presented in figure 7-20a, the $P_{\max}$ is consistently larger for bearing 2 compared to bearing 1, which is consistent with the lower $F_{\max}$ data for bearing 2 as shown in figure 7-19a. The T+L+V simulations resulted in a moderate increase in maximum axial load for both bearings 1 and 2, as expected. Figure 7-21 presents minimum axial load ($P_{\min}$) data for the LR bearings. For KJM 100% and SYL 75% with T+L+V components of excitation, the axial load is almost reduced to zero in the 1.8 m configuration and results in tension for the same simulation with the bearings in the 1.2 m configuration. For SYL 75% T+L+V in the 1.2 m support configuration a tension force of approximately 30 kN was recorded which corresponds to an axial pressure of -1.7 MPa (-250 psi).

Figures 7-22 through 7-25 present response data from the large intensity simulations (see table 6-3) performed with the LDR bearings in both the 1.8 m and 1.2 m support width configurations. Maximum horizontal displacement and shear force data for simulations performed with the LDR bearings are presented in figures 7-22 and 7-23. From the maximum horizontal displacement data presented in figure 7-22 the addition of the longitudinal (L) component again results in an increase in maximum horizontal displacement (with the exception of RIO) as expected. Simulations with T+L+V components of excitation result in a marginal change in the maximum horizontal displacement as compared to simulations with T+L components of excitation. Figure 7-23 presents maximum horizontal shear force data, and as was observed with the LR bearings, simulations with T+L components resulted in an increase in maximum horizontal shear force when compared to simulations with only T excitation, a consequence of the increased horizontal displacement. Comparing the results presented in figure 7-23a ($1.8\,\text{m}$) to those in 7-23b ($1.2\,\text{m}$), the increase in axial load fluctuation (and therefore maximum compressive load) results in a decrease in maximum horizontal shear force. Figures 7-24 and 7-25 present maximum and minimum axial load data, respectively, from simulations performed on the LDR bearings. Again the addition of the vertical component both increases the maximum axial load and decreases the minimum as was observed with the LR bearings. Although this result is expected, in the next section the contribution of vertical load due to the vertical component of excitation is quantified and used to evaluate design procedures accounting for the vertical component of excitation.

7.5.3.3 Contribution of the Vertical Component of Excitation

In this section the contribution of the vertical load on the isolation system (P_{EQ}) due to the vertical component of excitation is quantified using data recorded from the load cells for earthquake simulations performed with three components of excitation (T+L+V) and the LR and LDR isolation systems. To facilitate a direct comparison with the recorded vertical base acceleration and to compute amplification factors, the P_{EQ} response was normalized by the effective weight (W^*). In addition, transfer functions were generated from the calculated P_{EQ}/W^* and vertical base acceleration signals to identify which frequencies are being amplified and to assess whether the reduction in vertical stiffness discussed in Sections 2 and 5 has an impact on the vertical response of the isolation system.

Figure 7-26 presents the vertical load response calculated using (7-5) normalized by the effective weight (P_{EQ}/W^*) and recorded vertical acceleration histories from ACC3 (west platform) and ACC9 (east platform) for Test 104 (KJM 100%). In each plot, the maxima and minima are identified by a circle and square, respectively, and the value reported in the legend along with the corresponding symbol. From the results presented in figure 7-26 the amplification of vertical response is apparent and approximately 5 times the peak base acceleration with respect to ACC9. Amplification factors for simulations performed with the vertical component of excitation and the LR and LDR isolation system are presented in tables 7-4 and 7-5, respectively. These factors were calculated according to:

$$\text{Amplification} = \frac{P_{EQ} / W^*}{PGA} \tag{7-11}$$

where P_{EQ} / W^* is the maximum absolute value of P_{EQ} normalized by the weight W^* and PGA represents the peak ground (base) acceleration recorded by either ACC3 or ACC9. Also presented in these tables are the maximum and minimum P_{EQ} values (denoted $P_{EQ,\max}$ and $P_{EQ,\min}$, respectively), the effective weight, W^*, the peak base acceleration from ACC3 and ACC9 (denoted PGA_{ACC3} and PGA_{ACC9}, respectively) and the value of the amplification. An average value of the amplification was calculated due to the differences in PGA from the east and west simulators. Figures 7-27 and 7-28 present bar plots of the calculated amplification factors for the LR and LDR isolation systems, respectively. From figure 7-27a (LR in the 1.8 m support width) the amplification factors calculated from ACC3 (west platform) and ACC9 (east platform) vary for each simulation, however, the average values for BOL 100%, KJM 100%, and SYL 75% are 2.8, 4.2 and 2.3, respectively. Figure 7-27b presents amplification values for the LR bearings in the 1.2 m configuration with average values for BOL, KJM, and SYL of 3.5, 4.5 and 2.0, respectively. Figure 7-28 presents amplification values for the LDR bearing in the 1.8 m and 1.2 m support width configurations. From figure 7-28a (LR in the 1.8 m support width), the average amplification for RIO 100%, BOL 50% and KJM 50% are 3.0, 3.5 and 5.3, respectively. For the LDR bearings in the 1.2 m support configuration, the average amplification for RIO, BOL and KJM are 3.5, 4.6 and 5.6, respectively.

TABLE 7-4 Summary results from simulations with vertical excitation and the LR bearings

Test	$P_{EQ,\max}$ (kN)	$P_{EQ,\min}$ (kN)	W^* (kN)	$\frac{P_{EQ}}{W^*}$	PGA_{ACC3} (g)	PGA_{ACC9} (g)	Amp. ACC3	Amp. ACC9	Amp. Avg.
61	172	-150	204	0.84	0.39	0.25	2.2	3.4	2.8
67	278	-265	204	1.36	0.37	0.28	3.7	4.8	4.2
73	187	-150	203	0.92	0.66	0.29	1.4	3.2	2.3
98	188	-176	203	0.93	0.31	0.24	3.0	3.9	3.5
104	289	-277	204	1.42	0.31	0.31	4.5	4.6	4.5
110	198	-175	203	0.98	0.67	0.39	1.5	2.5	2.0

TABLE 7-5 Summary results from simulations with vertical excitation and the LDR bearing

Test	$P_{EQ,\max}$ (kN)	$P_{EQ,\min}$ (kN)	W^* (kN)	$\frac{P_{EQ}}{W^*}$	PGA_{ACC3} (g)	PGA_{ACC9} (g)	Amp. ACC3	Amp. ACC9	Amp. Avg.
24	181	-185	205	0.90	0.35	0.27	2.6	3.4	3.0
30	127	-128	204	0.63	0.24	0.14	2.6	4.5	3.5
36	264	-229	204	1.30	0.30	0.21	4.4	6.2	5.3
135	127	-140	201	0.70	0.19	0.21	3.6	3.3	3.5
141	113	-109	201	0.56	0.12	0.12	4.6	4.6	4.6
147	211	-185	201	1.05	0.20	0.18	5.3	5.8	5.6

The amplification of the vertical ground motions suggest the isolation system does not behave as an "almost" rigid system in the vertical direction and has a level of flexibility such that the vertical component of excitation is being amplified. To identify the frequency content being amplified in the vertical direction transfer functions were calculated using (7-6) and the calculated P_{EQ}/W^* response in conjunction with the recorded vertical acceleration histories from ACC3 and ACC9. Sample transfer functions calculated for the LR and LDR systems are presented in figure 7-29. As a point of reference, transfer functions generated from the results of white-noise testing (Test 150) in the fixed base configuration are also presented in this figure. Figure 7-29b presents the transfer function amplitudes calculated from the results of Test 67 corresponding to the LR bearings in the 1.8 m configuration and KJM at 100% intensity. Two additional vertical lines are plotted in this figure at 10.3 Hz (solid) and 10.8 Hz (dashed) correspond to the equivalent vertical frequencies calculated using the vertical stiffness of the isolators at maximum displacement and zero lateral displacement (see table 7-3). The transfer function amplitudes plotted in figure 7-29b show large amplitude peaks in the proximity of 10 Hz, specifically, a peak at 10 Hz with an amplitude of approximately 20 and a peak at 10.8 Hz with an amplitude of approximately 13. Similarly, presented in figure 7-29c are transfer function amplitudes calculated from the results of Test 147 corresponding to KJM 50% performed with the LDR bearings in the 1.2 m configuration. Again, two vertical lines are plotted in this figure, one at 9.7 Hz (solid) and the other at 10.2 Hz (dashed) which correspond to the equivalent vertical frequency considering the vertical stiffness of the LDR bearings at the maximum displacement and zero lateral displacement, respectively (see table 7-3). Again, large amplitude peaks are observed in the general proximity of 9 to 10 Hz. Specifically, peaks at 9.4 Hz with an amplitude of approximately 30 and 10.1 Hz with a amplitude of approximately 35.

7.6 Summary

From the results of white-noise testing performed in the fixed base configuration, the vertical frequency of the loaded truss-bridge was determined to be approximately 12 Hz. The vertical stiffness of the truss-bridge was estimated to be 118 kN/mm and on the same order of magnitude of the combined vertical stiffness (under zero lateral displacement) of the LR and LDR bearings. For earthquake simulation testing, the east and west simulators reproduced the target motions reasonably well with some deviations for SYL 75% and periods less than 0.5 s. In addition, the synchronization of the two tables in the horizontal direction was very good although some discrepancies were observed in the vertical direction. A comparison of the maximum response quantities from simulations performed with T, T+L, and T+L+V components of excitation illustrated the impact of axial load variation on the horizontal response of the LDR and LR bearings. The influence of the vertical component of excitation on the horizontal response was obscured by the axial load fluctuation generated by the overturning moment in both the 1.8 m and 1.2 m support width configurations. Focusing on simulations with all three components of excitation (T+L+V), significant amplification in the vertical response was observed for both the LR and LDR isolation systems. The calculated amplification values suggest using the PGA from the vertical component will results in un-conservative estimates of the vertical load on the isolation system due to the vertical component of excitation. Finally, the transfer function amplitudes plotted in figure 7-29 suggest the frequencies being amplified are in close proximity to the equivalent frequency of the bridge-isolation system. The impact of the stiffness reduction on the estimation of the vertical load due to the vertical component of excitation is evaluated in Section 9.

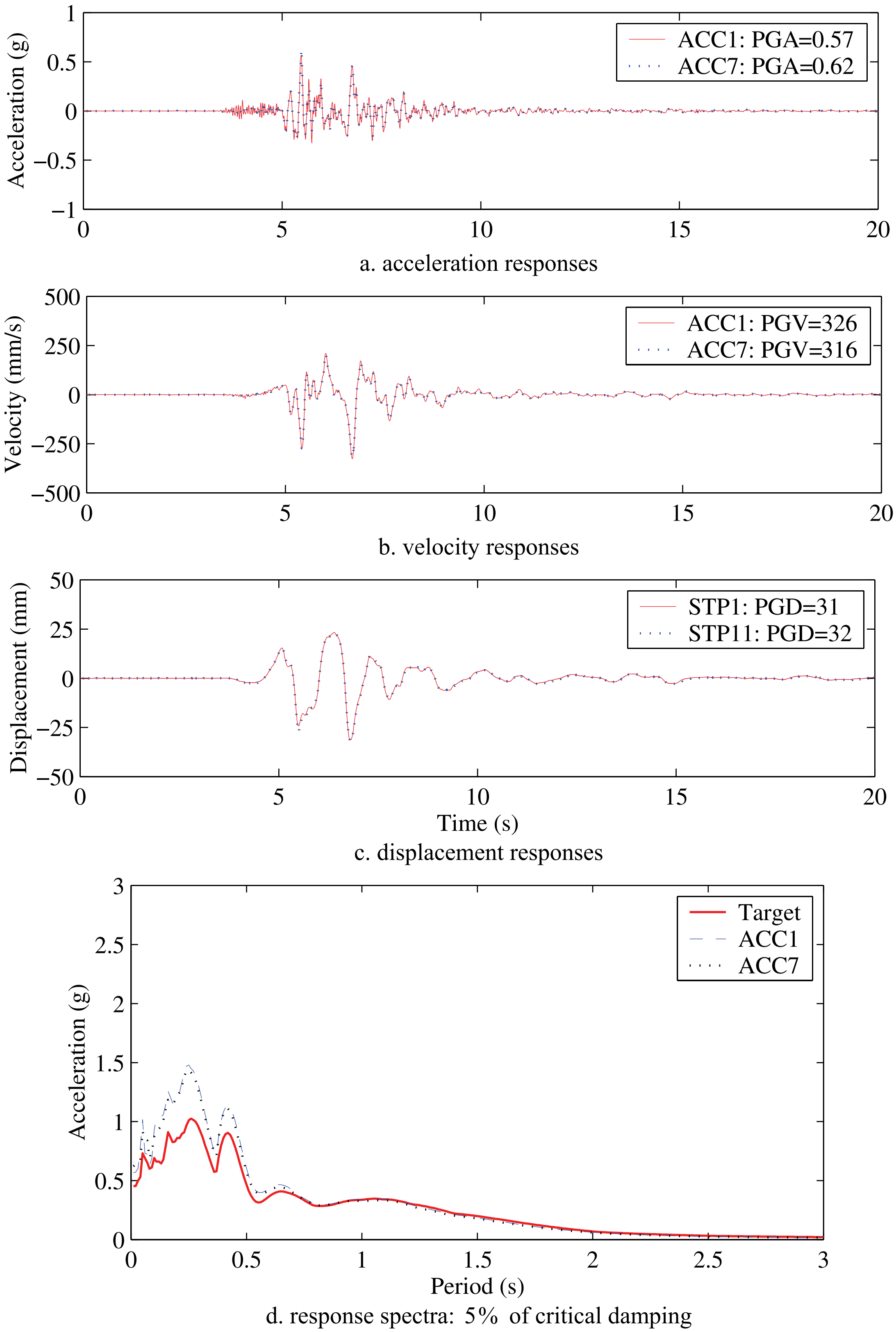

a. acceleration responses

b. velocity responses

c. displacement responses

d. response spectra: 5% of critical damping

FIGURE 7-4 Earthquake simulator motion in the $x-$direction from Test 110: SYL090 at 75% intensity and comparison of response spectra

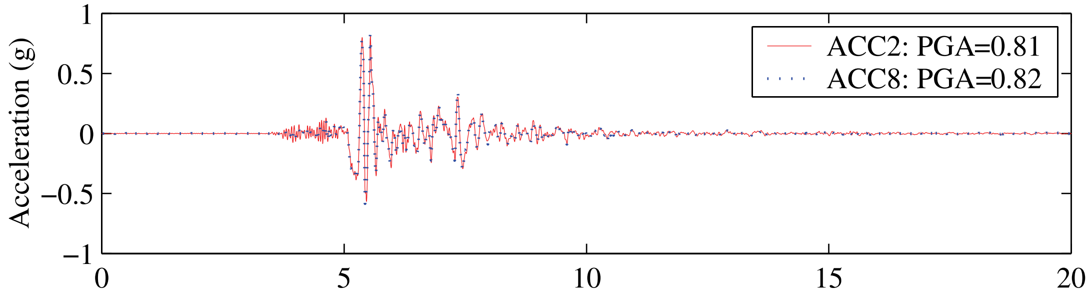

a. acceleration responses

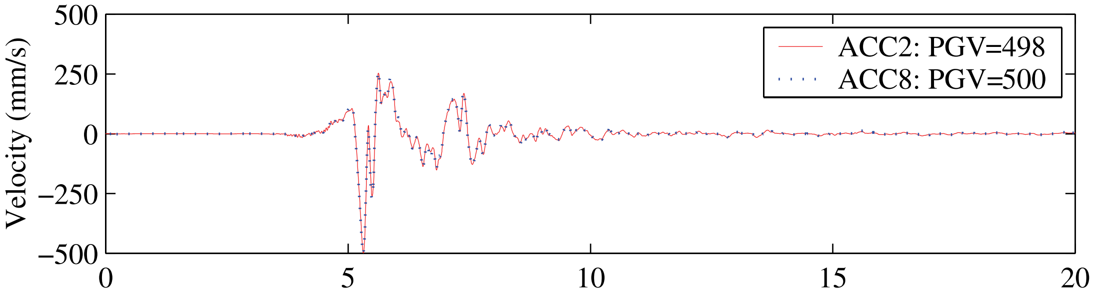

b. velocity responses

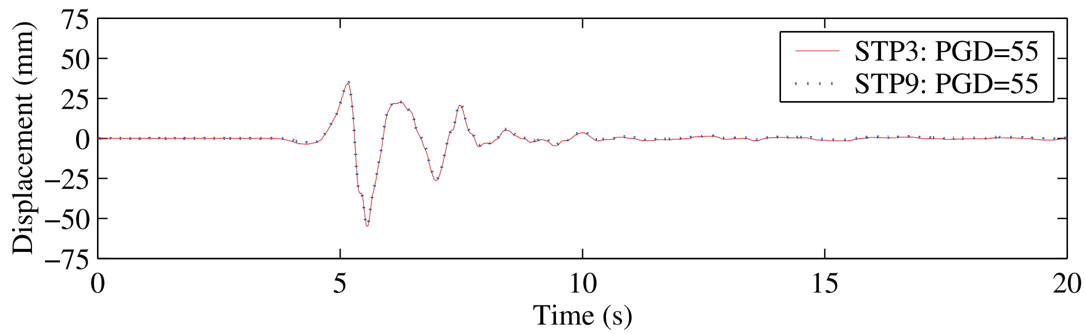

c. displacement responses

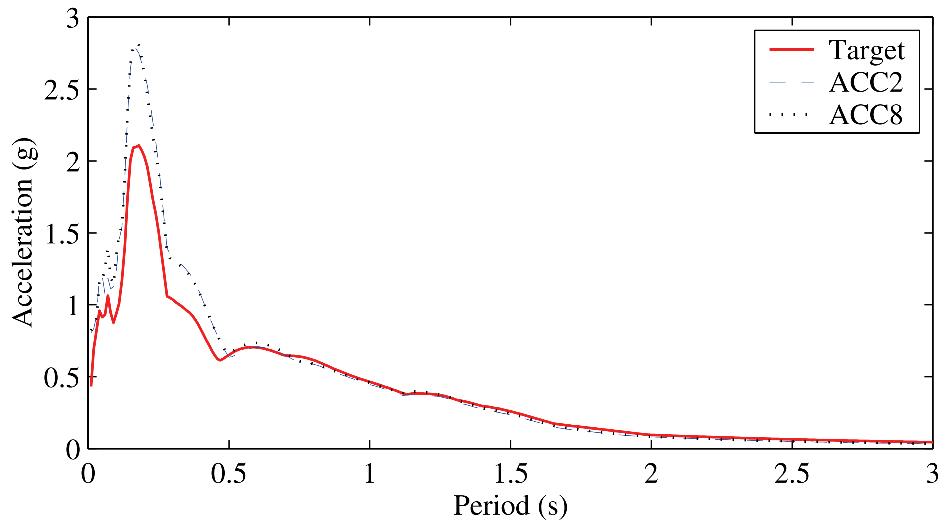

d. response spectra: 5% of critical damping

FIGURE 7-5 Earthquake simulator motion in the $y-$direction from Test 110: SYL360 at 75% intensity and comparison of response spectra

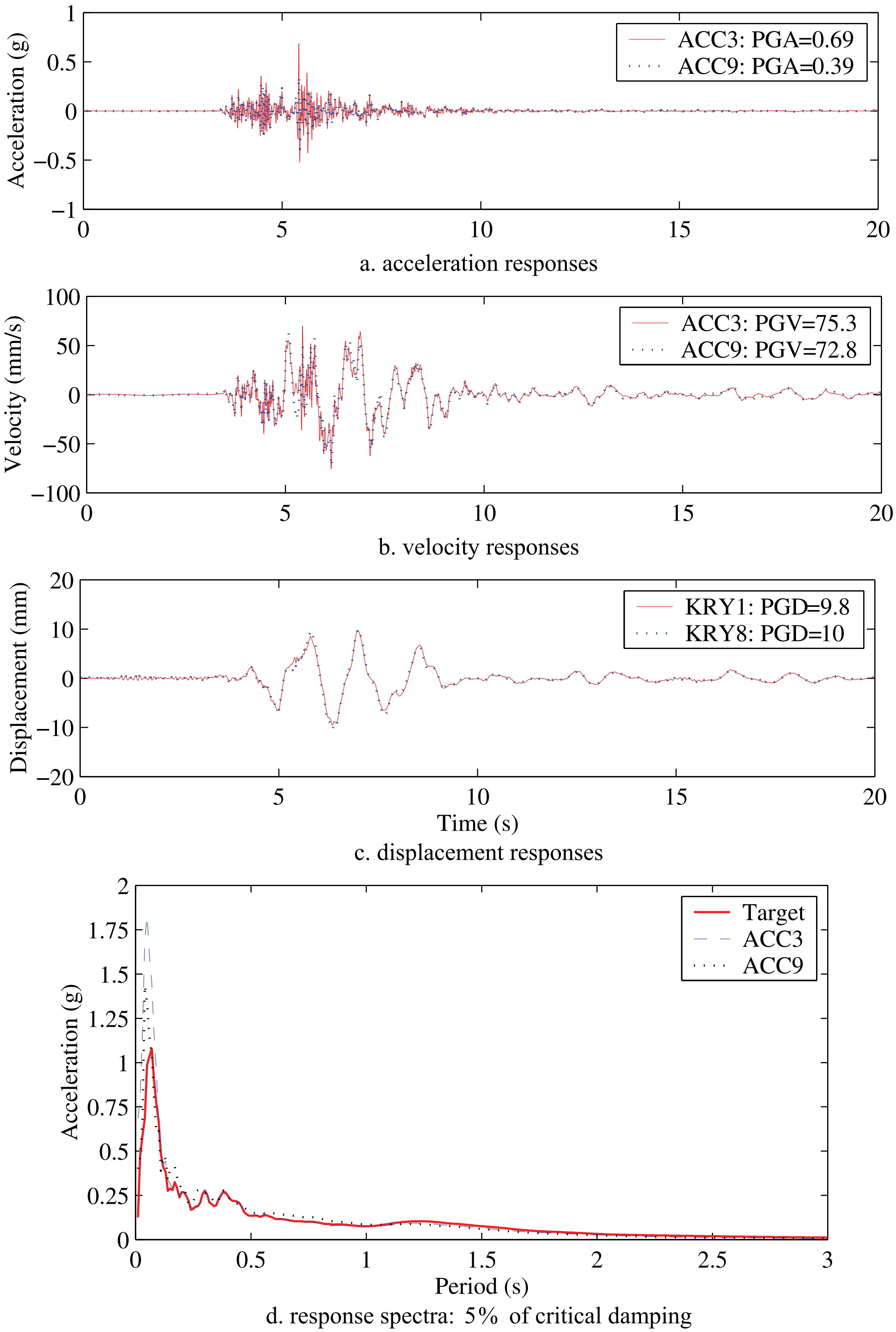

FIGURE 7-6 Earthquake simulator motion in the z – direction from Test 110: SYL-UP at 75% intensity and comparison of response spectra

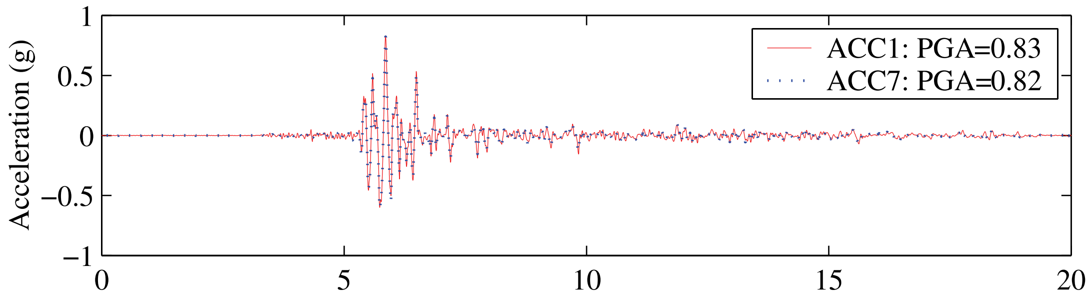

a. acceleration responses

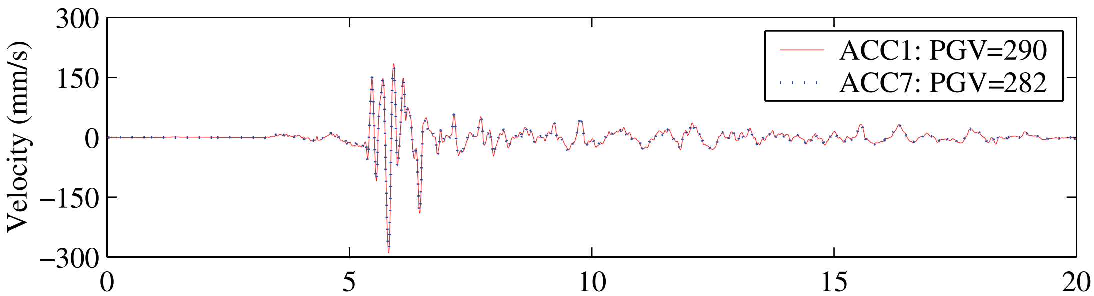

b. velocity responses

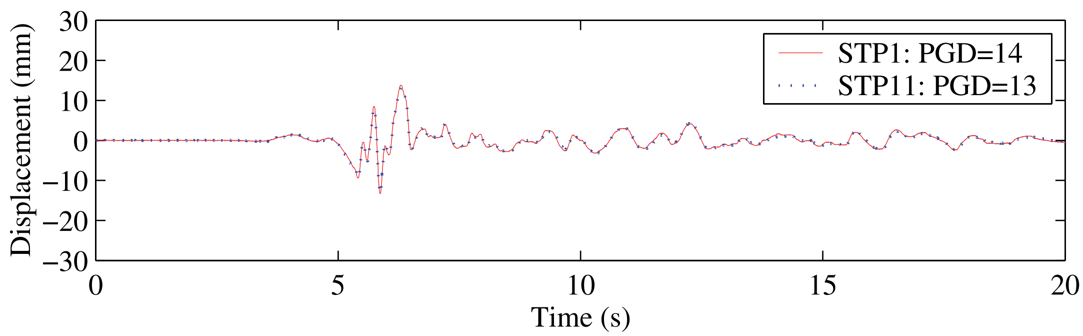

c. displacement responses

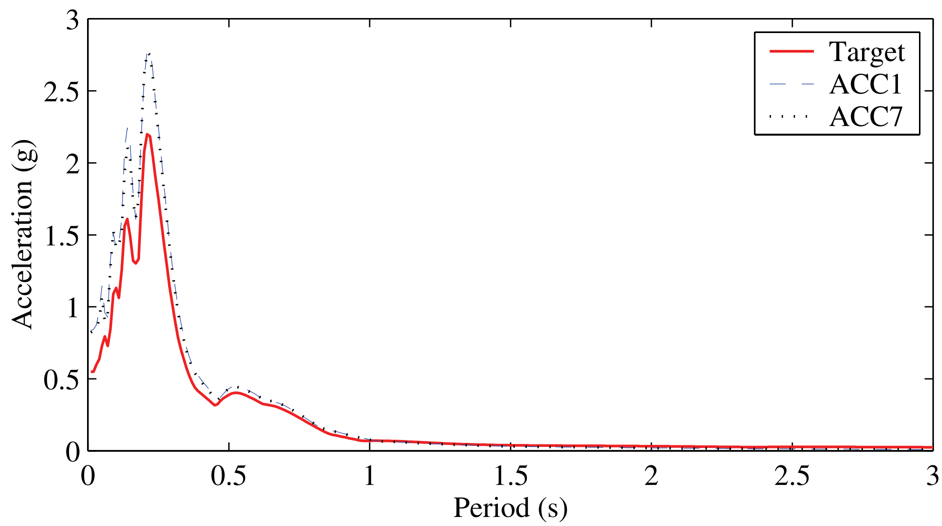

d. response spectra: 5% of critical damping

FIGURE 7-7 Earthquake simulator motion in the x – direction from Test 135: RIO360 at 100% intensity and comparison of response spectra

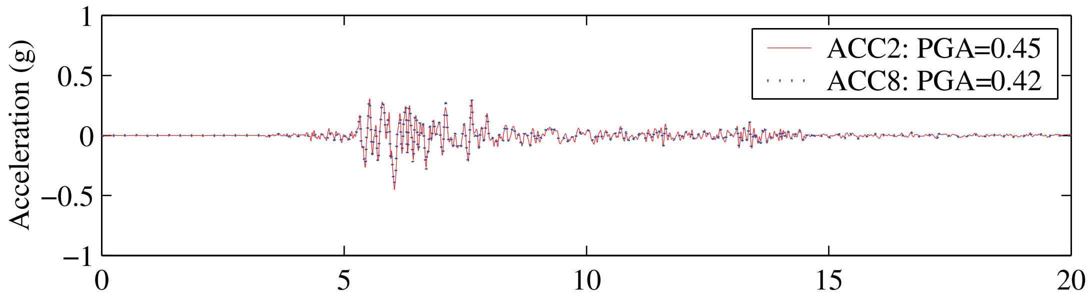

a. acceleration responses

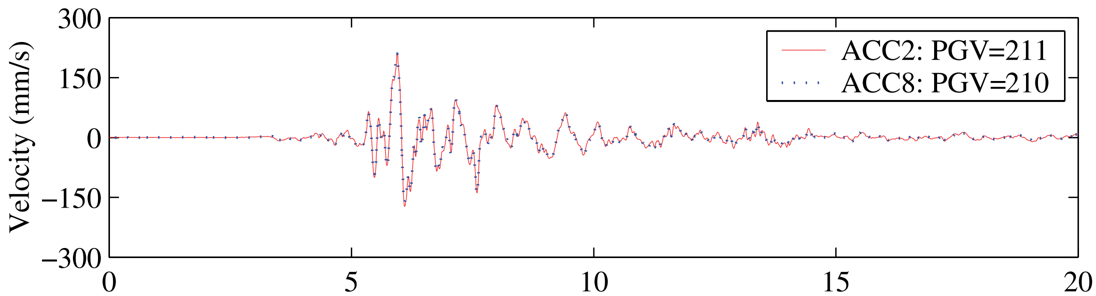

b. velocity responses

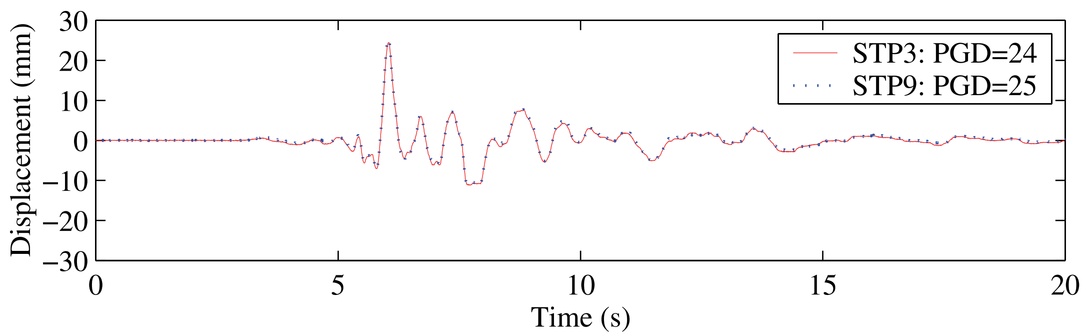

c. displacement responses

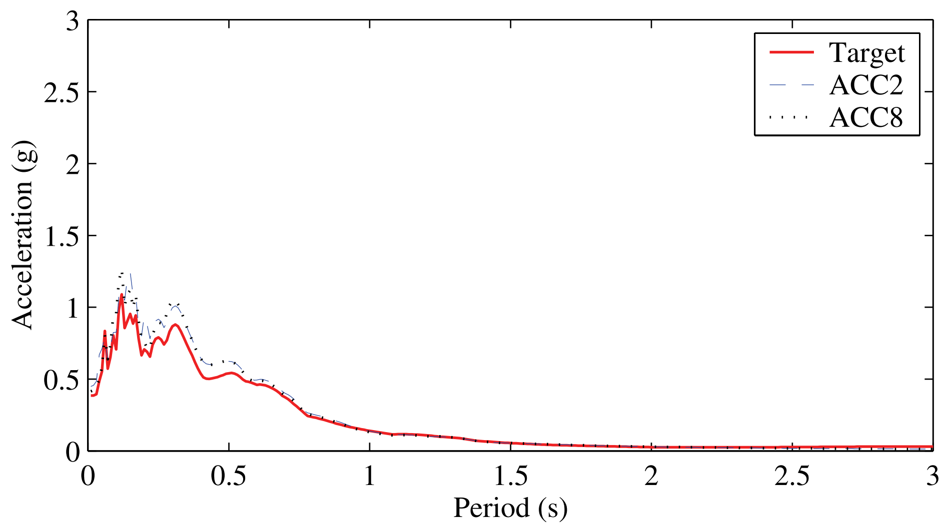

d. response spectra: 5% of critical damping

FIGURE 7-8 Earthquake simulator motion in the $y-$direction from Test 135: RIO270 at 100% intensity and comparison of response spectra

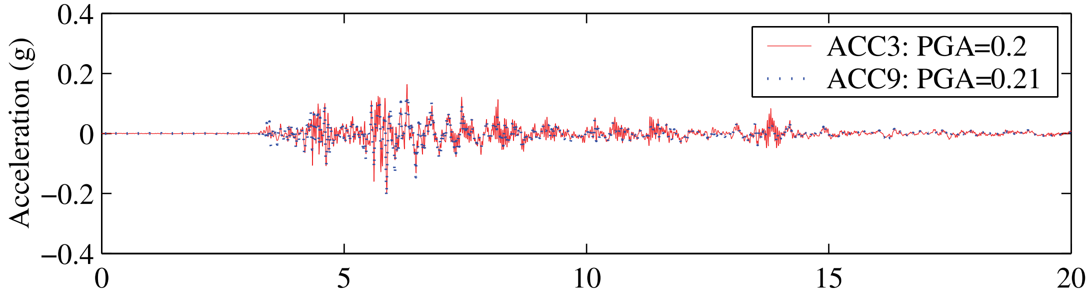

a. acceleration responses

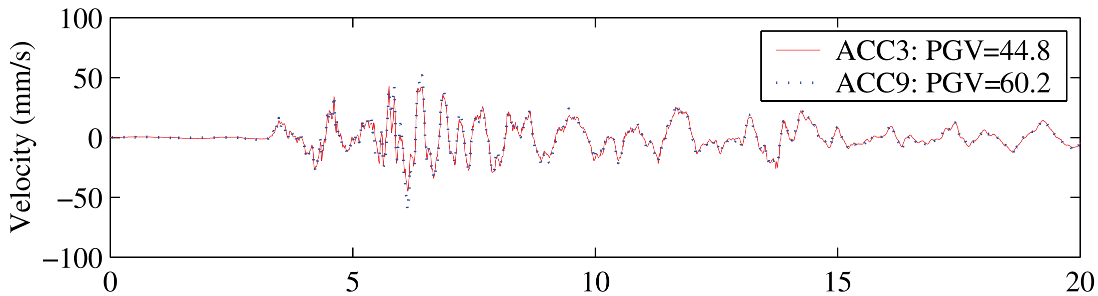

b. velocity responses

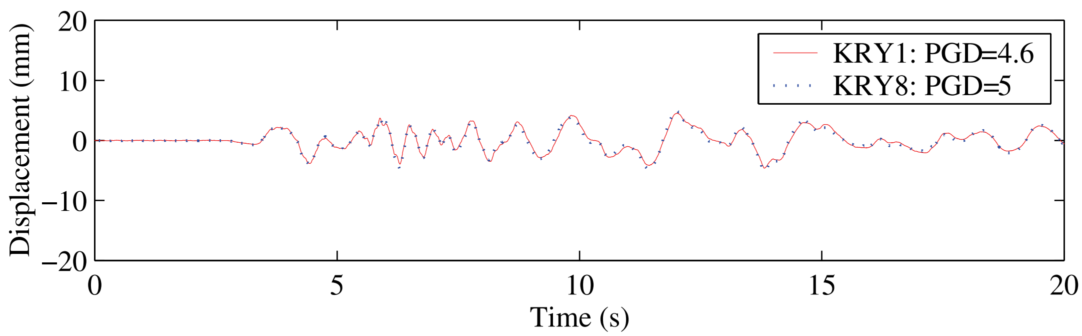

c. displacement responses

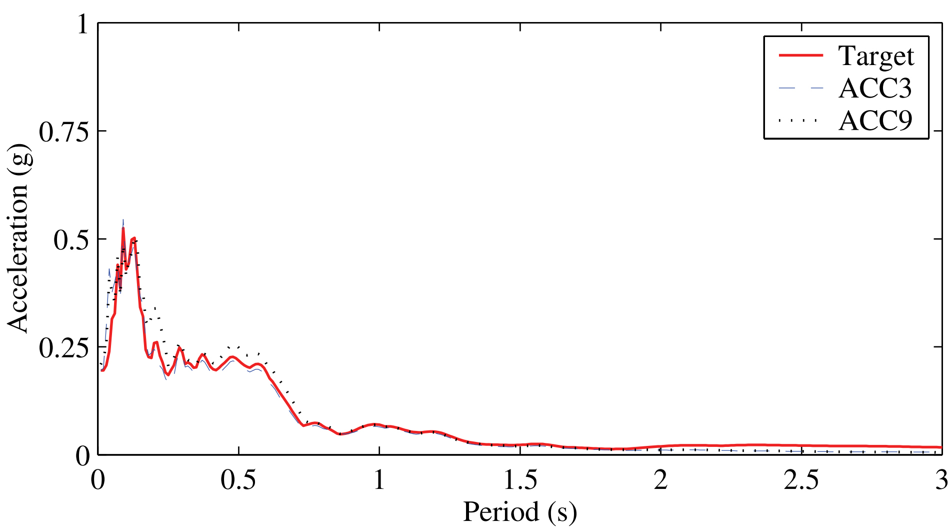

d. response spectra: 5% of critical damping

FIGURE 7-9 Earthquake simulator motion in the z – direction from Test 135: RIO-UP at 100% intensity and comparison of response spectra

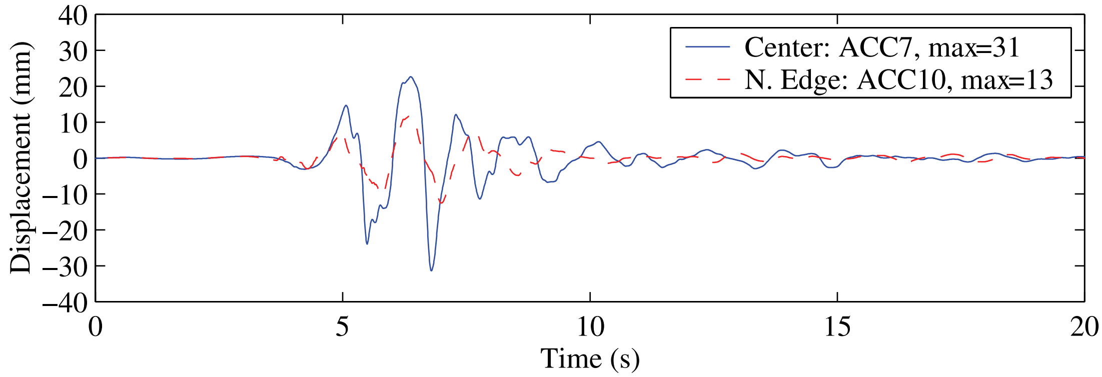

a. East simulator: $x-$direction

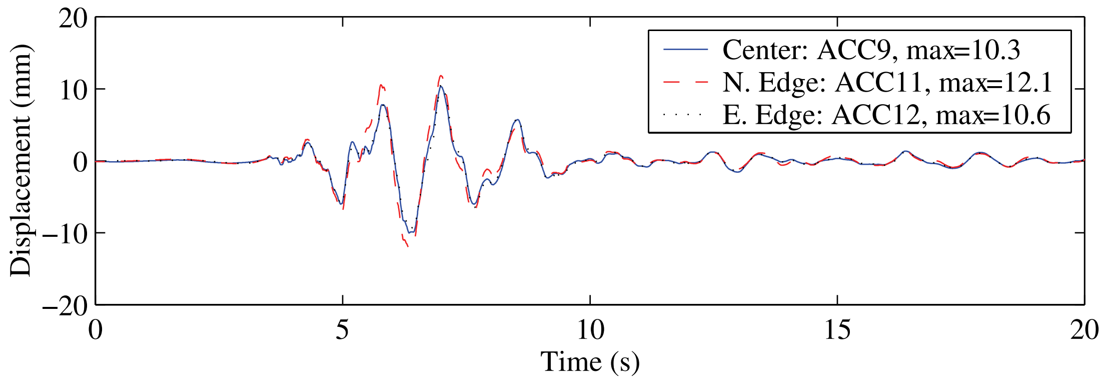

b. East simulator: $z-$direction

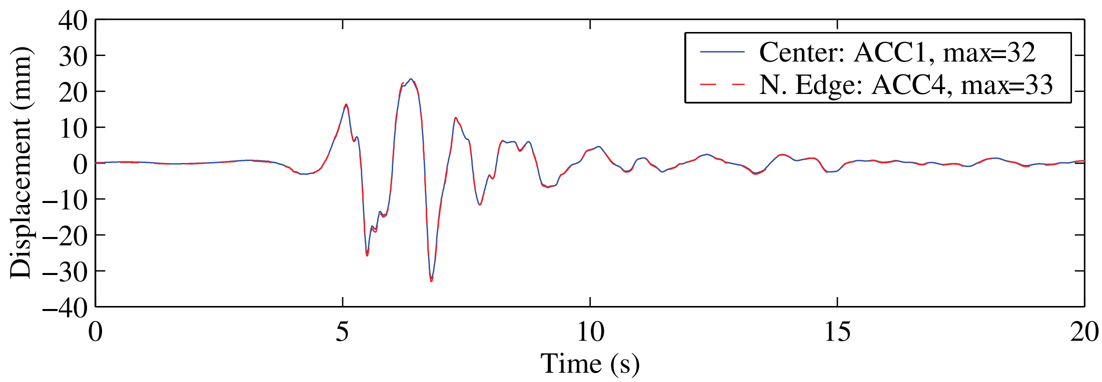

c. West simulator: $x-$direction

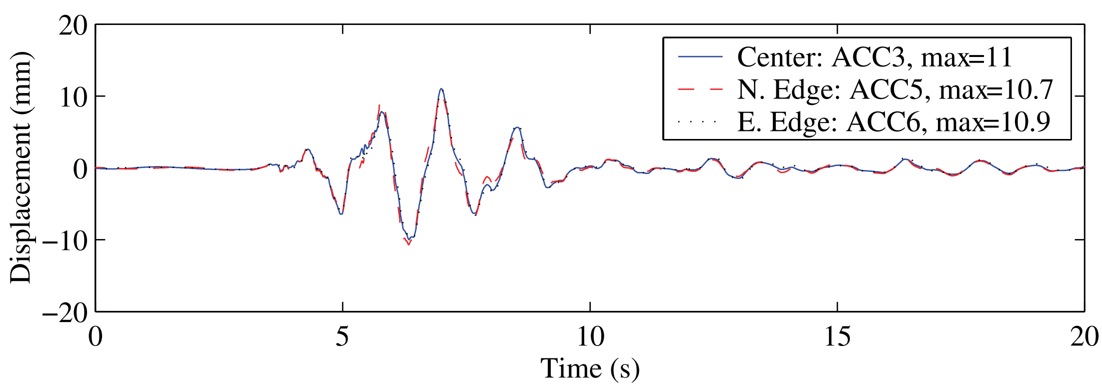

d. West simulator: $z-$direction

FIGURE 7-10 Earthquake simulator displacements determined from recorded accelerations for Test 110: SYL at 75% intensity

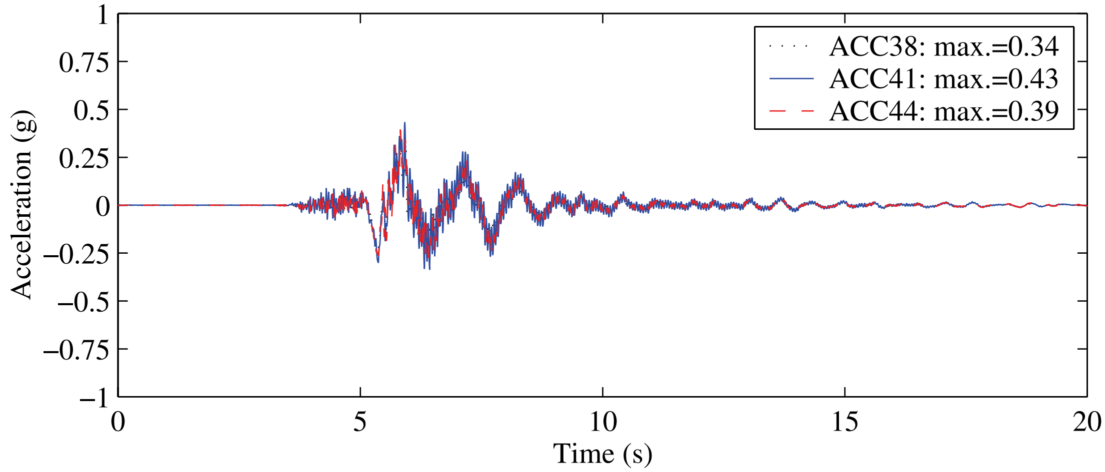

a. mass plates

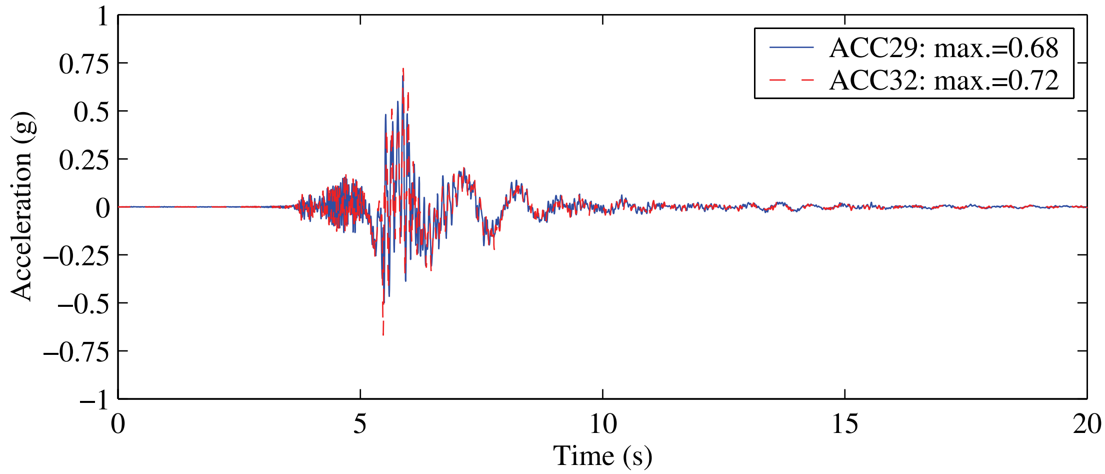

b. top end-plate of bearings 2 and 3

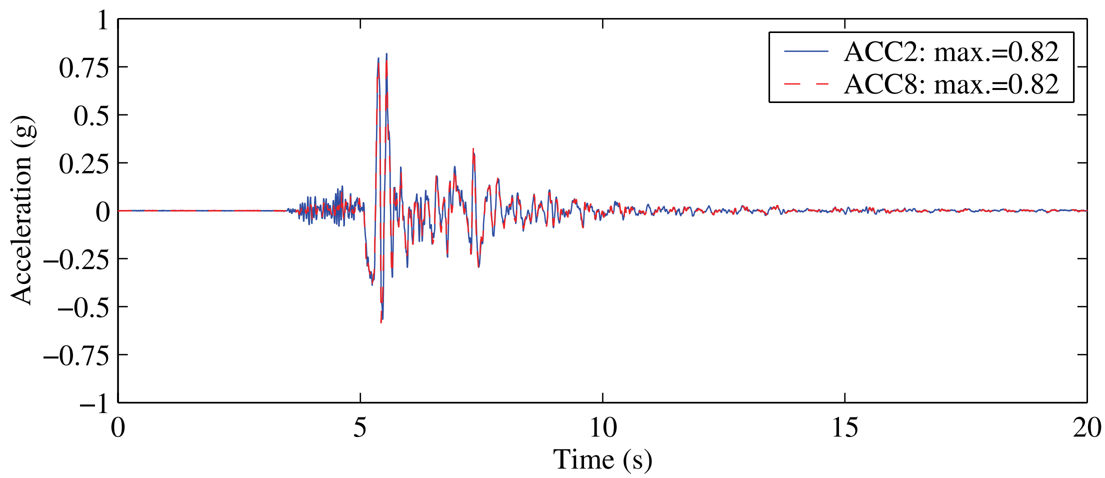

c. center of extension platforms

FIGURE 7-11 Recorded $y-$direction absolute acceleration responses for LR bearings with a 1.2m support width and 75% SYL (Test 110)

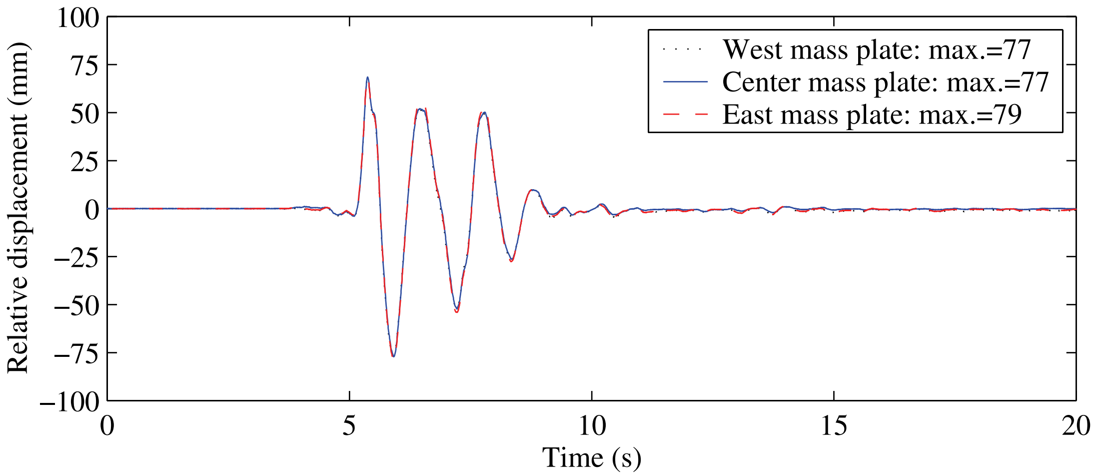

a. relative to simulator extension platforms: $y-$ direction

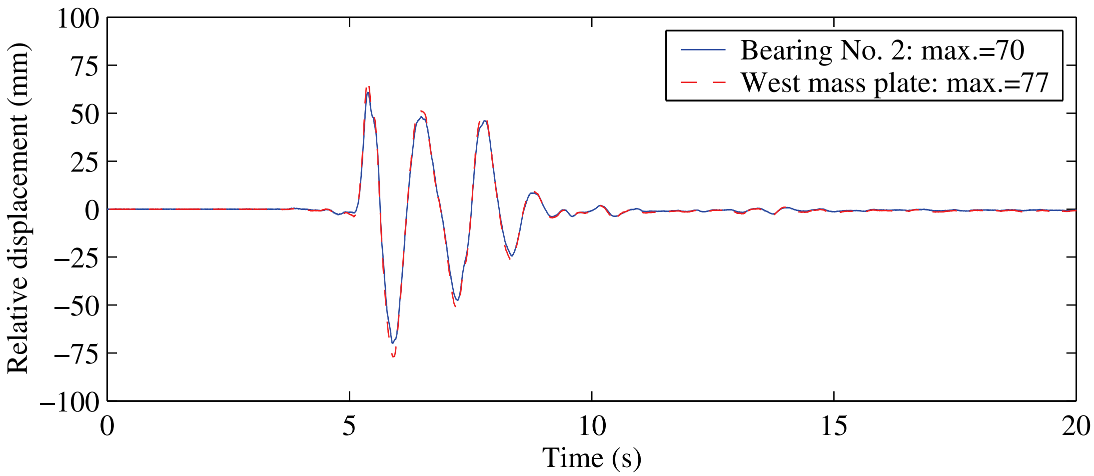

b. comparison of relative displacement responses: $y-$direction

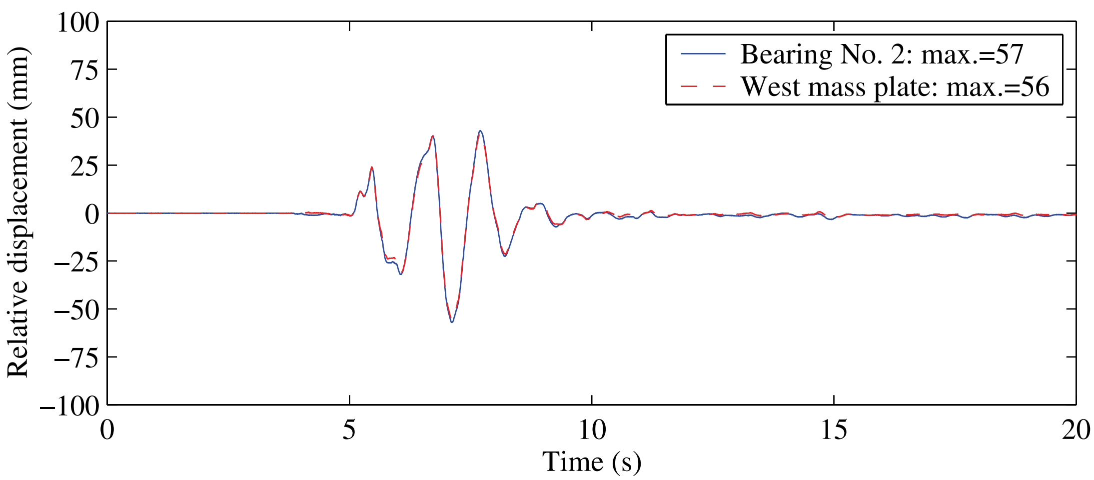

c. comparison of relative displacement responses: $x-$direction

FIGURE 7-12 Calculated relative displacement responses for LR bearings with a 1.2m support width and 75% SYL (Test 110)

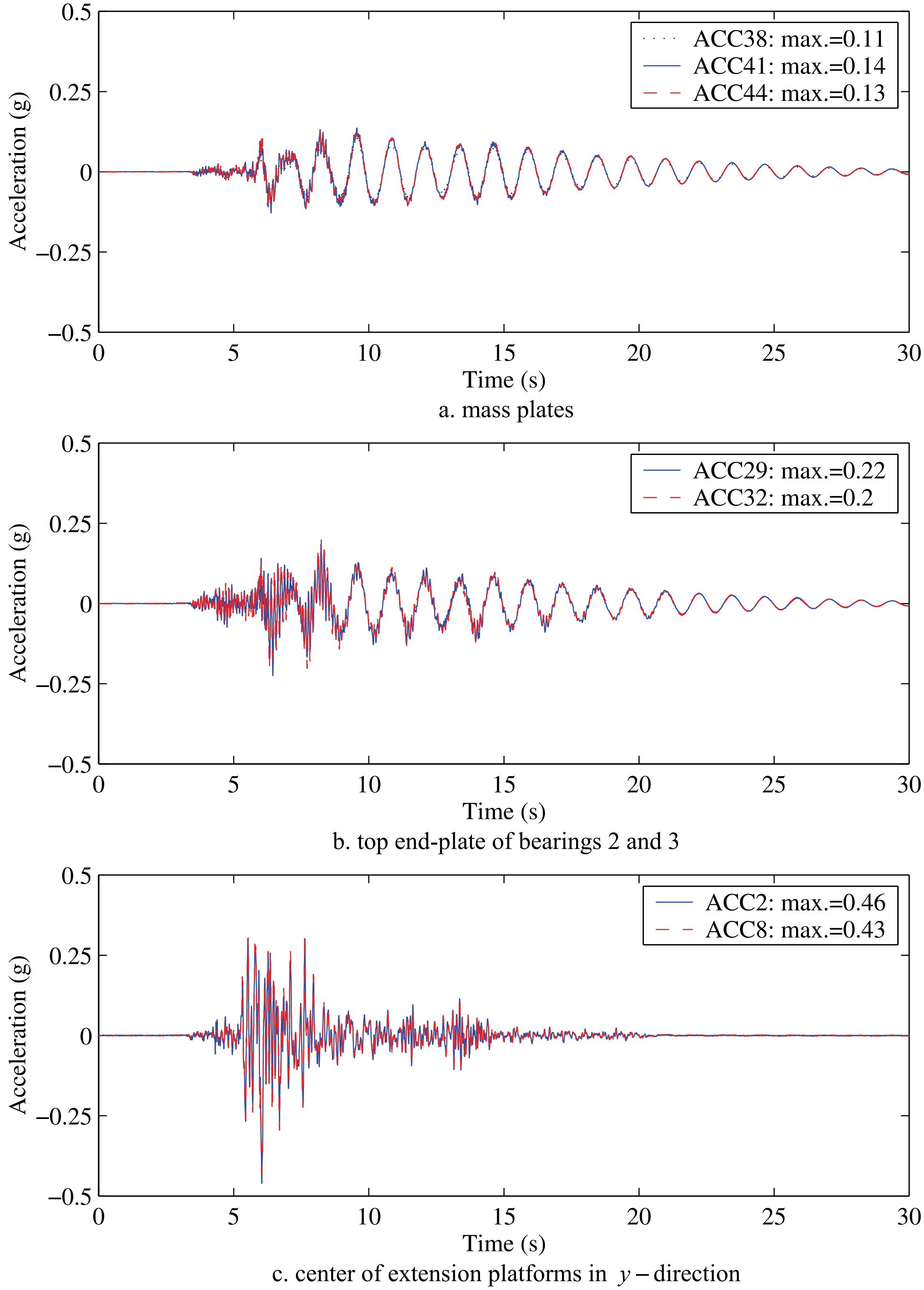

FIGURE 7-13 Recorded absolute acceleration responses for LDR bearings with a 1.2m support width and 100% RIO (Test 135)

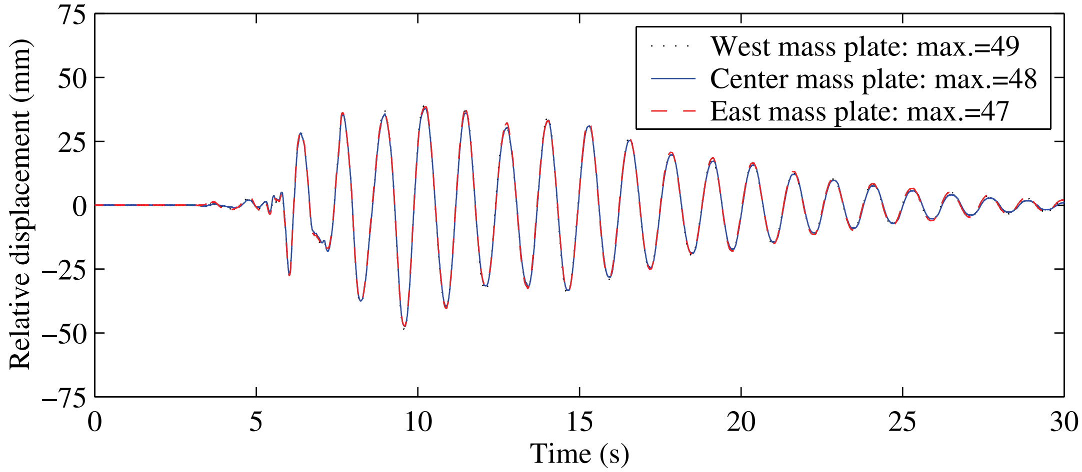

a. relative to simulator extension platforms: $y-$ direction

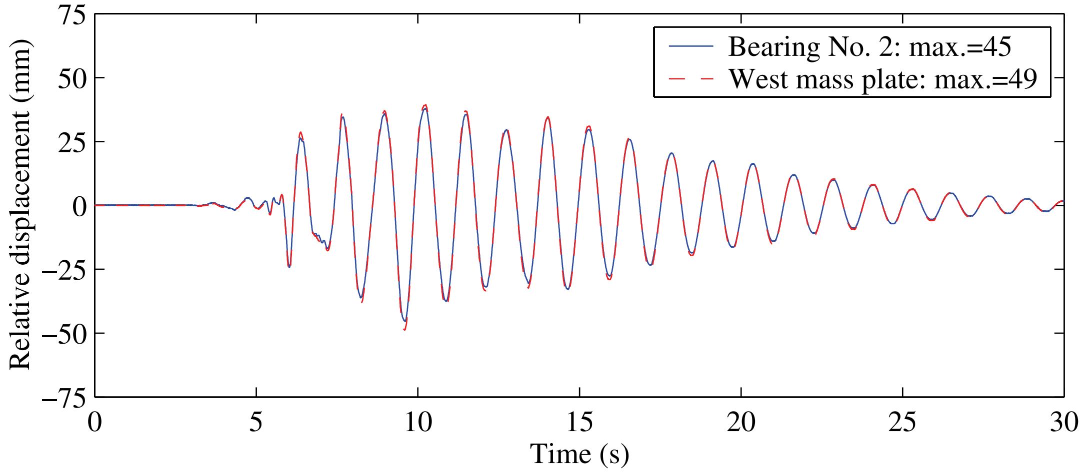

b. comparison of relative displacement responses: $y-$direction

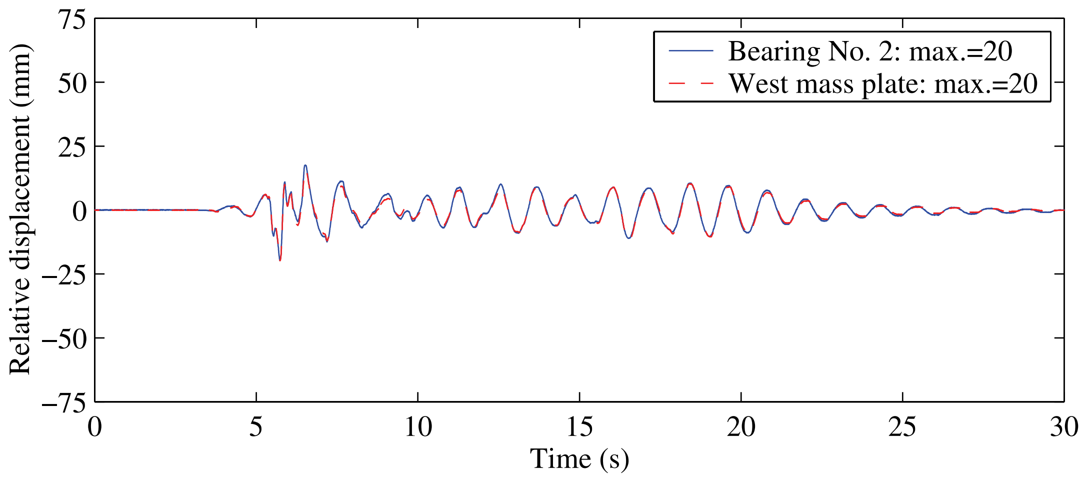

c. comparison of relative displacement responses: $x-$direction

FIGURE 7-14 Calculated relative displacement responses for LDR bearings with a 1.2m support width and 100% RIO (Test 135)

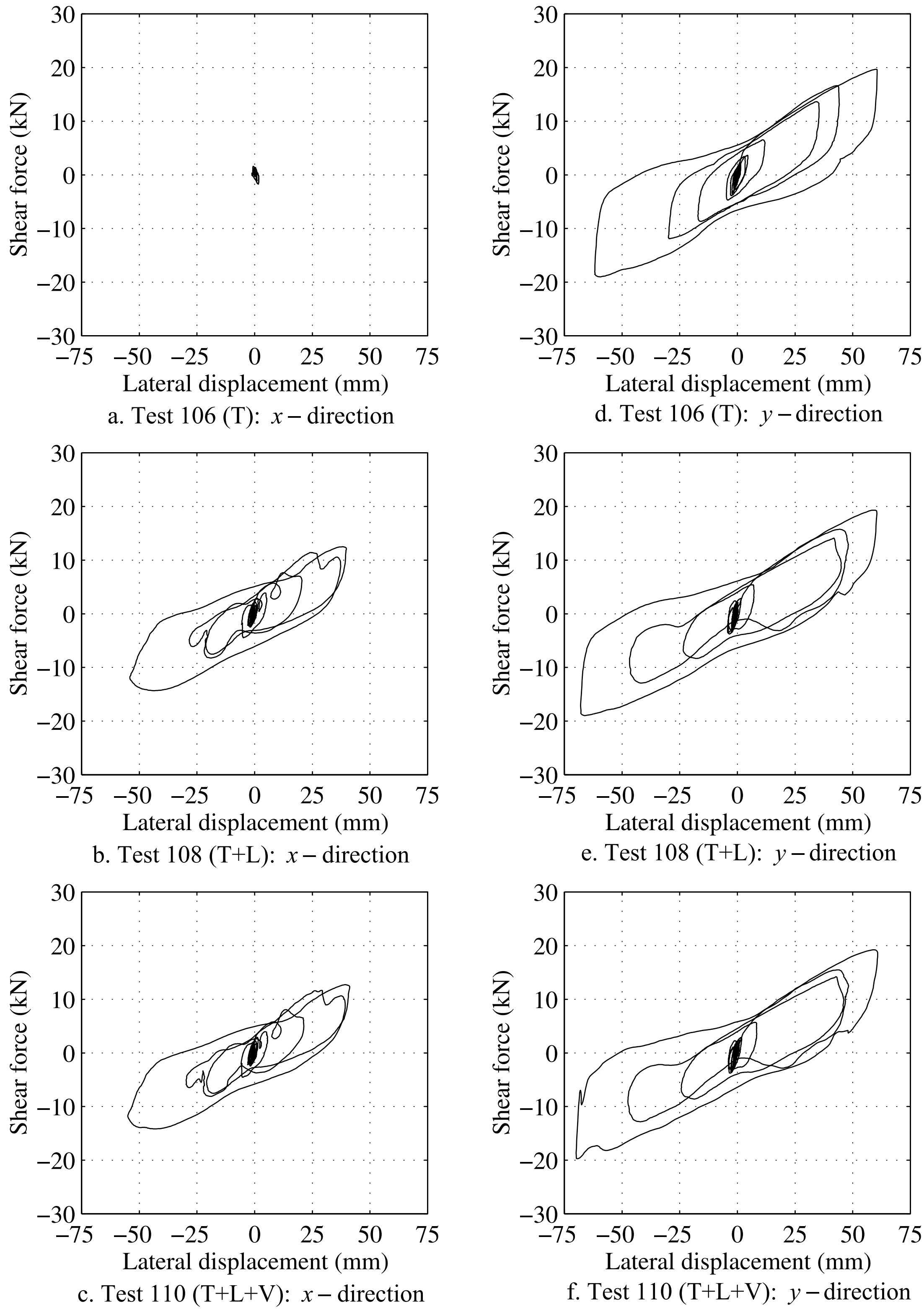

FIGURE 7-15 Shear force versus lateral displacement response of LR 1 for 75% SYL: Tests 106, 108 and 110

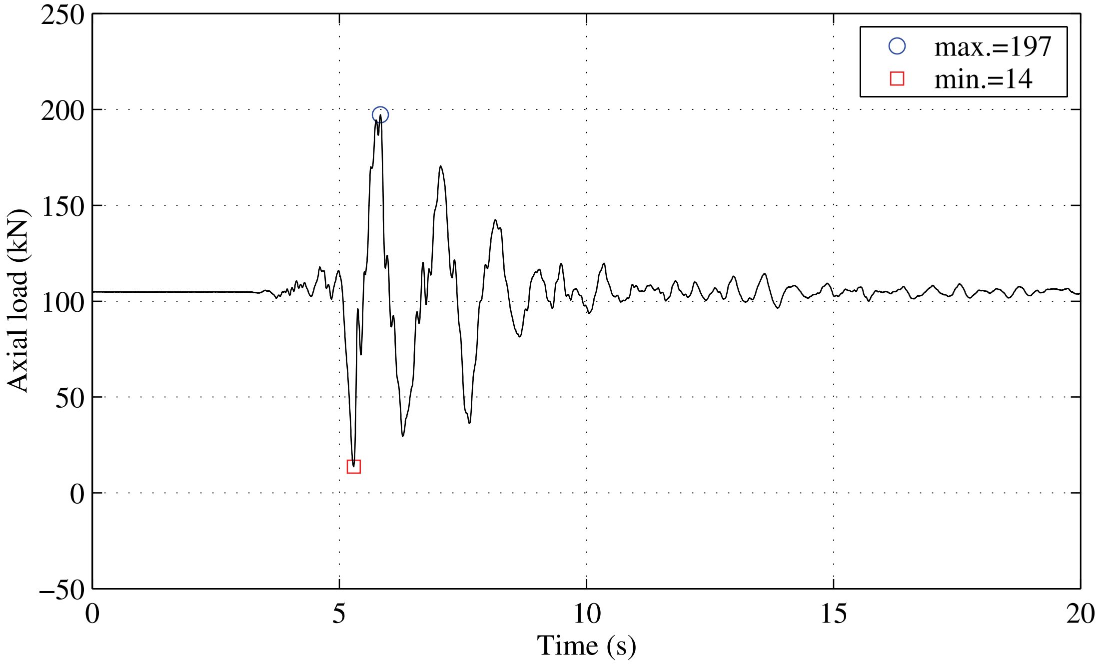

a. Test 108 (L+T)

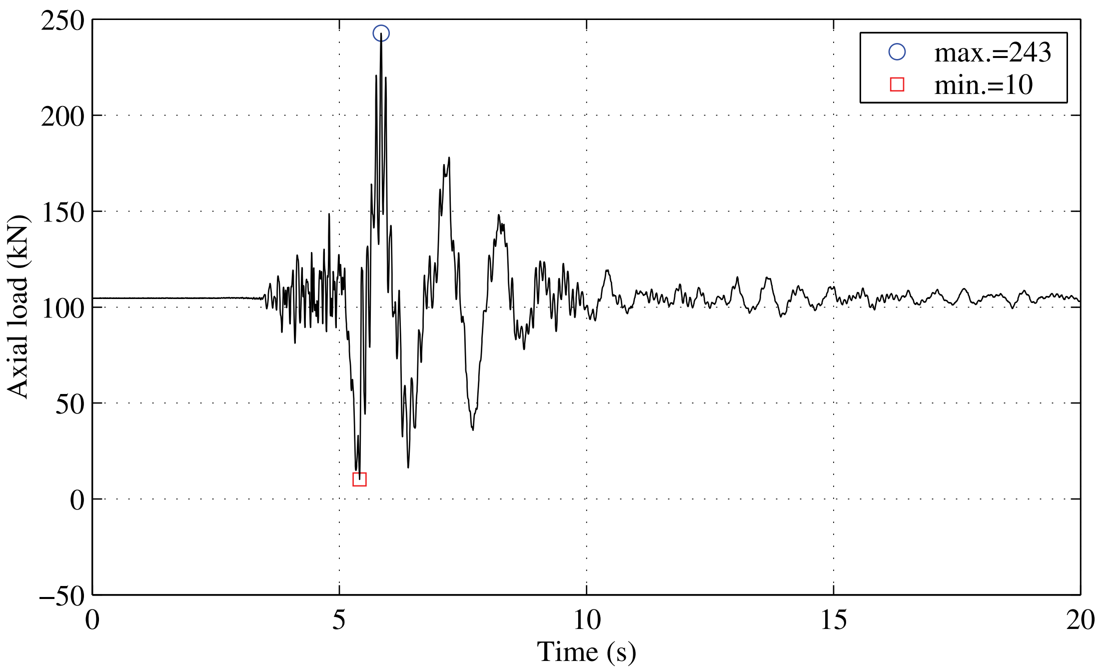

b. Test 110 (T+L+V)

FIGURE 7-16 Axial load response of LR 1 from Tests 108 and 110: SYL 75%

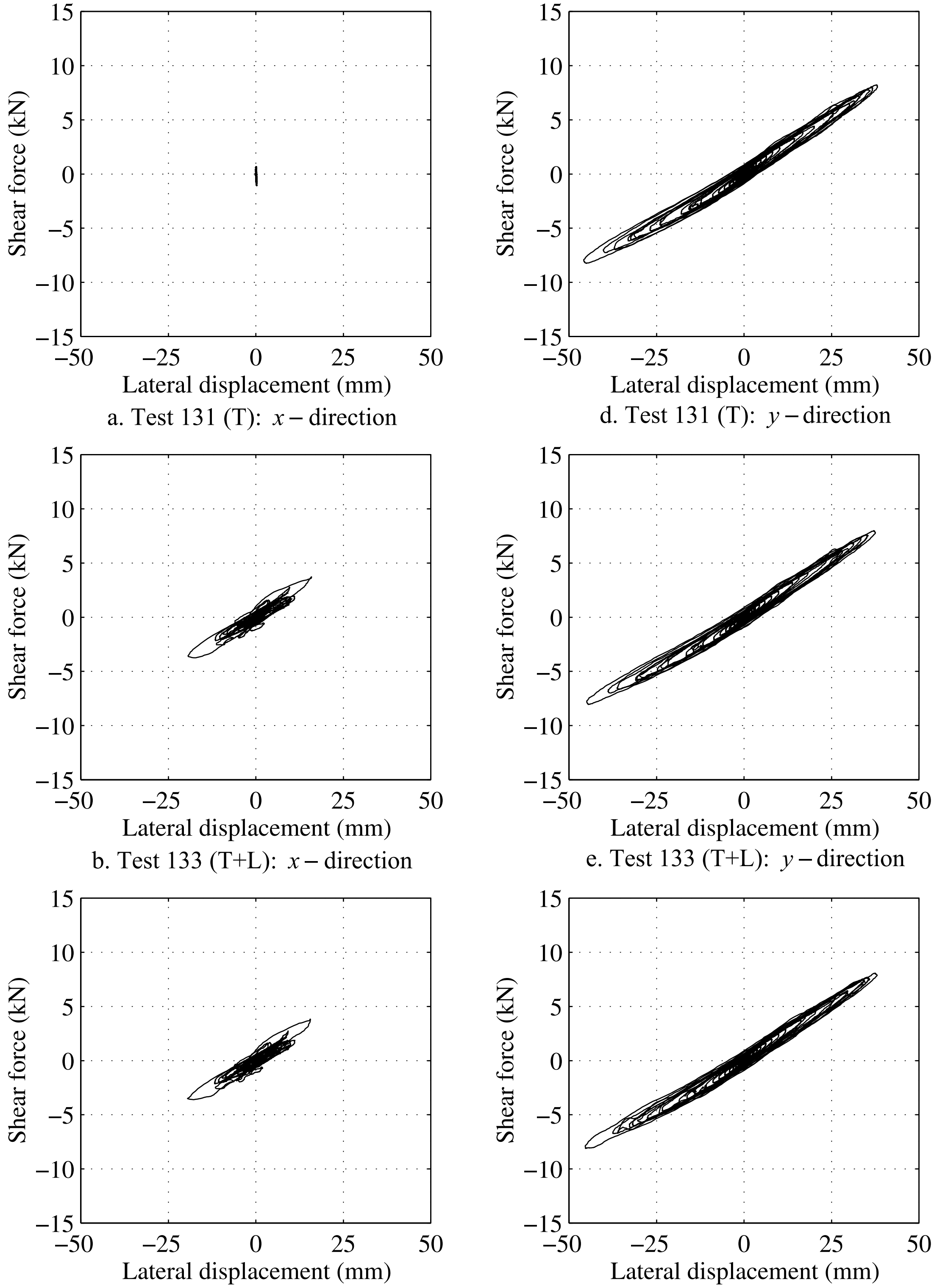

a. Test 131 (T): $x-$direction

d. Test 131 (T): $y-$direction

b. Test 133 (T+L): $x-$direction

e. Test 133 (T+L): $y-$direction

c. Test 135 (T+L+V): $x-$direction

f. Test 135 (T+L+V): $y-$direction

FIGURE 7-17 Shear force versus lateral displacement response of LDR 1 for 100% RIO: Tests 131, 133 and 135

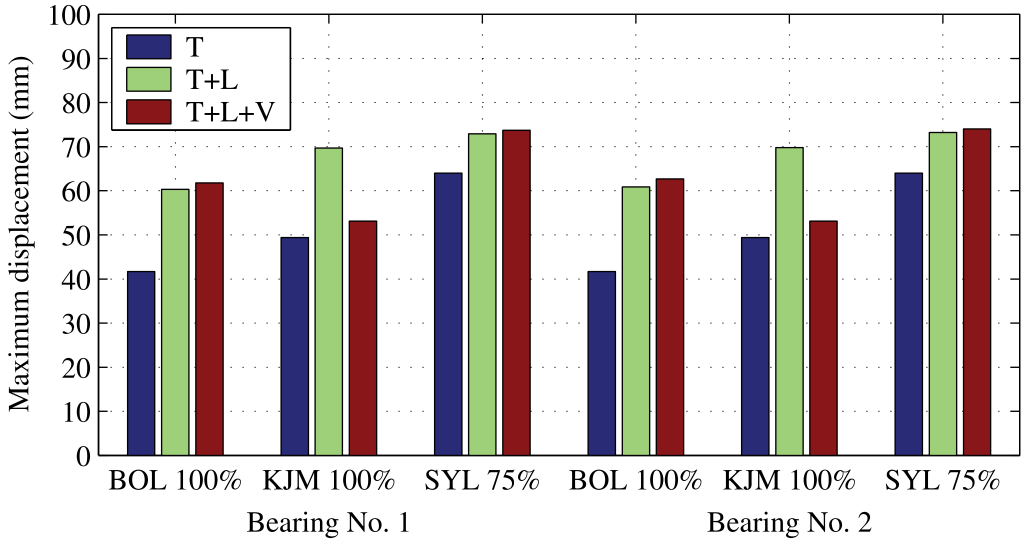

a. 1.8 m support width

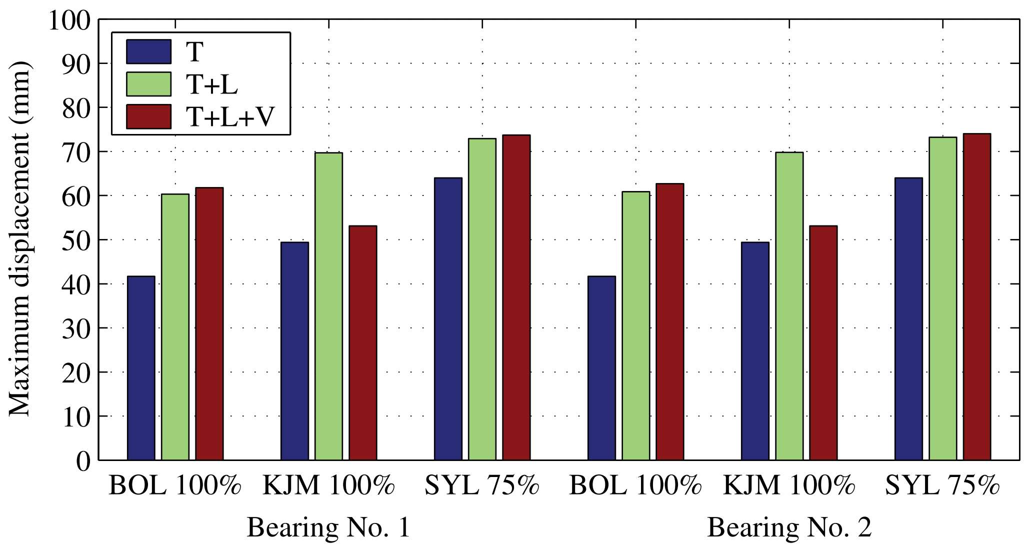

b. 1.2 m support width

FIGURE 7-18 Comparison of maximum horizontal displacement data from tests performed with LR bearings

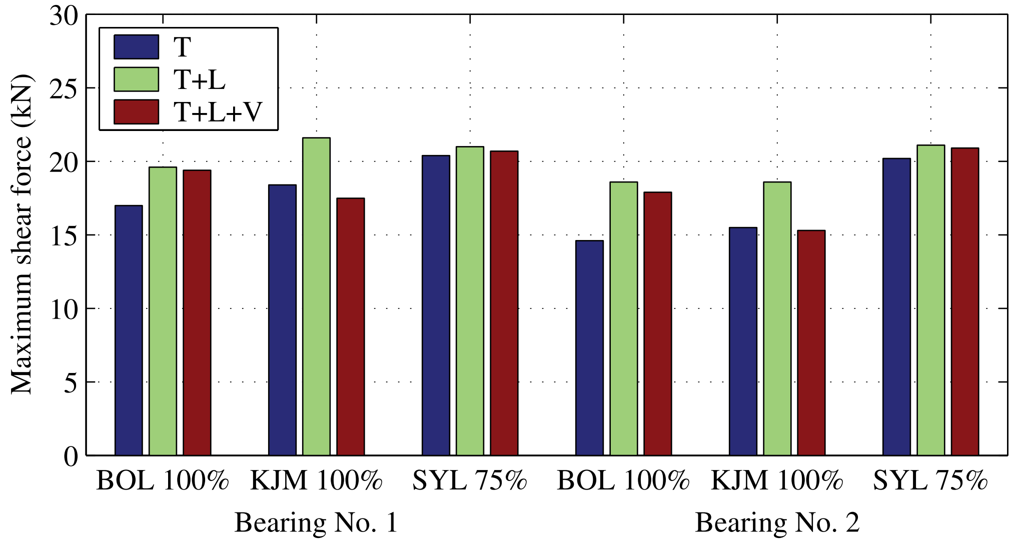

a. 1.8 m support width

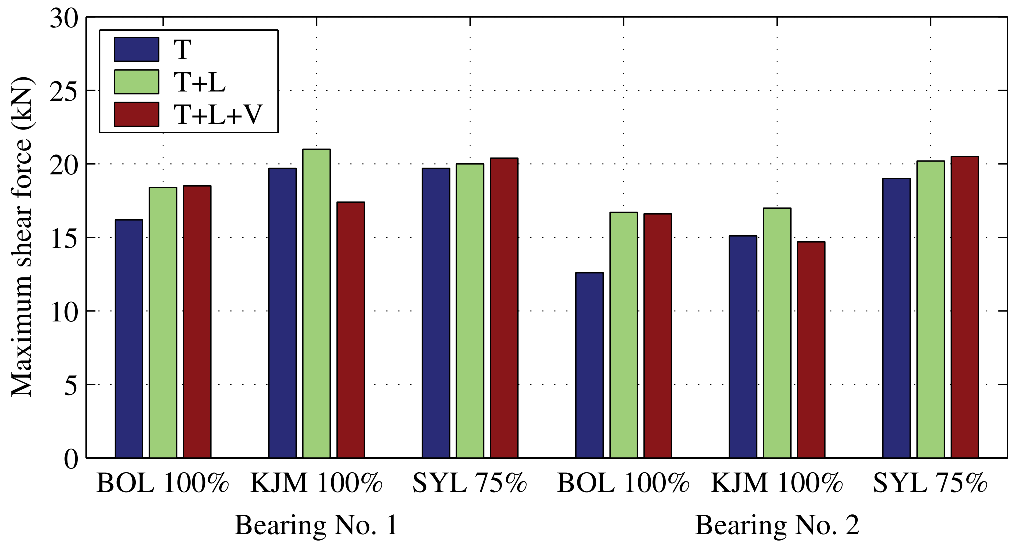

b. 1.2 m support width

FIGURE 7-19 Comparison of maximum horizontal shear force data from tests performed with LR bearings

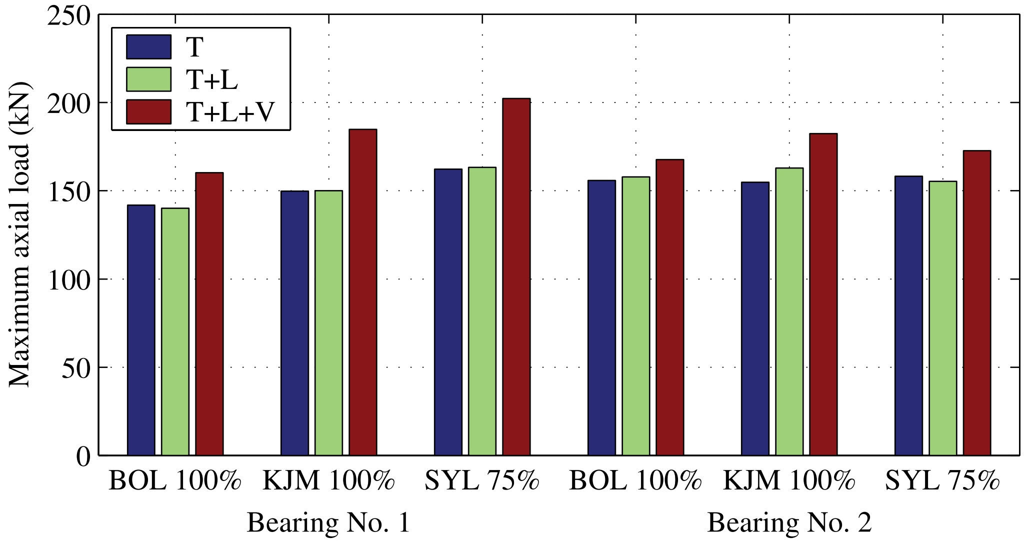

a. 1.8 m support width

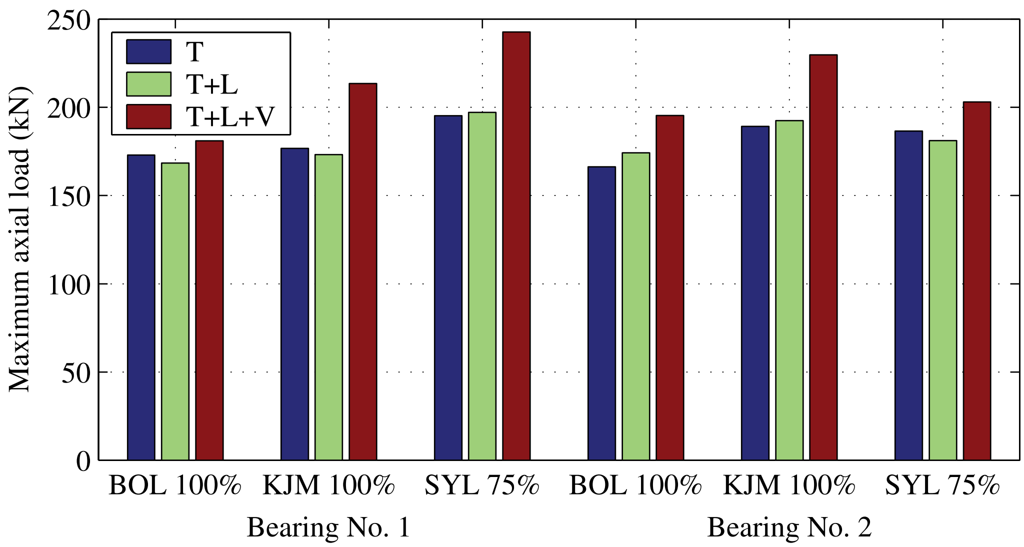

b. 1.2 m support width

FIGURE 7-20 Comparison of maximum axial load data from tests performed with LR bearings

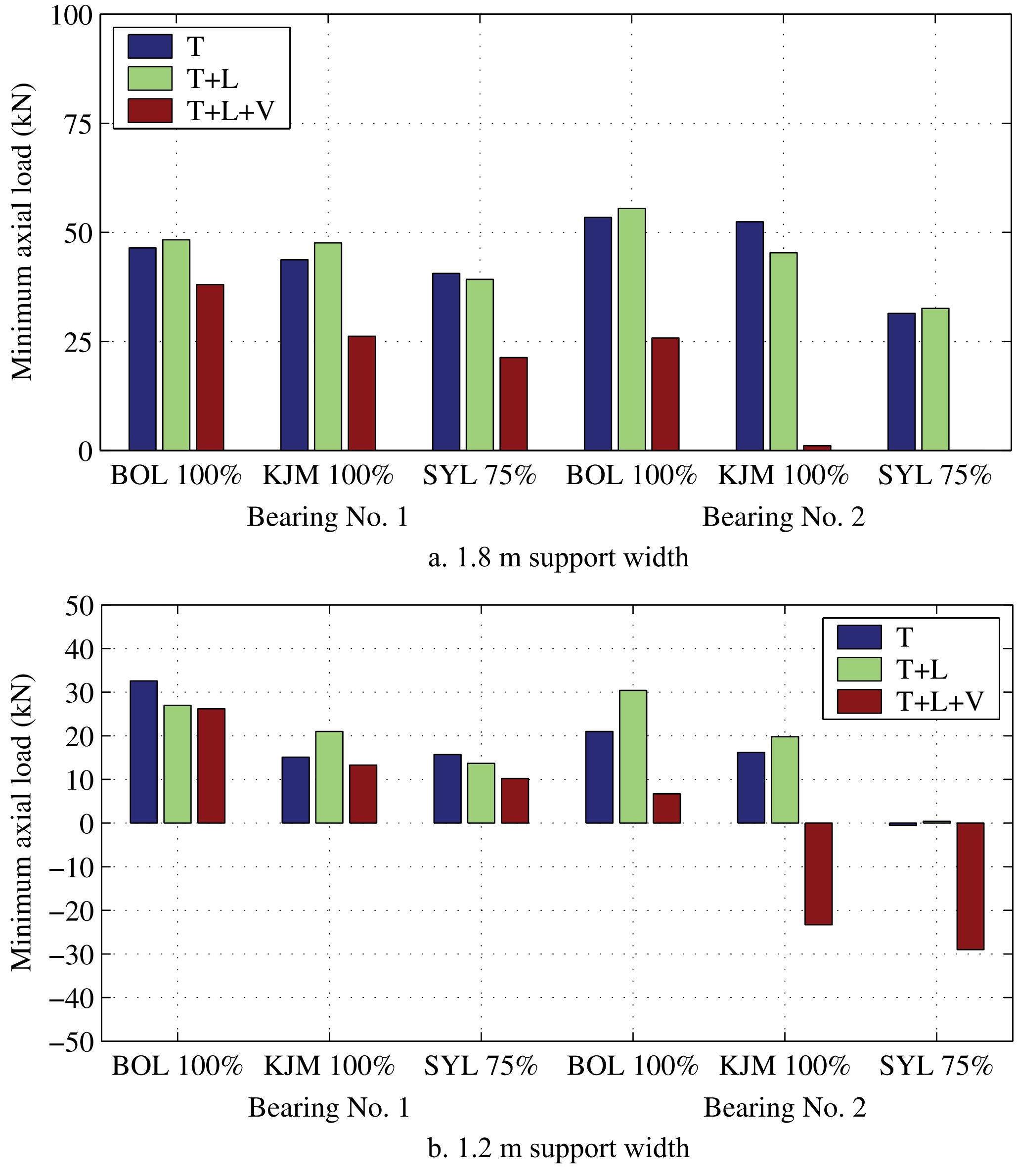

FIGURE 7-21 Comparison of minimum axial load data from tests performed with LR bearings

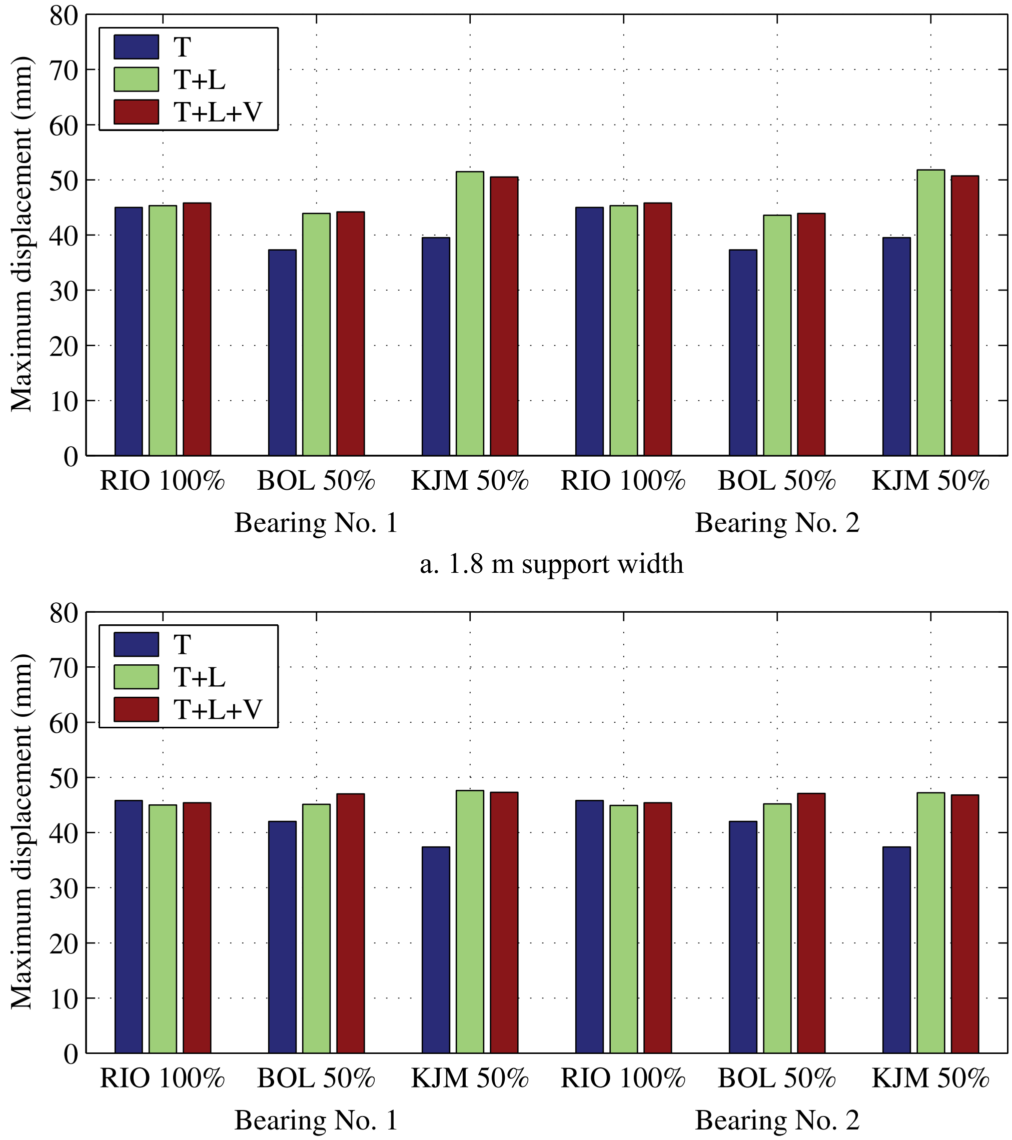

a. 1.8 m support width

b. 1.2 m support width

FIGURE 7-22 Comparison of maximum horizontal displacement data from tests performed with LDR bearings

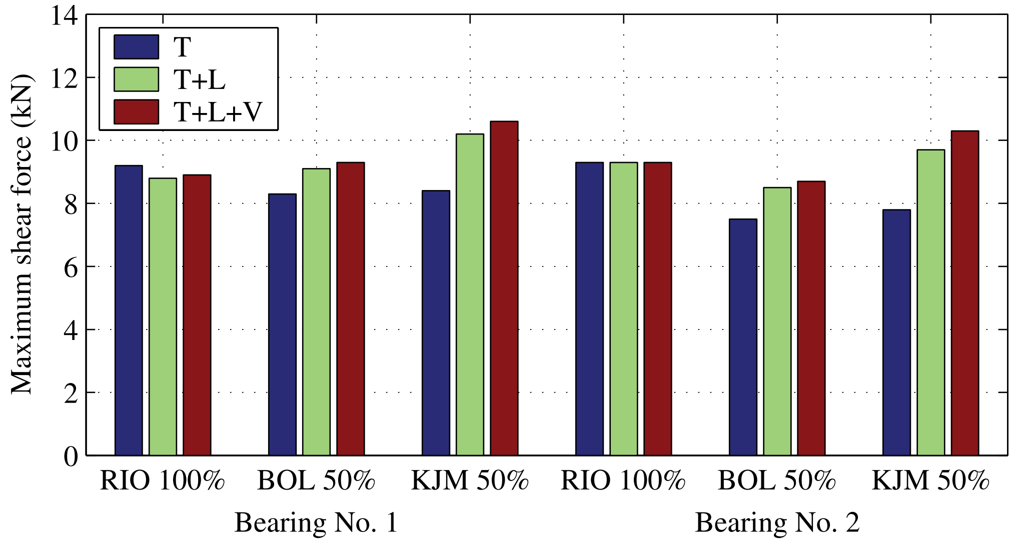

a. 1.8 m support width

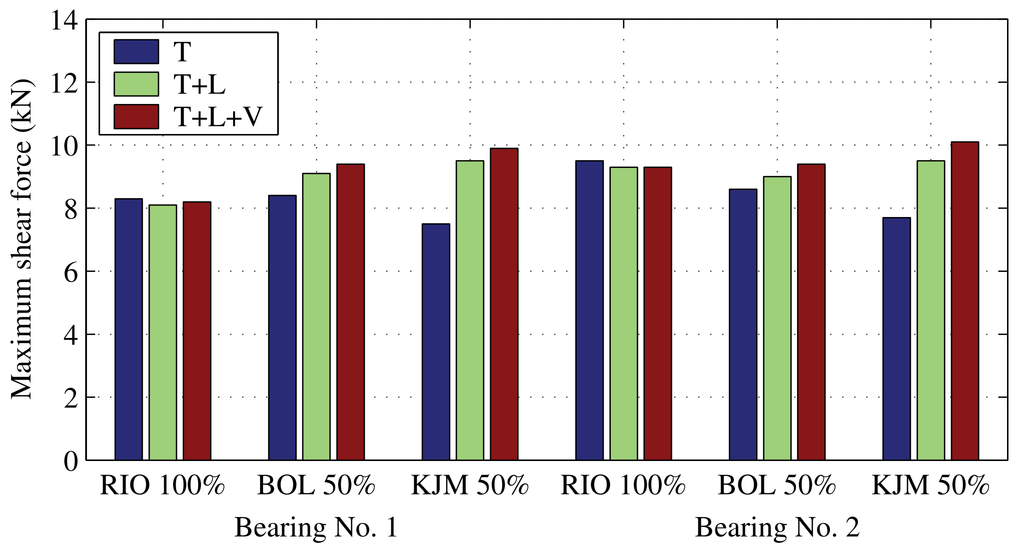

b. 1.2 m support width

FIGURE 7-23 Comparison of maximum horizontal shear force data from tests performed with LDR bearings

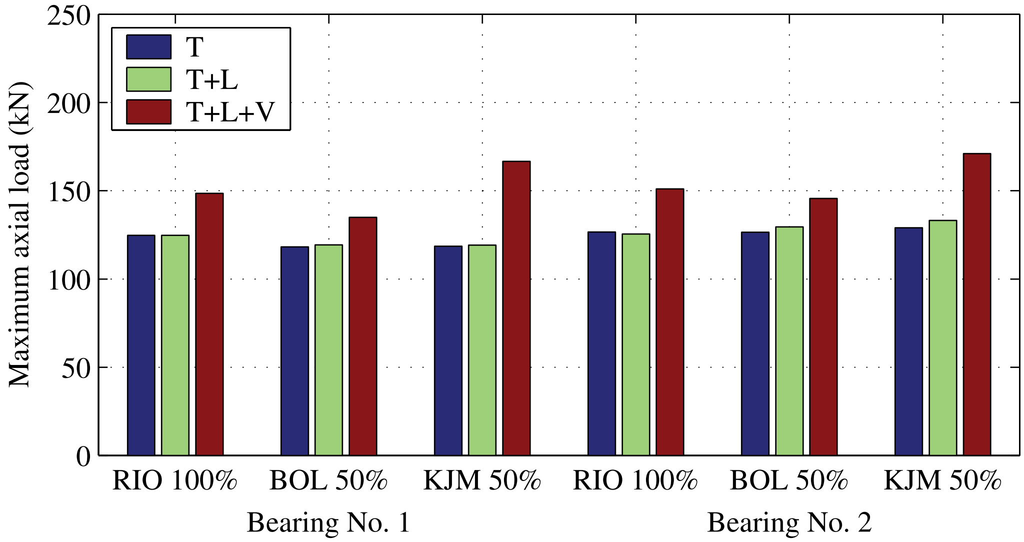

a. 1.8 m support width

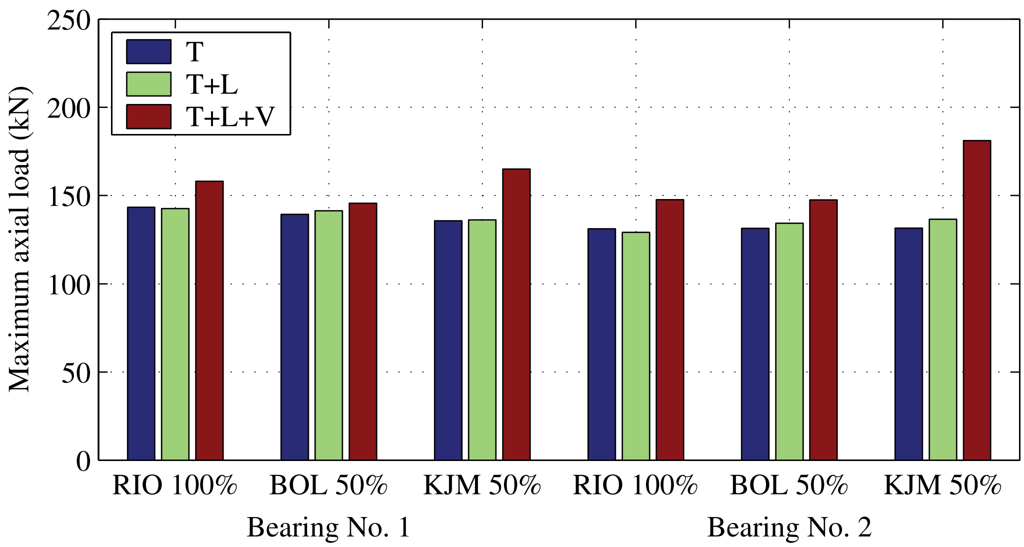

b. 1.2 m support width

FIGURE 7-24 Comparison of maximum axial load data from tests performed with LDR bearings

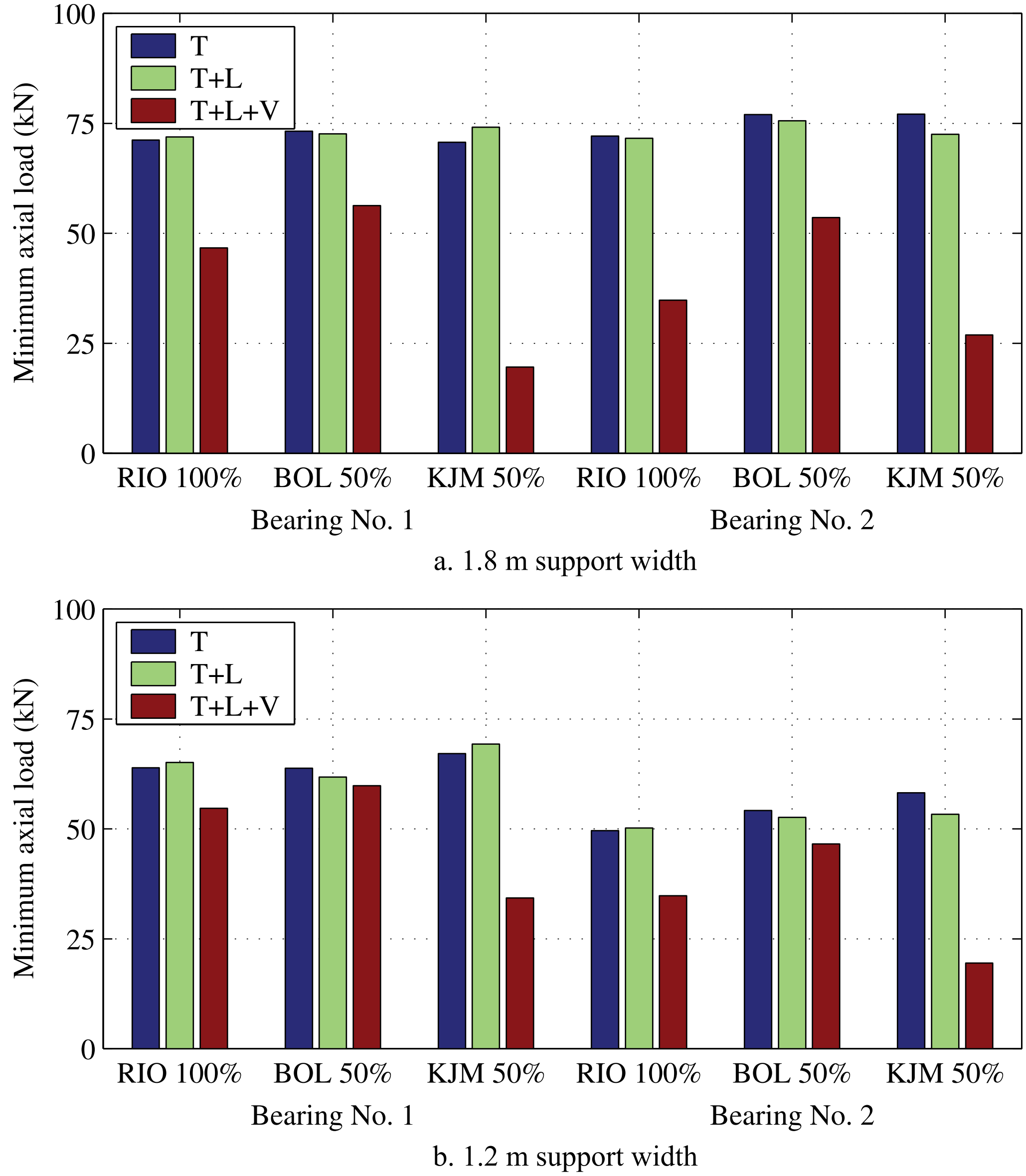

FIGURE 7-25 Comparison of minimum axial load data from tests performed with LDR bearings

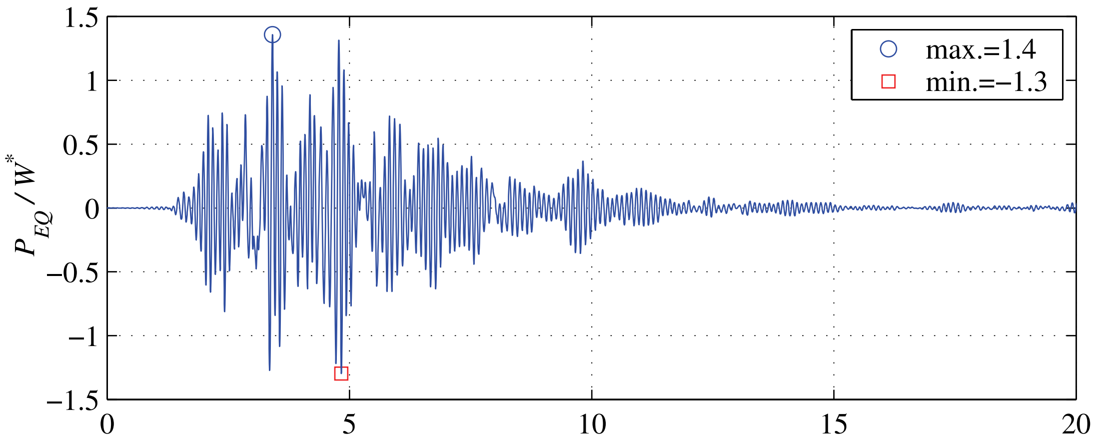

a. calculated P_{EQ} response normalized by W^*

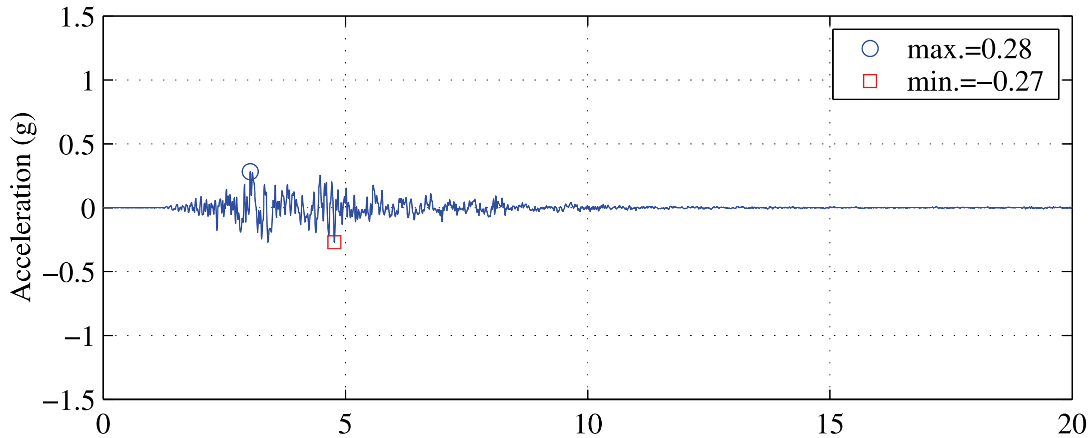

b. vertical acceleration recorded on east platform with ACC9

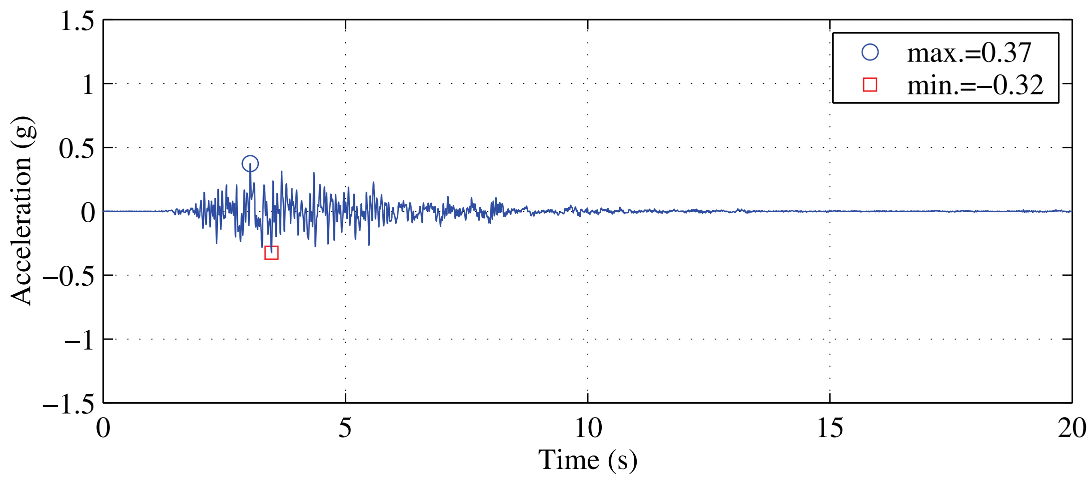

c. vertical acceleration recorded on west platform with ACC3

FIGURE 7-26 Normalized vertical load and recorded input accelerations with LR bearings and 100% KJM (Test 67)

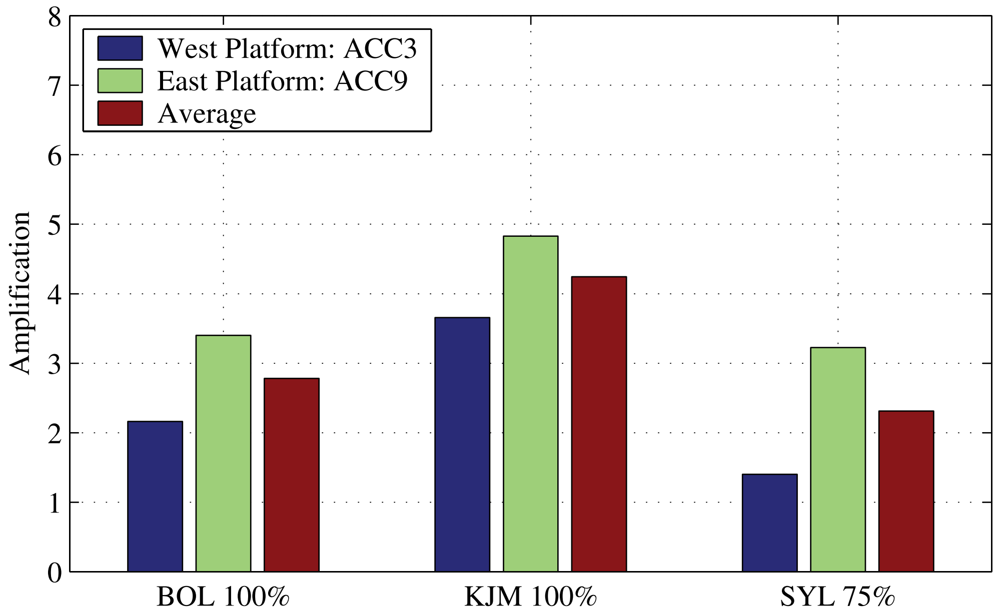

a. 1.8 m support width

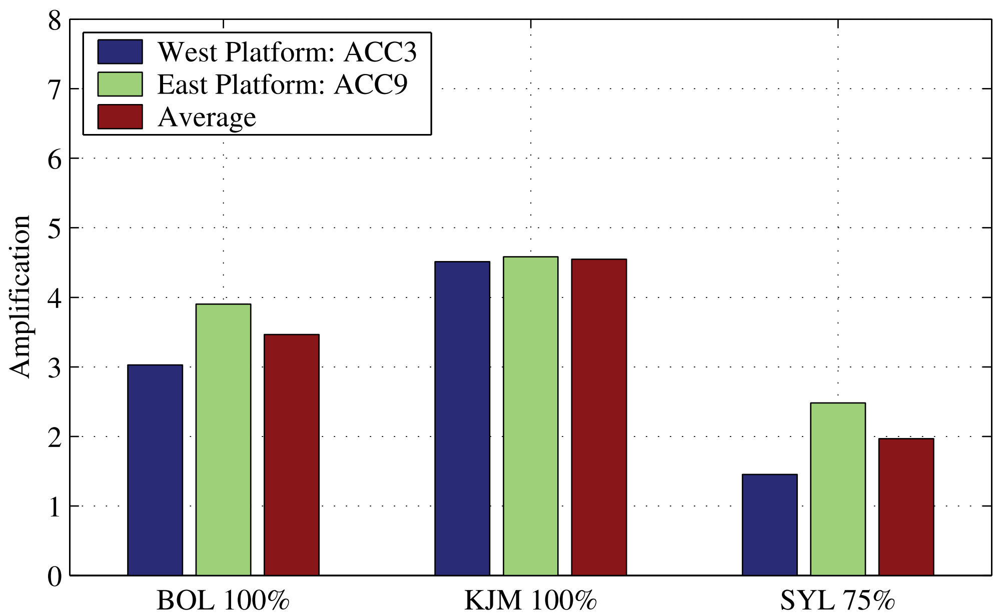

b. 1.2 m support width

FIGURE 7-27 Amplification factors from simulations performed with LR bearings

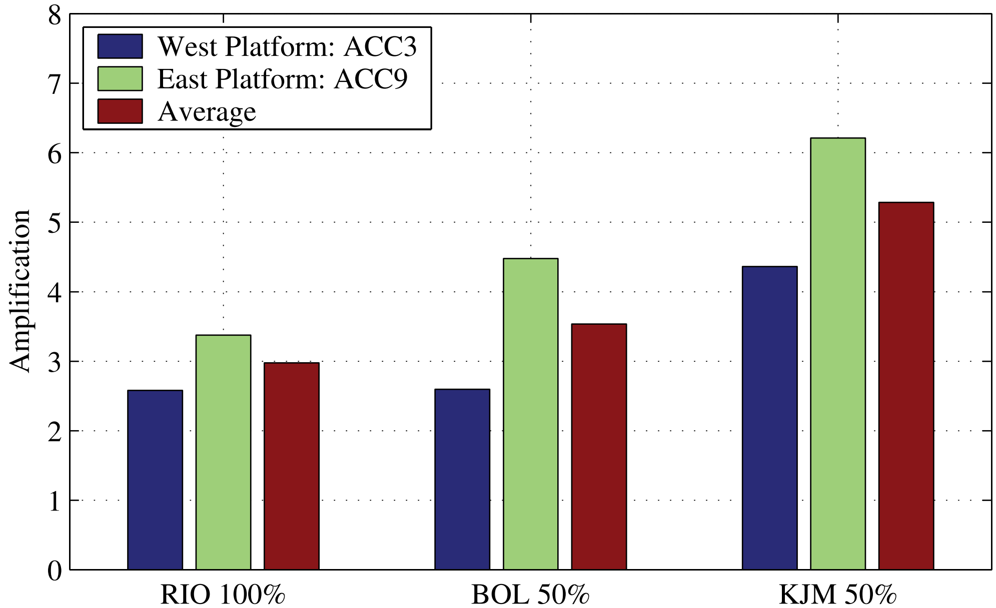

a. 1.8 m support width

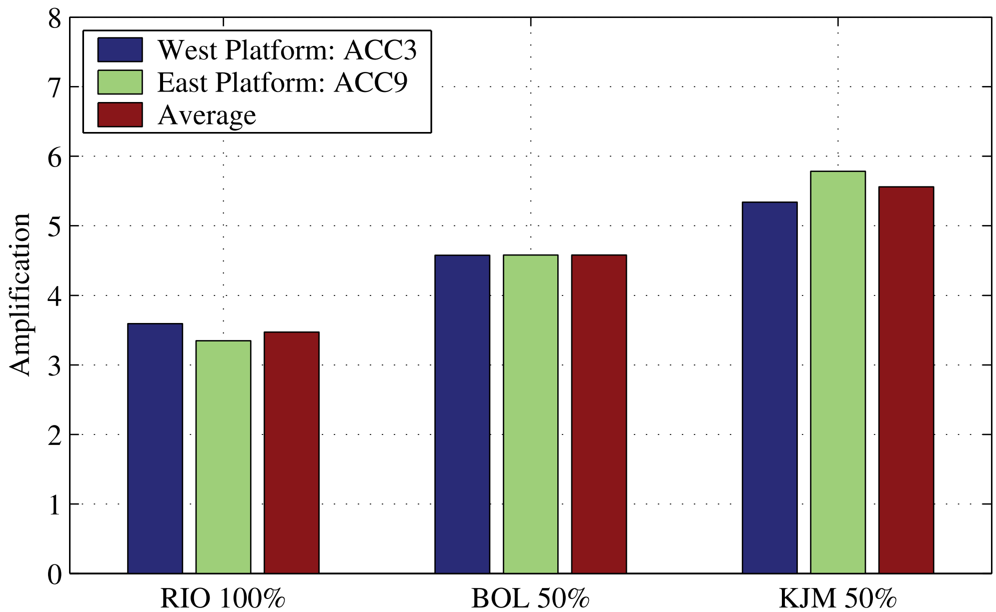

b. 1.2 m support width

FIGURE 7-28 Amplification factors from simulations performed with LDR bearings

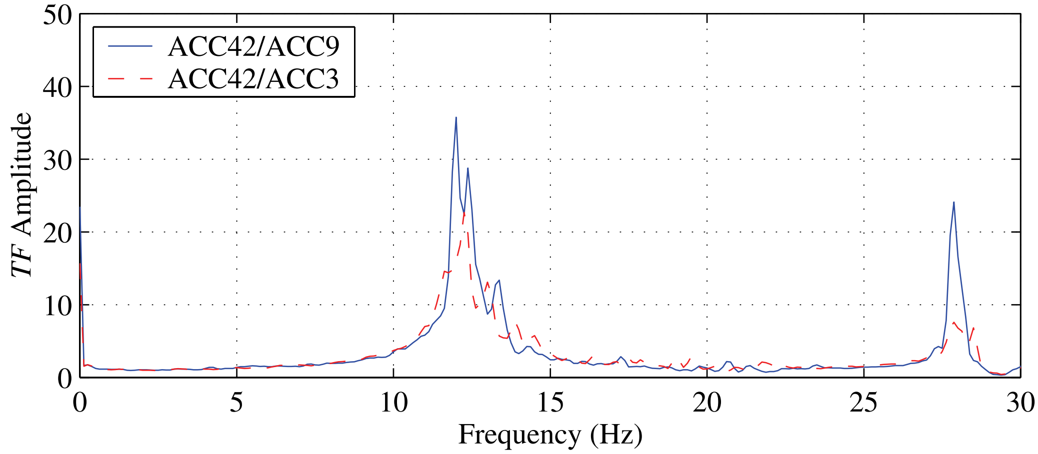

a. Test 150: fixed base white-noise

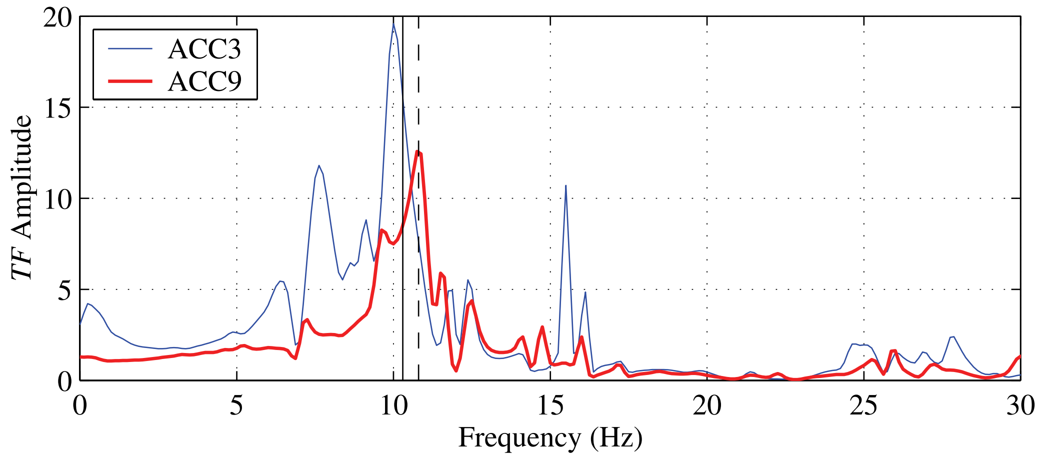

b. Test 67: LR KJM 100%

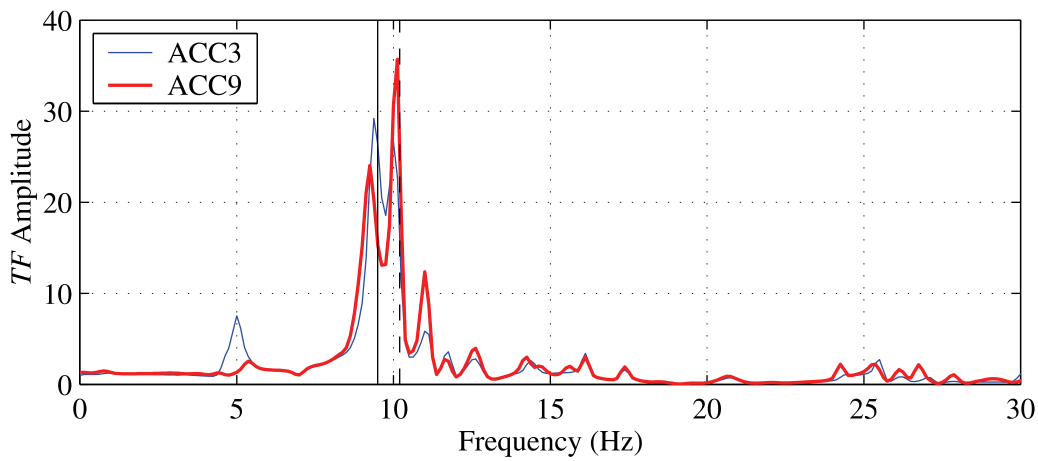

c. Test 147: LDR KJM 50%

FIGURE 7-29 Comparison of transfer function amplitudes from the vertical response of the truss-bridge in the fixed base, LR-isolated and LDR-isolated configurations

SECTION 8

FINITE ELEMENT ANALYSIS OF A LOW-DAMPING RUBBER BEARING

8.1 General

This section describes the development of a finite element (FE) model of the low-damping rubber (LDR) bearing(s) tested as part of this study and described in Sections 3, 5 and 7. The FE model was developed to further investigate the influence of lateral displacement on the vertical stiffness of the LDR bearings utilizing the finite element software package ABAQUS (HKS, 2004). A series of analyses was performed specifying various lateral displacements and vertical loading (identical to the lateral offset testing program described in Section 4) to determine the vertical force-displacement response of the LDR model from which the vertical stiffness was calculated. The normalized vertical stiffness results from the lateral offset analyses were used to further evaluate the validity of the two-spring formulation presented in Section 2. In addition, the results of FE analyses performed using experimentally determined values of the shear modulus and an assumed value of the bulk modulus are compared to the results of characterization tests performed on the LDR bearings to validate the FE model.

The remaining portions of this section are organized as follows. Section 8.2 presents a brief review of the finite element method and nonlinear analysis as it applies to the modeling of a LDR bearing. Section 8.3 describes the development of the FE model including; geometry, element selection, material models, boundary conditions and loading. Section 8.4 presents the results of various FE analyses (FEA) including; mesh selection, lateral offset and model validation. A summary is provided in Section 8.5.

8.2 Nonlinear Finite Element Analysis

A finite element model of the LDR bearing was developed to validate the two-spring model of Section 2 and to provide an independent computation of the vertical stiffness. Material nonlinearity is considered using a hyper-elastic material model (discussed in Section 8.3.4) that assumes nonlinear, elastic and isotropic material behavior and is characterized by an assumed strain energy density formulation. A mixed pressure-displacement formulation is used where displacement and pressure are independently interpolated (Bathe, 1996; HKS, 2004) to account for the nearly incompressible material behavior that is typical of natural rubber. The solution is obtained through incremental analysis in which an updated Lagrangian formulation is employed accounting for material, geometric and kinematic nonlinearities (Bathe, 1996). Newton's method is used to iterate displacement and pressure variables at each increment in the analysis (HKS, 2004).

8.3 Development of the LDR Model

8.3.1 General

This section describes various aspects associated with the development of a three-dimensional (3D) FE model of a low-damping rubber (LDR) bearing using the finite element package ABAQUS.

8.3.2 Geometry

The geometry of the FE model is based on the as-built dimensions and thicknesses of the LDR bearings as specified by the manufacturer. Although small differences between the as-built and actual dimensions were observed, specifically, the uniformity of the individual rubber layer thicknesses, these differences were not considered for the development of the FE model. Only one half of the bearing was modeled in 3D exploiting the symmetry of the bearing, boundary conditions and loading, thereby reducing the number of element and thus the computational effort required for each analysis. Therefore, the basic geometry of the FE model is one half of a hollow cylinder.

The dimensions of the FE model and the individual components comprising the bearing are as follows. In plan, the cylinder consists of an inner radius (R_i) and outer radius (R_o) equal to $15\ \text{mm}$ and $76\ \text{mm}$, respectively. In elevation, the model consists of 2 steel end-plates each $25\ \text{mm}$ thick forming the top and bottom surfaces, 20 intermediate rubber layers with thickness (t_r) equal to $3\ \text{mm}$ and 19 steel shim plates with thickness (t_s) also equal to $3\ \text{mm}$. Each steel shim plate is located between two intermediate rubber layers in an alternating fashion. The basic geometry of the FE model was discretized into three different mesh patterns to facilitate a mesh density analysis. Due to the circular geometry and to avoid large element aspect ratios, the nodes along the radial direction were spaced at a biased interval according to:

$$\Delta R = w \sum_{n=0}^{N} \frac{1}{b^n} \tag{8-1}$$

where ΔR is the annular width of the bearing equal to $R_o - R_i$, w is the radial width of the first element, N is the number of intermediate intervals (elements) in the radial direction and b is an additional parameter controlling the interval spacing. The value of b was chosen uniquely for each mesh to maintain an element aspect ratio (in plan) of approximately 1. Values of b along with the other parameters are presented in table 8-1 for each mesh pattern. Figure 8-1 presents illustrations of the three mesh patterns used for the mesh density analysis. A plan view of the half-section and a partial elevation view showing the top end-plate and the first few rubber layers is presented for each mesh pattern in this figure. For Mesh 1 (figure 8-1a), the model is discretized into 5 elements in the radial direction and at 20 degree increments in the circumferential direction. In elevation the end-plates and shim plates are discretized into a single element in thickness and the individual rubber layers are discretized into two elements in thickness, resulting in a total of $2,747$ elements. For Mesh 2 (figure 8-1b), the model is discretized into 10 elements in the radial direction and at 10 degree increments around the circumference. In elevation, the end-plates and shim plates are discretized into a single element in thickness whereas the rubber layers are discretized into four elements in thickness resulting in a total of $18,182$ elements. For Mesh 3 (figure 8-1c), the bearing is discretized into 20 element in the radial direction and at 5 degree increments in the circumferential direction. In elevation, the end-plates and shim plates are represented by a single element and the individual rubber layers by 4 elements in thickness, resulting in $72,722$ elements.

TABLE 8-1 Radial bias parameters for node geometry

Parameter and Units		Mesh		
		1	2	3
ΔR	(mm)	61.2	61.2	61.2
b	-	0.667	0.835	0.917
N	-	5	10	20
Elements	-	2,747	18,182	72,722

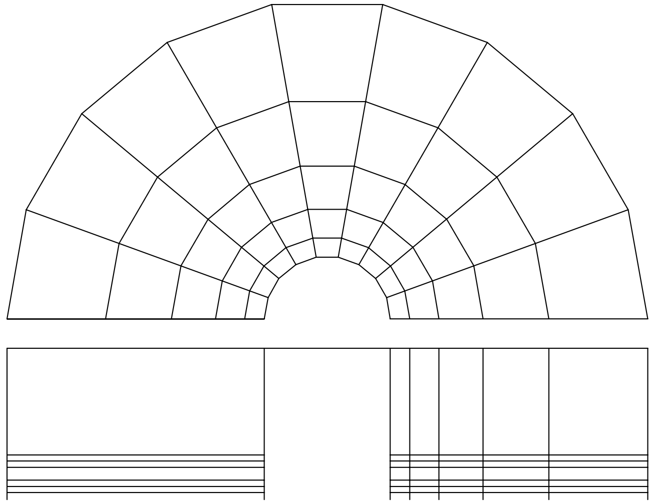

a. Mesh 1: 2,747 elements

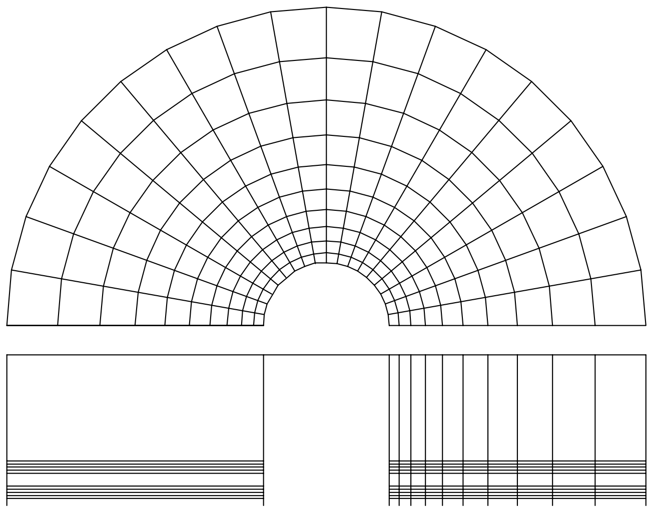

b. Mesh 2: 18,182 elements

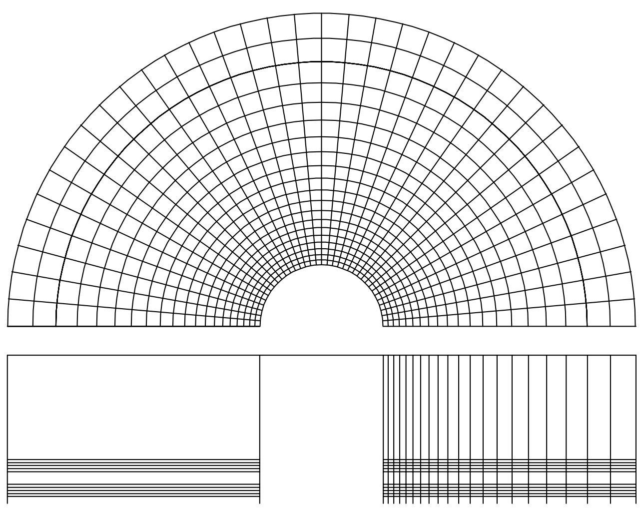

c. Mesh 3: 72,722 elements

FIGURE 8-1 Mesh patterns considered for the LDR model

8.3.3 Elements

Two different solid elements were selected from the ABAQUS element library and used to construct the FE model of the LDR bearing, specifically, one for the rubber material (C3D8H) and the other for the steel material (C3D8I). Both elements were chosen based on suitability to prevent locking, specifically, volumetric locking in the rubber due to the nearly incompressible behavior (large bulk modulus) and shear locking in the steel due to spurious shear stresses as a result of bending. The C3D8H element is an 8-node full integration mixed formulation solid element with linear displacement and constant pressure interpolation. With the C3D8H element, displacement and pressure are independently interpolated, however, the pressure interpolation is an order lower than the displacement interpolation to ensure nonlocking (Bathe, 1996). The C3D8I element is an 8-node full integration solid element with linear displacement interpolation that incorporates incompatible bending modes into the displacement formulation to eliminate spurious shear strains that might lead to shear locking (HKS, 2004; Cook et al., 2002).

8.3.4 Material Model

Vulcanized natural rubber is a nonlinear and nearly incompressible material. Under uni-axial tensile loading the stress-strain relationship is characterized by a high modulus of elasticity at low strain ($< 50\%$), a low modulus of elasticity at intermediate strain ($50 - 200\%$), and a high modulus of elasticity at high strain ($> 200\%$). Upon unloading the stress-strain response does not retrace the loading path but follows a similar slightly shifted path resulting in some un-recovered energy and a residual elongation at zero load. An illustration of the uni-axial stress-strain behavior of vulcanized natural rubber in both tension and compression is presented in figure 8-2 (Stanton and Roeder, 1982). This particular specimen was taken to failure with a corresponding elongation at break of approximately 500% strain. Typically, the bulk modulus is several thousand times larger than the shear modulus resulting in a Poisson's ratio (ν) ranging from 0.4985 to 0.4999 (Stanton and Roeder, 1982), with $\nu = 0.5$ being incompressible. The bulk modulus is defined as:

$$K = -\frac{p}{\Delta V / V} \tag{8-2}$$

where p is the hydrostatic pressure, ΔV is the change in volume and V is the initial volume. However, for lightly filled (low-damping) natural rubber the value of the bulk modulus typically ranges from $2000\,\text{MPa}$ to $2500\,\text{MPa}$.

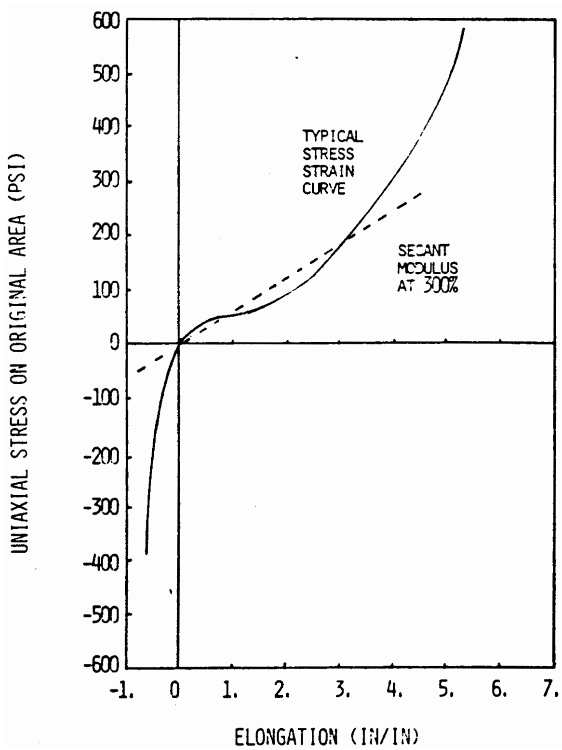

FIGURE 8-2 Illustration of uni-axial stress-strain curve for natural rubber (source: Stanton and Roeder, 1982)

A hyper-elastic material model was chosen to represent the rubber portion of the LDR bearing with ABAQUS. This model assumed elastic, nonlinear, isotropic material behavior and is defined by an assumed strain energy density potential (HKS, 2004). For this study, the neo-Hookean form of the strain energy potential was selected that requires two parameters, both directly related to engineering material parameters, namely, the shear modulus and the bulk modulus. The neo-Hookean form of the strain energy potential per unit volume as implemented in ABAQUS (HKS, 2004) is given by:

$$W_0 = C_{10}\left(\bar{I}_1 - 3\right) + \frac{1}{D_1}(J-1)^2 \tag{8-3}$$

where C_{10} and D_1 are strain independent material constants, $\bar{I}_1$ is the first (deviatoric) strain invariant and J is the total volume ratio. The material constants C_{10} and D_1 are related to the shear modulus (G) and bulk modulus (K) according to:

$$C_{10} = \frac{G}{2} \tag{8-4}$$

$$D_1 = \frac{2}{K} \tag{8-5}$$

and $\bar{I}_1$ is defined as:

$$\bar{I}_1 = \bar{\lambda}_1^2 + \bar{\lambda}_2^2 + \bar{\lambda}_3^2 \tag{8-6}$$

where $\bar{\lambda}_i$ are the deviatoric stretch ratios equal to $J^{-1/3}\lambda_i$ and λ_i is the ith principle stretch ratio defined as:

$$\lambda_i = 1 + \varepsilon_i \tag{8-7}$$

where ε_i is the principle strain in the $i-$direction. Although more robust strain energy potential formulations are available with ABAQUS (refer to HKS, 2004) accounting for non-constant shear modulus (Mooney-Rivlin) and stiffening at high shear strains (Ogden), these formulations require additional material constants that need to be determined through multiple material tests.

Table 8-2 presents, assumed and experimentally determined, material properties and calculated strain energy potential parameters used for the various analyses. Because the mesh density and lateral offset analyses were conducted prior to testing of the LDR bearings, typical values of the shear modulus and bulk modulus for low-damping natural rubber were assumed: 0.69 MPa (100 psi) and 1999 MPa ($290{,}000\text{ psi}$), respectively. Because the shear modulus of natural rubber is not strain-independent as assumed in the neo-Hookean formulation, two bounding values were estimated from the experimental data for the validation analyses. Both shear moduli represent tangent values and were estimated from the force response at zero shear strain (initial shear modulus) and 100% rubber shear strain from the force-displacement response of LDR 5M (M indicates cover was lathed down to 3 mm, see Section 5) subjected to uni-directional shear to a maximum shear strain amplitude of 150% with an axial (compressive pressure) of 3.45 MPa (500 psi). The initial and 100% shear strain tangent moduli were estimated to be 0.83 MPa (122 psi) and 0.72 MPa (104 psi), respectively. The shear strain amplitude of 100% represents the approximate average shear strain in an individual rubber layer due to a compressive load of 180 kN and was estimated as follows. The maximum shear strain in a hollow circular pad is calculated according to (Constantinou et al., 1992):

$$\gamma_{\max} = 6S\varepsilon_c f_{st} \tag{8-8}$$

where S is the shape factor equal to 10.2, f_{st} is an amplification factor to account for the central hole equal to 1.63 for the LDR geometry and ε_c is the compressive strain due to a compressive load of $180\,\mathrm{kN}$ obtained from the results of an axial load test performed on LDR 5 and equal to 3.1%. The average shear strain was estimated as:

$$\gamma_{\mathrm{avg}} = \frac{1}{3}\gamma_{\max} \tag{8-9}$$

which assumes a triangular distribution of shear strain in the radial direction, a reasonable approximation of the actual strain distribution, determined to be 103%. Experimental determination of the bulk modulus of rubber is a difficult task requiring special testing capabilities including a tri-axial testing apparatus and the ability to measure (very small) changes in volume. Access to such an apparatus was not possible during this study, therefore a value typical of Durometer A, Hardness 50 natural rubber was assumed. Values typically range from 2000 to $2500\,\mathrm{MPa}$. To investigate the sensitivity of the solution to the assumed value, three additional FE analyses were performed with K equal to $2000\,\mathrm{MPa}$, $2500\,\mathrm{MPa}$, and infinity ($D_1 = 0\,\mathrm{mm}^2/\mathrm{N}$). The results of these analyses are presented in Section 8.4.4 and show little change in the solution for values of K between $2000\,\mathrm{MPa}$ and $2500\,\mathrm{MPa}$.

The steel components of the LDR bearing were modeled using a simple linear elastic formulation with parameters E (Young's modulus) and ν (Poisson's ratio) assumed to be $200{,}000\,\mathrm{MPa}$ and 0.3, respectively. Although, these material parameters were assumed, the values are typical of hot rolled mild carbon steel from which the internal shim plates (ASTM A1011 Gr. 36) and internal end-plates (ASTM A36) were fabricated.

TABLE 8-2 Material properties and strain energy potential parameters

Type of Analysis	G (MPa)	K (MPa)	C_{10} (MPa)	D_1 (mm^2/N)
Mesh density	0.69	1999	0.345	0.001
Lateral offset	0.69	1999	0.345	0.001
Validation	0.83[1]	1999	0.414	0.001
	0.72[2]	1999	0.36	0.001

Notes:
1. Initial tangent modulus for LDR 5M
2. Tangent modulus at 100% rubber shear strain for LDR 5M

8.3.5 Boundary Conditions

The boundary conditions of the FE model were intended to replicate (within reason) the boundary conditions of the bearings in the single bearing testing machine (SBTM) during characterization and lateral offset testing (see, Section 4). In the SBTM the bottom bearing end-plate is connected to the 5-channel reaction load cell by four bolts providing a fixed-type condition, i.e., restrained translation and rotation in each direction (see figure 4-1). The top bearing end-plate is connected to the loading beam of the SBTM again using four bolts, and with the aid of hydraulic actuation, applies unidirectional shear and axial load to the bearing specimen. In addition, the SBTM control system is designed such that under normal operation (see, Section 4) the loading beam remains level as it translates horizontally. Figure 8-3 presents an illustration of a bearing in the un-deformed (figure 8-3a) and the deformed (figure 8-3b) configuration highlighting the boundary conditions assumed for the FE model, namely, fixed at the bottom end-plate and free to translate in the $1-$ and $3-$directions at the top end-plate.

To apply the prescribed boundary conditions to the FE model the degrees-of-freedom (DOFs) of the nodes located on the top and bottom end-plate surfaces were constrained to a control node located at the centroid of the corresponding half-section. Figure 8-4 presents a rendering of the FE model (Mesh 2) in the un-deformed configuration that shows the top end-plate surface, the cut surface and the global coordinate system. The control node (centroid) is located along the $2-$axis (see figure 8-4) at a radial distance of $33.38\,\mathrm{mm}$ from the center. For the top control node, translation in the $2-$direction and rotation about the $2-$axis were restrained. All DOFs of the base control node (3 translational and 3 rotational) were restrained to create a fixed condition. Because one half of the bearing is being modeled an additional restraint is required to prevent the intermediate rubber layers from bulging on the cut surface (normally restrained by the other half) and to prevent torsion due to lateral loading and small differences between the calculated centroid (using analytical curves) and the actual centroid of the discretized surface. To account for this in the FE model, all nodes located on the cut surface were restrained from translating in the $2-$direction.

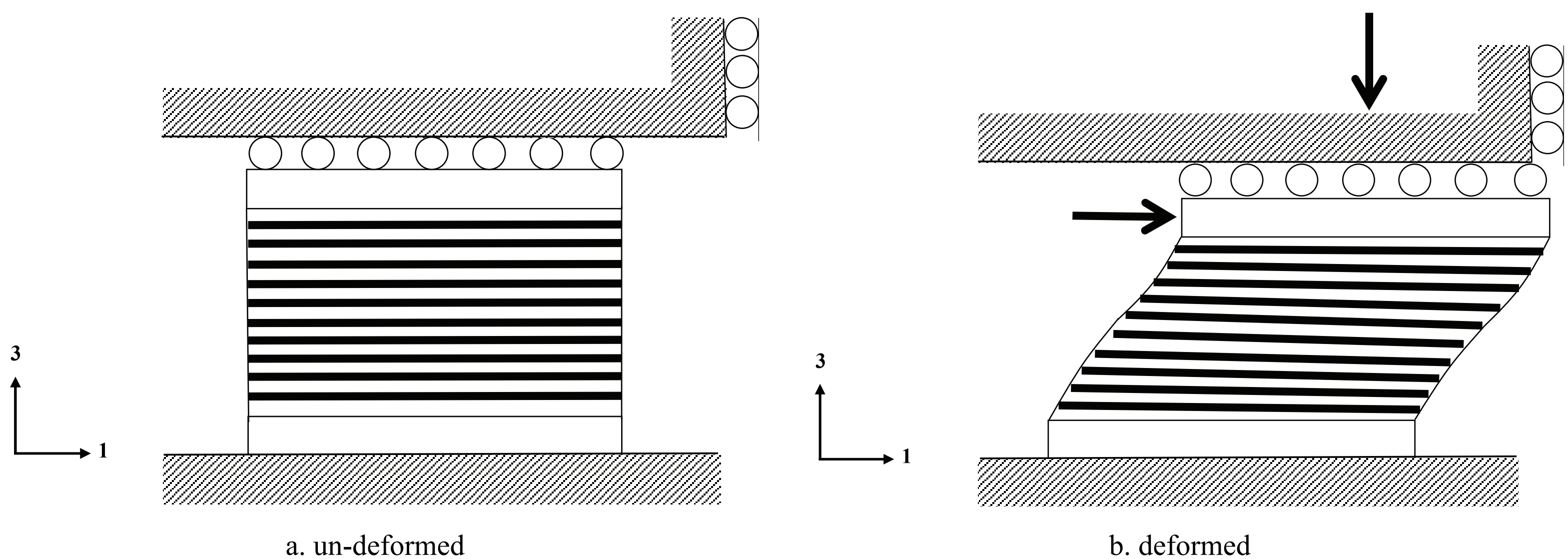

FIGURE 8-3 Illustration of bearing in the un-deformed and deformed configuration and corresponding boundary conditions

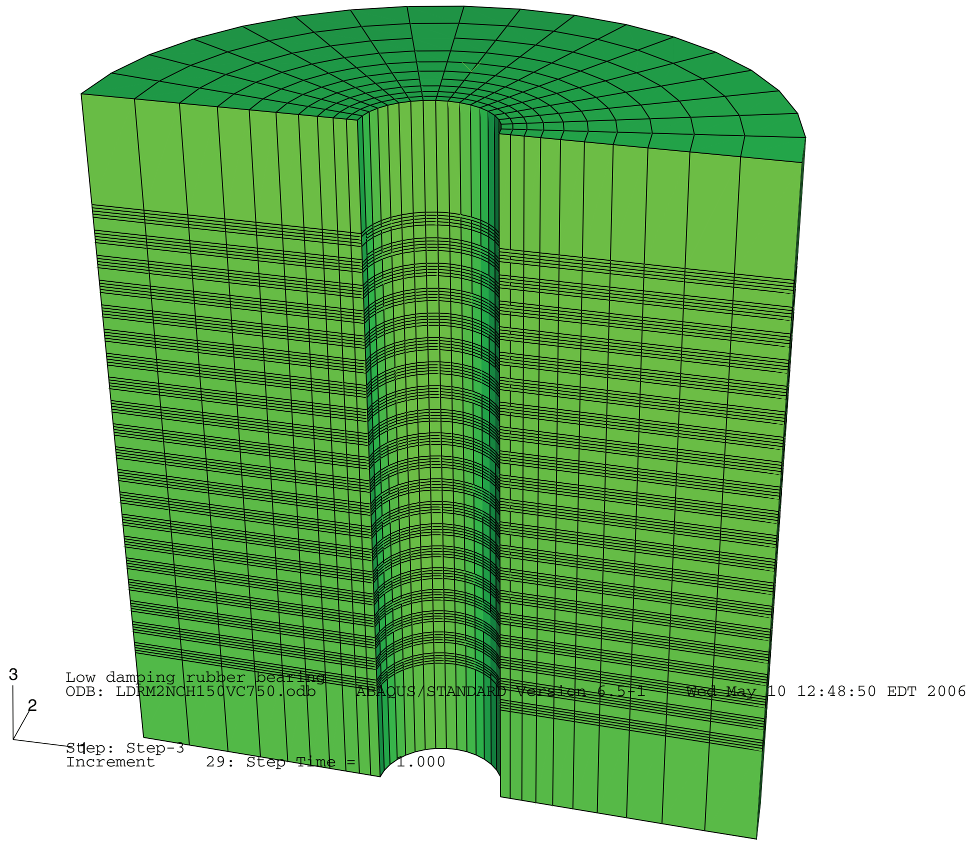

FIGURE 8-4 Rendering of FE model (Mesh 2) in the un-deformed configuration

8.3.6 Loading

The loading applied to the FE model varied based on the type of analysis, i.e., mesh density, lateral offset, and validation. For the mesh density analysis, a displacement-type boundary condition was utilized to specify a translation of the top control node along the $3-$axis (vertical) with a specified amplitude of -1.8 mm (compression). For the lateral offset analyses, the FE model was loaded in three steps that were intended to replicate the loading conditions of the bearing in the SBTM (see, Section 4). The first step consisted of an applied distributed load to the top surface of the top end-plate acting in the $3-$direction with a magnitude of -1.38 MPa (initial compressive pressure). For the second step, a horizontal translation with a magnitude of Δ was specified at the top control node in the $1-$direction using a displacement-type boundary conditions. The value of Δ varied from 0 mm (zero lateral displacement) to 152 mm, a lateral displacement equal to the bearing diameter. The third step applied a concentrated load at the top control node with a magnitude of $P/2$ (compressive load). Nodal reactions obtained from the FE results were multiplied by two for comparison purposes and to identify the force-response of the entire LDR bearing. The loading conditions for the two validation analyses were similar to those for the lateral offset analyses differing only in the number of steps. For validation of the compression stiffness, load was applied in two steps, first, the initial compressive pressure of $-1.38\ \text{MPa}$, and second, a concentrated load of $-78\ \text{kN}$ corresponding to a total compressive load on the entire bearing of $180\ \text{kN}$. For the validation of the shear stiffness, load was applied in two steps, first, an initial compressive pressure of $3.45\ \text{MPa}$, and second, a translation of the top control node in the $1-$direction of $90\ \text{mm}$ ($150\ \%$ rubber shear strain).

8.4 Results

8.4.1 General

This section presents results from the various FE analyses, including, the mesh density analyses used to select a mesh pattern for the subsequent analyses, i.e., lateral offset and validation.

8.4.2 Mesh Density Analysis

Finite element analysis was performed using ABAQUS and the three models, referred to herein as Mesh 1, Mesh 2 and Mesh 3 (see figure 8-1). To determine the sensitivity of the solution to the mesh pattern (or discretization) each model was subjected to compressive loading through a specified vertical translation in the $3-$direction with amplitude equal to $-1.8\ \text{mm}$ (compression) at the top control node.

Figure 8-5 presents both global (vertical load) and local (stress component S33) results obtained from FE analysis for each mesh pattern. In figure 8-5a, the calculated reaction (multiplied by two) at the base control node is plotted against the specified vertical translation of the top control node for each increment and mesh pattern. From the results plotted in this figure, the vertical force response for Mesh 2 and 3 are similar and substantially less than Mesh 1. Figure 8-5b presents average normal stress (S33) profiles for each mesh pattern. The average element stress (S33) was interpolated at the center of the element using the normal stress components at the integration points. Note, the location from which the stress profiles were calculated is inconsequential since the analysis becomes axisymmetric with only vertical loading. From the results potted in figure 8-5b the stress profile for Mesh 1 is coarse and differs substantial in magnitude from Mesh 2 and 3 that agree well, both with maximum S33 values of approximately $-14\ \text{MPa}$. Figure 8-6 presents the estimated vertical stiffness and computational effort associated with each mesh pattern.

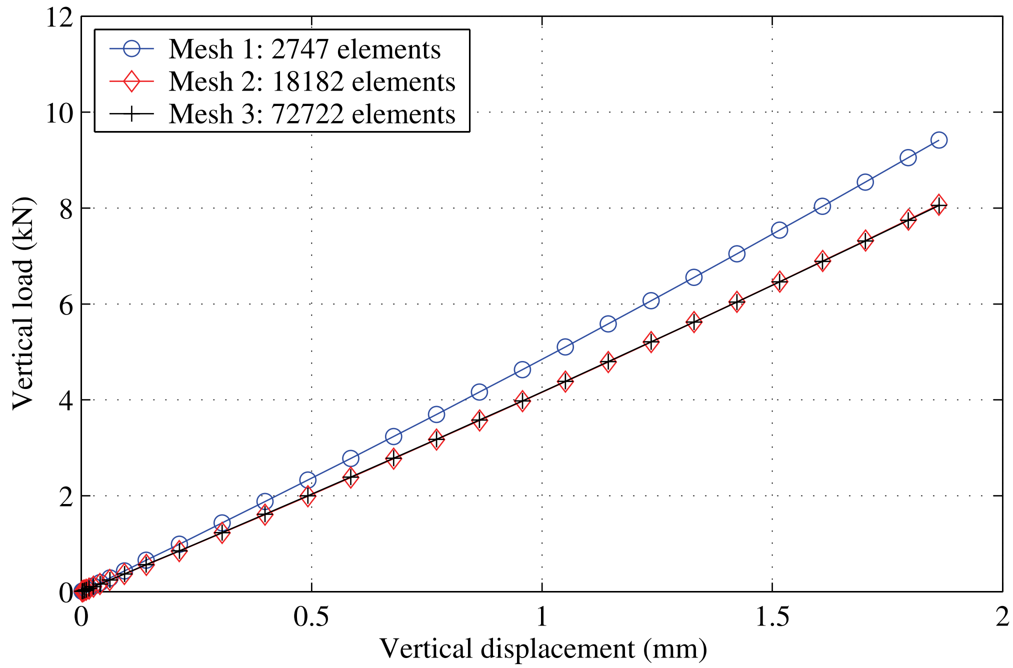

a. vertical force-displacement results for each mesh

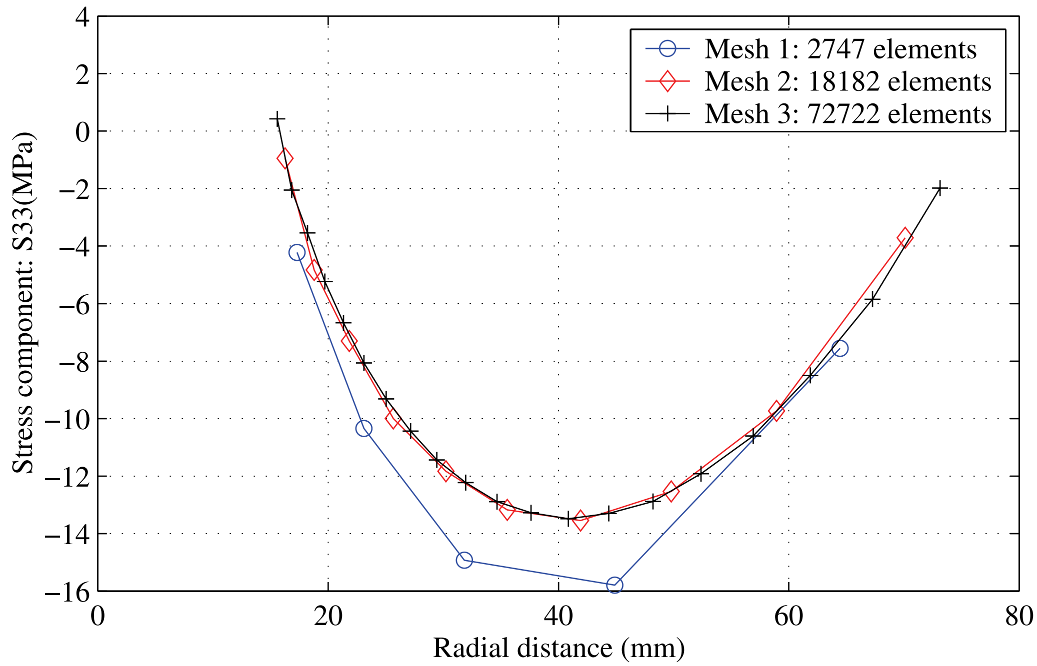

b. normal stress profile

FIGURE 8-5 Global and local results from the mesh density analyses

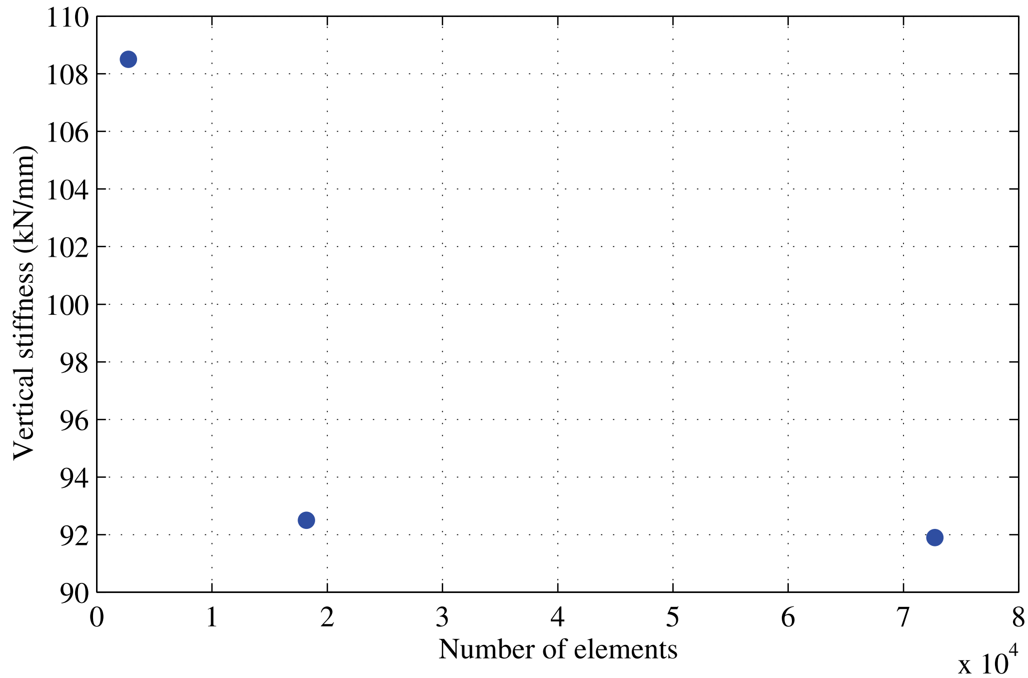

a. convergence

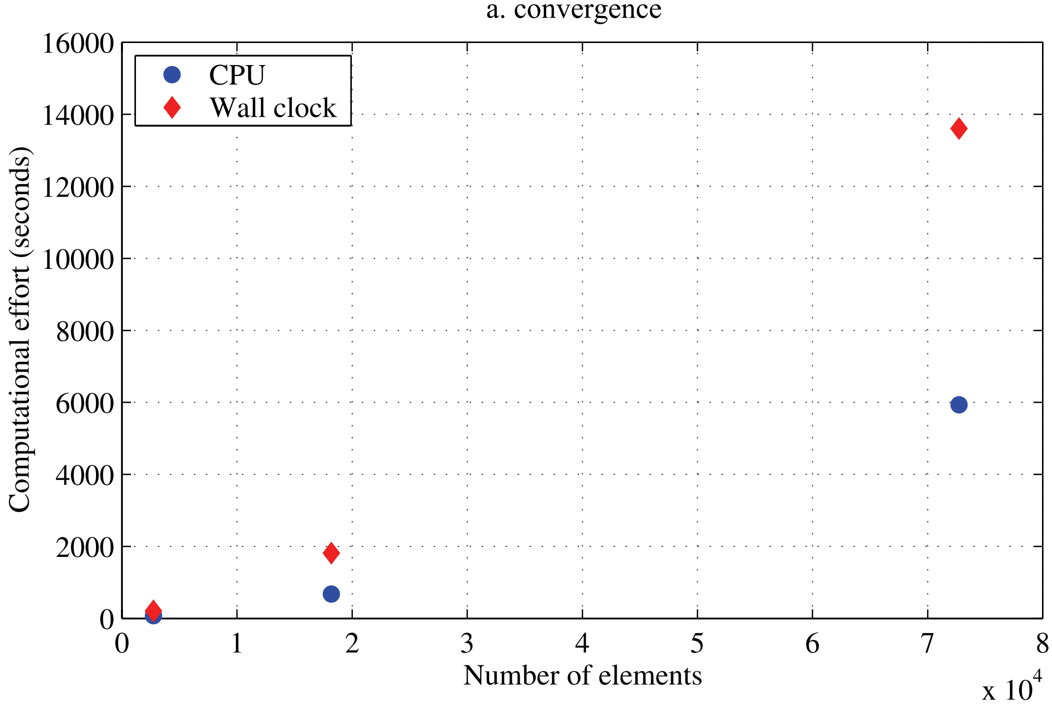

b. computational effort

FIGURE 8-6 Convergence and computational effort for the various mesh densities

From figure 8-6a, Mesh 1 (2,747 elements) results in a vertical stiffness of approximately 108.5 kN/mm whereas Meshes 2 (18,182 elements) and 3 (72,722 elements) result in a vertical stiffness of 92.5 kN/mm and 91.8 kN/mm, respectively. These results show that the vertical stiffness converges asymptotically as the number of elements increases and the difference between the predicted value for Mesh 2 and Mesh 3 is less than 1%: although the number of elements has quadrupled. Figure 8-6b presents a plot of the computational effort in terms of CPU (central processing unit) and wall clock time. From the results plotted in this figure, the additional computational effort for Mesh 3 is clear with approximately 1.6 hours of CPU time and 4 hours of total analysis time and substantially greater than the 0.2 hours and 0.5 hours for Mesh 2, respectively. Note, all analyses were performed using the same Silicon Graphics Inc. (SGI) machine with 8-1.5GHz processors. Based on the results presented in this section, the FE model with mesh pattern 2 was chosen for subsequent analyses.

8.4.3 Lateral Offset

A series of FE analyses (termed lateral offset) were performed with the LDR model that were intended to replicate the lateral offset testing performed on the LDR bearings (see Section 5). The results of these analyses are normalized to facilitate a direct comparison with the (normalized) experimental results. In addition, the normalized results from the FE analyses are compared with the predicted reduction in vertical stiffness using the two-spring formulation [see (2-42)].

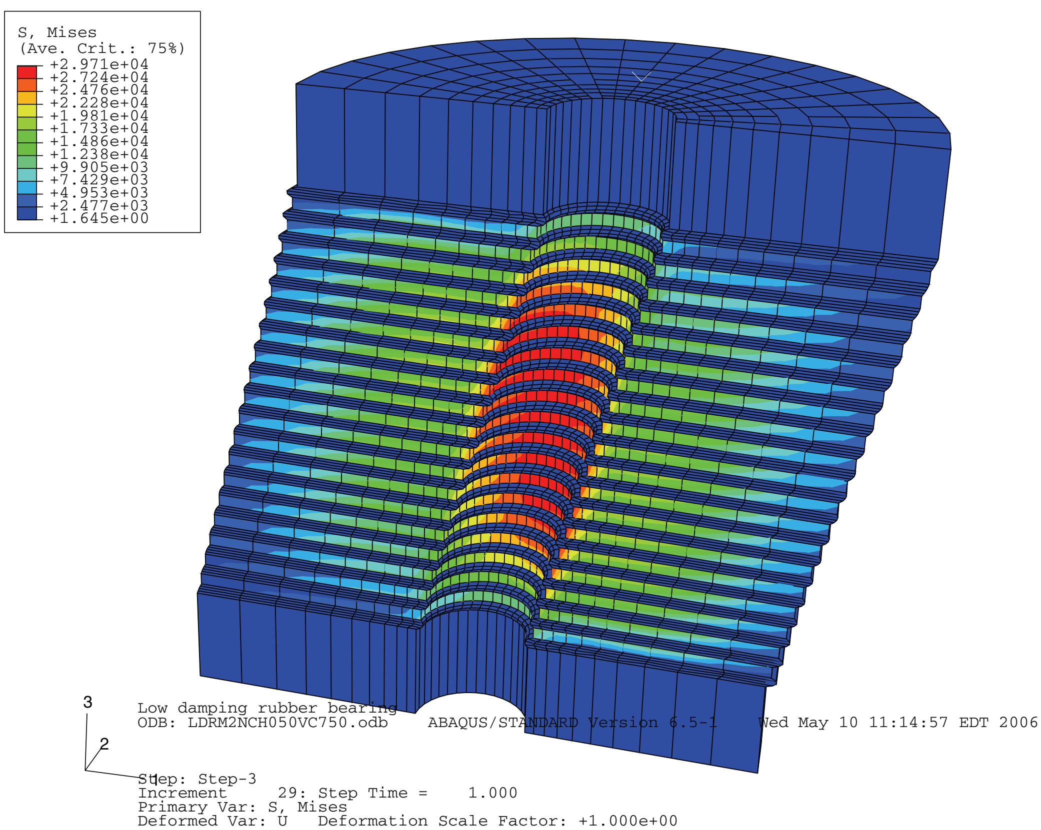

FIGURE 8-7 Graphical results from FEA of LDR model shown in the deformed configuration.

For each analysis, the FE model was loaded as described in Section 8.3.6, namely, applying an initial (compressive) pressure of $1.38\,\text{MPa}$, shearing the model to the specified lateral offset Δ, and applying a concentrated compressive load resulting in the desired maximum compressive load $P_{\max}$. As with the lateral offset testing, a combination of lateral offsets and maximum compressive loads were considered. Specifically, analyses were performed at lateral offsets of 0, 30, 60, 90, 120 and $152\,\text{mm}$ and maximum compressive loads of 60, 120 and $180\,\text{kN}$ which are identified herein by the corresponding target pressures (ρ) of 2.75, 5.2 and $9\,\text{MPa}$, respectively. The target pressure identifies the axial load for which the secant vertical stiffness was calculated. Figure 8-7 presents graphical results from FE analysis using ABAQUS. The results presented in this figure are Von Mises stress contours with the FE model in the deformed configuration corresponding to a lateral offset of $30\,\text{mm}$ ($50\,\%$ rubber shear strain) and a maximum compressive load of $60\,\text{kN}$ ($120\,\text{kN}$ for the entire bearing). From the results presented in figure 8-7, the maximum stress contour value reported is $29{,}710\,\text{psi}$ ($205\,\text{MPa}$) occurring in the intermediate steel shim plates around the mid-height of the bearing. Although this value is below the expected nominal yield stress for ASTM A36 steel, namely, $248\,\text{MPa}$ the maximum Von Mises stress reached and slightly exceeded $248\,\text{MPa}$ for analysis with $180\,\text{kN}$ of maximum compressive loading suggesting yielding of the intermediate steel shims might have occurred during lateral offset testing.

Figure 8-8 presents vertical force-displacement results from FE analyses with lateral offsets ranging from 0 to $152\,\text{mm}$ and a maximum compressive load of $60\,\text{kN}$. The force-displacement results presented in this figure clearly illustrate the reduction in vertical stiffness as a result of the increasing lateral offset. For $\Delta = 152\,\text{mm}$, a substantial increase in maximum vertical displacement (reduction in vertical stiffness) is observed when compared to the force-displacement response for $\Delta = 0\,\text{mm}$. Table 8-3 presents vertical stiffness values calculated from the vertical force-displacement response from the FE analyses. The vertical stiffness results reported in this table are denoted K_{vo} for analyses with $\Delta = 0\,\text{mm}$ and K_v for $\Delta > 0\,\text{mm}$ and is consistent with the notation used throughout this report. From the results presented in this table, for a given ρ the vertical stiffness decreases with increasing Δ and for $\Delta = 0\,\text{mm}$ the vertical stiffness increases with increasing ρ (or $P_{\max}$): a similar trend was observed from the results of experimental testing performed on the LDR bearings (see Section 5).

TABLE 8-3 Vertical stiffness results from lateral offset analyses

ρ (MPa)	K_{vo} (kN/mm)	K_v (kN/mm)				
	0 mm	30 mm	60 mm	90 mm	120 mm	152 mm
2.75	83.4	76.0	58.9	38.9	22.6	12.6
5.2	88.3	80.5	60.5	39.1	NA	NA
9	92.7	83.1	57.8	NA[1]	NA	NA

Notes:
1. Analysis not conducted – no results available

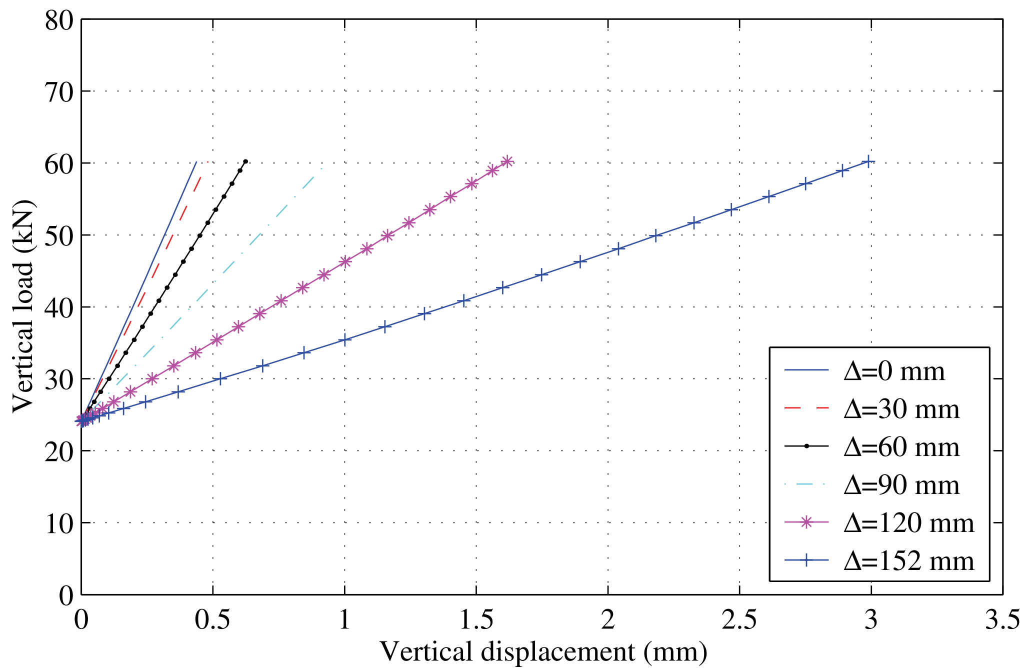

FIGURE 8-8 Vertical force-displacement results from FEA at each lateral offset and a maximum compressive load of 60 kN

Figure 8-9 presents vertical stiffness results normalized by the zero lateral displacement vertical stiffness (K_v / K_{vo}) plotted as a function of the lateral offset normalized by the bearing outer radius (Δ / R). Also plotted in figure 8-9 is the normalized vertical stiffness predicted by the two-spring formulation [see (2-42)]. From the results plotted in this figure, the FE model also exhibits a substantial reduction in vertical stiffness over the range of lateral displacements considered, further verifying the experimental data and analytical predictions. In addition, the K_v / K_{vo} results from the FE analyses agree well with the predicted values from the two-spring formulation. A slight reduction in K_v / K_{vo} is observed with increasing ρ for a given Δ / R. This results is inconsistent with the experimental results where K_v / K_{vo} was observed to increase with increasing ρ for a given Δ / R. The source of this inconsistency might be attributed to the difference in shear moduli exhibited by the natural rubber and that predicted by the neo-Hookean model at high shear strains (greater than 300%). For shear strains greater than 300% the natural rubber in the bearing is likely to exhibit a substantial increase in Young's modulus (and therefore shear modulus) as illustrated in figure 8-2 that is not captured by the neo-Hookean formulation. To illustrate the level of maximum shear strain for the various tests consider the lateral offset test with $\Delta = 60$ mm ($\Delta / R = 0.8$) and $P_{\max} = 180$ kN ($\rho = 9$ MPa). The total maximum shear strain (due to combine shear and compression) can be approximated as:

$$\gamma_{t,\max} = 6S\varepsilon_c f_{st} + \frac{\Delta}{T_r} = 4.1 \tag{8-10}$$

where $6S\varepsilon_c f_{st}$ is the maximum shear strain due to compression equal to 3.1 [see (8-8)] and Δ / T_r is the shear strain due to a lateral displacement Δ approximately equal to 1.0. In contrast, the total maximum shear strain ($\gamma_{t,\max}$) for the lateral offset test with $\Delta = 60$ mm ($\Delta / R = 0.8$) and $P_{\max} = 60$ kN ($\rho = 9$ MPa) is approximately equal to 1.7: two and one half times less than for $\Delta = 60$ mm and $P_{\max} = 180$ kN.

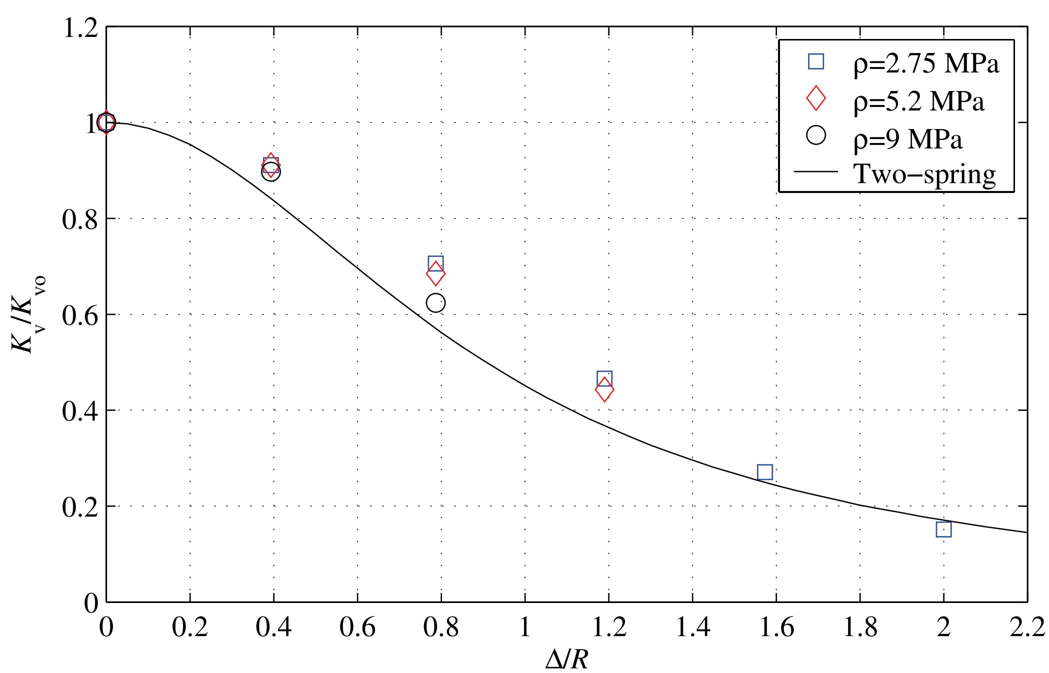

FIGURE 8-9 Normalized vertical stiffness data from FEA and comparison with two-spring formulation

8.4.4 Validation

Finite element analysis was performed with the LDR model using a value of the strain energy potential constant (C_{10}) calculated with the experimentally determined value of the shear modulus. Force-displacement results obtained from these FE analyses were compared with experimental vertical and lateral force-displacement results from tests performed on LDR 5M and 6 to validate the FE model. In addition, two FE analyses were performed to investigate the sensitivity of the solution to the assumed value of the bulk modulus, one with $D_1 = 0.8 \times 10^{-3}\ \text{mm}^2/\text{N}$ corresponding to a bulk modulus of $2500\ \text{MPa}$ and the other with $D_1 = 0\ \text{mm}^2/\text{N}$ corresponding to an infinitely large bulk modulus (incompressible material assumption).

As stated previously, two values of the shear modulus were estimated from the experimental results and used for the FE validation analysis. These bounding values of the tangent shear moduli were estimated from the shear force-displacement response of LDR 5M subjected to quasi-static loading to a maximum rubber shear strain of 150% with a (constant) compressive pressure of $3.45\ \text{MPa}$. Tangent shear moduli were estimated at zero rubber shear strain (initial) and a shear strain amplitude of 100% (estimated average shear strain under maximum compressive loading) and determined to be $0.83\ \text{MPa}$ and $0.72\ \text{MPa}$, respectively. For each value of the shear modulus two validation analyses were performed: (1) specifying an initial distributed (compressive) load of $3.45\ \text{MPa}$ and a lateral displacement at the top control node of $90\ \text{mm}$ (150% rubber shear strain) and (2) specifying an initial distributed (compressive) load of $1.38\ \text{MPa}$ and a concentrated vertical load at the top control node of $77\ \text{kN}$ resulting in a maximum compressive load of $90\ \text{kN}$ ($180\ \text{kN}$ for the entire bearing).

Figure 8-10 presents a comparison of FE results using the initial tangent shear modulus ($0.83\ \text{MPa}$) and the assumed bulk modulus of $1999\ \text{MPa}$ with the results obtained from lateral and vertical load tests performed on LDR 5M (with cover removed, see Section 5). In figure 8-10a the shear force responses agree well up to a lateral displacement of approximately $50\ \text{mm}$ (80% rubber shear strain). For displacements greater than $50\ \text{mm}$, the FE results over predict the experimental results. Figure 8-10b presents a comparison of the vertical force-displacement response from FE with those obtained from experimental testing. From the results presented in this figure the FE model under predicts the maximum vertical displacement.

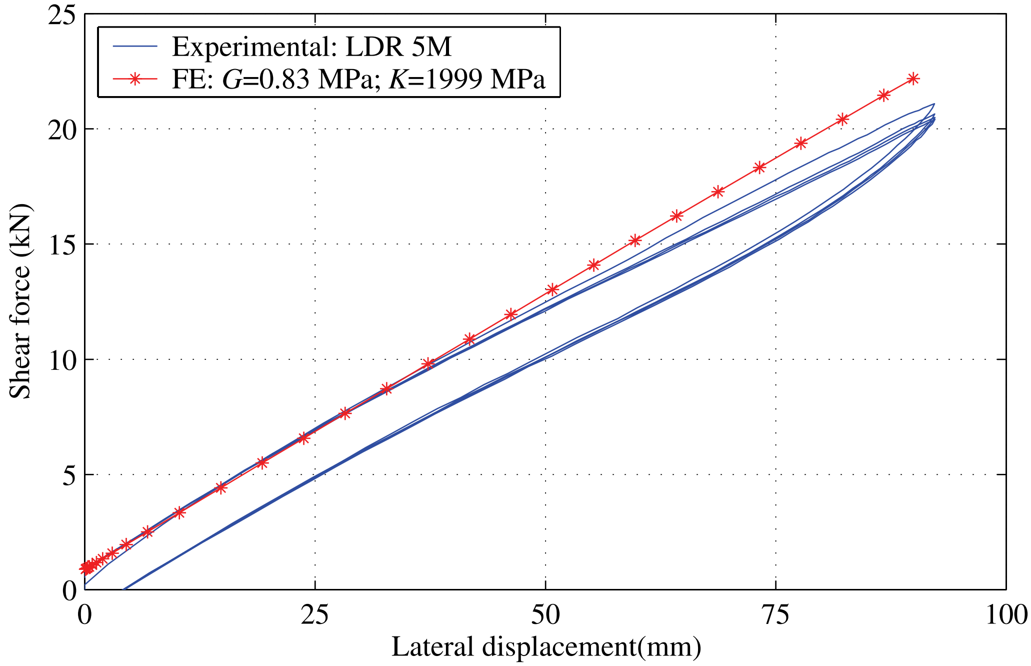

a. half-cycle shear response for: $\gamma = 150\%$ and $P = 60$ kN (3.45 MPa)

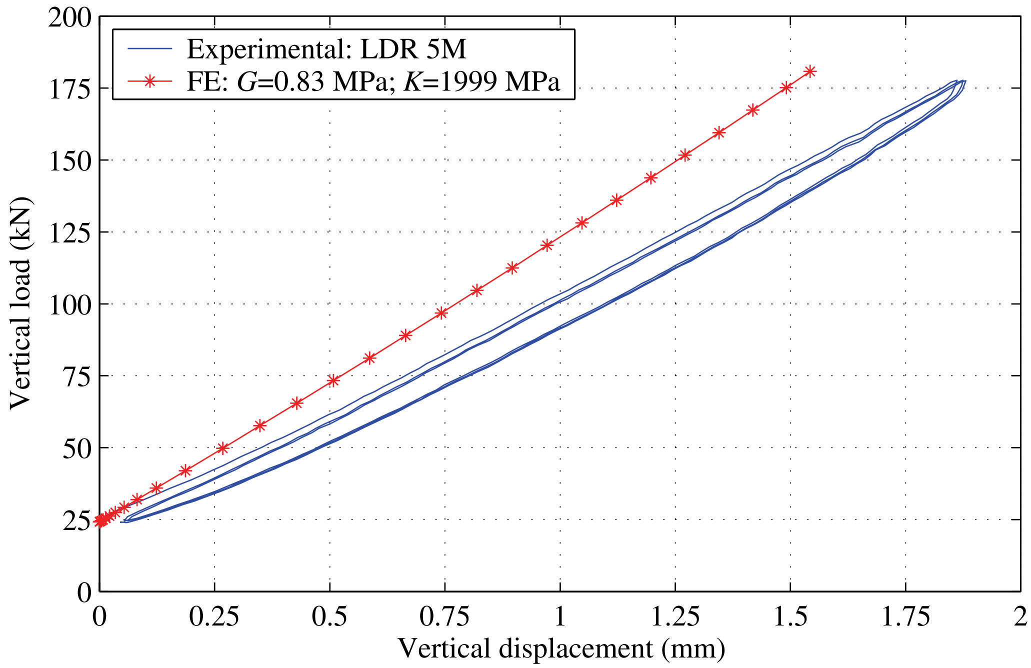

b. vertical force-displacement response for: $P_{max} = 180$ kN

FIGURE 8-10 Comparison of experimental and FE results with $G = 0.83$ MPa

Figure 8-11 presents a comparison of the FE results using the 100% tangent modulus (0.72 MPa) again with the experimental results from lateral and vertical tests preformed on LDR 5M. From figure 8-11a, the FE results under predict the shear force response over the entire range of lateral displacement however the slope (horizontal stiffness) agrees well with the horizontal stiffness of the experimental results between 50 mm and 75 mm as expected. Figure 8-11b presents a comparison of the FE and experimental results for vertical loading. From the results presented in this figure, the FE model predicts the vertical displacements (and thus vertical stiffness) reasonably well.

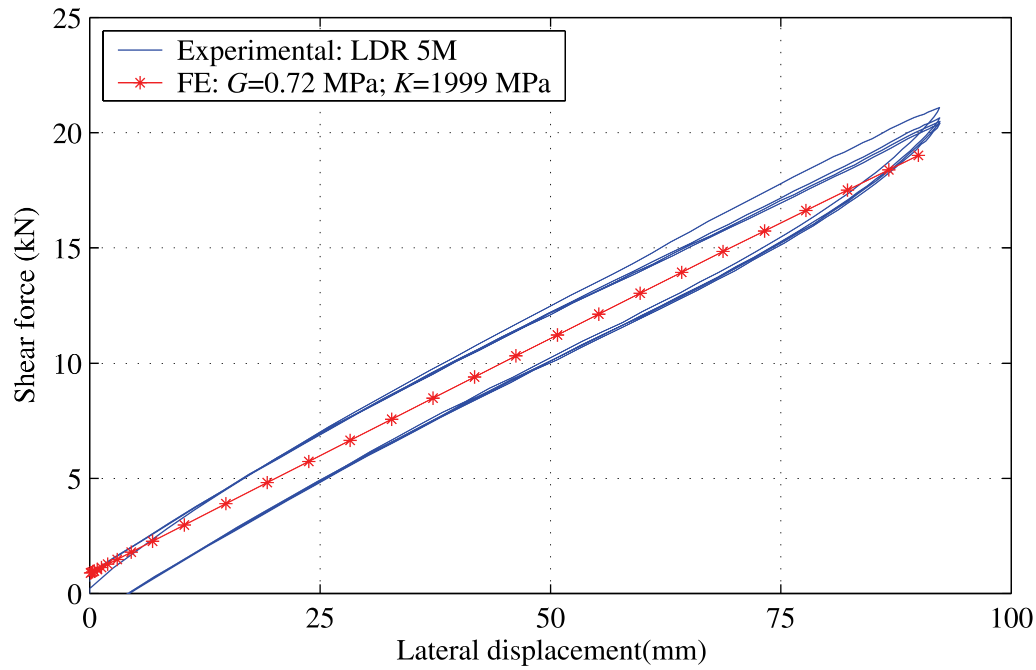

a. half-cycle shear response for: $\gamma = 150\%$ and $P = 60$ kN (3.45 MPa)

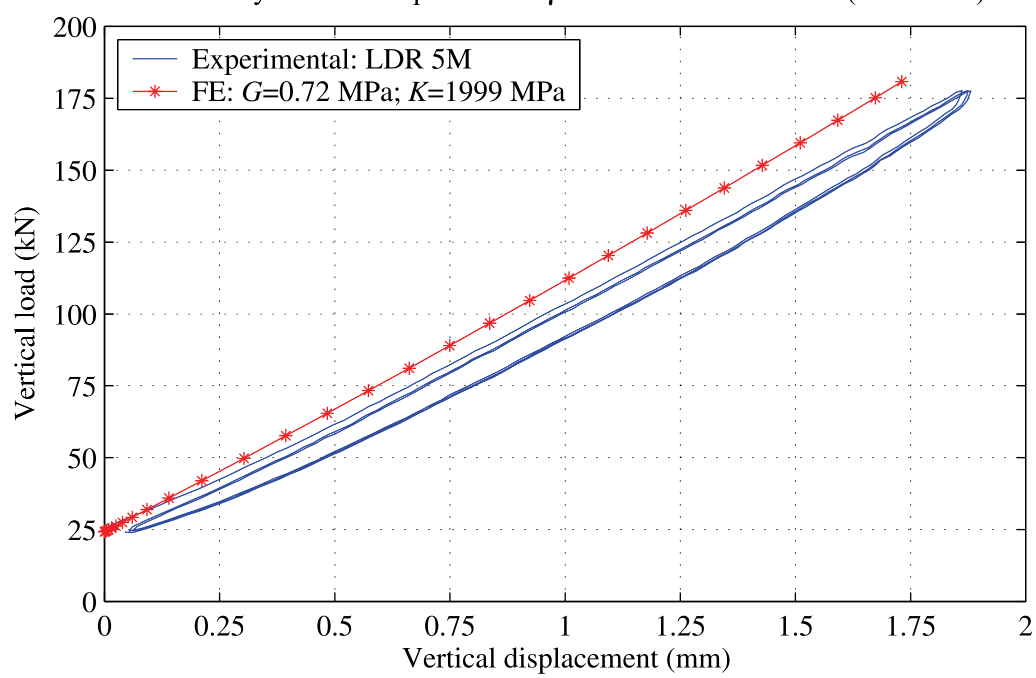

b. vertical force-displacement response for: $P_{\max} = 180$ kN

FIGURE 8-11 Comparison of experimental and FE results with $G = 0.72$ MPa

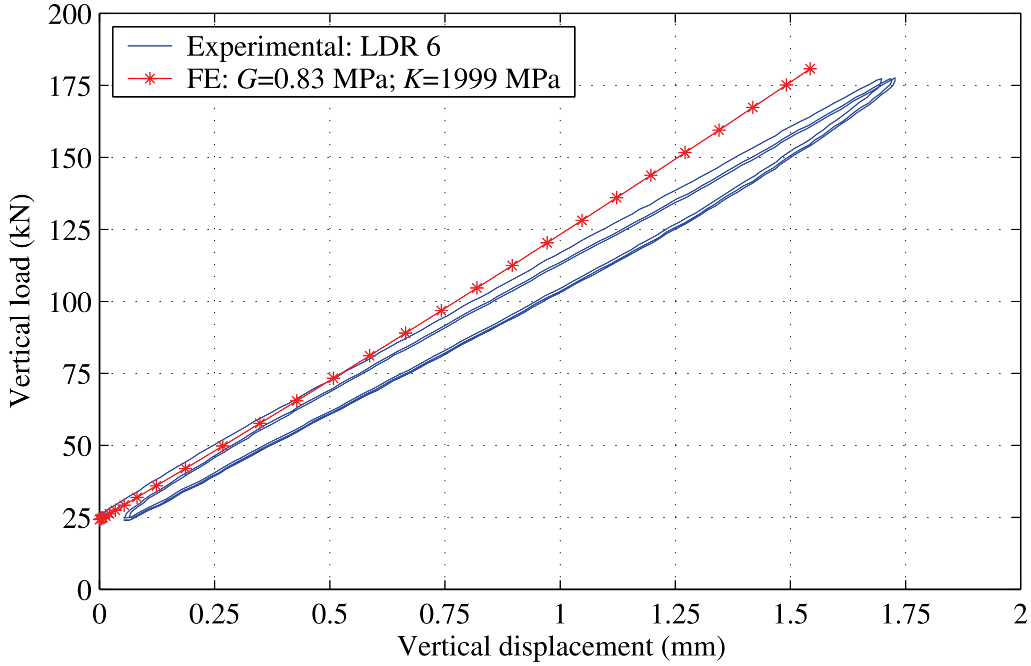

a. half-cycle shear response for: $\gamma = 150\%$ and $P = 60$ kN (3.45 MPa)

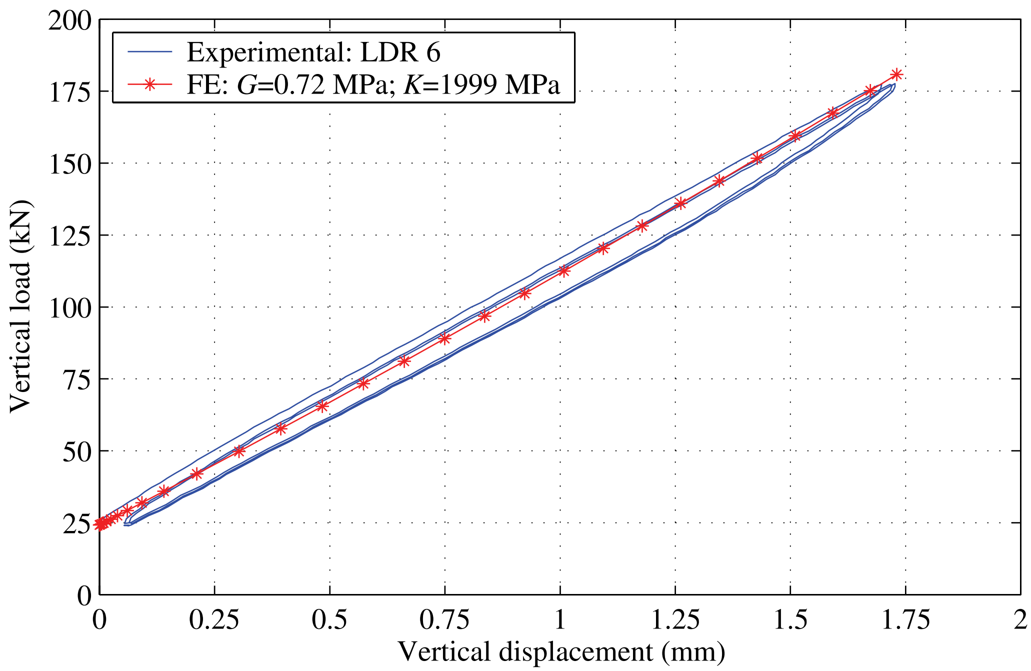

b. vertical force-displacement response for: $P_{max} = 180$ kN

FIGURE 8-12 Comparison of experimental and FE results for LDR 6

TABLE 8-4 Comparison of vertical stiffness values calculated from experimental and FEA results

LDR No.	G (MPa)	K_{vo} (kN/mm) Experimental	FE	Error (%)
5M	0.83	86.3	106.3	23
	0.72	86.3	95.3	10
6	0.83	90.4	106.3	18
	0.72	90.4	95.3	5

Additionally, figure 8-12 presents the results of FE analysis using $G = 0.83\,\text{MPa}$ and $G = 0.72\,\text{MPa}$ with the results of an axial load test performed on LDR 6. From figure 8-12a, the FE results agree well with the experimental results up to approximately $100\,\text{kN}$ after which the FE results under predict the vertical displacement (over predict stiffness). From figure 8-12b ($G = 0.72\,\text{MPa}$) the FE and experimental results are observed to agree very well. However, it should be noted, considerable variation in vertical stiffness results were observed from axial load tests performed with different bearings of the same type and is reported in Section 5. Two factors contribute to the variation in vertical stiffness for LDR 5M and 6. First, variability is introduced through the individual rubber layer thicknesses and second, the rubber cover had been removed from LDR 5 then referred to 5M, which contributed, albeit marginally, to the vertical stiffness. Table 8-4 presents vertical stiffness values calculated from the experimental and FE results for both LDR 5M and LDR 6. Also presented in this table is an error estimate calculated taking the experimental value as the true value. From the results presented in table 8-4, the vertical stiffness determined from FEA with $G = 0.72\,\text{MPa}$ agrees well with the experimentally determined vertical stiffness from LDR 5M and 6 with approximately $10\,\%$ and $5\,\%$ error, respectively.

To illustrate the sensitivity of the solution to the assumed value of the bulk modulus, two additional analyses were performed one corresponding to $K = 2500\,\text{MPa}$ and $K \to \infty$ (incompressible material assumption), both with $G = 0.72\,\text{MPa}$. These results were compared to those from the FEA with $G = 0.72\,\text{MPa}$ and $K = 1999\,\text{MPa}$ and are presented in figure 8-13. From the results presented in this figure, the vertical force-displacement response for $K = 1999\,\text{MPa}$ and $K = 2500\,\text{MPa}$ do not differ substantially, however, the incompressible assumption leads to an approximately $20\,\%$ larger vertical stiffness when compared with $K = 1999\,\text{MPa}$.

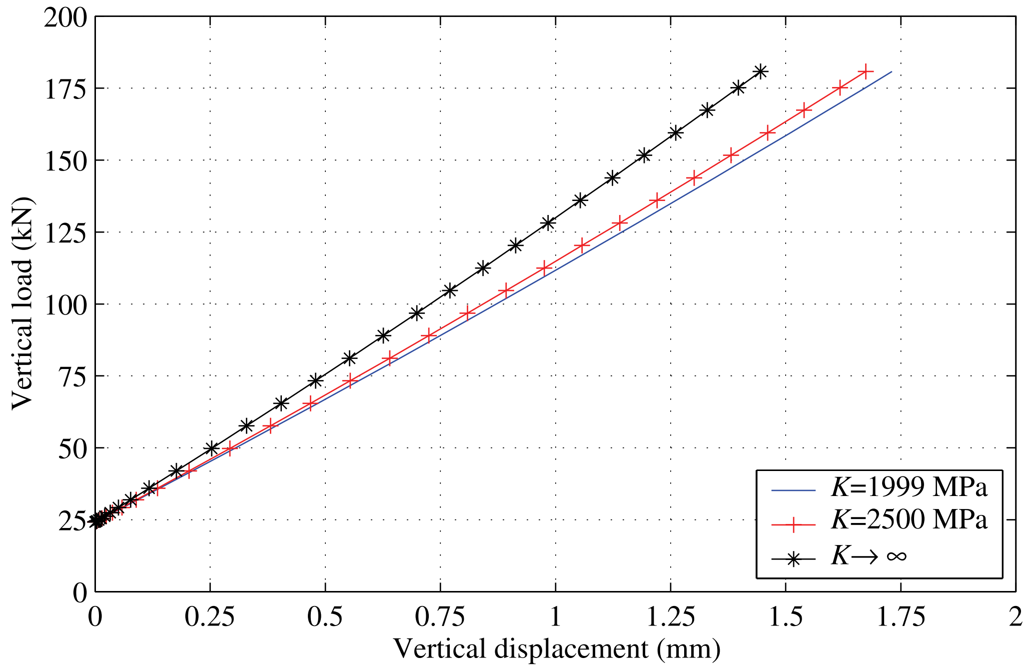

FIGURE 8-13 Vertical force-displacement results from FEA for three values of the bulk modulus

8.5 Summary

This section described the development of a FE model of a LDR bearing. Finite element analysis was performed to: selected a mesh pattern, to further investigate the influence of lateral displacement on the vertical stiffness of LDR bearings and to validate the FE model by way of a comparison with experimental results obtained from tests performed on the LDR bearings. From the FEA results and various comparisons the following observations were made: (1) the FE results show a substantial reduction in vertical stiffness over the range of lateral displacements considered as was observed with the experimental data and (in normalized form) agree well with the predicted reduction using the two-spring formulation, (2) although the exact value of the bulk modulus could not be determined the FE solution does not differ substantially for the range of values that is typical of lightly filled natural rubber, and (3) considering bounding values of the tangent shear modulus the FE results were observed to agree reasonably well with experimental results given the simplicity of the neo-Hookean model and the variability in the individual rubber layers of the LDR bearings.

SECTION 9

COMPARISON OF RESULTS

9.1 General

This section presents qualitative and quantitative comparisons of experimental results with the results of various formulations, finite element (FE) analysis, and equivalent linear static procedures. In the first portion of this section, the measured reduction in vertical stiffness from lateral offset testing performed on the low-damping rubber (LDR) and lead-rubber (LR) bearings are compared with the predicted reductions in vertical stiffness from the three formulations presented in Section 2. Both qualitative (graphical) and quantitative (residual analysis) comparisons are presented. Subsequently, the results of lateral offset tests performed on the LDR bearings are compared with the results of FE analysis of a three-dimensional (3D) LDR model. In addition, the FE results are compared with results of analysis using the two-spring formulation. In the second-to-last section, the results of earthquake simulation testing performed with three components of excitation are used to evaluate an equivalent linear static (ELS) procedure to compute the vertical load on the isolation system due to vertical component of excitation. A brief summary and discussion is presented at the end of the section.

9.2 Reduction in Vertical Stiffness

9.2.1 General

The values of vertical stiffness obtained from the lateral offset tests were normalized to facilitate a direct graphical comparison of the experimental data with: (1) the values predicted by the various formulations for the reduction in vertical stiffness, and (2) the results of the finite element (FE) study. Normalizing the results in this manner also enabled a residual analysis to be conducted. The results of which are used as quantitative indicators of the difference between the predicted values and the experimentally observed values. Although presented previously, the normalization procedure is described here for convenience: the values of vertical stiffness obtained from the lateral offset tests, K_v, were normalized by the vertical stiffness at zero lateral displacement, K_{vo}, determined from axial load tests. The measured lateral offsets, Δ, were normalized by the bearing outer radius, R.

9.2.2 Comparison of Experimental Results and Analytical Formulations

The normalized vertical stiffness data (K_v / K_{vo}) from the low-damping (LDR) and lead-rubber (LR) bearings are plotted in figures 9-1a and 9-1b, respectively, along with the predicted reduction from the two-spring formulation. Also plotted in each of these figures is a horizontal reference (dashed) line at $K_v / K_{vo} = 1$. From figure 9-1a, the reduction in vertical stiffness of the LDR bearings is evident from the experimental data. The two-spring formulation over predicts the reduction in vertical stiffness for each lateral offset and pressure with the exception of LDR 6 at $\Delta / R \approx 0.4$ and $\rho = 2.75$ MPa where K_v / K_{vo} is observed to lie slightly below two-spring prediction. The experimental data from the LDR bearings agree well with the two-spring formulation for $\rho = 2.75$ MPa over the range of lateral displacement considered. However, for the intermediate and large vertical pressures ($\rho = 5.2$ MPa and 9 MPa) more significant differences between the two-spring formulation and the experimental data are observed, specifically, at $\Delta / R \approx 0.4$ and $\Delta / R \approx 0.8$. A plausible explanation for the difference with the larger pressures is provided in the subsequent section comparing the experimental and FE analysis results. From figure 9-1b, the reduction in vertical stiffness is again apparent from the LR bearing data. The experimental data is observed to agree reasonably well with the two-spring formulation over the range of lateral displacements and for each axial load amplitude (or target pressure). In addition, the two-spring formulation again over predicts the reduction in vertical stiffness with the exception of LR 5 at $\Delta / R \approx 0.4$ and $\rho = 5.2$ MPa where the experimental data point lies slightly below the predicted value from the two-spring formulation. Finally, the experimental data for both the LDR and LR bearings show a nonzero vertical stiffness at $\Delta / R = 2$, a lateral displacement equal to the bearing diameter, that is approximately equal to $20\,\%$ of K_{vo} (the zero lateral displacement vertical stiffness). This result agrees well with the predicted value from the two-spring formulation at $\Delta / R = 2$ of 0.17 (or $17\,\%$); see (2-42).

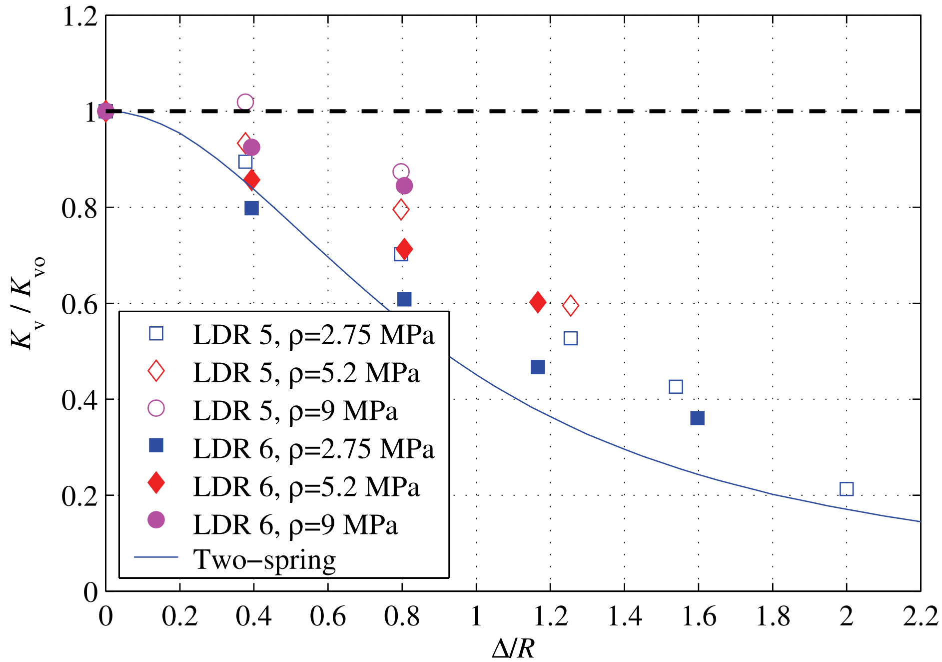

a. LDR bearings

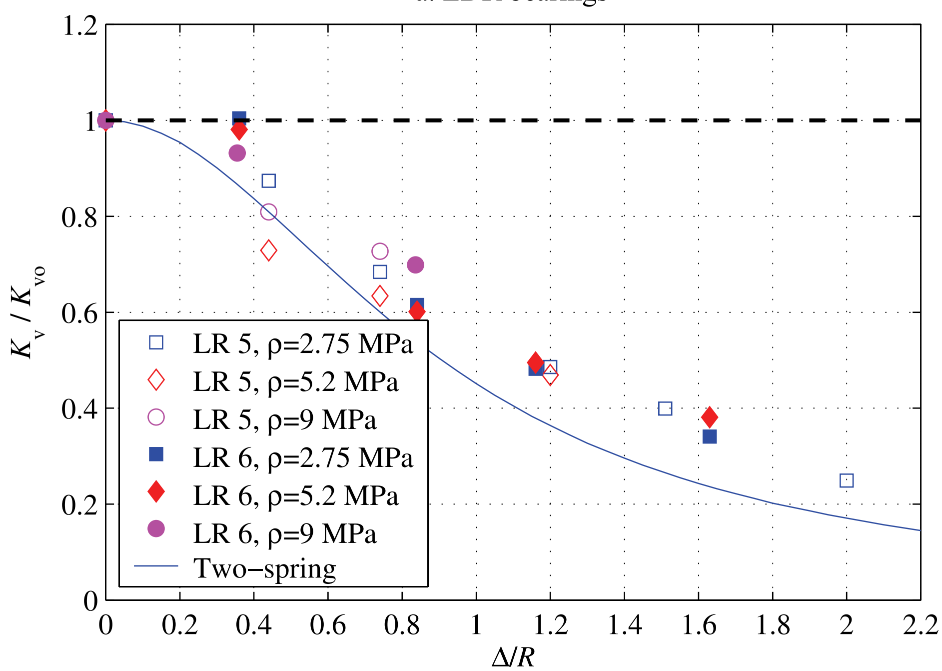

b. LR bearings

FIGURE 9-1 Comparison of normalized vertical stiffness data from the LDR and LR bearings with the two-spring formulation

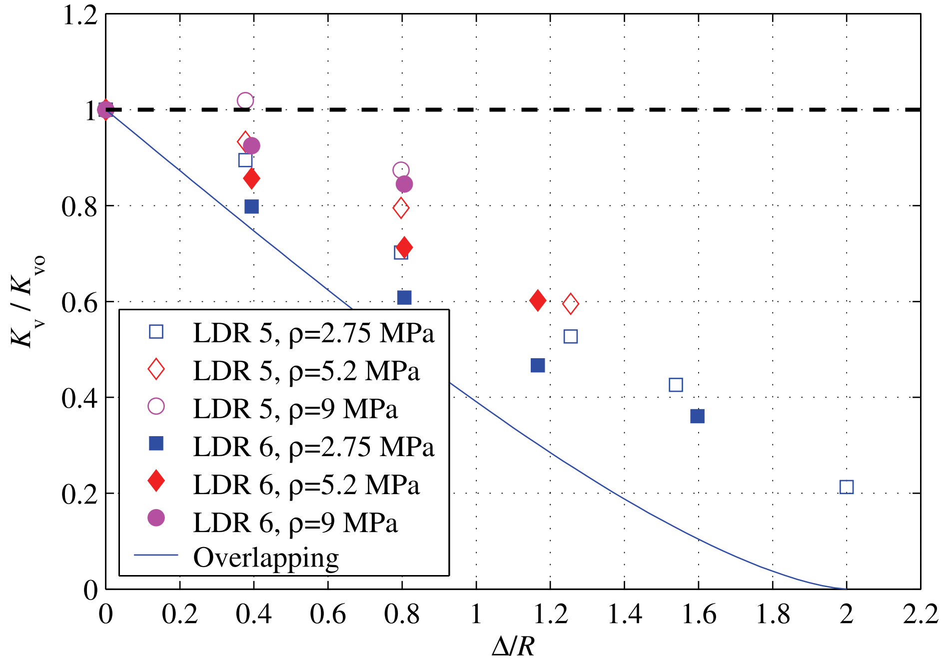

a. LDR bearings

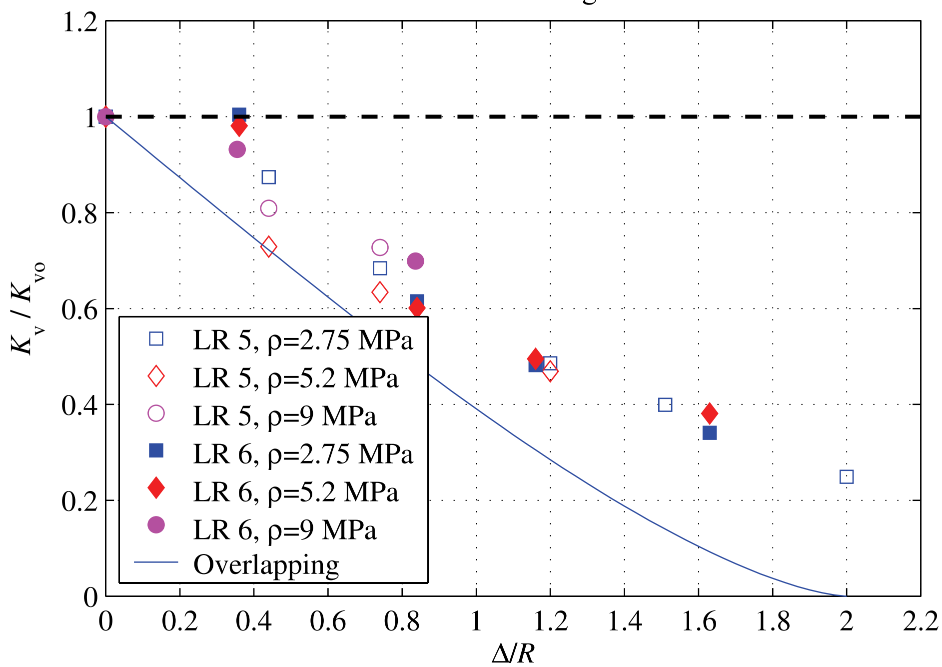

b. LR bearings

FIGURE 9-2 Comparison of normalized vertical stiffness data from the LDR and LR bearings with the overlapping area formulation

Figure 9-2 presents a comparison of the experimental data from the LDR and LR bearings (figures 9-2a and 9-2b, respectively) with the predicted reduction from the overlapping area formulation (see Section 2). The presentation of figure 9-2 is similar to the presentation of figure 9-1. From the results presented in figure 9-2a (LDR), the overlapping area formulation substantially over predicts the reduction in vertical stiffness for most lateral offsets and target pressure. This formulation predicts $K_v / K_{vo} = 0$ at $\Delta / R = 2$, which does not agree with the experimental observations. Similar conclusion can be drawn from figure 9-2b (LR), where the overlapping area formulation over predicts the reduction in vertical stiffness for each lateral offset and target pressure. Importantly, the overlapping area formulation does not capture the trend observed in the experimental data.

A comparison of the experimental data for both bearing types with the predicted reductions using the piecewise linear formulation, also referred to herein as the linear formulation, is presented in figure 9-3. From figure 9-3a (LDR), the experimental data is observed to agree reasonably well with the linear formulation, however, this formulation under estimates the reduction in vertical stiffness for LDR 6 at nearly all lateral offsets with $\rho = 2.75$ MPa . In figure 9-3b (LR), the linear formulation agrees reasonably well with the experimental data in an average sense.

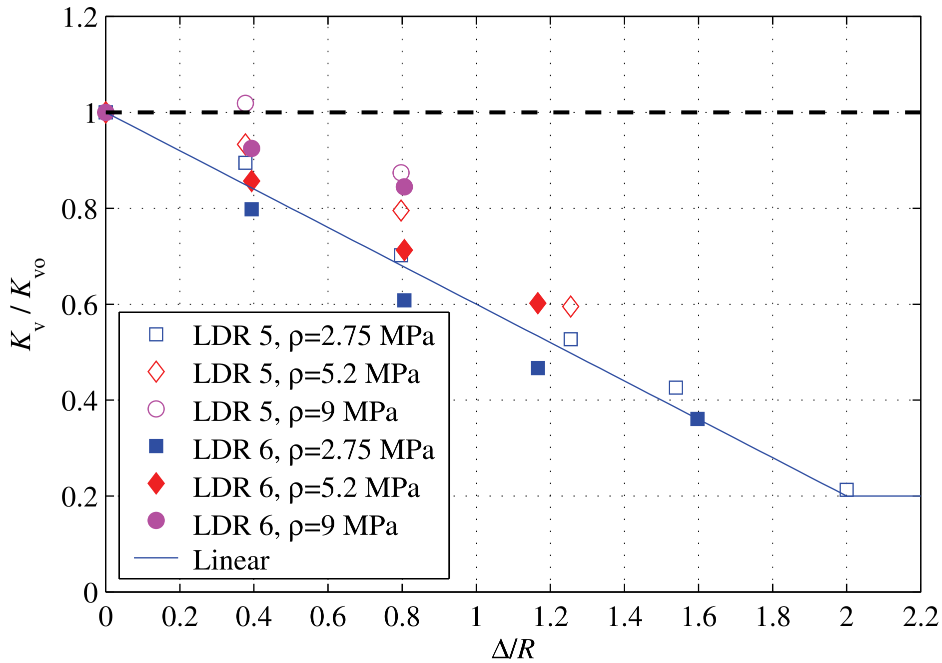

a. LDR bearings

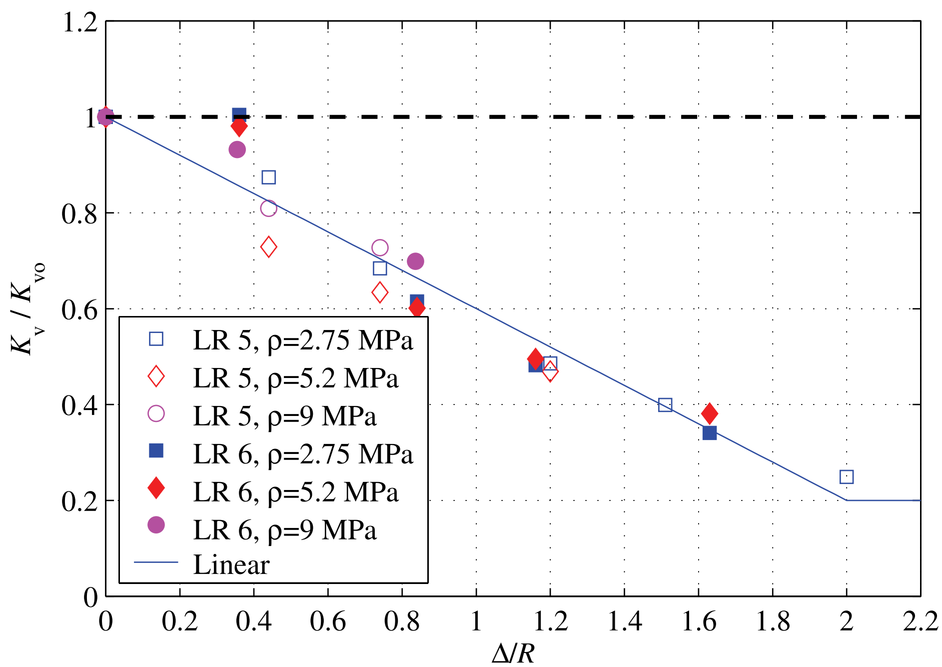

b. LR bearings

FIGURE 9-3 Comparison of normalized vertical stiffness data from the LDR and LR bearings with the piecewise linear formulation

TABLE 9-1 Results from the residual analysis

Formulation	ρ (MPa)	Bearing type and number				Sub-Total	Total
		LDR		LR			
		5	6	5	6		
Two-spring	2.75	0.57	0.3	0.48	0.42	1.77	4.7
	5.2	0.56	0.4	0.22	0.59	1.77	
	9	0.48	0.37	0.13	0.22	1.20	
Overlapping Area	2.75	1.11	0.57	1.01	0.79	3.48	8.0
	5.2	0.8	0.62	0.29	1.04	2.75	
	9	0.63	0.52	0.27	0.37	1.79	
Linear	2.75	0.15	0.18	0.16	0.26	0.75	2.6
	5.2	0.29	0.12	0.22	0.46	1.09	
	9	0.36	0.25	0.04	0.11	0.76	

Residual analysis was performed to quantify the difference between the predicted values of a particular formulation and the experimental values. For this analysis, the difference between the experimental and the predicted value was summed for each bearing, pressure and formulation and calculated according to:

$$R_m = \sum_{i=1}^{m} \left| \left(\frac{K_v}{K_{vo}} \right)_{e,i} + \left(\frac{K_v}{K_{vo}} \right)_{t,i} \right| \tag{9-1}$$

where the subscript e represents the experimentally determined value; the subscript t represents the predicted value from a particular formulation and m represent the number of offsets for a particular target pressure. Cumulative residual values calculated for each bearing, axial load amplitude and formulation are presented in table 9-1. Also included in this table are residual sub-totals (for each target pressure) and residual totals (for each formulation). From table 9-1, the linear formulation resulted in the lowest residual value (2.6) followed by the two-spring model (4.7) then the overlapping area formulation (8.0).

9.2.3 Comparison of Experimental and Finite Element Analysis Results

The results of the finite element (FE) analyses were normalized in the same manner to facilitate a graphical comparison with the normalized experimental results from tests performed on LDR 5 and 6. This comparison is presented in figure 9-4. Figure 9-4a presents the experimental results from tests performed on LDR 5 with the FE results for each lateral offset and target pressure. In this figure the experimental results are shown by hollow markers and denoted "Exp." in the legend whereas the FE results are shown by corresponding solid markers and denoted "FE" in the legend. A solid line is also included in these plots and represents the reduction in vertical stiffness predicted by the two-spring formulation. Figure 9-4b presents the experimental results from LDR 6 with the FE results. Note the presentation of figure 9-4b is identical to that of figure 9-4a. From the results presented in these figures, the experimental and FE results compare well for $\rho = 2.75\text{ MPa}$ over the range of Δ / R considered. However, for larger pressures, specifically 5.2 and 9 MPa, the FE results tend to over predict the measured reduction in vertical stiffness. At a given lateral offset (Δ / R) the FE results show K_v / K_{vo} decreases with increasing ρ whereas the experimental results show the opposite trend, specifically, increasing K_v / K_{vo} with increasing ρ. Additionally, the FE results compare well to the predicted reduction from the two-spring formulation for each Δ / R including the predicted K_v / K_{vo} value at $\Delta / R = 2$.

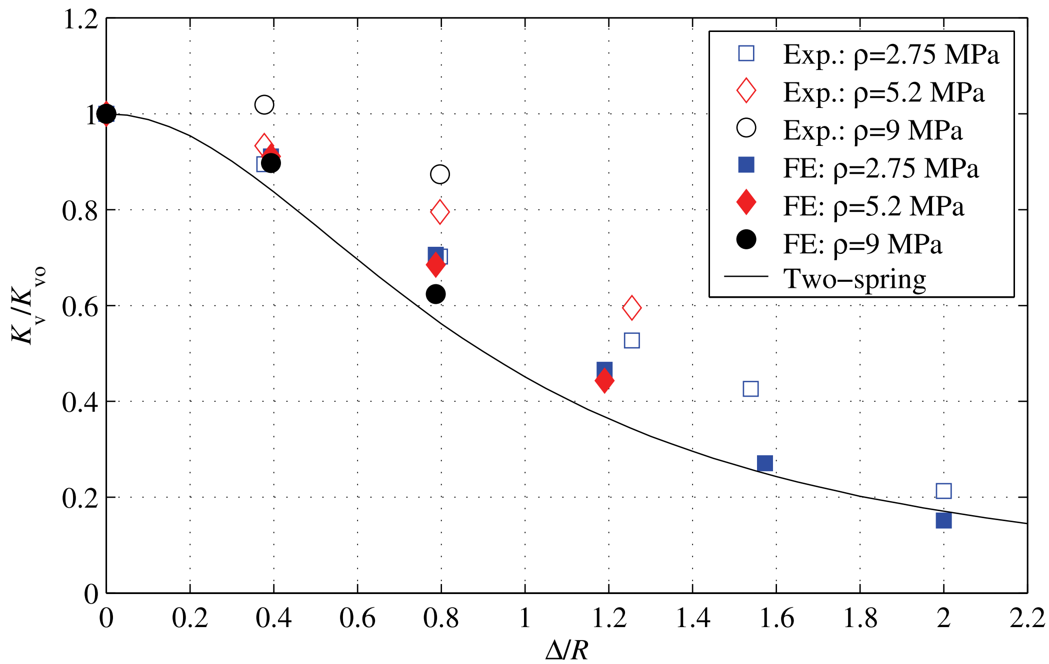

a. comparison with LDR 5

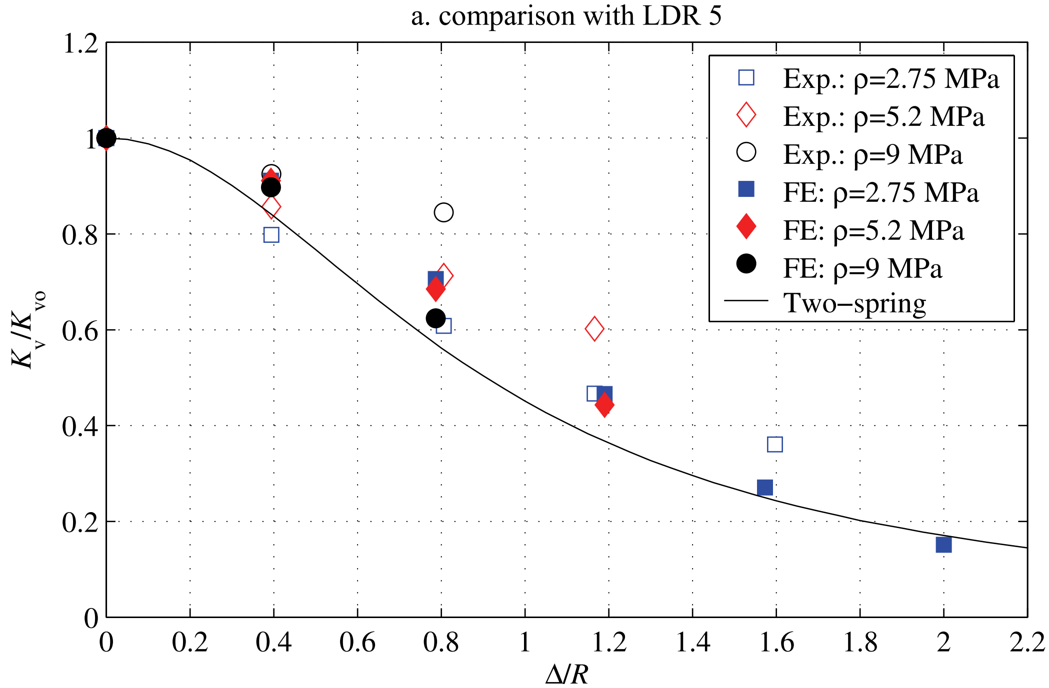

b. comparison with LDR 6

FIGRE 9-4 Comparison of experimental and finite element results for LDR bearings

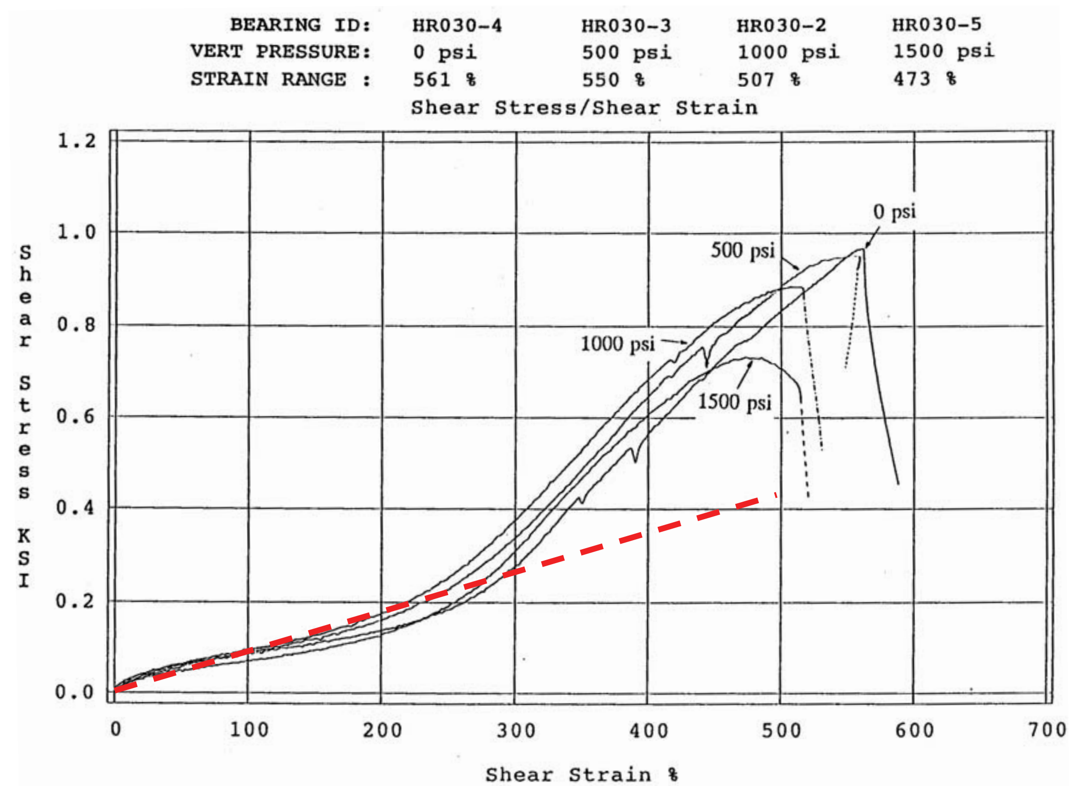

FIGURE 9-5 Stress-strain results from tests performed on high-damping rubber bearings taken to failure (source: Kelly, 1991)

The difference between the K_v / K_{vo} values from the experimental data and the FE results for the intermediate and large ρ might be attributed to a substantial increase in the stiffness of the natural rubber (shear modulus) at high shear strains (greater than $300\,\%$) that is not captured by the neo-Hookean material model used for the FE model or the two-spring formulation. To illustrate this hypothesis, the total shear strain in an individual rubber layer is estimated at a particular lateral offset ($\Delta / R = 0.8$) for two levels of ρ ($2.75\,\text{MPa}$ and $9\,\text{MPa}$) and used in conjunction with experimental data from tests performed with high damping rubber (HDR) bearings taken to failure (maximum shear strains exceeding $500\,\%$). Unfortunately, shear stress-strain data for shear strains greater than approximately $250\,\%$ could not be obtained from the LDR (or LR) bearing used in this study due to the combination of the stroke of the horizontal actuator, part of the SBTM, and the total thickness of rubber. In lieu of this data, results from tests performed on high damping rubber (HDR) bearings taken to failure (Kelly, 1991) are used to illustrate the possible shear stress-strain response under large shear strain ($300-600\,\%$). The results of tests performed on the HDR bearings are presented in figure 9-5, noting, the vertical axis is in units of *ksi* or kips per square inch and the vertical pressure in units of *psi* or pounds per square inch. A dashed line was superimposed on the experimental data representing the approximate shear stress-strain relationship assumed for the FE analysis. The results presented in this figure show the increase in shear modulus (stiffening) for shear strains greater than approximately $250\,\%$ for the HDR bearings and the substantial difference between the plausible response and that assumed for the FE analysis at large shear strain noting that the onset of strain stiffening in LDR would likely occur at slightly larger shear strain than with the HDR bearings.

To illustrate the level of shear strain under combined loading the maximum total and average total shear strains were estimated for two lateral offset tests. The maximum total shear strain in a hollow circular pad due to combined loading (compression and shear) is approximated according to:

$$\gamma_{t,\max} \approx 6S\varepsilon_c f_{st} + \frac{\Delta}{T_r} \tag{9-2}$$

where $6S\varepsilon_c f_{st}$ (also presented in Section 8) represents the maximum shear strain due to compressive loading (Constantinou, 1992) and Δ / T_r is the shear strain due to lateral displacement. The average total shear strain was estimated (assuming a triangular shear strain distribution) according to:

$$\gamma_{t,\text{avg}} \approx \frac{1}{3}[6S\varepsilon_c f_{st}] + \frac{\Delta}{T_r} \tag{9-3}$$

where S is the shape factor equal to 10.2 for the LDR bearings, ε_c is the compressive strain due to an applied load $P_{\max}$, f_{st} is a factor accounting for the central hole equal to 1.62 for the LDR bearings, Δ is the lateral displacement, and T_r is the total rubber thickness approximately equal to 60 mm.

TABLE 9-2 Estimated maximum and average shear strain under combined loading

ρ (MPa)	Δ / R	Δ (mm)	$P_{\max}$ (kN)	ε_c^1 $\left(\frac{\text{mm}}{\text{mm}}\right)$	$\gamma_{t,\max}$ (%)	$\gamma_{t,\text{avg}}$ (%)
2.75	0.8	61	60	0.018	177	127
9	0.8	61	180	0.073	409	204

Notes:
1. Compressive strains determined from axial load tests conducted to maximum axial load amplitude listed

Table 9-2 presents the estimated maximum and average shear strain ($\gamma_{t,\max}$ and $\gamma_{t,avg}$) values for tests performed with $\rho = 2.75\,\text{MPa}$ and $\rho = 9\,\text{MPa}$ both with a normalized lateral offset of $\Delta / R = 0.8$. From the results presented in this table, the maximum and average shear strain for $\rho = 2.75\,\text{MPa}$ and $\Delta / R = 0.8$ are $177\,\%$ and $127\,\%$, respectively. For the lateral offset test with $\rho = 9\,\text{MPa}$ and $\Delta / R = 0.8$ the maximum and average total shear strain are estimated to be $409\,\%$ and $204\,\%$, respectively. The estimated maximum total shear from the $\rho = 2.75\,\text{MPa}$ and $\Delta / R = 0.8$ test is approximately $200\,\%$, that, from figure 9-5 corresponds to a region of strain where the assumed relationship for the FE analysis would likely agree well with the plausible stress-strain response. However, for $\rho = 9\,\text{MPa}$ and $\Delta / R = 0.8$ the estimated maximum total shear strain is approximately $400\,\%$ which is well into the stiffening region for the HDR bearing and likely for the LDR bearings. A higher order stain energy density formulation could be used for the FE analysis to attempt to capture the stiffening behavior of the material, however, such formulations require extensive material testing data to accurately reproduce the various modes of deformation.

9.3 Vertical Earthquake Load

9.3.1 General

The results of earthquake simulation tests performed with three components of excitation (Transverse + Longitudinal + Vertical) were used to determined the contribution to the vertical load due to the vertical component of excitation (P_{EQ}). In this section, an equivalent linear static (ELS) procedure is used to estimate the vertical load due to vertical excitation considering: (1) the vertical stiffness of the isolators under zero lateral displacement (K_{vo}) and (2) the vertical stiffness of the isolators at the maximum horizontal displacement (K_v). The results of the ELS procedure are compared to the experimentally determined P_{EQ} values to investigate whether the reduction in vertical stiffness should be considered for calculation of the vertical load using the ELS procedure.

9.3.2 Estimation of the Vertical Load using an Equivalent Linear Static Procedure

The maximum axial load on the bearings due to vertical earthquake shaking was estimated using the spectral acceleration ($S_{a,vo}$) and the effective weight (W^*) of the isolated truss-bridge and calculated according to:

$$P_{vo} = S_{a,vo} \cdot W^* \tag{9-4}$$

where the spectral acceleration was determined from the average of the elastic response spectra generated using the recorded acceleration histories from the east (ACC9) and west (ACC3) extension platforms for an appropriate level of damping and at the equivalent vertical period of the bridge-isolation system considering the unreduced (K_{vo}) vertical stiffness of the isolators.

The elastic response spectra were generated for 1% and 2% of critical damping for the LDR and LR bearings, respectively, corresponding to the effective vertical damping determined from the results of characterization testing (see Section 5). The equivalent period of the bridge-isolation system, assuming full vertical stiffness (K_{vo}), was calculated according to:

$$T_{vo} = 2\pi\sqrt{\frac{W^*}{K_{eq,vo} \cdot g}} \tag{9-5}$$

where W^* is the effective weight of the bridge, g is the gravitational acceleration constant, and $K_{eq,vo}$ is the equivalent stiffness of the bridge-isolation system calculated as:

$$\frac{1}{K_{eq,vo}} = \frac{1}{K_{bv}} + \frac{1}{4 \cdot K_{vo}} \tag{9-6}$$

where K_{bv} is the generalized vertical stiffness of the truss-bridge equal to $119\ \text{kN/mm}$ (see Section 7) and K_{vo} is the unreduced (zero lateral displacement) vertical stiffness of an individual LDR or LR bearing determined from the results of characterization testing (see Section 5). The effective period of the bridge-isolation system (T_v) using the reduced vertical stiffness (K_v) of the LDR and LR bearings was calculated in a similar manner.

Figure 9-6 presents sample elastic response spectra generated from recorded acceleration histories from Tests 104 and 147 and illustrates the identification of the average spectral acceleration. Figure 9-6a presents elastic response spectra calculated from the recorded acceleration histories from Test 147 (corresponding to LDR in the $1.2\ \text{m}$ configuration and KJM 50 %). Also shown in this figure is the average of the two spectra from which the spectral acceleration value was determined. The equivalent period (T_{vo}) of the bridge-LDR system was estimated to be $0.098\ \text{s}$ ($10.2\ \text{Hz}$) that corresponds to an average spectral acceleration of $0.67\ \text{g}$ assuming 1% of critical damping. Figure 9-6b presents elastic response spectra generated using recorded acceleration histories from Test 104 (corresponding to LR in the 1.2 m configuration and KJM 100 %). The equivalent period of the bridge-LR system was estimated to be 0.092 s (10.9 Hz) and corresponds to an average spectral acceleration of 1.11 g assuming 2 % of critical damping.

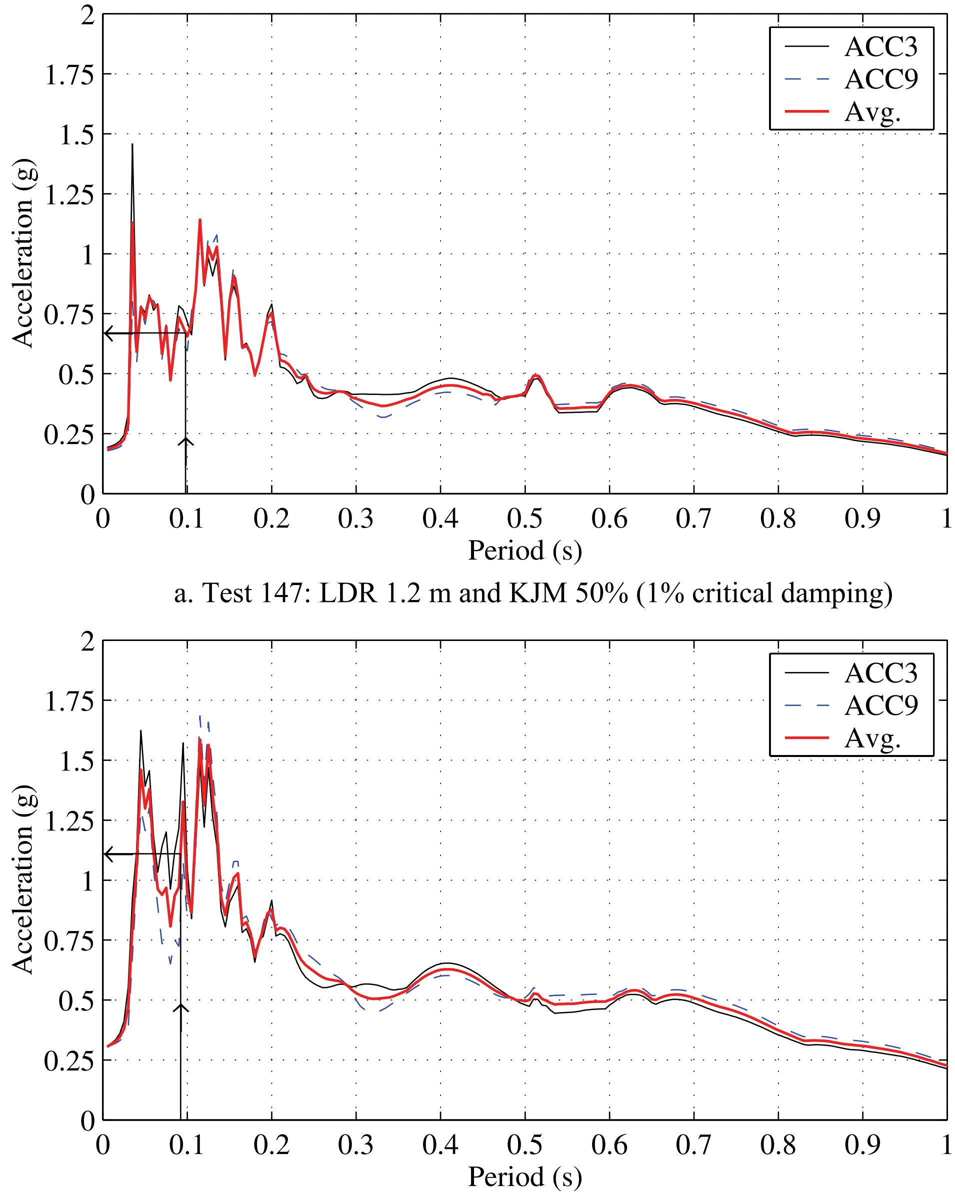

a. Test 147: LDR 1.2 m and KJM 50% (1% critical damping)

b. Test 104: LR 1.2 m and KJM 100% (2% critical damping)

FIGURE 9-6 Sample elastic response spectra and selected spectral acceleration for T_{vo} and ζ

Summary values and results of the ELS procedure using spectra from earthquake simulations performed with the LDR and LR bearings are presented in tables 9-3 and 9-4, respectively. Table 9-3 presents the estimated axial load due to the vertical component of excitation considering the unreduced vertical stiffness of the LDR bearings (K_{vo}) to compute P_{vo} and the reduced vertical stiffness (K_v) to compute P_v, respectively. Also listed in this table is the test number; a description of the excitation and support width configuration; the maximum horizontal displacement, $u_{\max}$; the equivalent bridge-isolation system stiffness assuming unreduced and reduced vertical stiffness, denoted $K_{eq,vo}$ and $K_{eq,v}$, respectively; the equivalent periods, T_{vo} and T_v calculated using (9-5); and the corresponding average spectral accelerations, $S_{a,vo}$ and $S_{a,v}$. For Test 147, a 35% percent reduction in the vertical stiffness of the LDR bearings ($1-K_v/K_{vo}$) calculated using (2-42) translates into a 13% reduction in the effective vertical stiffness ($K_{eq,v}/K_{eq,vo}$) that further translates into an approximately 5% increase in the equivalent period (T_v/T_{vo}) which, depending on the shape of the spectrum, might or might not result in a substantial difference in spectral acceleration. In this case, using the spectra generated from the recorded acceleration histories, the difference in equivalent periods resulted in a 21% difference in average spectral acceleration ($S_{a,v}/S_{a,vo}$). However, using a code specified uniform hazard spectrum (FEMA, 2000), such a difference in effective period will have no significant impact on the spectral acceleration. Similarly, table 9-4 presents values of P_{vo} and P_v for tests performed with the LR bearings. Again, although there is some variation in P_{vo} and P_v for each test, the difference between the equivalent periods (T_v and T_{vo}) is small. Values of P_{vo} and P_v presented in tables 9-3 and 9-4 are compared with the experimentally determined values (P_{EQ}) in the subsequent section.

TABLE 9-3 Calculated vertical load for LDR-bridge system using Equivalent Linear Static Procedure

Test	Description		u_{max} (mm)	$K^{1}_{eq,vo}$ $\left(\frac{kN}{mm}\right)$	$K^{2}_{eq,v}$ $\left(\frac{kN}{mm}\right)$	T^{3}_{vo} (s)	T^{3}_{v} (s)	$S^{4}_{a,vo}$ (s)	$S^{4}_{a,v}$ (g)	P^{3}_{vo} (kN)	P^{3}_{v} (kN)
24	RIO 100%	1.8 m	45.8	86.6	77.4	0.098	0.103	0.95	0.75	195	154
30	BOL 50%	1.8 m	44.2		78.0		0.103	0.68	0.74	139	151
36	KJM 50%	1.8 m	50.5		75.6		0.104	1.31	2.04	268	417
135	RIO 100%	1.2 m	45.4		77.5		0.103	0.63	0.71	128	145
141	BOL 50%	1.2 m	47.0		77.0		0.104	0.39	0.40	81	82
147	KJM 50%	1.2 m	47.3		76.8		0.104	0.67	0.69	137	141

Notes:
1. Equivalent stiffness of bridge and isolation system under zero lateral displacement (K_{vo})
2. Equivalent stiffness of bridge and isolation system at maximum displacement (K_{v})
3. Calculated using the effective weight: W^{*}=205 kN
4. Spectral acceleration for 1% critical damping

TABLE 9-4 Calculated vertical load for LR-bridge system using Equivalent Linear Static Procedure

Test	Description		u_{max} (mm)	$K^{1}_{eq,vo}$ $\left(\frac{kN}{mm}\right)$	$K^{2}_{eq,v}$ $\left(\frac{kN}{mm}\right)$	T^{3}_{vo} (s)	T^{3}_{v} (s)	$S^{4}_{a,vo}$ (s)	$S^{4}_{a,v}$ (g)	P^{3}_{vo} (kN)	P^{3}_{v} (kN)
61	BOL 100%	1.8 m	61.8	96.7	84.1	0.092	0.099	0.99	0.72	202	148
67	KJM 100%	1.8 m	53.1		87.1		0.097	1.33	1.33	273	273
73	SYL75%	1.8 m	73.7		79.7		0.102	1.34	1.03	274	211
98	BOL 100%	1.2 m	59.4		85.0		0.099	0.91	0.72	187	148
104	KJM 100%	1.2 m	51.4		87.6		0.097	1.11	1.17	228	240
110	SYL 75%	1.2 m	73.3		79.9		0.102	1.10	0.77	226	158

Notes:
1. Equivalent stiffness of bridge and isolation system under zero lateral displacement (K_{vo})
2. Equivalent stiffness of bridge and isolation system at maximum displacement (K_{v})
3. Calculated using the effective weight: W^{*}=205 kN
4. Spectral acceleration for 2% critical damping

9.3.3 Comparison of the Estimated and Experimentally Determined Vertical Load

Experimentally determined values of the vertical load due to the vertical component of excitation (P_{EQ}) were presented in Section 7 and presented, for convenience, in tables 9-5 and 9-6 for tests conducted with LDR and LR bearings, respectively. In each of these tables the maximum ($P_{EQ,\max}$) and minimum ($P_{EQ,\min}$) are reported for each test determined from the four load cell normal signals and equilibrium in the vertical direction, see (7-5). The maximum of the absolute values, P_{EQ}, was determined according to (9-7).

$$P_{EQ} = \max\left(|P_{EQ,\max}|, |P_{EQ,\min}|\right) \tag{9-7}$$

TABLE 9-5 Experimentally determined values of the vertical load from earthquake simulation with LDR bearings

Test	Description	$P_{EQ,\max}$ (kN)	$P_{EQ,\min}$ (kN)	P_{EQ} (kN)
24	RIO 100% 1.8 m	181	185	185
30	BOL 50% 1.8 m	127	128	128
36	KJM 50% 1.8 m	264	229	264
135	RIO 100% 1.2 m	127	140	140
141	BOL 50% 1.2 m	113	109	113
147	KJM 50% 1.2 m	211	185	211

TABLE 9-6 Experimentally determined values of the vertical load from earthquake simulation with LR bearings

Test	Description	$P_{EQ,\max}$ (kN)	$P_{EQ,\min}$ (kN)	P_{EQ} (kN)
61	BOL 100% 1.8 m	172	150	172
67	KJM 100% 1.8 m	278	265	278
73	SYL 75% 1.8 m	187	150	187
98	BOL 100% 1.2 m	188	176	188
104	KJM 100% 1.2 m	289	277	289
110	SYL 75% 1.2 m	198	175	198

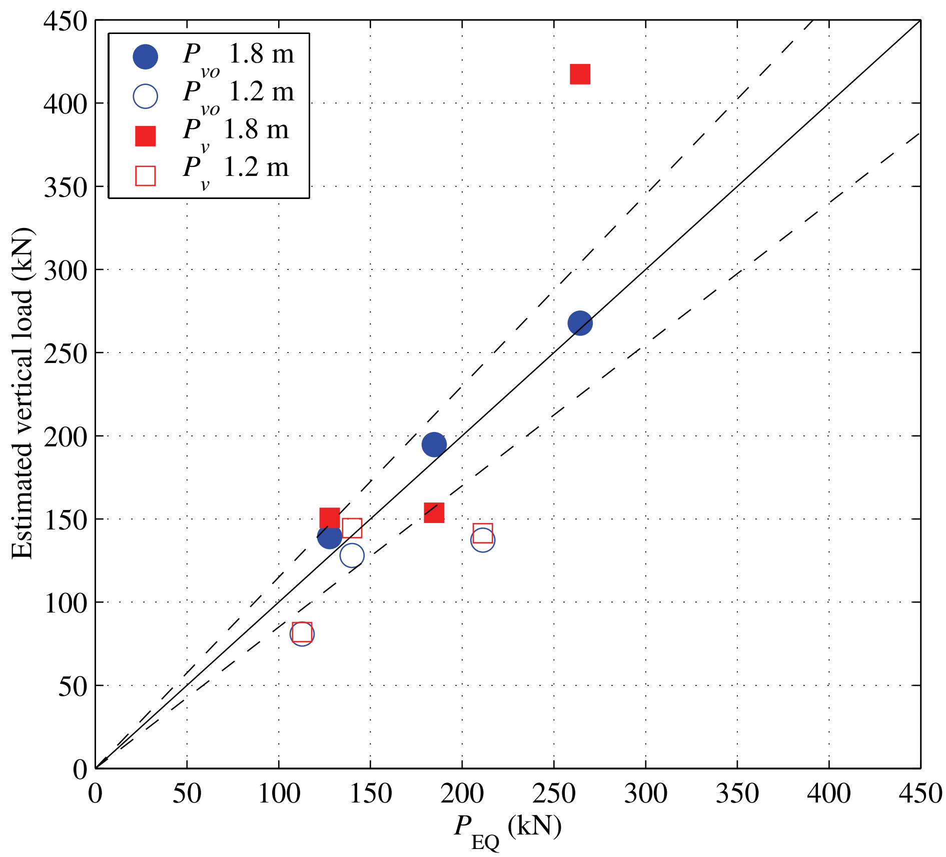

FIGURE 9-7 Comparison of estimated and experimentally determined vertical load for the LDR-isolated bridge

Figure 9-7 presents a comparison of the estimated vertical load (P_{vo} and P_v) with the experimentally determined vertical load (P_{EQ}) for simulation performed with three components of excitation (T+L+V) and the LDR bearings. In this figure the $x-$axis represents the experimentally determined vertical load (P_{EQ}) and the $y-$axis represents the estimated vertical load using the ELS procedure. The estimated values considering the unreduced vertical stiffness (P_{vo}) are identified by solid and hollow circles representing 1.8 m and 1.2 m support configuration, respectively, whereas values estimated using the reduced vertical stiffness (P_v) are identified by solid and hollow squares again representing the 1.8 m and 1.2 m support configuration. Also plotted in this figure are three reference lines, a solid line with slope equal to 1.0 and two dashed lines with slope equal to 1.15 and 0.85. From the data plotted in figure 9-7, P_{vo} and P_v estimate P_{EQ} reasonably well with the majority of data points lying within ±15 % of P_{EQ}, however, in two instances both P_{vo} and P_v under predict the axial load due to the vertical earthquake shaking, P_{EQ}. In addition, using the full vertical stiffness of the LDR bearings (K_{vo}) appears to result in a slightly improved estimate of the vertical load further suggesting the reduction in vertical stiffness might not effect the vertical response significantly. Figure 9-8 presents a comparison of P_{vo} and P_v with P_{EQ} for simulations conducted with LR bearings. The presentation of figure 9-8 is identical to that of figure 9-7. From the results presented in figure 9-8, the use of P_{vo} and P_v estimate P_{EQ} reasonably well and in close proximity to ±15 % of P_{EQ}. However, the vertical load estimated using the full vertical stiffness of the isolator (P_{vo}) conservatively predicts the experimentally determined vertical load (P_{EQ}) in more instances than P_v which was calculated with the reduced vertical stiffness.

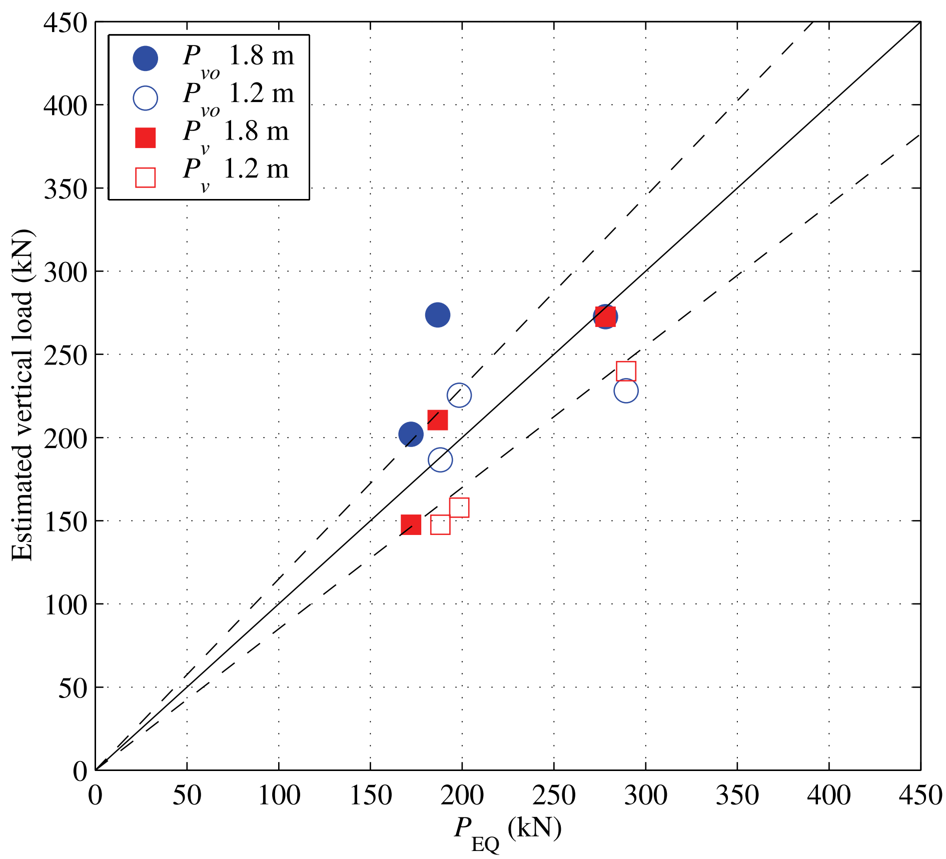

FIGURE 9-8 Comparison of estimated and experimentally determined vertical load for the LR-isolated bridge

9.4 Summary and Discussion

This section compared the results of an experimental and analytical investigation of the influence of lateral displacement on the vertical stiffness of LDR and LR seismic isolation bearings. In addition, the results of earthquake simulation testing performed on a quarter-scale isolated bridge model were compared with the results of an equivalent linear static procedure for the estimation of the vertical load due to the vertical component of excitation.

The following comments are provided based on the comparison of results from the investigation of the influence of lateral displacement on the vertical stiffness of LDR and LR bearings. Of the three formulations the piecewise linear resulted in the lowest residual (or best predictor) of the experimental data. However, the piecewise linear formulation does not capture the physical behavior and in some instances under predicts the reduction in vertical stiffness. In addition, the piecewise linear formulation was empirically formulated and might not predict well the reduction in vertical stiffness for bearings with different proportions. The two-spring formulation resulted in the second lowest residual value and over estimated the reduction in vertical stiffness for all but two cases. Importantly, the two-spring formulation captures the physical behavior, and hence the general trend of the experimental data and predicts that approximately $20\,\%$ of the unreduced vertical stiffness remains at a lateral displacement equal to the bearing diameter corroborated by the experimental data. The overlapping area formulation resulted in the largest residual and while over estimating the measured reduction in vertical stiffness for all lateral displacements, the formulation does not capture the physical behavior and predicts zero vertical stiffness at a lateral displacement equal to the bearing diameter that is not supported by the experimental data. For the lowest level of axial pressure, the FE results compared well with the results of lateral offset tests performed with the LDR bearings. The difference between the FE and experimental results for the intermediate and highest axial pressure is likely due to differences between the actual shear stress-strain behavior of the natural rubber and that assumed for the FE model at high shear strains. In addition, the FE results were shown graphically to agree well with the two-spring formulation, further validating the utility of the two-spring formulation.

From the results of the equivalent linear static procedure, no appreciable improvement in the prediction of the vertical load was observed by considering the reduction in vertical stiffness of the LDR and LR bearings when compared to the experimentally determined values. This suggests the vertical response is not significantly effected by the reduction in vertical stiffness for this particular structure, isolation system and bin of ground motions. For this study, the ELS procedure considering the unreduced vertical stiffness (K_{vo}) of the bearings resulted in reasonably good predictions of the experimentally determined vertical load, however, the accuracy (conservatism) of the procedure will likely rely on the characterization of the vertical component of excitation.

SECTION 10

SUMMARY, CONCLUSIONS AND RECOMMENDATIONS

10.1 Summary

This report presented an experimental and analytical study of the coupled horizontal-vertical response of elastomeric and lead-rubber bearings focusing on the influence of lateral displacement on the vertical stiffness. The objectives of this study were to experimentally and analytically investigate the influence of lateral displacement on the vertical stiffness of low-damping rubber (LDR) and lead-rubber (LR) bearings and to use these results to evaluate existing and proposed formulations to predict the vertical stiffness at a given lateral displacement. In addition, earthquake simulation testing was performed to investigate the coupled horizontal-vertical response of a bridge model isolated with LDR or LR bearings. The results of earthquake simulations performed with three components of excitation, namely, transverse (T), longitudinal (L) and vertical (V) were used to evaluate an equivalent linear static procedure for the estimation of the vertical load due to the vertical component of excitation. For the equivalent linear calculation the equivalent vertical period of the bridge-isolation system was calculated considering the vertical stiffness of the LDR and LR bearing under zero lateral displacement (K_{vo}) and a reduced vertical stiffness (K_v).

Three formulations were considered to predict the vertical stiffness at a given lateral displacement. The first, a two-spring formulation, based on the model of Koh and Kelly (1987) is capable of reproducing the modes of deformation of an elastomeric bearing subjected to combined loading (Kelly, 1997). In addition, the spring properties of the two-spring model can be related to the mechanical properties of an elastomeric bearing providing a physical understanding of the coupled behavior. For convenience the simplified two-spring formulation is presented again in normalized form here:

$$\frac{K_v}{K_{vo}} = \frac{1}{\left[1 + \frac{12}{\pi^2}\left(\frac{\Delta}{R}\right)^2\right]} \tag{10-1}$$

where Δ is the lateral displacement, R is the radius of the bearing and K_{vo} is the vertical stiffness under zero lateral displacement. The second formulation was based on a widely accepted procedure for the estimation of the critical buckling load of an elastomeric bearing subjected to combined compression and lateral displacement (Buckle and Liu, 1994; Naeim and Kelly, 1999). With this procedure the vertical stiffness is reduced by the ratio of the overlapping area, between the top and bottom load plates, to the bonded rubber area for lateral displacements greater than zero (see figure 2-5). Again, for convenience the overlapping area formulation is presented here:

$$\frac{K_v}{K_{vo}} = \left(\frac{A_r}{A_b}\right) \tag{10-2}$$

where A_b is the bonded rubber area equal to πR^2 and A_r is the reduced area calculated according to:

$$A_r = \frac{D^2(\phi - \sin\phi)}{4} \tag{10-3}$$

where $D = 2R$ and ϕ calculated according to (10-4).

$$\phi = 2\cos^{-1}\left(\frac{\Delta}{D}\right) \tag{10-4}$$

Although a reasonable methodology, the overlapping formulation does not fully capture the behavior of an elastomeric bearing subjected to combined loading but rather accounts for the reduction in the vertical stiffness through a column with reduced cross-sectional area predicting $K_v = 0$ at $\Delta = 2R$.

The third formulation, a piecewise linear expression, was empirically formulated based on the knowledge of full vertical stiffness at $\Delta = 0$ and experimental evidence of the vertical stiffness observed for $\Delta = 2R$. The piecewise linear formulation is presented again here:

$$\begin{aligned} \frac{K_v}{K_{vo}} &= 1 - 0.4\left(\frac{\Delta}{R}\right) && \text{for} \quad \Delta/R \le 2 \\ \frac{K_v}{K_{vo}} &= 0.2 && \text{for} \quad \Delta/R > 2 \end{aligned} \tag{10-5}$$

Although, the piecewise linear formulation offers a simple relationship it has no theoretical basis.

The results of characterization testing were used to determine the mechanical properties of the LDR and LR bearings and to estimate material properties including the shear modulus and effective yield strength of the lead-core (LR only). Due to the uncertainty of the contribution of the disproportionately thick rubber cover (12 mm) to the horizontal stiffness, the 12 mm rubber cover of LDR 5 was lathed to an approximate thickness of 3 mm and re-tested. From the results of tests performed with 12 mm and 3 mm of cover thickness, the 12 mm cover was shown to contribute substantially to the horizontal stiffness and negligibly to the vertical stiffness. The effective shear modulus (G_{eff}) and damping ratio (β_{eff}) of LDR 5 with 3 mm of cover (LDR 5M) were determined to be 0.82 MPa and $2.7\,\%$, respectively, at a shear strain amplitude of $104\,\%$ and frequency of 0.01 Hz. Results from axial load tests were used to determine the vertical stiffness of the LDR and LR bearings. From the results of these tests, the vertical stiffness was observed to vary considerably between bearings of the same type although no appreciable differences were observed from the results of horizontal shear tests. For example, the vertical stiffness of the two LDR bearings differed by $8\,\%$ and the LR bearing by $13\,\%$ from tests conducted to the largest axial load amplitude. The differences in vertical stiffness was attributed to variations in the individual rubber layer thicknesses observed after cutting one of each type of bearing in half for inspection following completion of the testing program. Experimentally determined values of the vertical stiffness were compared to theoretical predictions to evaluate the assumption of incompressible material. Assuming the material to be incompressible ($K \to \infty$) resulted in theoretical values that substantially over estimated the vertical stiffness for both the LDR and LR bearings. Theoretical values of the vertical stiffness calculated using an assumed value of the bulk modulus (K) of 2000 MPa agreed reasonable well with the experimentally determined values.

The results of the lateral offset testing showed the vertical stiffness of the LDR and LR bearings reduces with increasing lateral offset over the range of lateral displacement considered in this study. At a lateral displacement equal to the bearing diameter ($\Delta = 2R$) the vertical stiffness of the LDR and LR bearings was determined to be approximately $20\,\%$ of the vertical stiffness at zero lateral displacement (K_{vo}). The two-spring formulation was shown to predict the reduction in vertical stiffness reasonably well typically over estimating the experimental data for each lateral displacement. For the LDR bearings, better agreement was observed for the lower and intermediate axial load amplitudes.

A 3D finite element (FE) model of a LDR bearing was developed in ABAQUS and analyzed to further investigate the influence of lateral displacement on the vertical stiffness of elastomeric bearings. Bounding values of the tangent shear modulus (G) determined from characterization tests performed on LDR 5M were used to perform validation compression and shear analyses. The results of the FE analyses showed a substantial reduction in vertical stiffness over the range of lateral displacements considered in the experimental studies; the results of the FE analysis agreed well with the experimental data from the lower and intermediate axial load amplitudes and the predicted reduction using the two-spring formulation. Although the exact value of the bulk modulus could not be determined, the FE solutions did not vary substantially for values of the bulk modulus ranging from $2000\ \text{MPa}$ to $2500\ \text{MPa}$, which are typical values for lightly filled natural rubber. Results of the FE analyses performed using the initial tangent shear modulus ($0.83\ \text{MPa}$) overestimated the experimentally determined vertical stiffness for LDR 5M and 6 by approximately 20%. However, the results of FE analysis performed using the tangent shear modulus ($0.72\ \text{MPa}$) at a rubber shear strain of 100% (the estimated average shear strain under the compressive loading conditions) showed better agreement with the experimentally determined values from LDR 5M and 6 with a 10% and 5% difference, respectively.

Earthquake simulation testing was performed on a quarter-scale isolated bridge model with isolation systems composed entirely of LR or LDR bearings. The results of earthquake simulation testing were used to investigate the influence of multiple components of excitation on the response of the isolation system and individual bearings and to investigate the effect of the reduction in vertical stiffness observed with the LDR and LR bearings on the vertical response. In addition, white-noise testing was performed on the bridge model in the fixed base configuration to identify natural frequencies and to estimate the generalized stiffness of the truss-bridge. From the results of white-noise testing, the vertical frequency of the loaded truss-bridge was determined to be approximately $12\ \text{Hz}$ from which the generalized vertical stiffness was determined to be $118\ \text{kN/mm}$. Because the vertical stiffness is on the order of the combined vertical stiffness (under zero lateral displacement) of the LR and LDR bearings, $320\ \text{kN/mm}$ and $520\ \text{kN/mm}$, respectively, the equivalent stiffness of the bridge-isolation system was considered for the calculation of the vertical frequency of the system. A comparison of the maximum response quantities from simulations performed with T, T+L, and T+L+V components of excitation illustrated the impact of axial-load variation on the horizontal response of the LDR and LR bearings. The influence of the vertical component of excitation on the horizontal response was obscured by the axial load fluctuation generated by the overturning moment in both the $1.8\,\text{m}$ and $1.2\,\text{m}$ support-width configurations. Significant amplification in the vertical response was observed from simulations performed with all three components of excitation (T+L+V) for both the LR and LDR isolation systems. Transfer functions generated from the vertical response showed amplification of the response in close proximity to the frequency of the bridge-isolation system considering the zero lateral displacement and reduced vertical stiffness of the individual isolation bearings. The most pronounced amplification were observed from the results of simulation performed using the 1995 Kobe JMA records. Finally, an equivalent linear static procedure was used to estimation the vertical load on the isolation system due to the vertical component of excitation. The results of the equivalent linear procedure were compared with values determined experimentally to evaluate the procedure and to determined whether the reduction in vertical stiffness should be considered for the calculation of the vertical load due to vertical ground shaking.

10.2 Conclusions

The key conclusions of this study are as follows:

1. The vertical stiffness of the low-damping rubber (LDR) and lead-rubber (LR) bearings decreased with increasing lateral displacement. For the LDR and LR bearings the vertical stiffness reduced by $40-50\,\%$ at lateral displacements equivalent to $150\,\%$ rubber shear strain.

2. At a lateral displacement equal to the bonded rubber diameter ($\Delta / R = 2$), the vertical stiffness of the LDR and LR bearings was observed to be approximately $20\,\%$ of the vertical stiffness at zero lateral displacement (K_{vo}).

3. The Koh-Kelly two-spring formulation [(2-42) and (10-1)] compared well with the experimentally determined vertical stiffness at each lateral offset with the exception of tests performed on the LDR bearings at the largest axial load amplitude. The deviation between the two-spring formulation and the experimental data was attributed to the likely substantial increase in shear modulus for the large shear strains (greater than $300\,\%$) occurring with the largest axial load amplitude and various lateral offsets.

4. The overlapping area formulation [(2-43) and (10-2)] substantially over predicted the reduction in vertical stiffness for most lateral offsets and predicts zero vertical stiffness at a lateral displacement equal to two times the radius of the bearing: a result that does not agree with experimental data.

5. The piecewise linear formulation [(2-46) and (10-5)] agreed well with the experimental data and resulted in the lowest cumulative residual. However, the formulation has no theoretical basis and does capture the trends observed from the experimental data.

6. The two-spring formulation was further corroborated by the results of the FE analysis that accounted for material and geometric nonlinearities, although the neo-Hookean model was unable to capture suspected stiffening behavior of the natural rubber at large shear strains.

7. Significant amplification of the vertical response was observed for both the LDR and LR isolation systems suggesting the use of the peak ground acceleration (PGA) of the vertical component will lead to un-conservative estimates of the vertical load due to vertical ground shaking. The flexibility of the isolation or isolation-structural system should be considering for the purpose of estimating the vertical load using the equivalent linear static procedure.

8. The equivalent linear static procedure considering the full vertical stiffness of the bearings resulted in estimates of the vertical load on the isolation system that agreed reasonably well with the experimentally determined values. For this bridge-isolation system, considering the reduced vertical stiffness of the individual bearings for the equivalent linear static procedure lead to no substantial improvement in the estimated vertical load as compared with the values estimated using the vertical stiffness at zero lateral displacement. It is important to note the spectral accelerations used for the equivalent linear static procedure were determined from response spectra generated from recorded acceleration histories and that the accuracy of this procedure will likely depend on the characterization of the vertical design spectrum.

10.3 Recommendations for Future Research

The following recommendations are provided based on the observations, results and finding of this study:

1. The LDR and LR bearings used for this experimental investigation were identically proportioned resulting in shape factors of 10.2 and 12.2, respectively, the difference being due to the addition of the lead-core restraining the rubber layers from bulging along the inner circumference of each bonded rubber layer. Typically, shape factors for elastomeric bearings range from 10 to 20 although values greater than 15 are undesirable due to the large shear strains that develop under design level compressive loading. Further experimental validation of the two-spring formulations is recommended for a wide range of shape factors.

2. Update the current mathematical model for elastomeric and lead-rubber bearings, that typically uses a coupled Bouc-Wen formulation for the horizontal response and a linear spring with constant stiffness for the vertical direction, with the formulations derived from the two-spring model (Koh and Kelly, 1987) that will account for the influence of axial load on the horizontal stiffness and the influence of lateral displacement on the vertical stiffness.

3. A comprehensive parametric study is needed to determine the influence of the vertical component on the response of structures isolated with elastomeric and lead-rubber bearings accounting for a range of superstructure flexibility. The results of this study should provide insight into the correlation between the maximum horizontal and vertical responses.

SECTION 11

REFERENCES

AASHTO. (1999). *Guide specifications for seismic isolation design*, AASHTO, Washington, D.C.

AISC. (2001). *Manual of Steel construction: Load and Resistance Factor Design. 3rd Edition*, American Institute of Steel Construction, Chicago, IL.

Bathe, K. J. (1996). Finite element procedures, Prentice Hall, Englewood Cliffs, N.J.

Bracci, J. M., Reinhorn, A. M., and Mander, J. B. (1992). "Seismic Resistance of Reinforced Concrete Frame Structures Designed Only for Gravity Loads: Part I - Design and Properties of a One-Third Scale Model Structure." *Technical Report NCEER-92-0027*, National Center for Earthquake Engineering Research, State University of New York at Buffalo, Buffalo, N.Y.

Buckle, I., Nagarajaiah, S., and Ferrell, K. (2002). "Stability of elastomeric isolation bearings: Experimental study." *Journal of Structural Engineering,* ASCE, 128(1), 3-11.

Buckle, I. G., and Liu, H. (1994). "Experimental determination of critical loads of elastomeric isolator at high shear strain." *NCEER Bull.*, 8(3), 1-5.

Chalhoub, M. S., and Kelly, J. M. (1990). "Effect of Bulk Compressibility on the Stiffness of Cylindrical Base Isolation Bearings." *International Journal of Solids Structures*, 26(7), 743-760.

Clough, R. W., and Penzien, J. (1975). *Dynamics of structures*, McGraw-Hill, New York.

Constantinou, M. C., Kartoum, A., and Kelly, J. M. (1992). "Analysis of compression of hollow circular elastomeric bearings." *Engineering Structures*, 14(2), 103-111.

Cook, R. D., Malkus, David S., Plesha, Michael E., Witt, Robert J. (2002). *Concepts and applications of finite element analysis*, Wiley, New York.

CSI. (2002). *SAP2000: Analysis Reference Manual: Version 8.0*, Berkeley, CA.

FEMA. (2000). *NEHRP Recommended Provisions for Seismic Regulations for New Buildings and Other Structures*, FEMA 368, Building Seismic Safety Council for the Federal Emergency Management Agency, Washington, D.C.

Harris, H. G., and Sabnis, G. M. (1999). *Structural modeling and experimental techniques*, CRC Press, Boca Raton.

HITEC. (1998a). *Evaluation findings for Skellerup base isolation elastomeric bearings*, Civil Engineering Research Foundation, Washington, DC.

HITEC. (1998b). *Evaluation findings for Dynamic Isolation Systems, Inc. elastomeric bearings*, Civil Engineering Research Foundation, Washington, DC.

HKS. (2004). *ABAQUS Standard User's Manual: Version 6.5*. Hibbitt, Karlsson & Sorensen, Inc., Pawtucket, RI.

Huang, W. H. (2002). "Bi-directional Testing, Modeling, and System Response of Seismically Isolated Bridges," *Ph.D. Dissertation*, University of California, Berkeley, Berkeley.

Kasalanati, A., and Constantinou, M. C. (1999). "Experimental Study of Bridge Elastomeric and Other Isolation and Energy Dissipation Systems with Emphasis on Uplift Prevention and High Velocity Near-Source Seismic Excitation." *Technical Report MCEER-99-0004*, Multidisciplinary Center for Earthquake Engineering Research, State University of New York at Buffalo, Buffalo, N.Y.

Kelly, J. M. (1991). "Dynamic and failure characteristics of Bridgestone isolation bearings." *Rep. UCB/EERC-91/04*, Earthquake Engineering Research Center, College of Engineering, University of California, Berkeley, Calif.

Kelly, J. M. (1997). *Earthquake-resistant design with rubber*, New York, London.

Koh, C. G., and Kelly, J. M. (1987). "Effects of axial load on elastomeric isolation bearings." *UBC/EERC-86/12*, Earthquake Engineering Research Center, College of Engineering, University of California, Berkeley, Calif.

Math Works. (1999). *MATLAB Function Reference: Version 5*, The MathWorks Inc., Natick, MA.

Mokha, A. S., Constantinou, M. C., and Reinhorn, A. M. (1993). "Verification of friction model of teflon bearings under triaxial load." *Journal of Structural Engineering*, ASCE, 119(1), 240-261.

Mosqueda, G., Whittaker, A. S., and Fenves, G. L. (2004). "Characterization and modeling of friction pendulum bearings subjected to multiple components of excitation." *Journal of Structural Engineering,* ASCE, 130(3), 433-442.

Naeim, F., and Kelly, J. M. (1999). *Design of seismic isolated structures : from theory to practice*, John Wiley.

Nagarajaiah, S., and Ferrell, K. (1999). "Stability of elastomeric seismic isolation bearings." *Journal of Structural Engineering,* ASCE, 125(9), 946-954.

Nagarajaiah, S., Reinhorn, A. M., and Constantinou, M. C. (1991). "Nonlinear dynamic analysis of 3-d-base-isolated structures." *Journal of Structural Engineering,* ASCE, 117, 2035-2054.

PEER. (2004). "Pacific Earthquake Engineering Research: Strong motion database." <http://peer.berkeley.edu/smcat/>.

Reinhorn, A. (2005). "CIE616: Experimental Methods in Structural Engineering." *Course notes*, State University of New York, University at Buffalo.

Sabnis, G. M. (1983). *Structural modeling and experimental techniques*, Prentice-Hall, Englewood Cliffs, N.J.

SEESL. (2005). "State University of New York at Buffalo: Structural Engineering and Earthquake Simulation Laboratory." <http://www.nees.buffalo.edu/>.

Stanton, J. F. and Roeder, C. W. (1982), "Elastomeric Bearings Design, Construction, and Materials", *NCHRCP Report 248*, Transportation Research Board, Washington, D.C.

Note

Appendices A through D (pages 223-294) in “A Study of the Coupled Horizontal-Vertical Behavior of Elastomeric and Lead-Rubber Seismic Isolation Bearings” are included in PDF format on the CD in the back of this book. The title and page numbers are as follows:

MCEER Technical Reports

MCEER publishes technical reports on a variety of subjects written by authors funded through MCEER. These reports are available from both MCEER Publications and the National Technical Information Service (NTIS). Requests for reports should be directed to MCEER Publications, MCEER, University at Buffalo, State University of New York, Red Jacket Quadrangle, Buffalo, New York 14261. Reports can also be requested through NTIS, 5285 Port Royal Road, Springfield, Virginia 22161. NTIS accession numbers are shown in parenthesis, if available.

NCEER-87-0001 "First-Year Program in Research, Education and Technology Transfer," 3/5/87, (PB88-134275, A04, MF-A01).

NCEER-87-0002 "Experimental Evaluation of Instantaneous Optimal Algorithms for Structural Control," by R.C. Lin, T.T. Soong and A.M. Reinhorn, 4/20/87, (PB88-134341, A04, MF-A01).

NCEER-87-0003 "Experimentation Using the Earthquake Simulation Facilities at University at Buffalo," by A.M. Reinhorn and R.L. Ketter, to be published.

NCEER-87-0004 "The System Characteristics and Performance of a Shaking Table," by J.S. Hwang, K.C. Chang and G.C. Lee, 6/1/87, (PB88-134259, A03, MF-A01). This report is available only through NTIS (see address given above).

NCEER-87-0005 "A Finite Element Formulation for Nonlinear Viscoplastic Material Using a Q Model," by O. Gyebi and G. Dasgupta, 11/2/87, (PB88-213764, A08, MF-A01).

NCEER-87-0006 "Symbolic Manipulation Program (SMP) - Algebraic Codes for Two and Three Dimensional Finite Element Formulations," by X. Lee and G. Dasgupta, 11/9/87, (PB88-218522, A05, MF-A01).

NCEER-87-0007 "Instantaneous Optimal Control Laws for Tall Buildings Under Seismic Excitations," by J.N. Yang, A. Akbarpour and P. Ghaemmaghami, 6/10/87, (PB88-134333, A06, MF-A01). This report is only available through NTIS (see address given above).

NCEER-87-0008 "IDARC: Inelastic Damage Analysis of Reinforced Concrete Frame - Shear-Wall Structures," by Y.J. Park, A.M. Reinhorn and S.K. Kunnath, 7/20/87, (PB88-134325, A09, MF-A01). This report is only available through NTIS (see address given above).

NCEER-87-0009 "Liquefaction Potential for New York State: A Preliminary Report on Sites in Manhattan and Buffalo," by M. Budhu, V. Vijayakumar, R.F. Giese and L. Baumgras, 8/31/87, (PB88-163704, A03, MF-A01). This report is available only through NTIS (see address given above).

NCEER-87-0010 "Vertical and Torsional Vibration of Foundations in Inhomogeneous Media," by A.S. Veletsos and K.W. Dotson, 6/1/87, (PB88-134291, A03, MF-A01). This report is only available through NTIS (see address given above).

NCEER-87-0011 "Seismic Probabilistic Risk Assessment and Seismic Margins Studies for Nuclear Power Plants," by Howard H.M. Hwang, 6/15/87, (PB88-134267, A03, MF-A01). This report is only available through NTIS (see address given above).

NCEER-87-0012 "Parametric Studies of Frequency Response of Secondary Systems Under Ground-Acceleration Excitations," by Y. Yong and Y.K. Lin, 6/10/87, (PB88-134309, A03, MF-A01). This report is only available through NTIS (see address given above).

NCEER-87-0013 "Frequency Response of Secondary Systems Under Seismic Excitation," by J.A. HoLung, J. Cai and Y.K. Lin, 7/31/87, (PB88-134317, A05, MF-A01). This report is only available through NTIS (see address given above).

NCEER-87-0014 "Modelling Earthquake Ground Motions in Seismically Active Regions Using Parametric Time Series Methods," by G.W. Ellis and A.S. Cakmak, 8/25/87, (PB88-134283, A08, MF-A01). This report is only available through NTIS (see address given above).

NCEER-87-0015 "Detection and Assessment of Seismic Structural Damage," by E. DiPasquale and A.S. Cakmak, 8/25/87, (PB88-163712, A05, MF-A01). This report is only available through NTIS (see address given above).

NCEER-87-0016 "Pipeline Experiment at Parkfield, California," by J. Isenberg and E. Richardson, 9/15/87, (PB88-163720, A03, MF-A01). This report is available only through NTIS (see address given above).

NCEER-87-0017 "Digital Simulation of Seismic Ground Motion," by M. Shinozuka, G. Deodatis and T. Harada, 8/31/87, (PB88-155197, A04, MF-A01). This report is available only through NTIS (see address given above).

NCEER-87-0018 "Practical Considerations for Structural Control: System Uncertainty, System Time Delay and Truncation of Small Control Forces," J.N. Yang and A. Akbarpour, 8/10/87, (PB88-163738, A08, MF-A01). This report is only available through NTIS (see address given above).

NCEER-87-0019 "Modal Analysis of Nonclassically Damped Structural Systems Using Canonical Transformation," by J.N. Yang, S. Sarkani and F.X. Long, 9/27/87, (PB88-187851, A04, MF-A01).

NCEER-87-0020 "A Nonstationary Solution in Random Vibration Theory," by J.R. Red-Horse and P.D. Spanos, 11/3/87, (PB88-163746, A03, MF-A01).

NCEER-87-0021 "Horizontal Impedances for Radially Inhomogeneous Viscoelastic Soil Layers," by A.S. Veletsos and K.W. Dotson, 10/15/87, (PB88-150859, A04, MF-A01).

NCEER-87-0022 "Seismic Damage Assessment of Reinforced Concrete Members," by Y.S. Chung, C. Meyer and M. Shinozuka, 10/9/87, (PB88-150867, A05, MF-A01). This report is available only through NTIS (see address given above).

NCEER-87-0023 "Active Structural Control in Civil Engineering," by T.T. Soong, 11/11/87, (PB88-187778, A03, MF-A01).

NCEER-87-0024 "Vertical and Torsional Impedances for Radially Inhomogeneous Viscoelastic Soil Layers," by K.W. Dotson and A.S. Veletsos, 12/87, (PB88-187786, A03, MF-A01).

NCEER-87-0025 "Proceedings from the Symposium on Seismic Hazards, Ground Motions, Soil-Liquefaction and Engineering Practice in Eastern North America," October 20-22, 1987, edited by K.H. Jacob, 12/87, (PB88-188115, A23, MF-A01). This report is available only through NTIS (see address given above).

NCEER-87-0026 "Report on the Whittier-Narrows, California, Earthquake of October 1, 1987," by J. Pantelic and A. Reinhorn, 11/87, (PB88-187752, A03, MF-A01). This report is available only through NTIS (see address given above).

NCEER-87-0027 "Design of a Modular Program for Transient Nonlinear Analysis of Large 3-D Building Structures," by S. Srivastav and J.F. Abel, 12/30/87, (PB88-187950, A05, MF-A01). This report is only available through NTIS (see address given above).

NCEER-87-0028 "Second-Year Program in Research, Education and Technology Transfer," 3/8/88, (PB88-219480, A04, MF-A01).

NCEER-88-0001 "Workshop on Seismic Computer Analysis and Design of Buildings With Interactive Graphics," by W. McGuire, J.F. Abel and C.H. Conley, 1/18/88, (PB88-187760, A03, MF-A01). This report is only available through NTIS (see address given above).

NCEER-88-0002 "Optimal Control of Nonlinear Flexible Structures," by J.N. Yang, F.X. Long and D. Wong, 1/22/88, (PB88-213772, A06, MF-A01).

NCEER-88-0003 "Substructuring Techniques in the Time Domain for Primary-Secondary Structural Systems," by G.D. Manolis and G. Juhn, 2/10/88, (PB88-213780, A04, MF-A01).

NCEER-88-0004 "Iterative Seismic Analysis of Primary-Secondary Systems," by A. Singhal, L.D. Lutes and P.D. Spanos, 2/23/88, (PB88-213798, A04, MF-A01).

NCEER-88-0005 "Stochastic Finite Element Expansion for Random Media," by P.D. Spanos and R. Ghanem, 3/14/88, (PB88-213806, A03, MF-A01).

NCEER-88-0006 "Combining Structural Optimization and Structural Control," by F.Y. Cheng and C.P. Pantelides, 1/10/88, (PB88-213814, A05, MF-A01).

NCEER-88-0007 "Seismic Performance Assessment of Code-Designed Structures," by H.H-M. Hwang, J-W. Jaw and H-J. Shau, 3/20/88, (PB88-219423, A04, MF-A01). This report is only available through NTIS (see address given above).

NCEER-88-0008 "Reliability Analysis of Code-Designed Structures Under Natural Hazards," by H.H-M. Hwang, H. Ushiba and M. Shinozuka, 2/29/88, (PB88-229471, A07, MF-A01). This report is only available through NTIS (see address given above).

NCEER-88-0009 "Seismic Fragility Analysis of Shear Wall Structures," by J-W Jaw and H.H-M. Hwang, 4/30/88, (PB89-102867, A04, MF-A01).

NCEER-88-0010 "Base Isolation of a Multi-Story Building Under a Harmonic Ground Motion - A Comparison of Performances of Various Systems," by F-G Fan, G. Ahmadi and I.G. Tadjbakhsh, 5/18/88, (PB89-122238, A06, MF-A01). This report is only available through NTIS (see address given above).

NCEER-88-0011 "Seismic Floor Response Spectra for a Combined System by Green's Functions," by F.M. Lavelle, L.A. Bergman and P.D. Spanos, 5/1/88, (PB89-102875, A03, MF-A01).

NCEER-88-0012 "A New Solution Technique for Randomly Excited Hysteretic Structures," by G.Q. Cai and Y.K. Lin, 5/16/88, (PB89-102883, A03, MF-A01).

NCEER-88-0013 "A Study of Radiation Damping and Soil-Structure Interaction Effects in the Centrifuge," by K. Weissman, supervised by J.H. Prevost, 5/24/88, (PB89-144703, A06, MF-A01).

NCEER-88-0014 "Parameter Identification and Implementation of a Kinematic Plasticity Model for Frictional Soils," by J.H. Prevost and D.V. Griffiths, to be published.

NCEER-88-0015 "Two- and Three- Dimensional Dynamic Finite Element Analyses of the Long Valley Dam," by D.V. Griffiths and J.H. Prevost, 6/17/88, (PB89-144711, A04, MF-A01).

NCEER-88-0016 "Damage Assessment of Reinforced Concrete Structures in Eastern United States," by A.M. Reinhorn, M.J. Seidel, S.K. Kunnath and Y.J. Park, 6/15/88, (PB89-122220, A04, MF-A01). This report is only available through NTIS (see address given above).

NCEER-88-0017 "Dynamic Compliance of Vertically Loaded Strip Foundations in Multilayered Viscoelastic Soils," by S. Ahmad and A.S.M. Israil, 6/17/88, (PB89-102891, A04, MF-A01).

NCEER-88-0018 "An Experimental Study of Seismic Structural Response With Added Viscoelastic Dampers," by R.C. Lin, Z. Liang, T.T. Soong and R.H. Zhang, 6/30/88, (PB89-122212, A05, MF-A01). This report is available only through NTIS (see address given above).

NCEER-88-0019 "Experimental Investigation of Primary - Secondary System Interaction," by G.D. Manolis, G. Juhn and A.M. Reinhorn, 5/27/88, (PB89-122204, A04, MF-A01).

NCEER-88-0020 "A Response Spectrum Approach For Analysis of Nonclassically Damped Structures," by J.N. Yang, S. Sarkani and F.X. Long, 4/22/88, (PB89-102909, A04, MF-A01).

NCEER-88-0021 "Seismic Interaction of Structures and Soils: Stochastic Approach," by A.S. Veletsos and A.M. Prasad, 7/21/88, (PB89-122196, A04, MF-A01). This report is only available through NTIS (see address given above).

NCEER-88-0022 "Identification of the Serviceability Limit State and Detection of Seismic Structural Damage," by E. DiPasquale and A.S. Cakmak, 6/15/88, (PB89-122188, A05, MF-A01). This report is available only through NTIS (see address given above).

NCEER-88-0023 "Multi-Hazard Risk Analysis: Case of a Simple Offshore Structure," by B.K. Bhartia and E.H. Vanmarcke, 7/21/88, (PB89-145213, A05, MF-A01).

NCEER-88-0024 "Automated Seismic Design of Reinforced Concrete Buildings," by Y.S. Chung, C. Meyer and M. Shinozuka, 7/5/88, (PB89-122170, A06, MF-A01). This report is available only through NTIS (see address given above).

NCEER-88-0025 "Experimental Study of Active Control of MDOF Structures Under Seismic Excitations," by L.L. Chung, R.C. Lin, T.T. Soong and A.M. Reinhorn, 7/10/88, (PB89-122600, A04, MF-A01).

NCEER-88-0026 "Earthquake Simulation Tests of a Low-Rise Metal Structure," by J.S. Hwang, K.C. Chang, G.C. Lee and R.L. Ketter, 8/1/88, (PB89-102917, A04, MF-A01).

NCEER-88-0027 "Systems Study of Urban Response and Reconstruction Due to Catastrophic Earthquakes," by F. Kozin and H.K. Zhou, 9/22/88, (PB90-162348, A04, MF-A01).

NCEER-88-0028 "Seismic Fragility Analysis of Plane Frame Structures," by H.H-M. Hwang and Y.K. Low, 7/31/88, (PB89-131445, A06, MF-A01).

NCEER-88-0029 "Response Analysis of Stochastic Structures," by A. Kardara, C. Bucher and M. Shinozuka, 9/22/88, (PB89-174429, A04, MF-A01).

NCEER-88-0030 "Nonnormal Accelerations Due to Yielding in a Primary Structure," by D.C.K. Chen and L.D. Lutes, 9/19/88, (PB89-131437, A04, MF-A01).

NCEER-88-0031 "Design Approaches for Soil-Structure Interaction," by A.S. Veletsos, A.M. Prasad and Y. Tang, 12/30/88, (PB89-174437, A03, MF-A01). This report is available only through NTIS (see address given above).

NCEER-88-0032 "A Re-evaluation of Design Spectra for Seismic Damage Control," by C.J. Turkstra and A.G. Tallin, 11/7/88, (PB89-145221, A05, MF-A01).

NCEER-88-0033 "The Behavior and Design of Noncontact Lap Splices Subjected to Repeated Inelastic Tensile Loading," by V.E. Sagan, P. Gergely and R.N. White, 12/8/88, (PB89-163737, A08, MF-A01).

NCEER-88-0034 "Seismic Response of Pile Foundations," by S.M. Mamoon, P.K. Banerjee and S. Ahmad, 11/1/88, (PB89-145239, A04, MF-A01).

NCEER-88-0035 "Modeling of R/C Building Structures With Flexible Floor Diaphragms (IDARC2)," by A.M. Reinhorn, S.K. Kunnath and N. Panahshahi, 9/7/88, (PB89-207153, A07, MF-A01).

NCEER-88-0036 "Solution of the Dam-Reservoir Interaction Problem Using a Combination of FEM, BEM with Particular Integrals, Modal Analysis, and Substructuring," by C-S. Tsai, G.C. Lee and R.L. Ketter, 12/31/88, (PB89-207146, A04, MF-A01).

NCEER-88-0037 "Optimal Placement of Actuators for Structural Control," by F.Y. Cheng and C.P. Pantelides, 8/15/88, (PB89-162846, A05, MF-A01).

NCEER-88-0038 "Teflon Bearings in Aseismic Base Isolation: Experimental Studies and Mathematical Modeling," by A. Mokha, M.C. Constantinou and A.M. Reinhorn, 12/5/88, (PB89-218457, A10, MF-A01). This report is available only through NTIS (see address given above).

NCEER-88-0039 "Seismic Behavior of Flat Slab High-Rise Buildings in the New York City Area," by P. Weidlinger and M. Ettouney, 10/15/88, (PB90-145681, A04, MF-A01).

NCEER-88-0040 "Evaluation of the Earthquake Resistance of Existing Buildings in New York City," by P. Weidlinger and M. Ettouney, 10/15/88, to be published.

NCEER-88-0041 "Small-Scale Modeling Techniques for Reinforced Concrete Structures Subjected to Seismic Loads," by W. Kim, A. El-Attar and R.N. White, 11/22/88, (PB89-189625, A05, MF-A01).

NCEER-88-0042 "Modeling Strong Ground Motion from Multiple Event Earthquakes," by G.W. Ellis and A.S. Cakmak, 10/15/88, (PB89-174445, A03, MF-A01).

NCEER-88-0043 "Nonstationary Models of Seismic Ground Acceleration," by M. Grigoriu, S.E. Ruiz and E. Rosenblueth, 7/15/88, (PB89-189617, A04, MF-A01).

NCEER-88-0044 "SARCF User's Guide: Seismic Analysis of Reinforced Concrete Frames," by Y.S. Chung, C. Meyer and M. Shinozuka, 11/9/88, (PB89-174452, A08, MF-A01).

NCEER-88-0045 "First Expert Panel Meeting on Disaster Research and Planning," edited by J. Pantelic and J. Stoyle, 9/15/88, (PB89-174460, A05, MF-A01).

NCEER-88-0046 "Preliminary Studies of the Effect of Degrading Infill Walls on the Nonlinear Seismic Response of Steel Frames," by C.Z. Chrysostomou, P. Gergely and J.F. Abel, 12/19/88, (PB89-208383, A05, MF-A01).

NCEER-88-0047 "Reinforced Concrete Frame Component Testing Facility - Design, Construction, Instrumentation and Operation," by S.P. Pessiki, C. Conley, T. Bond, P. Gergely and R.N. White, 12/16/88, (PB89-174478, A04, MF-A01).

NCEER-89-0001 "Effects of Protective Cushion and Soil Compliancy on the Response of Equipment Within a Seismically Excited Building," by J.A. HoLung, 2/16/89, (PB89-207179, A04, MF-A01).

NCEER-89-0002 "Statistical Evaluation of Response Modification Factors for Reinforced Concrete Structures," by H.H-M. Hwang and J-W. Jaw, 2/17/89, (PB89-207187, A05, MF-A01).

NCEER-89-0003 "Hysteretic Columns Under Random Excitation," by G-Q. Cai and Y.K. Lin, 1/9/89, (PB89-196513, A03, MF-A01).

NCEER-89-0004 "Experimental Study of `Elephant Foot Bulge' Instability of Thin-Walled Metal Tanks," by Z-H. Jia and R.L. Ketter, 2/22/89, (PB89-207195, A03, MF-A01).

NCEER-89-0005 "Experiment on Performance of Buried Pipelines Across San Andreas Fault," by J. Isenberg, E. Richardson and T.D. O'Rourke, 3/10/89, (PB89-218440, A04, MF-A01). This report is available only through NTIS (see address given above).

NCEER-89-0006 "A Knowledge-Based Approach to Structural Design of Earthquake-Resistant Buildings," by M. Subramani, P. Gergely, C.H. Conley, J.F. Abel and A.H. Zaghw, 1/15/89, (PB89-218465, A06, MF-A01).

NCEER-89-0007 "Liquefaction Hazards and Their Effects on Buried Pipelines," by T.D. O'Rourke and P.A. Lane, 2/1/89, (PB89-218481, A09, MF-A01).

NCEER-89-0008 "Fundamentals of System Identification in Structural Dynamics," by H. Imai, C-B. Yun, O. Maruyama and M. Shinozuka, 1/26/89, (PB89-207211, A04, MF-A01).

NCEER-89-0009 "Effects of the 1985 Michoacan Earthquake on Water Systems and Other Buried Lifelines in Mexico," by A.G. Ayala and M.J. O'Rourke, 3/8/89, (PB89-207229, A06, MF-A01).

NCEER-89-R010 "NCEER Bibliography of Earthquake Education Materials," by K.E.K. Ross, Second Revision, 9/1/89, (PB90-125352, A05, MF-A01). This report is replaced by NCEER-92-0018.

NCEER-89-0011 "Inelastic Three-Dimensional Response Analysis of Reinforced Concrete Building Structures (IDARC-3D), Part I - Modeling," by S.K. Kunnath and A.M. Reinhorn, 4/17/89, (PB90-114612, A07, MF-A01). This report is available only through NTIS (see address given above).

NCEER-89-0012 "Recommended Modifications to ATC-14," by C.D. Poland and J.O. Malley, 4/12/89, (PB90-108648, A15, MF-A01).

NCEER-89-0013 "Repair and Strengthening of Beam-to-Column Connections Subjected to Earthquake Loading," by M. Corazao and A.J. Durrani, 2/28/89, (PB90-109885, A06, MF-A01).

NCEER-89-0014 "Program EXKAL2 for Identification of Structural Dynamic Systems," by O. Maruyama, C-B. Yun, M. Hoshiya and M. Shinozuka, 5/19/89, (PB90-109877, A09, MF-A01).

NCEER-89-0015 "Response of Frames With Bolted Semi-Rigid Connections, Part I - Experimental Study and Analytical Predictions," by P.J. DiCorso, A.M. Reinhorn, J.R. Dickerson, J.B. Radziminski and W.L. Harper, 6/1/89, to be published.

NCEER-89-0016 "ARMA Monte Carlo Simulation in Probabilistic Structural Analysis," by P.D. Spanos and M.P. Mignolet, 7/10/89, (PB90-109893, A03, MF-A01).

NCEER-89-P017 "Preliminary Proceedings from the Conference on Disaster Preparedness - The Place of Earthquake Education in Our Schools," Edited by K.E.K. Ross, 6/23/89, (PB90-108606, A03, MF-A01).

NCEER-89-0017 "Proceedings from the Conference on Disaster Preparedness - The Place of Earthquake Education in Our Schools," Edited by K.E.K. Ross, 12/31/89, (PB90-207895, A012, MF-A02). This report is available only through NTIS (see address given above).

NCEER-89-0018 "Multidimensional Models of Hysteretic Material Behavior for Vibration Analysis of Shape Memory Energy Absorbing Devices, by E.J. Graesser and F.A. Cozzarelli, 6/7/89, (PB90-164146, A04, MF-A01).

NCEER-89-0019 "Nonlinear Dynamic Analysis of Three-Dimensional Base Isolated Structures (3D-BASIS)," by S. Nagarajaiah, A.M. Reinhorn and M.C. Constantinou, 8/3/89, (PB90-161936, A06, MF-A01). This report has been replaced by NCEER-93-0011.

NCEER-89-0020 "Structural Control Considering Time-Rate of Control Forces and Control Rate Constraints," by F.Y. Cheng and C.P. Pantelides, 8/3/89, (PB90-120445, A04, MF-A01).

NCEER-89-0021 "Subsurface Conditions of Memphis and Shelby County," by K.W. Ng, T-S. Chang and H-H.M. Hwang, 7/26/89, (PB90-120437, A03, MF-A01).

NCEER-89-0022 "Seismic Wave Propagation Effects on Straight Jointed Buried Pipelines," by K. Elhmadi and M.J. O'Rourke, 8/24/89, (PB90-162322, A10, MF-A02).

NCEER-89-0023 "Workshop on Serviceability Analysis of Water Delivery Systems," edited by M. Grigoriu, 3/6/89, (PB90-127424, A03, MF-A01).

NCEER-89-0024 "Shaking Table Study of a 1/5 Scale Steel Frame Composed of Tapered Members," by K.C. Chang, J.S. Hwang and G.C. Lee, 9/18/89, (PB90-160169, A04, MF-A01).

NCEER-89-0025 "DYNA1D: A Computer Program for Nonlinear Seismic Site Response Analysis - Technical Documentation," by Jean H. Prevost, 9/14/89, (PB90-161944, A07, MF-A01). This report is available only through NTIS (see address given above).

NCEER-89-0026 "1:4 Scale Model Studies of Active Tendon Systems and Active Mass Dampers for Aseismic Protection," by A.M. Reinhorn, T.T. Soong, R.C. Lin, Y.P. Yang, Y. Fukao, H. Abe and M. Nakai, 9/15/89, (PB90-173246, A10, MF-A02). This report is available only through NTIS (see address given above).

NCEER-89-0027 "Scattering of Waves by Inclusions in a Nonhomogeneous Elastic Half Space Solved by Boundary Element Methods," by P.K. Hadley, A. Askar and A.S. Cakmak, 6/15/89, (PB90-145699, A07, MF-A01).

NCEER-89-0028 "Statistical Evaluation of Deflection Amplification Factors for Reinforced Concrete Structures," by H.H.M. Hwang, J-W. Jaw and A.L. Ch'ng, 8/31/89, (PB90-164633, A05, MF-A01).

NCEER-89-0029 "Bedrock Accelerations in Memphis Area Due to Large New Madrid Earthquakes," by H.H.M. Hwang, C.H.S. Chen and G. Yu, 11/7/89, (PB90-162330, A04, MF-A01).

NCEER-89-0030 "Seismic Behavior and Response Sensitivity of Secondary Structural Systems," by Y.Q. Chen and T.T. Soong, 10/23/89, (PB90-164658, A08, MF-A01).

NCEER-89-0031 "Random Vibration and Reliability Analysis of Primary-Secondary Structural Systems," by Y. Ibrahim, M. Grigoriu and T.T. Soong, 11/10/89, (PB90-161951, A04, MF-A01).

NCEER-89-0032 "Proceedings from the Second U.S. - Japan Workshop on Liquefaction, Large Ground Deformation and Their Effects on Lifelines, September 26-29, 1989," Edited by T.D. O'Rourke and M. Hamada, 12/1/89, (PB90-209388, A22, MF-A03).

NCEER-89-0033 "Deterministic Model for Seismic Damage Evaluation of Reinforced Concrete Structures," by J.M. Bracci, A.M. Reinhorn, J.B. Mander and S.K. Kunnath, 9/27/89, (PB91-108803, A06, MF-A01).

NCEER-89-0034 "On the Relation Between Local and Global Damage Indices," by E. DiPasquale and A.S. Cakmak, 8/15/89, (PB90-173865, A05, MF-A01).

NCEER-89-0035 "Cyclic Undrained Behavior of Nonplastic and Low Plasticity Silts," by A.J. Walker and H.E. Stewart, 7/26/89, (PB90-183518, A10, MF-A01).

NCEER-89-0036 "Liquefaction Potential of Surficial Deposits in the City of Buffalo, New York," by M. Budhu, R. Giese and L. Baumgrass, 1/17/89, (PB90-208455, A04, MF-A01).

NCEER-89-0037 "A Deterministic Assessment of Effects of Ground Motion Incoherence," by A.S. Veletsos and Y. Tang, 7/15/89, (PB90-164294, A03, MF-A01).

NCEER-89-0038 "Workshop on Ground Motion Parameters for Seismic Hazard Mapping," July 17-18, 1989, edited by R.V. Whitman, 12/1/89, (PB90-173923, A04, MF-A01).

NCEER-89-0039 "Seismic Effects on Elevated Transit Lines of the New York City Transit Authority," by C.J. Costantino, C.A. Miller and E. Heymsfield, 12/26/89, (PB90-207887, A06, MF-A01).

NCEER-89-0040 "Centrifugal Modeling of Dynamic Soil-Structure Interaction," by K. Weissman, Supervised by J.H. Prevost, 5/10/89, (PB90-207879, A07, MF-A01).

NCEER-89-0041 "Linearized Identification of Buildings With Cores for Seismic Vulnerability Assessment," by I-K. Ho and A.E. Aktan, 11/1/89, (PB90-251943, A07, MF-A01).

NCEER-90-0001 "Geotechnical and Lifeline Aspects of the October 17, 1989 Loma Prieta Earthquake in San Francisco," by T.D. O'Rourke, H.E. Stewart, F.T. Blackburn and T.S. Dickerman, 1/90, (PB90-208596, A05, MF-A01).

NCEER-90-0002 "Nonnormal Secondary Response Due to Yielding in a Primary Structure," by D.C.K. Chen and L.D. Lutes, 2/28/90, (PB90-251976, A07, MF-A01).

NCEER-90-0003 "Earthquake Education Materials for Grades K-12," by K.E.K. Ross, 4/16/90, (PB91-251984, A05, MF-A05). This report has been replaced by NCEER-92-0018.

NCEER-90-0004 "Catalog of Strong Motion Stations in Eastern North America," by R.W. Busby, 4/3/90, (PB90-251984, A05, MF-A01).

NCEER-90-0005 "NCEER Strong-Motion Data Base: A User Manual for the GeoBase Release (Version 1.0 for the Sun3)," by P. Friberg and K. Jacob, 3/31/90 (PB90-258062, A04, MF-A01).

NCEER-90-0006 "Seismic Hazard Along a Crude Oil Pipeline in the Event of an 1811-1812 Type New Madrid Earthquake," by H.H.M. Hwang and C-H.S. Chen, 4/16/90, (PB90-258054, A04, MF-A01).

NCEER-90-0007 "Site-Specific Response Spectra for Memphis Sheahan Pumping Station," by H.H.M. Hwang and C.S. Lee, 5/15/90, (PB91-108811, A05, MF-A01).

NCEER-90-0008 "Pilot Study on Seismic Vulnerability of Crude Oil Transmission Systems," by T. Ariman, R. Dobry, M. Grigoriu, F. Kozin, M. O'Rourke, T. O'Rourke and M. Shinozuka, 5/25/90, (PB91-108837, A06, MF-A01).

NCEER-90-0009 "A Program to Generate Site Dependent Time Histories: EQGEN," by G.W. Ellis, M. Srinivasan and A.S. Cakmak, 1/30/90, (PB91-108829, A04, MF-A01).

NCEER-90-0010 "Active Isolation for Seismic Protection of Operating Rooms," by M.E. Talbott, Supervised by M. Shinozuka, 6/8/9, (PB91-110205, A05, MF-A01).

NCEER-90-0011 "Program LINEARID for Identification of Linear Structural Dynamic Systems," by C-B. Yun and M. Shinozuka, 6/25/90, (PB91-110312, A08, MF-A01).

NCEER-90-0012 "Two-Dimensional Two-Phase Elasto-Plastic Seismic Response of Earth Dams," by A.N. Yiagos, Supervised by J.H. Prevost, 6/20/90, (PB91-110197, A13, MF-A02).

NCEER-90-0013 "Secondary Systems in Base-Isolated Structures: Experimental Investigation, Stochastic Response and Stochastic Sensitivity," by G.D. Manolis, G. Juhn, M.C. Constantinou and A.M. Reinhorn, 7/1/90, (PB91-110320, A08, MF-A01).

NCEER-90-0014 "Seismic Behavior of Lightly-Reinforced Concrete Column and Beam-Column Joint Details," by S.P. Pessiki, C.H. Conley, P. Gergely and R.N. White, 8/22/90, (PB91-108795, A11, MF-A02).

NCEER-90-0015 "Two Hybrid Control Systems for Building Structures Under Strong Earthquakes," by J.N. Yang and A. Danielians, 6/29/90, (PB91-125393, A04, MF-A01).

NCEER-90-0016 "Instantaneous Optimal Control with Acceleration and Velocity Feedback," by J.N. Yang and Z. Li, 6/29/90, (PB91-125401, A03, MF-A01).

NCEER-90-0017 "Reconnaissance Report on the Northern Iran Earthquake of June 21, 1990," by M. Mehrain, 10/4/90, (PB91-125377, A03, MF-A01).

NCEER-90-0018 "Evaluation of Liquefaction Potential in Memphis and Shelby County," by T.S. Chang, P.S. Tang, C.S. Lee and H. Hwang, 8/10/90, (PB91-125427, A09, MF-A01).

NCEER-90-0019 "Experimental and Analytical Study of a Combined Sliding Disc Bearing and Helical Steel Spring Isolation System," by M.C. Constantinou, A.S. Mokha and A.M. Reinhorn, 10/4/90, (PB91-125385, A06, MF-A01). This report is available only through NTIS (see address given above).

NCEER-90-0020 "Experimental Study and Analytical Prediction of Earthquake Response of a Sliding Isolation System with a Spherical Surface," by A.S. Mokha, M.C. Constantinou and A.M. Reinhorn, 10/11/90, (PB91-125419, A05, MF-A01).

NCEER-90-0021 "Dynamic Interaction Factors for Floating Pile Groups," by G. Gazetas, K. Fan, A. Kaynia and E. Kausel, 9/10/90, (PB91-170381, A05, MF-A01).

NCEER-90-0022 "Evaluation of Seismic Damage Indices for Reinforced Concrete Structures," by S. Rodriguez-Gomez and A.S. Cakmak, 9/30/90, PB91-171322, A06, MF-A01).

NCEER-90-0023 "Study of Site Response at a Selected Memphis Site," by H. Desai, S. Ahmad, E.S. Gazetas and M.R. Oh, 10/11/90, (PB91-196857, A03, MF-A01).

NCEER-90-0024 "A User's Guide to Strongmo: Version 1.0 of NCEER's Strong-Motion Data Access Tool for PCs and Terminals," by P.A. Friberg and C.A.T. Susch, 11/15/90, (PB91-171272, A03, MF-A01).

NCEER-90-0025 "A Three-Dimensional Analytical Study of Spatial Variability of Seismic Ground Motions," by L-L. Hong and A.H.-S. Ang, 10/30/90, (PB91-170399, A09, MF-A01).

NCEER-90-0026 "MUMOID User's Guide - A Program for the Identification of Modal Parameters," by S. Rodriguez-Gomez and E. DiPasquale, 9/30/90, (PB91-171298, A04, MF-A01).

NCEER-90-0027 "SARCF-II User's Guide - Seismic Analysis of Reinforced Concrete Frames," by S. Rodriguez-Gomez, Y.S. Chung and C. Meyer, 9/30/90, (PB91-171280, A05, MF-A01).

NCEER-90-0028 "Viscous Dampers: Testing, Modeling and Application in Vibration and Seismic Isolation," by N. Makris and M.C. Constantinou, 12/20/90 (PB91-190561, A06, MF-A01).

NCEER-90-0029 "Soil Effects on Earthquake Ground Motions in the Memphis Area," by H. Hwang, C.S. Lee, K.W. Ng and T.S. Chang, 8/2/90, (PB91-190751, A05, MF-A01).

NCEER-91-0001 "Proceedings from the Third Japan-U.S. Workshop on Earthquake Resistant Design of Lifeline Facilities and Countermeasures for Soil Liquefaction, December 17-19, 1990," edited by T.D. O'Rourke and M. Hamada, 2/1/91, (PB91-179259, A99, MF-A04).

NCEER-91-0002 "Physical Space Solutions of Non-Proportionally Damped Systems," by M. Tong, Z. Liang and G.C. Lee, 1/15/91, (PB91-179242, A04, MF-A01).

NCEER-91-0003 "Seismic Response of Single Piles and Pile Groups," by K. Fan and G. Gazetas, 1/10/91, (PB92-174994, A04, MF-A01).

NCEER-91-0004 "Damping of Structures: Part 1 - Theory of Complex Damping," by Z. Liang and G. Lee, 10/10/91, (PB92-197235, A12, MF-A03).

NCEER-91-0005 "3D-BASIS - Nonlinear Dynamic Analysis of Three Dimensional Base Isolated Structures: Part II," by S. Nagarajaiah, A.M. Reinhorn and M.C. Constantinou, 2/28/91, (PB91-190553, A07, MF-A01). This report has been replaced by NCEER-93-0011.

NCEER-91-0006 "A Multidimensional Hysteretic Model for Plasticity Deforming Metals in Energy Absorbing Devices," by E.J. Graesser and F.A. Cozzarelli, 4/9/91, (PB92-108364, A04, MF-A01).

NCEER-91-0007 "A Framework for Customizable Knowledge-Based Expert Systems with an Application to a KBES for Evaluating the Seismic Resistance of Existing Buildings," by E.G. Ibarra-Anaya and S.J. Fenves, 4/9/91, (PB91-210930, A08, MF-A01).

NCEER-91-0008 "Nonlinear Analysis of Steel Frames with Semi-Rigid Connections Using the Capacity Spectrum Method," by G.G. Deierlein, S-H. Hsieh, Y-J. Shen and J.F. Abel, 7/2/91, (PB92-113828, A05, MF-A01).

NCEER-91-0009 "Earthquake Education Materials for Grades K-12," by K.E.K. Ross, 4/30/91, (PB91-212142, A06, MF-A01). This report has been replaced by NCEER-92-0018.

NCEER-91-0010 "Phase Wave Velocities and Displacement Phase Differences in a Harmonically Oscillating Pile," by N. Makris and G. Gazetas, 7/8/91, (PB92-108356, A04, MF-A01).

NCEER-91-0011 "Dynamic Characteristics of a Full-Size Five-Story Steel Structure and a 2/5 Scale Model," by K.C. Chang, G.C. Yao, G.C. Lee, D.S. Hao and Y.C. Yeh," 7/2/91, (PB93-116648, A06, MF-A02).

NCEER-91-0012 "Seismic Response of a 2/5 Scale Steel Structure with Added Viscoelastic Dampers," by K.C. Chang, T.T. Soong, S-T. Oh and M.L. Lai, 5/17/91, (PB92-110816, A05, MF-A01).

NCEER-91-0013 "Earthquake Response of Retaining Walls; Full-Scale Testing and Computational Modeling," by S. Alampalli and A-W.M. Elgamal, 6/20/91, to be published.

NCEER-91-0014 "3D-BASIS-M: Nonlinear Dynamic Analysis of Multiple Building Base Isolated Structures," by P.C. Tsopelas, S. Nagarajaiah, M.C. Constantinou and A.M. Reinhorn, 5/28/91, (PB92-113885, A09, MF-A02).

NCEER-91-0015 "Evaluation of SEAOC Design Requirements for Sliding Isolated Structures," by D. Theodossiou and M.C. Constantinou, 6/10/91, (PB92-114602, A11, MF-A03).

NCEER-91-0016 "Closed-Loop Modal Testing of a 27-Story Reinforced Concrete Flat Plate-Core Building," by H.R. Somaprasad, T. Toksoy, H. Yoshiyuki and A.E. Aktan, 7/15/91, (PB92-129980, A07, MF-A02).

NCEER-91-0017 "Shake Table Test of a 1/6 Scale Two-Story Lightly Reinforced Concrete Building," by A.G. El-Attar, R.N. White and P. Gergely, 2/28/91, (PB92-222447, A06, MF-A02).

NCEER-91-0018 "Shake Table Test of a 1/8 Scale Three-Story Lightly Reinforced Concrete Building," by A.G. El-Attar, R.N. White and P. Gergely, 2/28/91, (PB93-116630, A08, MF-A02).

NCEER-91-0019 "Transfer Functions for Rigid Rectangular Foundations," by A.S. Veletsos, A.M. Prasad and W.H. Wu, 7/31/91, to be published.

NCEER-91-0020 "Hybrid Control of Seismic-Excited Nonlinear and Inelastic Structural Systems," by J.N. Yang, Z. Li and A. Danielians, 8/1/91, (PB92-143171, A06, MF-A02).

NCEER-91-0021 "The NCEER-91 Earthquake Catalog: Improved Intensity-Based Magnitudes and Recurrence Relations for U.S. Earthquakes East of New Madrid," by L. Seeber and J.G. Armbruster, 8/28/91, (PB92-176742, A06, MF-A02).

NCEER-91-0022 "Proceedings from the Implementation of Earthquake Planning and Education in Schools: The Need for Change - The Roles of the Changemakers," by K.E.K. Ross and F. Winslow, 7/23/91, (PB92-129998, A12, MF-A03).

NCEER-91-0023 "A Study of Reliability-Based Criteria for Seismic Design of Reinforced Concrete Frame Buildings," by H.H.M. Hwang and H-M. Hsu, 8/10/91, (PB92-140235, A09, MF-A02).

NCEER-91-0024 "Experimental Verification of a Number of Structural System Identification Algorithms," by R.G. Ghanem, H. Gavin and M. Shinozuka, 9/18/91, (PB92-176577, A18, MF-A04).

NCEER-91-0025 "Probabilistic Evaluation of Liquefaction Potential," by H.H.M. Hwang and C.S. Lee," 11/25/91, (PB92-143429, A05, MF-A01).

NCEER-91-0026 "Instantaneous Optimal Control for Linear, Nonlinear and Hysteretic Structures - Stable Controllers," by J.N. Yang and Z. Li, 11/15/91, (PB92-163807, A04, MF-A01).

NCEER-91-0027 "Experimental and Theoretical Study of a Sliding Isolation System for Bridges," by M.C. Constantinou, A. Kartoum, A.M. Reinhorn and P. Bradford, 11/15/91, (PB92-176973, A10, MF-A03).

NCEER-92-0001 "Case Studies of Liquefaction and Lifeline Performance During Past Earthquakes, Volume 1: Japanese Case Studies," Edited by M. Hamada and T. O'Rourke, 2/17/92, (PB92-197243, A18, MF-A04).

NCEER-92-0002 "Case Studies of Liquefaction and Lifeline Performance During Past Earthquakes, Volume 2: United States Case Studies," Edited by T. O'Rourke and M. Hamada, 2/17/92, (PB92-197250, A20, MF-A04).

NCEER-92-0003 "Issues in Earthquake Education," Edited by K. Ross, 2/3/92, (PB92-222389, A07, MF-A02).

NCEER-92-0004 "Proceedings from the First U.S. - Japan Workshop on Earthquake Protective Systems for Bridges," Edited by I.G. Buckle, 2/4/92, (PB94-142239, A99, MF-A06).

NCEER-92-0005 "Seismic Ground Motion from a Haskell-Type Source in a Multiple-Layered Half-Space," A.P. Theoharis, G. Deodatis and M. Shinozuka, 1/2/92, to be published.

NCEER-92-0006 "Proceedings from the Site Effects Workshop," Edited by R. Whitman, 2/29/92, (PB92-197201, A04, MF-A01).

NCEER-92-0007 "Engineering Evaluation of Permanent Ground Deformations Due to Seismically-Induced Liquefaction," by M.H. Baziar, R. Dobry and A-W.M. Elgamal, 3/24/92, (PB92-222421, A13, MF-A03).

NCEER-92-0008 "A Procedure for the Seismic Evaluation of Buildings in the Central and Eastern United States," by C.D. Poland and J.O. Malley, 4/2/92, (PB92-222439, A20, MF-A04).

NCEER-92-0009 "Experimental and Analytical Study of a Hybrid Isolation System Using Friction Controllable Sliding Bearings," by M.Q. Feng, S. Fujii and M. Shinozuka, 5/15/92, (PB93-150282, A06, MF-A02).

NCEER-92-0010 "Seismic Resistance of Slab-Column Connections in Existing Non-Ductile Flat-Plate Buildings," by A.J. Durrani and Y. Du, 5/18/92, (PB93-116812, A06, MF-A02).

NCEER-92-0011 "The Hysteretic and Dynamic Behavior of Brick Masonry Walls Upgraded by Ferrocement Coatings Under Cyclic Loading and Strong Simulated Ground Motion," by H. Lee and S.P. Prawel, 5/11/92, to be published.

NCEER-92-0012 "Study of Wire Rope Systems for Seismic Protection of Equipment in Buildings," by G.F. Demetriades, M.C. Constantinou and A.M. Reinhorn, 5/20/92, (PB93-116655, A08, MF-A02).

NCEER-92-0013 "Shape Memory Structural Dampers: Material Properties, Design and Seismic Testing," by P.R. Witting and F.A. Cozzarelli, 5/26/92, (PB93-116663, A05, MF-A01).

NCEER-92-0014 "Longitudinal Permanent Ground Deformation Effects on Buried Continuous Pipelines," by M.J. O'Rourke, and C. Nordberg, 6/15/92, (PB93-116671, A08, MF-A02).

NCEER-92-0015 "A Simulation Method for Stationary Gaussian Random Functions Based on the Sampling Theorem," by M. Grigoriu and S. Balopoulou, 6/11/92, (PB93-127496, A05, MF-A01).

NCEER-92-0016 "Gravity-Load-Designed Reinforced Concrete Buildings: Seismic Evaluation of Existing Construction and Detailing Strategies for Improved Seismic Resistance," by G.W. Hoffmann, S.K. Kunnath, A.M. Reinhorn and J.B. Mander, 7/15/92, (PB94-142007, A08, MF-A02).

NCEER-92-0017 "Observations on Water System and Pipeline Performance in the Limón Area of Costa Rica Due to the April 22, 1991 Earthquake," by M. O'Rourke and D. Ballantyne, 6/30/92, (PB93-126811, A06, MF-A02).

NCEER-92-0018 "Fourth Edition of Earthquake Education Materials for Grades K-12," Edited by K.E.K. Ross, 8/10/92, (PB93-114023, A07, MF-A02).

NCEER-92-0019 "Proceedings from the Fourth Japan-U.S. Workshop on Earthquake Resistant Design of Lifeline Facilities and Countermeasures for Soil Liquefaction," Edited by M. Hamada and T.D. O'Rourke, 8/12/92, (PB93-163939, A99, MF-E11).

NCEER-92-0020 "Active Bracing System: A Full Scale Implementation of Active Control," by A.M. Reinhorn, T.T. Soong, R.C. Lin, M.A. Riley, Y.P. Wang, S. Aizawa and M. Higashino, 8/14/92, (PB93-127512, A06, MF-A02).

NCEER-92-0021 "Empirical Analysis of Horizontal Ground Displacement Generated by Liquefaction-Induced Lateral Spreads," by S.F. Bartlett and T.L. Youd, 8/17/92, (PB93-188241, A06, MF-A02).

NCEER-92-0022 "IDARC Version 3.0: Inelastic Damage Analysis of Reinforced Concrete Structures," by S.K. Kunnath, A.M. Reinhorn and R.F. Lobo, 8/31/92, (PB93-227502, A07, MF-A02).

NCEER-92-0023 "A Semi-Empirical Analysis of Strong-Motion Peaks in Terms of Seismic Source, Propagation Path and Local Site Conditions, by M. Kamiyama, M.J. O'Rourke and R. Flores-Berrones, 9/9/92, (PB93-150266, A08, MF-A02).

NCEER-92-0024 "Seismic Behavior of Reinforced Concrete Frame Structures with Nonductile Details, Part I: Summary of Experimental Findings of Full Scale Beam-Column Joint Tests," by A. Beres, R.N. White and P. Gergely, 9/30/92, (PB93-227783, A05, MF-A01).

NCEER-92-0025 "Experimental Results of Repaired and Retrofitted Beam-Column Joint Tests in Lightly Reinforced Concrete Frame Buildings," by A. Beres, S. El-Borgi, R.N. White and P. Gergely, 10/29/92, (PB93-227791, A05, MF-A01).

NCEER-92-0026 "A Generalization of Optimal Control Theory: Linear and Nonlinear Structures," by J.N. Yang, Z. Li and S. Vongchavalitkul, 11/2/92, (PB93-188621, A05, MF-A01).

NCEER-92-0027 "Seismic Resistance of Reinforced Concrete Frame Structures Designed Only for Gravity Loads: Part I - Design and Properties of a One-Third Scale Model Structure," by J.M. Bracci, A.M. Reinhorn and J.B. Mander, 12/1/92, (PB94-104502, A08, MF-A02).

NCEER-92-0028 "Seismic Resistance of Reinforced Concrete Frame Structures Designed Only for Gravity Loads: Part II - Experimental Performance of Subassemblages," by L.E. Aycardi, J.B. Mander and A.M. Reinhorn, 12/1/92, (PB94-104510, A08, MF-A02).

NCEER-92-0029 "Seismic Resistance of Reinforced Concrete Frame Structures Designed Only for Gravity Loads: Part III - Experimental Performance and Analytical Study of a Structural Model," by J.M. Bracci, A.M. Reinhorn and J.B. Mander, 12/1/92, (PB93-227528, A09, MF-A01).

NCEER-92-0030 "Evaluation of Seismic Retrofit of Reinforced Concrete Frame Structures: Part I - Experimental Performance of Retrofitted Subassemblages," by D. Choudhuri, J.B. Mander and A.M. Reinhorn, 12/8/92, (PB93-198307, A07, MF-A02).

NCEER-92-0031 "Evaluation of Seismic Retrofit of Reinforced Concrete Frame Structures: Part II - Experimental Performance and Analytical Study of a Retrofitted Structural Model," by J.M. Bracci, A.M. Reinhorn and J.B. Mander, 12/8/92, (PB93-198315, A09, MF-A03).

NCEER-92-0032 "Experimental and Analytical Investigation of Seismic Response of Structures with Supplemental Fluid Viscous Dampers," by M.C. Constantinou and M.D. Symans, 12/21/92, (PB93-191435, A10, MF-A03). This report is available only through NTIS (see address given above).

NCEER-92-0033 "Reconnaissance Report on the Cairo, Egypt Earthquake of October 12, 1992," by M. Khater, 12/23/92, (PB93-188621, A03, MF-A01).

NCEER-92-0034 "Low-Level Dynamic Characteristics of Four Tall Flat-Plate Buildings in New York City," by H. Gavin, S. Yuan, J. Grossman, E. Pekelis and K. Jacob, 12/28/92, (PB93-188217, A07, MF-A02).

NCEER-93-0001 "An Experimental Study on the Seismic Performance of Brick-Infilled Steel Frames With and Without Retrofit," by J.B. Mander, B. Nair, K. Wojtkowski and J. Ma, 1/29/93, (PB93-227510, A07, MF-A02).

NCEER-93-0002 "Social Accounting for Disaster Preparedness and Recovery Planning," by S. Cole, E. Pantoja and V. Razak, 2/22/93, (PB94-142114, A12, MF-A03).

NCEER-93-0003 "Assessment of 1991 NEHRP Provisions for Nonstructural Components and Recommended Revisions," by T.T. Soong, G. Chen, Z. Wu, R-H. Zhang and M. Grigoriu, 3/1/93, (PB93-188639, A06, MF-A02).

NCEER-93-0004 "Evaluation of Static and Response Spectrum Analysis Procedures of SEAOC/UBC for Seismic Isolated Structures," by C.W. Winters and M.C. Constantinou, 3/23/93, (PB93-198299, A10, MF-A03).

NCEER-93-0005 "Earthquakes in the Northeast - Are We Ignoring the Hazard? A Workshop on Earthquake Science and Safety for Educators," edited by K.E.K. Ross, 4/2/93, (PB94-103066, A09, MF-A02).

NCEER-93-0006 "Inelastic Response of Reinforced Concrete Structures with Viscoelastic Braces," by R.F. Lobo, J.M. Bracci, K.L. Shen, A.M. Reinhorn and T.T. Soong, 4/5/93, (PB93-227486, A05, MF-A02).

NCEER-93-0007 "Seismic Testing of Installation Methods for Computers and Data Processing Equipment," by K. Kosar, T.T. Soong, K.L. Shen, J.A. HoLung and Y.K. Lin, 4/12/93, (PB93-198299, A07, MF-A02).

NCEER-93-0008 "Retrofit of Reinforced Concrete Frames Using Added Dampers," by A. Reinhorn, M. Constantinou and C. Li, to be published.

NCEER-93-0009 "Seismic Behavior and Design Guidelines for Steel Frame Structures with Added Viscoelastic Dampers," by K.C. Chang, M.L. Lai, T.T. Soong, D.S. Hao and Y.C. Yeh, 5/1/93, (PB94-141959, A07, MF-A02).

NCEER-93-0010 "Seismic Performance of Shear-Critical Reinforced Concrete Bridge Piers," by J.B. Mander, S.M. Waheed, M.T.A. Chaudhary and S.S. Chen, 5/12/93, (PB93-227494, A08, MF-A02).

NCEER-93-0011 "3D-BASIS-TABS: Computer Program for Nonlinear Dynamic Analysis of Three Dimensional Base Isolated Structures," by S. Nagarajaiah, C. Li, A.M. Reinhorn and M.C. Constantinou, 8/2/93, (PB94-141819, A09, MF-A02).

NCEER-93-0012 "Effects of Hydrocarbon Spills from an Oil Pipeline Break on Ground Water," by O.J. Helweg and H.H.M. Hwang, 8/3/93, (PB94-141942, A06, MF-A02).

NCEER-93-0013 "Simplified Procedures for Seismic Design of Nonstructural Components and Assessment of Current Code Provisions," by M.P. Singh, L.E. Suarez, E.E. Matheu and G.O. Maldonado, 8/4/93, (PB94-141827, A09, MF-A02).

NCEER-93-0014 "An Energy Approach to Seismic Analysis and Design of Secondary Systems," by G. Chen and T.T. Soong, 8/6/93, (PB94-142767, A11, MF-A03).

NCEER-93-0015 "Proceedings from School Sites: Becoming Prepared for Earthquakes - Commemorating the Third Anniversary of the Loma Prieta Earthquake," Edited by F.E. Winslow and K.E.K. Ross, 8/16/93, (PB94-154275, A16, MF-A02).

NCEER-93-0016 "Reconnaissance Report of Damage to Historic Monuments in Cairo, Egypt Following the October 12, 1992 Dahshur Earthquake," by D. Sykora, D. Look, G. Croci, E. Karaesmen and E. Karaesmen, 8/19/93, (PB94-142221, A08, MF-A02).

NCEER-93-0017 "The Island of Guam Earthquake of August 8, 1993," by S.W. Swan and S.K. Harris, 9/30/93, (PB94-141843, A04, MF-A01).

NCEER-93-0018 "Engineering Aspects of the October 12, 1992 Egyptian Earthquake," by A.W. Elgamal, M. Amer, K. Adalier and A. Abul-Fadl, 10/7/93, (PB94-141983, A05, MF-A01).

NCEER-93-0019 "Development of an Earthquake Motion Simulator and its Application in Dynamic Centrifuge Testing," by I. Krstelj, Supervised by J.H. Prevost, 10/23/93, (PB94-181773, A-10, MF-A03).

NCEER-93-0020 "NCEER-Taisei Corporation Research Program on Sliding Seismic Isolation Systems for Bridges: Experimental and Analytical Study of a Friction Pendulum System (FPS)," by M.C. Constantinou, P. Tsopelas, Y-S. Kim and S. Okamoto, 11/1/93, (PB94-142775, A08, MF-A02).

NCEER-93-0021 "Finite Element Modeling of Elastomeric Seismic Isolation Bearings," by L.J. Billings, Supervised by R. Shepherd, 11/8/93, to be published.

NCEER-93-0022 "Seismic Vulnerability of Equipment in Critical Facilities: Life-Safety and Operational Consequences," by K. Porter, G.S. Johnson, M.M. Zadeh, C. Scawthorn and S. Eder, 11/24/93, (PB94-181765, A16, MF-A03).

NCEER-93-0023 "Hokkaido Nansei-oki, Japan Earthquake of July 12, 1993, by P.I. Yanev and C.R. Scawthorn, 12/23/93, (PB94-181500, A07, MF-A01).

NCEER-94-0001 "An Evaluation of Seismic Serviceability of Water Supply Networks with Application to the San Francisco Auxiliary Water Supply System," by I. Markov, Supervised by M. Grigoriu and T. O'Rourke, 1/21/94, (PB94-204013, A07, MF-A02).

NCEER-94-0002 "NCEER-Taisei Corporation Research Program on Sliding Seismic Isolation Systems for Bridges: Experimental and Analytical Study of Systems Consisting of Sliding Bearings, Rubber Restoring Force Devices and Fluid Dampers," Volumes I and II, by P. Tsopelas, S. Okamoto, M.C. Constantinou, D. Ozaki and S. Fujii, 2/4/94, (PB94-181740, A09, MF-A02 and PB94-181757, A12, MF-A03).

NCEER-94-0003 "A Markov Model for Local and Global Damage Indices in Seismic Analysis," by S. Rahman and M. Grigoriu, 2/18/94, (PB94-206000, A12, MF-A03).

NCEER-94-0004 "Proceedings from the NCEER Workshop on Seismic Response of Masonry Infills," edited by D.P. Abrams, 3/1/94, (PB94-180783, A07, MF-A02).

NCEER-94-0005 "The Northridge, California Earthquake of January 17, 1994: General Reconnaissance Report," edited by J.D. Goltz, 3/11/94, (PB94-193943, A10, MF-A03).

NCEER-94-0006 "Seismic Energy Based Fatigue Damage Analysis of Bridge Columns: Part I - Evaluation of Seismic Capacity," by G.A. Chang and J.B. Mander, 3/14/94, (PB94-219185, A11, MF-A03).

NCEER-94-0007 "Seismic Isolation of Multi-Story Frame Structures Using Spherical Sliding Isolation Systems," by T.M. Al-Hussaini, V.A. Zayas and M.C. Constantinou, 3/17/94, (PB94-193745, A09, MF-A02).

NCEER-94-0008 "The Northridge, California Earthquake of January 17, 1994: Performance of Highway Bridges," edited by I.G. Buckle, 3/24/94, (PB94-193851, A06, MF-A02).

NCEER-94-0009 "Proceedings of the Third U.S.-Japan Workshop on Earthquake Protective Systems for Bridges," edited by I.G. Buckle and I. Friedland, 3/31/94, (PB94-195815, A99, MF-A06).

NCEER-94-0010 "3D-BASIS-ME: Computer Program for Nonlinear Dynamic Analysis of Seismically Isolated Single and Multiple Structures and Liquid Storage Tanks," by P.C. Tsopelas, M.C. Constantinou and A.M. Reinhorn, 4/12/94, (PB94-204922, A09, MF-A02).

NCEER-94-0011 "The Northridge, California Earthquake of January 17, 1994: Performance of Gas Transmission Pipelines," by T.D. O'Rourke and M.C. Palmer, 5/16/94, (PB94-204989, A05, MF-A01).

NCEER-94-0012 "Feasibility Study of Replacement Procedures and Earthquake Performance Related to Gas Transmission Pipelines," by T.D. O'Rourke and M.C. Palmer, 5/25/94, (PB94-206638, A09, MF-A02).

NCEER-94-0013 "Seismic Energy Based Fatigue Damage Analysis of Bridge Columns: Part II - Evaluation of Seismic Demand," by G.A. Chang and J.B. Mander, 6/1/94, (PB95-18106, A08, MF-A02).

NCEER-94-0014 "NCEER-Taisei Corporation Research Program on Sliding Seismic Isolation Systems for Bridges: Experimental and Analytical Study of a System Consisting of Sliding Bearings and Fluid Restoring Force/Damping Devices," by P. Tsopelas and M.C. Constantinou, 6/13/94, (PB94-219144, A10, MF-A03).

NCEER-94-0015 "Generation of Hazard-Consistent Fragility Curves for Seismic Loss Estimation Studies," by H. Hwang and J-R. Huo, 6/14/94, (PB95-181996, A09, MF-A02).

NCEER-94-0016 "Seismic Study of Building Frames with Added Energy-Absorbing Devices," by W.S. Pong, C.S. Tsai and G.C. Lee, 6/20/94, (PB94-219136, A10, A03).

NCEER-94-0017 "Sliding Mode Control for Seismic-Excited Linear and Nonlinear Civil Engineering Structures," by J. Yang, J. Wu, A. Agrawal and Z. Li, 6/21/94, (PB95-138483, A06, MF-A02).

NCEER-94-0018 "3D-BASIS-TABS Version 2.0: Computer Program for Nonlinear Dynamic Analysis of Three Dimensional Base Isolated Structures," by A.M. Reinhorn, S. Nagarajaiah, M.C. Constantinou, P. Tsopelas and R. Li, 6/22/94, (PB95-182176, A08, MF-A02).

NCEER-94-0019 "Proceedings of the International Workshop on Civil Infrastructure Systems: Application of Intelligent Systems and Advanced Materials on Bridge Systems," Edited by G.C. Lee and K.C. Chang, 7/18/94, (PB95-252474, A20, MF-A04).

NCEER-94-0020 "Study of Seismic Isolation Systems for Computer Floors," by V. Lambrou and M.C. Constantinou, 7/19/94, (PB95-138533, A10, MF-A03).

NCEER-94-0021 "Proceedings of the U.S.-Italian Workshop on Guidelines for Seismic Evaluation and Rehabilitation of Unreinforced Masonry Buildings," Edited by D.P. Abrams and G.M. Calvi, 7/20/94, (PB95-138749, A13, MF-A03).

NCEER-94-0022 "NCEER-Taisei Corporation Research Program on Sliding Seismic Isolation Systems for Bridges: Experimental and Analytical Study of a System Consisting of Lubricated PTFE Sliding Bearings and Mild Steel Dampers," by P. Tsopelas and M.C. Constantinou, 7/22/94, (PB95-182184, A08, MF-A02).

NCEER-94-0023 "Development of Reliability-Based Design Criteria for Buildings Under Seismic Load," by Y.K. Wen, H. Hwang and M. Shinozuka, 8/1/94, (PB95-211934, A08, MF-A02).

NCEER-94-0024 "Experimental Verification of Acceleration Feedback Control Strategies for an Active Tendon System," by S.J. Dyke, B.F. Spencer, Jr., P. Quast, M.K. Sain, D.C. Kaspari, Jr. and T.T. Soong, 8/29/94, (PB95-212320, A05, MF-A01).

NCEER-94-0025 "Seismic Retrofitting Manual for Highway Bridges," Edited by I.G. Buckle and I.F. Friedland, published by the Federal Highway Administration (PB95-212676, A15, MF-A03).

NCEER-94-0026 "Proceedings from the Fifth U.S.-Japan Workshop on Earthquake Resistant Design of Lifeline Facilities and Countermeasures Against Soil Liquefaction," Edited by T.D. O'Rourke and M. Hamada, 11/7/94, (PB95-220802, A99, MF-E08).

NCEER-95-0001 "Experimental and Analytical Investigation of Seismic Retrofit of Structures with Supplemental Damping: Part 1 - Fluid Viscous Damping Devices," by A.M. Reinhorn, C. Li and M.C. Constantinou, 1/3/95, (PB95-266599, A09, MF-A02).

NCEER-95-0002 "Experimental and Analytical Study of Low-Cycle Fatigue Behavior of Semi-Rigid Top-And-Seat Angle Connections," by G. Pekcan, J.B. Mander and S.S. Chen, 1/5/95, (PB95-220042, A07, MF-A02).

NCEER-95-0003 "NCEER-ATC Joint Study on Fragility of Buildings," by T. Anagnos, C. Rojahn and A.S. Kiremidjian, 1/20/95, (PB95-220026, A06, MF-A02).

NCEER-95-0004 "Nonlinear Control Algorithms for Peak Response Reduction," by Z. Wu, T.T. Soong, V. Gattulli and R.C. Lin, 2/16/95, (PB95-220349, A05, MF-A01).

NCEER-95-0005 "Pipeline Replacement Feasibility Study: A Methodology for Minimizing Seismic and Corrosion Risks to Underground Natural Gas Pipelines," by R.T. Eguchi, H.A. Seligson and D.G. Honegger, 3/2/95, (PB95-252326, A06, MF-A02).

NCEER-95-0006 "Evaluation of Seismic Performance of an 11-Story Frame Building During the 1994 Northridge Earthquake," by F. Naeim, R. DiSulio, K. Benuska, A. Reinhorn and C. Li, to be published.

NCEER-95-0007 "Prioritization of Bridges for Seismic Retrofitting," by N. Basöz and A.S. Kiremidjian, 4/24/95, (PB95-252300, A08, MF-A02).

NCEER-95-0008 "Method for Developing Motion Damage Relationships for Reinforced Concrete Frames," by A. Singhal and A.S. Kiremidjian, 5/11/95, (PB95-266607, A06, MF-A02).

NCEER-95-0009 "Experimental and Analytical Investigation of Seismic Retrofit of Structures with Supplemental Damping: Part II - Friction Devices," by C. Li and A.M. Reinhorn, 7/6/95, (PB96-128087, A11, MF-A03).

NCEER-95-0010 "Experimental Performance and Analytical Study of a Non-Ductile Reinforced Concrete Frame Structure Retrofitted with Elastomeric Spring Dampers," by G. Pekcan, J.B. Mander and S.S. Chen, 7/14/95, (PB96-137161, A08, MF-A02).

NCEER-95-0011 "Development and Experimental Study of Semi-Active Fluid Damping Devices for Seismic Protection of Structures," by M.D. Symans and M.C. Constantinou, 8/3/95, (PB96-136940, A23, MF-A04).

NCEER-95-0012 "Real-Time Structural Parameter Modification (RSPM): Development of Innervated Structures," by Z. Liang, M. Tong and G.C. Lee, 4/11/95, (PB96-137153, A06, MF-A01).

NCEER-95-0013 "Experimental and Analytical Investigation of Seismic Retrofit of Structures with Supplemental Damping: Part III - Viscous Damping Walls," by A.M. Reinhorn and C. Li, 10/1/95, (PB96-176409, A11, MF-A03).

NCEER-95-0014 "Seismic Fragility Analysis of Equipment and Structures in a Memphis Electric Substation," by J-R. Huo and H.H.M. Hwang, 8/10/95, (PB96-128087, A09, MF-A02).

NCEER-95-0015 "The Hanshin-Awaji Earthquake of January 17, 1995: Performance of Lifelines," Edited by M. Shinozuka, 11/3/95, (PB96-176383, A15, MF-A03).

NCEER-95-0016 "Highway Culvert Performance During Earthquakes," by T.L. Youd and C.J. Beckman, available as NCEER-96-0015.

NCEER-95-0017 "The Hanshin-Awaji Earthquake of January 17, 1995: Performance of Highway Bridges," Edited by I.G. Buckle, 12/1/95, to be published.

NCEER-95-0018 "Modeling of Masonry Infill Panels for Structural Analysis," by A.M. Reinhorn, A. Madan, R.E. Valles, Y. Reichmann and J.B. Mander, 12/8/95, (PB97-110886, MF-A01, A06).

NCEER-95-0019 "Optimal Polynomial Control for Linear and Nonlinear Structures," by A.K. Agrawal and J.N. Yang, 12/11/95, (PB96-168737, A07, MF-A02).

NCEER-95-0020 "Retrofit of Non-Ductile Reinforced Concrete Frames Using Friction Dampers," by R.S. Rao, P. Gergely and R.N. White, 12/22/95, (PB97-133508, A10, MF-A02).

NCEER-95-0021 "Parametric Results for Seismic Response of Pile-Supported Bridge Bents," by G. Mylonakis, A. Nikolaou and G. Gazetas, 12/22/95, (PB97-100242, A12, MF-A03).

NCEER-95-0022 "Kinematic Bending Moments in Seismically Stressed Piles," by A. Nikolaou, G. Mylonakis and G. Gazetas, 12/23/95, (PB97-113914, MF-A03, A13).

NCEER-96-0001 "Dynamic Response of Unreinforced Masonry Buildings with Flexible Diaphragms," by A.C. Costley and D.P. Abrams," 10/10/96, (PB97-133573, MF-A03, A15).

NCEER-96-0002 "State of the Art Review: Foundations and Retaining Structures," by I. Po Lam, to be published.

NCEER-96-0003 "Ductility of Rectangular Reinforced Concrete Bridge Columns with Moderate Confinement," by N. Wehbe, M. Saiidi, D. Sanders and B. Douglas, 11/7/96, (PB97-133557, A06, MF-A02).

NCEER-96-0004 "Proceedings of the Long-Span Bridge Seismic Research Workshop," edited by I.G. Buckle and I.M. Friedland, to be published.

NCEER-96-0005 "Establish Representative Pier Types for Comprehensive Study: Eastern United States," by J. Kulicki and Z. Prucz, 5/28/96, (PB98-119217, A07, MF-A02).

NCEER-96-0006 "Establish Representative Pier Types for Comprehensive Study: Western United States," by R. Imbsen, R.A. Schamber and T.A. Osterkamp, 5/28/96, (PB98-118607, A07, MF-A02).

NCEER-96-0007 "Nonlinear Control Techniques for Dynamical Systems with Uncertain Parameters," by R.G. Ghanem and M.I. Bujakov, 5/27/96, (PB97-100259, A17, MF-A03).

NCEER-96-0008 "Seismic Evaluation of a 30-Year Old Non-Ductile Highway Bridge Pier and Its Retrofit," by J.B. Mander, B. Mahmoodzadegan, S. Bhadra and S.S. Chen, 5/31/96, (PB97-110902, MF-A03, A10).

NCEER-96-0009 "Seismic Performance of a Model Reinforced Concrete Bridge Pier Before and After Retrofit," by J.B. Mander, J.H. Kim and C.A. Ligozio, 5/31/96, (PB97-110910, MF-A02, A10).

NCEER-96-0010 "IDARC2D Version 4.0: A Computer Program for the Inelastic Damage Analysis of Buildings," by R.E. Valles, A.M. Reinhorn, S.K. Kunnath, C. Li and A. Madan, 6/3/96, (PB97-100234, A17, MF-A03).

NCEER-96-0011 "Estimation of the Economic Impact of Multiple Lifeline Disruption: Memphis Light, Gas and Water Division Case Study," by S.E. Chang, H.A. Seligson and R.T. Eguchi, 8/16/96, (PB97-133490, A11, MF-A03).

NCEER-96-0012 "Proceedings from the Sixth Japan-U.S. Workshop on Earthquake Resistant Design of Lifeline Facilities and Countermeasures Against Soil Liquefaction, Edited by M. Hamada and T. O'Rourke, 9/11/96, (PB97-133581, A99, MF-A06).

NCEER-96-0013 "Chemical Hazards, Mitigation and Preparedness in Areas of High Seismic Risk: A Methodology for Estimating the Risk of Post-Earthquake Hazardous Materials Release," by H.A. Seligson, R.T. Eguchi, K.J. Tierney and K. Richmond, 11/7/96, (PB97-133565, MF-A02, A08).

NCEER-96-0014 "Response of Steel Bridge Bearings to Reversed Cyclic Loading," by J.B. Mander, D-K. Kim, S.S. Chen and G.J. Premus, 11/13/96, (PB97-140735, A12, MF-A03).

NCEER-96-0015 "Highway Culvert Performance During Past Earthquakes," by T.L. Youd and C.J. Beckman, 11/25/96, (PB97-133532, A06, MF-A01).

NCEER-97-0001 "Evaluation, Prevention and Mitigation of Pounding Effects in Building Structures," by R.E. Valles and A.M. Reinhorn, 2/20/97, (PB97-159552, A14, MF-A03).

NCEER-97-0002 "Seismic Design Criteria for Bridges and Other Highway Structures," by C. Rojahn, R. Mayes, D.G. Anderson, J. Clark, J.H. Hom, R.V. Nutt and M.J. O'Rourke, 4/30/97, (PB97-194658, A06, MF-A03).

NCEER-97-0003 “Proceedings of the U.S.-Italian Workshop on Seismic Evaluation and Retrofit,” Edited by D.P. Abrams and G.M. Calvi, 3/19/97, (PB97-194666, A13, MF-A03).

NCEER-97-0004 "Investigation of Seismic Response of Buildings with Linear and Nonlinear Fluid Viscous Dampers," by A.A. Seleemah and M.C. Constantinou, 5/21/97, (PB98-109002, A15, MF-A03).

NCEER-97-0005 "Proceedings of the Workshop on Earthquake Engineering Frontiers in Transportation Facilities," edited by G.C. Lee and I.M. Friedland, 8/29/97, (PB98-128911, A25, MR-A04).

NCEER-97-0006 "Cumulative Seismic Damage of Reinforced Concrete Bridge Piers," by S.K. Kunnath, A. El-Bahy, A. Taylor and W. Stone, 9/2/97, (PB98-108814, A11, MF-A03).

NCEER-97-0007 "Structural Details to Accommodate Seismic Movements of Highway Bridges and Retaining Walls," by R.A. Imbsen, R.A. Schamber, E. Thorkildsen, A. Kartoum, B.T. Martin, T.N. Rosser and J.M. Kulicki, 9/3/97, (PB98-108996, A09, MF-A02).

NCEER-97-0008 "A Method for Earthquake Motion-Damage Relationships with Application to Reinforced Concrete Frames," by A. Singhal and A.S. Kiremidjian, 9/10/97, (PB98-108988, A13, MF-A03).

NCEER-97-0009 "Seismic Analysis and Design of Bridge Abutments Considering Sliding and Rotation," by K. Fishman and R. Richards, Jr., 9/15/97, (PB98-108897, A06, MF-A02).

NCEER-97-0010 "Proceedings of the FHWA/NCEER Workshop on the National Representation of Seismic Ground Motion for New and Existing Highway Facilities," edited by I.M. Friedland, M.S. Power and R.L. Mayes, 9/22/97, (PB98-128903, A21, MF-A04).

NCEER-97-0011 "Seismic Analysis for Design or Retrofit of Gravity Bridge Abutments," by K.L. Fishman, R. Richards, Jr. and R.C. Divito, 10/2/97, (PB98-128937, A08, MF-A02).

NCEER-97-0012 "Evaluation of Simplified Methods of Analysis for Yielding Structures," by P. Tsopelas, M.C. Constantinou, C.A. Kircher and A.S. Whittaker, 10/31/97, (PB98-128929, A10, MF-A03).

NCEER-97-0013 "Seismic Design of Bridge Columns Based on Control and Repairability of Damage," by C-T. Cheng and J.B. Mander, 12/8/97, (PB98-144249, A11, MF-A03).

NCEER-97-0014 "Seismic Resistance of Bridge Piers Based on Damage Avoidance Design," by J.B. Mander and C-T. Cheng, 12/10/97, (PB98-144223, A09, MF-A02).

NCEER-97-0015 “Seismic Response of Nominally Symmetric Systems with Strength Uncertainty,” by S. Balopoulou and M. Grigoriu, 12/23/97, (PB98-153422, A11, MF-A03).

NCEER-97-0016 “Evaluation of Seismic Retrofit Methods for Reinforced Concrete Bridge Columns,” by T.J. Wipf, F.W. Klaiber and F.M. Russo, 12/28/97, (PB98-144215, A12, MF-A03).

NCEER-97-0017 “Seismic Fragility of Existing Conventional Reinforced Concrete Highway Bridges,” by C.L. Mullen and A.S. Cakmak, 12/30/97, (PB98-153406, A08, MF-A02).

NCEER-97-0018 “Loss Asssessment of Memphis Buildings,” edited by D.P. Abrams and M. Shinozuka, 12/31/97, (PB98-144231, A13, MF-A03).

NCEER-97-0019 “Seismic Evaluation of Frames with Infill Walls Using Quasi-static Experiments,” by K.M. Mosalam, R.N. White and P. Gergely, 12/31/97, (PB98-153455, A07, MF-A02).

NCEER-97-0020 “Seismic Evaluation of Frames with Infill Walls Using Pseudo-dynamic Experiments,” by K.M. Mosalam, R.N. White and P. Gergely, 12/31/97, (PB98-153430, A07, MF-A02).

NCEER-97-0021 “Computational Strategies for Frames with Infill Walls: Discrete and Smeared Crack Analyses and Seismic Fragility,” by K.M. Mosalam, R.N. White and P. Gergely, 12/31/97, (PB98-153414, A10, MF-A02).

NCEER-97-0022 "Proceedings of the NCEER Workshop on Evaluation of Liquefaction Resistance of Soils," edited by T.L. Youd and I.M. Idriss, 12/31/97, (PB98-155617, A15, MF-A03).

MCEER-98-0001 "Extraction of Nonlinear Hysteretic Properties of Seismically Isolated Bridges from Quick-Release Field Tests," by Q. Chen, B.M. Douglas, E.M. Maragakis and I.G. Buckle, 5/26/98, (PB99-118838, A06, MF-A01).

MCEER-98-0002 "Methodologies for Evaluating the Importance of Highway Bridges," by A. Thomas, S. Eshenaur and J. Kulicki, 5/29/98, (PB99-118846, A10, MF-A02).

MCEER-98-0003 "Capacity Design of Bridge Piers and the Analysis of Overstrength," by J.B. Mander, A. Dutta and P. Goel, 6/1/98, (PB99-118853, A09, MF-A02).

MCEER-98-0004 "Evaluation of Bridge Damage Data from the Loma Prieta and Northridge, California Earthquakes," by N. Basoz and A. Kiremidjian, 6/2/98, (PB99-118861, A15, MF-A03).

MCEER-98-0005 "Screening Guide for Rapid Assessment of Liquefaction Hazard at Highway Bridge Sites," by T. L. Youd, 6/16/98, (PB99-118879, A06, not available on microfiche).

MCEER-98-0006 "Structural Steel and Steel/Concrete Interface Details for Bridges," by P. Ritchie, N. Kauhl and J. Kulicki, 7/13/98, (PB99-118945, A06, MF-A01).

MCEER-98-0007 "Capacity Design and Fatigue Analysis of Confined Concrete Columns," by A. Dutta and J.B. Mander, 7/14/98, (PB99-118960, A14, MF-A03).

MCEER-98-0008 "Proceedings of the Workshop on Performance Criteria for Telecommunication Services Under Earthquake Conditions," edited by A.J. Schiff, 7/15/98, (PB99-118952, A08, MF-A02).

MCEER-98-0009 "Fatigue Analysis of Unconfined Concrete Columns," by J.B. Mander, A. Dutta and J.H. Kim, 9/12/98, (PB99-123655, A10, MF-A02).

MCEER-98-0010 "Centrifuge Modeling of Cyclic Lateral Response of Pile-Cap Systems and Seat-Type Abutments in Dry Sands," by A.D. Gadre and R. Dobry, 10/2/98, (PB99-123606, A13, MF-A03).

MCEER-98-0011 "IDARC-BRIDGE: A Computational Platform for Seismic Damage Assessment of Bridge Structures," by A.M. Reinhorn, V. Simeonov, G. Mylonakis and Y. Reichman, 10/2/98, (PB99-162919, A15, MF-A03).

MCEER-98-0012 "Experimental Investigation of the Dynamic Response of Two Bridges Before and After Retrofitting with Elastomeric Bearings," by D.A. Wendichansky, S.S. Chen and J.B. Mander, 10/2/98, (PB99-162927, A15, MF-A03).

MCEER-98-0013 "Design Procedures for Hinge Restrainers and Hinge Sear Width for Multiple-Frame Bridges," by R. Des Roches and G.L. Fenves, 11/3/98, (PB99-140477, A13, MF-A03).

MCEER-98-0014 "Response Modification Factors for Seismically Isolated Bridges," by M.C. Constantinou and J.K. Quarshie, 11/3/98, (PB99-140485, A14, MF-A03).

MCEER-98-0015 "Proceedings of the U.S.-Italy Workshop on Seismic Protective Systems for Bridges," edited by I.M. Friedland and M.C. Constantinou, 11/3/98, (PB2000-101711, A22, MF-A04).

MCEER-98-0016 "Appropriate Seismic Reliability for Critical Equipment Systems: Recommendations Based on Regional Analysis of Financial and Life Loss," by K. Porter, C. Scawthorn, C. Taylor and N. Blais, 11/10/98, (PB99-157265, A08, MF-A02).

MCEER-98-0017 "Proceedings of the U.S. Japan Joint Seminar on Civil Infrastructure Systems Research," edited by M. Shinozuka and A. Rose, 11/12/98, (PB99-156713, A16, MF-A03).

MCEER-98-0018 "Modeling of Pile Footings and Drilled Shafts for Seismic Design," by I. PoLam, M. Kapuskar and D. Chaudhuri, 12/21/98, (PB99-157257, A09, MF-A02).

MCEER-99-0001 "Seismic Evaluation of a Masonry Infilled Reinforced Concrete Frame by Pseudodynamic Testing," by S.G. Buonopane and R.N. White, 2/16/99, (PB99-162851, A09, MF-A02).

MCEER-99-0002 "Response History Analysis of Structures with Seismic Isolation and Energy Dissipation Systems: Verification Examples for Program SAP2000," by J. Scheller and M.C. Constantinou, 2/22/99, (PB99-162869, A08, MF-A02).

MCEER-99-0003 "Experimental Study on the Seismic Design and Retrofit of Bridge Columns Including Axial Load Effects," by A. Dutta, T. Kokorina and J.B. Mander, 2/22/99, (PB99-162877, A09, MF-A02).

MCEER-99-0004 "Experimental Study of Bridge Elastomeric and Other Isolation and Energy Dissipation Systems with Emphasis on Uplift Prevention and High Velocity Near-source Seismic Excitation," by A. Kasalanati and M. C. Constantinou, 2/26/99, (PB99-162885, A12, MF-A03).

MCEER-99-0005 "Truss Modeling of Reinforced Concrete Shear-flexure Behavior," by J.H. Kim and J.B. Mander, 3/8/99, (PB99-163693, A12, MF-A03).

MCEER-99-0006 "Experimental Investigation and Computational Modeling of Seismic Response of a 1:4 Scale Model Steel Structure with a Load Balancing Supplemental Damping System," by G. Pekcan, J.B. Mander and S.S. Chen, 4/2/99, (PB99-162893, A11, MF-A03).

MCEER-99-0007 "Effect of Vertical Ground Motions on the Structural Response of Highway Bridges," by M.R. Button, C.J. Cronin and R.L. Mayes, 4/10/99, (PB2000-101411, A10, MF-A03).

MCEER-99-0008 "Seismic Reliability Assessment of Critical Facilities: A Handbook, Supporting Documentation, and Model Code Provisions," by G.S. Johnson, R.E. Sheppard, M.D. Quilici, S.J. Eder and C.R. Scawthorn, 4/12/99, (PB2000-101701, A18, MF-A04).

MCEER-99-0009 "Impact Assessment of Selected MCEER Highway Project Research on the Seismic Design of Highway Structures," by C. Rojahn, R. Mayes, D.G. Anderson, J.H. Clark, D'Appolonia Engineering, S. Gloyd and R.V. Nutt, 4/14/99, (PB99-162901, A10, MF-A02).

MCEER-99-0010 "Site Factors and Site Categories in Seismic Codes," by R. Dobry, R. Ramos and M.S. Power, 7/19/99, (PB2000-101705, A08, MF-A02).

MCEER-99-0011 "Restrainer Design Procedures for Multi-Span Simply-Supported Bridges," by M.J. Randall, M. Saiidi, E. Maragakis and T. Isakovic, 7/20/99, (PB2000-101702, A10, MF-A02).

MCEER-99-0012 "Property Modification Factors for Seismic Isolation Bearings," by M.C. Constantinou, P. Tsopelas, A. Kasalanati and E. Wolff, 7/20/99, (PB2000-103387, A11, MF-A03).

MCEER-99-0013 "Critical Seismic Issues for Existing Steel Bridges," by P. Ritchie, N. Kauhl and J. Kulicki, 7/20/99, (PB2000-101697, A09, MF-A02).

MCEER-99-0014 "Nonstructural Damage Database," by A. Kao, T.T. Soong and A. Vender, 7/24/99, (PB2000-101407, A06, MF-A01).

MCEER-99-0015 "Guide to Remedial Measures for Liquefaction Mitigation at Existing Highway Bridge Sites," by H.G. Cooke and J. K. Mitchell, 7/26/99, (PB2000-101703, A11, MF-A03).

MCEER-99-0016 "Proceedings of the MCEER Workshop on Ground Motion Methodologies for the Eastern United States," edited by N. Abrahamson and A. Becker, 8/11/99, (PB2000-103385, A07, MF-A02).

MCEER-99-0017 "Quindío, Colombia Earthquake of January 25, 1999: Reconnaissance Report," by A.P. Asfura and P.J. Flores, 10/4/99, (PB2000-106893, A06, MF-A01).

MCEER-99-0018 "Hysteretic Models for Cyclic Behavior of Deteriorating Inelastic Structures," by M.V. Sivaselvan and A.M. Reinhorn, 11/5/99, (PB2000-103386, A08, MF-A02).

MCEER-99-0019 "Proceedings of the 7th U.S.- Japan Workshop on Earthquake Resistant Design of Lifeline Facilities and Countermeasures Against Soil Liquefaction," edited by T.D. O'Rourke, J.P. Bardet and M. Hamada, 11/19/99, (PB2000-103354, A99, MF-A06).

MCEER-99-0020 "Development of Measurement Capability for Micro-Vibration Evaluations with Application to Chip Fabrication Facilities," by G.C. Lee, Z. Liang, J.W. Song, J.D. Shen and W.C. Liu, 12/1/99, (PB2000-105993, A08, MF-A02).

MCEER-99-0021 "Design and Retrofit Methodology for Building Structures with Supplemental Energy Dissipating Systems," by G. Pekcan, J.B. Mander and S.S. Chen, 12/31/99, (PB2000-105994, A11, MF-A03).

MCEER-00-0001 "The Marmara, Turkey Earthquake of August 17, 1999: Reconnaissance Report," edited by C. Scawthorn; with major contributions by M. Bruneau, R. Eguchi, T. Holzer, G. Johnson, J. Mander, J. Mitchell, W. Mitchell, A. Papageorgiou, C. Scaethorn, and G. Webb, 3/23/00, (PB2000-106200, A11, MF-A03).

MCEER-00-0002 "Proceedings of the MCEER Workshop for Seismic Hazard Mitigation of Health Care Facilities," edited by G.C. Lee, M. Ettouney, M. Grigoriu, J. Hauer and J. Nigg, 3/29/00, (PB2000-106892, A08, MF-A02).

MCEER-00-0003 "The Chi-Chi, Taiwan Earthquake of September 21, 1999: Reconnaissance Report," edited by G.C. Lee and C.H. Loh, with major contributions by G.C. Lee, M. Bruneau, I.G. Buckle, S.E. Chang, P.J. Flores, T.D. O'Rourke, M. Shinozuka, T.T. Soong, C-H. Loh, K-C. Chang, Z-J. Chen, J-S. Hwang, M-L. Lin, G-Y. Liu, K-C. Tsai, G.C. Yao and C-L. Yen, 4/30/00, (PB2001-100980, A10, MF-A02).

MCEER-00-0004 "Seismic Retrofit of End-Sway Frames of Steel Deck-Truss Bridges with a Supplemental Tendon System: Experimental and Analytical Investigation," by G. Pekcan, J.B. Mander and S.S. Chen, 7/1/00, (PB2001-100982, A10, MF-A02).

MCEER-00-0005 "Sliding Fragility of Unrestrained Equipment in Critical Facilities," by W.H. Chong and T.T. Soong, 7/5/00, (PB2001-100983, A08, MF-A02).

MCEER-00-0006 "Seismic Response of Reinforced Concrete Bridge Pier Walls in the Weak Direction," by N. Abo-Shadi, M. Saiidi and D. Sanders, 7/17/00, (PB2001-100981, A17, MF-A03).

MCEER-00-0007 "Low-Cycle Fatigue Behavior of Longitudinal Reinforcement in Reinforced Concrete Bridge Columns," by J. Brown and S.K. Kunnath, 7/23/00, (PB2001-104392, A08, MF-A02).

MCEER-00-0008 "Soil Structure Interaction of Bridges for Seismic Analysis," I. PoLam and H. Law, 9/25/00, (PB2001-105397, A08, MF-A02).

MCEER-00-0009 "Proceedings of the First MCEER Workshop on Mitigation of Earthquake Disaster by Advanced Technologies (MEDAT-1), edited by M. Shinozuka, D.J. Inman and T.D. O'Rourke, 11/10/00, (PB2001-105399, A14, MF-A03).

MCEER-00-0010 "Development and Evaluation of Simplified Procedures for Analysis and Design of Buildings with Passive Energy Dissipation Systems," by O.M. Ramirez, M.C. Constantinou, C.A. Kircher, A.S. Whittaker, M.W. Johnson, J.D. Gomez and C. Chrysostomou, 11/16/01, (PB2001-105523, A23, MF-A04).

MCEER-00-0011 "Dynamic Soil-Foundation-Structure Interaction Analyses of Large Caissons," by C-Y. Chang, C-M. Mok, Z-L. Wang, R. Settgast, F. Waggoner, M.A. Ketchum, H.M. Gonnermann and C-C. Chin, 12/30/00, (PB2001-104373, A07, MF-A02).

MCEER-00-0012 "Experimental Evaluation of Seismic Performance of Bridge Restrainers," by A.G. Vlassis, E.M. Maragakis and M. Saiid Saiidi, 12/30/00, (PB2001-104354, A09, MF-A02).

MCEER-00-0013 "Effect of Spatial Variation of Ground Motion on Highway Structures," by M. Shinozuka, V. Saxena and G. Deodatis, 12/31/00, (PB2001-108755, A13, MF-A03).

MCEER-00-0014 "A Risk-Based Methodology for Assessing the Seismic Performance of Highway Systems," by S.D. Werner, C.E. Taylor, J.E. Moore, II, J.S. Walton and S. Cho, 12/31/00, (PB2001-108756, A14, MF-A03).

MCEER-01-0001 "Experimental Investigation of P-Delta Effects to Collapse During Earthquakes," by D. Vian and M. Bruneau, 6/25/01, (PB2002-100534, A17, MF-A03).

MCEER-01-0002 "Proceedings of the Second MCEER Workshop on Mitigation of Earthquake Disaster by Advanced Technologies (MEDAT-2)," edited by M. Bruneau and D.J. Inman, 7/23/01, (PB2002-100434, A16, MF-A03).

MCEER-01-0003 "Sensitivity Analysis of Dynamic Systems Subjected to Seismic Loads," by C. Roth and M. Grigoriu, 9/18/01, (PB2003-100884, A12, MF-A03).

MCEER-01-0004 "Overcoming Obstacles to Implementing Earthquake Hazard Mitigation Policies: Stage 1 Report," by D.J. Alesch and W.J. Petak, 12/17/01, (PB2002-107949, A07, MF-A02).

MCEER-01-0005 "Updating Real-Time Earthquake Loss Estimates: Methods, Problems and Insights," by C.E. Taylor, S.E. Chang and R.T. Eguchi, 12/17/01, (PB2002-107948, A05, MF-A01).

MCEER-01-0006 "Experimental Investigation and Retrofit of Steel Pile Foundations and Pile Bents Under Cyclic Lateral Loadings," by A. Shama, J. Mander, B. Blabac and S. Chen, 12/31/01, (PB2002-107950, A13, MF-A03).

MCEER-02-0001 "Assessment of Performance of Bolu Viaduct in the 1999 Duzce Earthquake in Turkey" by P.C. Roussis, M.C. Constantinou, M. Erdik, E. Durukal and M. Dicleli, 5/8/02, (PB2003-100883, A08, MF-A02).

MCEER-02-0002 "Seismic Behavior of Rail Counterweight Systems of Elevators in Buildings," by M.P. Singh, Rildova and L.E. Suarez, 5/27/02. (PB2003-100882, A11, MF-A03).

MCEER-02-0003 "Development of Analysis and Design Procedures for Spread Footings," by G. Mylonakis, G. Gazetas, S. Nikolaou and A. Chauncey, 10/02/02, (PB2004-101636, A13, MF-A03, CD-A13).

MCEER-02-0004 "Bare-Earth Algorithms for Use with SAR and LIDAR Digital Elevation Models," by C.K. Huyck, R.T. Eguchi and B. Houshmand, 10/16/02, (PB2004-101637, A07, CD-A07).

MCEER-02-0005 "Review of Energy Dissipation of Compression Members in Concentrically Braced Frames," by K.Lee and M. Bruneau, 10/18/02, (PB2004-101638, A10, CD-A10).

MCEER-03-0001 "Experimental Investigation of Light-Gauge Steel Plate Shear Walls for the Seismic Retrofit of Buildings" by J. Berman and M. Bruneau, 5/2/03, (PB2004-101622, A10, MF-A03, CD-A10).

MCEER-03-0002 "Statistical Analysis of Fragility Curves," by M. Shinozuka, M.Q. Feng, H. Kim, T. Uzawa and T. Ueda, 6/16/03, (PB2004-101849, A09, CD-A09).

MCEER-03-0003 "Proceedings of the Eighth U.S.-Japan Workshop on Earthquake Resistant Design f Lifeline Facilities and Countermeasures Against Liquefaction," edited by M. Hamada, J.P. Bardet and T.D. O'Rourke, 6/30/03, (PB2004-104386, A99, CD-A99).

MCEER-03-0004 "Proceedings of the PRC-US Workshop on Seismic Analysis and Design of Special Bridges," edited by L.C. Fan and G.C. Lee, 7/15/03, (PB2004-104387, A14, CD-A14).

MCEER-03-0005 "Urban Disaster Recovery: A Framework and Simulation Model," by S.B. Miles and S.E. Chang, 7/25/03, (PB2004-104388, A07, CD-A07).

MCEER-03-0006 "Behavior of Underground Piping Joints Due to Static and Dynamic Loading," by R.D. Meis, M. Maragakis and R. Siddharthan, 11/17/03, (PB2005-102194, A13, MF-A03, CD-A00).

MCEER-03-0007 "Seismic Vulnerability of Timber Bridges and Timber Substructures," by A.A. Shama, J.B. Mander, I.M. Friedland and D.R. Allicock, 12/15/03.

MCEER-04-0001 "Experimental Study of Seismic Isolation Systems with Emphasis on Secondary System Response and Verification of Accuracy of Dynamic Response History Analysis Methods," by E. Wolff and M. Constantinou, 1/16/04 (PB2005-102195, A99, MF-E08, CD-A00).

MCEER-04-0002 "Tension, Compression and Cyclic Testing of Engineered Cementitious Composite Materials," by K. Kesner and S.L. Billington, 3/1/04, (PB2005-102196, A08, CD-A08).

MCEER-04-0003 "Cyclic Testing of Braces Laterally Restrained by Steel Studs to Enhance Performance During Earthquakes," by O.C. Celik, J.W. Berman and M. Bruneau, 3/16/04, (PB2005-102197, A13, MF-A03, CD-A00).

MCEER-04-0004 "Methodologies for Post Earthquake Building Damage Detection Using SAR and Optical Remote Sensing: Application to the August 17, 1999 Marmara, Turkey Earthquake," by C.K. Huyck, B.J. Adams, S. Cho, R.T. Eguchi, B. Mansouri and B. Houshmand, 6/15/04, (PB2005-104888, A10, CD-A00).

MCEER-04-0005 "Nonlinear Structural Analysis Towards Collapse Simulation: A Dynamical Systems Approach," by M.V. Sivaselvan and A.M. Reinhorn, 6/16/04, (PB2005-104889, A11, MF-A03, CD-A00).

MCEER-04-0006 "Proceedings of the Second PRC-US Workshop on Seismic Analysis and Design of Special Bridges," edited by G.C. Lee and L.C. Fan, 6/25/04, (PB2005-104890, A16, CD-A00).

MCEER-04-0007 "Seismic Vulnerability Evaluation of Axially Loaded Steel Built-up Laced Members," by K. Lee and M. Bruneau, 6/30/04, (PB2005-104891, A16, CD-A00).

MCEER-04-0008 "Evaluation of Accuracy of Simplified Methods of Analysis and Design of Buildings with Damping Systems for Near-Fault and for Soft-Soil Seismic Motions," by E.A. Pavlou and M.C. Constantinou, 8/16/04, (PB2005-104892, A08, MF-A02, CD-A00).

MCEER-04-0009 "Assessment of Geotechnical Issues in Acute Care Facilities in California," by M. Lew, T.D. O'Rourke, R. Dobry and M. Koch, 9/15/04, (PB2005-104893, A08, CD-A00).

MCEER-04-0010 "Scissor-Jack-Damper Energy Dissipation System," by A.N. Sigaher-Boyle and M.C. Constantinou, 12/1/04 (PB2005-108221).

MCEER-04-0011 "Seismic Retrofit of Bridge Steel Truss Piers Using a Controlled Rocking Approach," by M. Pollino and M. Bruneau, 12/20/04 (PB2006-105795).

MCEER-05-0001 "Experimental and Analytical Studies of Structures Seismically Isolated with an Uplift-Restraint Isolation System," by P.C. Roussis and M.C. Constantinou, 1/10/05 (PB2005-108222).

MCEER-05-0002 "A Versatile Experimentation Model for Study of Structures Near Collapse Applied to Seismic Evaluation of Irregular Structures," by D. Kusumastuti, A.M. Reinhorn and A. Rutenberg, 3/31/05 (PB2006-101523).

MCEER-05-0003 "Proceedings of the Third PRC-US Workshop on Seismic Analysis and Design of Special Bridges," edited by L.C. Fan and G.C. Lee, 4/20/05, (PB2006-105796).

MCEER-05-0004 "Approaches for the Seismic Retrofit of Braced Steel Bridge Piers and Proof-of-Concept Testing of an Eccentrically Braced Frame with Tubular Link," by J.W. Berman and M. Bruneau, 4/21/05 (PB2006-101524).

MCEER-05-0005 "Simulation of Strong Ground Motions for Seismic Fragility Evaluation of Nonstructural Components in Hospitals," by A. Wanitkorkul and A. Filiatrault, 5/26/05 (PB2006-500027).

MCEER-05-0006 "Seismic Safety in California Hospitals: Assessing an Attempt to Accelerate the Replacement or Seismic Retrofit of Older Hospital Facilities," by D.J. Alesch, L.A. Arendt and W.J. Petak, 6/6/05 (PB2006-105794).

MCEER-05-0007 "Development of Seismic Strengthening and Retrofit Strategies for Critical Facilities Using Engineered Cementitious Composite Materials," by K. Kesner and S.L. Billington, 8/29/05 (PB2006-111701).

MCEER-05-0008 "Experimental and Analytical Studies of Base Isolation Systems for Seismic Protection of Power Transformers," by N. Murota, M.Q. Feng and G-Y. Liu, 9/30/05 (PB2006-111702).

MCEER-05-0009 "3D-BASIS-ME-MB: Computer Program for Nonlinear Dynamic Analysis of Seismically Isolated Structures," by P.C. Tsopelas, P.C. Roussis, M.C. Constantinou, R. Buchanan and A.M. Reinhorn, 10/3/05 (PB2006-111703).

MCEER-05-0010 "Steel Plate Shear Walls for Seismic Design and Retrofit of Building Structures," by D. Vian and M. Bruneau, 12/15/05 (PB2006-111704).

MCEER-05-0011 "The Performance-Based Design Paradigm," by M.J. Astrella and A. Whittaker, 12/15/05 (PB2006-111705).

MCEER-06-0001 "Seismic Fragility of Suspended Ceiling Systems," H. Badillo-Almaraz, A.S. Whittaker, A.M. Reinhorn and G.P. Cimellaro, 2/4/06 (PB2006-111706).

MCEER-06-0002 "Multi-Dimensional Fragility of Structures," by G.P. Cimellaro, A.M. Reinhorn and M. Bruneau, 3/1/06.

MCEER-06-0003 "Built-Up Shear Links as Energy Dissipators for Seismic Protection of Bridges," by P. Dusicka, A.M. Itani and I.G. Buckle, 3/15/06 (PB2006-111708).

MCEER-06-0004 "Analytical Investigation of the Structural Fuse Concept," by R.E. Vargas and M. Bruneau, 3/16/06 (PB2006-111709).

MCEER-06-0005 "Experimental Investigation of the Structural Fuse Concept," by R.E. Vargas and M. Bruneau, 3/17/06 (PB2006-111710).

MCEER-06-0006 "Further Development of Tubular Eccentrically Braced Frame Links for the Seismic Retrofit of Braced Steel Truss Bridge Piers," by J.W. Berman and M. Bruneau, 3/27/06.

MCEER-06-0007 "REDARS Validation Report," by S. Cho, C.K. Huyck, S. Ghosh and R.T. Eguchi, 8/8/06.

MCEER-06-0008 "Review of Current NDE Technologies for Post-Earthquake Assessment of Retrofitted Bridge Columns," by J.W. Song, Z. Liang and G.C. Lee, 8/21/06.

MCEER-06-0009 "Liquefaction Remediation in Silty Soils Using Dynamic Compaction and Stone Columns," by S. Thevanayagam, G.R. Martin, R. Nashed, T. Shenthan, T. Kanagalingam and N. Ecemis, 8/28/06.

MCEER-06-0010 "Conceptual Design and Experimental Investigation of Polymer Matrix Composite Infill Panels for Seismic Retrofitting," by W. Jung, M. Chiewanichakorn and A.J. Aref, 9/21/06.

MCEER-06-0011 "A Study of the Coupled Horizontal-Vertical Behavior of Elastomeric and Lead-Rubber Seismic Isolation Bearings," by G.P. Warn and A.S. Whittaker, 9/22/06.

MCEER
EARTHQUAKE ENGINEERING TO EXTREME EVENTS
University at Buffalo, The State University of New York
Red Jacket Quadrangle ▪ Buffalo, New York 14261
Phone: (716) 645-3391 ▪ Fax: (716) 645-3399
E-mail: *mceer@buffalo.edu* ▪ WWW Site *http://mceer.buffalo.edu*
University at Buffalo *The State University of New York*

ISSN 1520-295X